Airborne measurements of gaseous sulfuric acid, atmospheric ions, and air pollutants in the troposphere and lower stratosphere above Europe

Dissertation

Marcel Zauner-Wieczorek, 2022

Airborne measurements of gaseous sulfuric acid, atmospheric ions, and air pollutants in the troposphere and lower stratosphere above Europe

Dissertation

zur Erlangung des Doktorgrades

der Naturwissenschaften

vorgelegt beim Fachbereich 11 Geowissenschaften / Geographie

der Johann Wolfang Goethe-Universität

in Frankfurt am Main

von

Marcel Zauner-Wieczorek

aus Mannheim

Frankfurt, 2022

(D30)

Vom Fachbereich 11 Geowissenschaften/Geografie der

Johann Wolfgang Goethe-Universität als Dissertation angenommen.

Dekan: Prof. Dr. Jürgen Runge

Gutachter: Prof. Dr. Joachim Curtius
PD Dr. Andreas Kürten

Datum der Disputation: 07.06.2023

Gewidmet denen,

die ausgeschlossen werden vom wissenschaftlichen System

aufgrund ihrer sozialen, ethnischen oder geografischen Herkunft,

einer Be_hinderung oder anderer Gründe.

Deutsche Zusammenfassung

Ob Klimawandel oder Luftverschmutzung: Die chemischen und physikalischen Prozesse in der Atmosphäre haben wichtige Auswirkungen auf die menschliche Gesundheit und Ökosysteme. Dabei ist die Atmosphäre mehr als ein Gemisch aus Stickstoff, Sauerstoff, Wasserdampf, Helium und Kohlenstoffdioxid. Es gibt zahlreiche Spurengase, deren Gesamtanteil am Volumen weniger als 1 % ausmacht. In dieser Arbeit werden Stickstoffoxide, Schwefeldioxid, Kohlenstoffmonoxid und Schwefelsäure näher betrachtet, die im Rahmen der flugzeugbasierten Messkampagne *Chemistry of the Atmosphere: field experiment in Europe* (CAFE-EU)/BLUESKY gemessen wurden.

Die Stickstoffoxide NO und NO_2, als NO_x zusammengefasst, besitzen hauptsächlich anthropogene Quellen, allen voran fossile Verbrennung und industrielle Prozesse. Zwischen NO und NO_2 besteht ein photochemisches Gleichgewicht, sodass in der Atmosphäre vor allem NO_2 in relevanten Konzentrationen vorkommt; dies wirkt aufgrund der Bildung von Salpetersäure, HNO_3, in wässriger Lösung beim Einatmen ätzend und ist entsprechend gesundheitsschädlich. Troposphärisches Ozon, O_3, wesentlicher Bestandteil von Sommersmog, wird hauptsächlich durch die Reaktion von NO mit Peroxiden (HO_2 und RO_2) gebildet. In der Stratosphäre entstehen NO_x hauptsächlich durch die Photodissoziation von Lachgas, N_2O, das aufgrund seiner langen Lebenszeit von der Tropo- in die Stratosphäre transportiert werden kann und dort die wichtigste Stickstoffquelle darstellt. In der Stratosphäre tragen NO_x zum katalytischen Abbaumechanismus des Ozons bei (Bliefert, 2002; Seinfeld and Pandis, 2016).

Schwefeldioxid, SO_2, ist ein toxisches Gas, dessen atmosphärische Quellen hauptsächlich anthropogen sind, nämlich fossile Verbrennung und industrielle Prozesse; Senken sind trockene und feuchte Deposition, wobei letztere zu saurem Regen führen kann. Seit den 1980ern sinken die globalen SO_2-Emissionen. SO_2 kann in der Atmosphäre zu Sulfat und Schwefelsäure oxidiert werden, was Hauptbestandteil des Wintersmogs ist. Der wichtigste Mechanismus ist die Oxidation mit dem Hydroxylradikal, $OH^{\cdot}$, unter Beteiligung von Wasserdampf. In der

Stratosphäre ist Carbonylsulfid, OCS, die wichtigste Schwefelquelle, da es analog zum N_2O dank seiner langen Lebenszeit von der Tropo- in die Stratosphäre transportiert werden kann (Bliefert, 2002; Seinfeld und Pandis, 2016). Typische Konzentrationen von Schwefelsäure sind 10^5 cm^{-3} nachts und 10^7 cm^{-3} tagsüber in der Troposphäre sowie 10^5 cm^{-3} tagsüber in der Stratosphäre (Clarke et al., 1999; Weber et al., 1999; Fiedler et al., 2005; Arnold, 2008; Kürten et al., 2016; Berresheim et al., 2000).

Kohlenstoffmonoxid, CO, ist ein toxisches Gas, das zu gleichen Teilen durch direkte Emissionen (v.a. Biomasseverbrennung und fossile Verbrennung) und In-situ-Oxidation (v.a. von Methan, Isopren und industriellen Kohlenwasserstoffen) in die Atmosphäre gelangt. Die Hauptsenke ist die Reaktion mit $OH^{\cdot}$ in der Troposphäre. Seit 2000 sinkt die globale CO-Konzentration (Bliefert, 2002).

Doch neben Gasen sind auch Aerosolpartikel fester Bestandteil des Gemisches Luft, welche luftgetragene feste oder flüssige Teilchen sind. Primäre Aerosolpartikel werden direkt als solche in die Atmosphäre emittiert, während sekundäre Aerosolpartikel in der Atmosphäre gebildet werden, indem gasförmige Vorläufersubstanzen mit geringer Flüchtigkeit auf primären Partikeln kondensieren oder durch Zusammenclustern und Anwachsen komplett neue Partikel bilden. Aerosolpartikel ermöglichen als Wolkenkondensationskeime erst die Bildung von Wolken und wirken somit – neben ihrem direkten reflektierenden Effekt – durch Änderung der Wolkenbedeckung und -eigenschaften insgesamt kühlend aufs Klima und beeinflussen die lokalen und globalen Wasserkreisläufe. Doch sie haben auch negative Auswirkungen auf die menschliche Gesundheit und sind für eine Verkürzung der durchschnittlichen Lebensdauer in Regionen mit hohen Feinstaubbelastungen verantwortlich (Seinfeld und Pandis, 2016; Bellouin et al., 2020; World Health Organization, 2016).

Neben den bisher betrachteten neutralen, also ungeladenen Gasen und Partikeln sind Ionen in der Gasphase sowie geladene Partikel ebenfalls Bestandteil der Atmosphäre. Sie spielen bei vielen atmosphärischen Prozessen eine wichtige Rolle, wie etwa bei Gewittern, Radiowellenübertragung und ionen-induzierter Nukleation von Aerosolpartikeln. Die Hauptquellen für Ionisation in der Tropo- und Stratosphäre ist die galaktische kosmische Strahlung, die entgegen ihrem Namen hauptsächlich aus Protonen und α-Partikeln (primäre Partikel genannt) besteht und in der Erdatmosphäre durch Kollision mit Luftmolekülen Teilchenschauer von sekundären Partikeln (u.a. Myonen, Pionen und Neutrinos) hervorruft. Die primären und sekundären Partikel können die Luftmoleküle ionisieren unter Entstehung von N^+, N_2^+, O^+, O_2^+ und Elektronen. Sauerstoff reagiert rasch mit letzteren zu O^- und O_2^-. Diese

Kationen und Anionen reagieren weiter, bis Ionenclustern der Summenformeln $(HNO_3)_n(H_2O)_mNO_3^-$ und $H^+(H_2O)_n(B)_m$ gebildet werden, wobei B Basen wie Methanol, Aceton, Ammoniak oder Pyridin sind. Weitere Ionisationsquellen sind der Zerfall des Radioisotops ^{222}Rn in Bodennähe und ionisierende Solarstrahlung oberhalb der Stratosphäre. Atmosphärische Ionen haben zwei wichtige Senken: die Wiedervereinigung, auch Rekombination genannt, bei der sich ein Kation und ein Anion gegenseitig neutralisieren sowie das Anhaften an Aerosolpartikeln. Letztere Senke ist vor allem in der Troposphäre aufgrund der relativ hohen Konzentration an Aerosolpartikeln relevant (Arnold, 2008; Viggiano und Arnold, 1995; Bazilevskaya et al., 2008; Hirsikko et al., 2011).

Die Ion-Ion-Rekombination kann durch den Rekombinationskoeffizienten α beschrieben werden, der als Reaktionsratenkoeffizient die Einheit $cm^{-3}\ s^{-1}$ besitzt und temperatur- und druckabhängig ist. Ein Übersichtsartikel über die verschiedenen Theorien und Parametrisierungen für α in Abhängigkeit von Druck und Temperatur bzw. Höhe, dessen Ziel es ist, das bestehende Wissen zusammenzufassen und der Community der Atmosphärenwissenschaften zugänglich zu machen, ist Teil dieser Dissertation (Zauner-Wieczorek et al., 2022b). Thomson hat eine Theorie zur Beschreibung von α entwickelt, die einem thermodynamischen Ansatz folgt. Zentraler Bestandteil der Theorie ist der Kollisionsradius d um die Ionen, bei dem sie sich gegenseitig elektrisch anziehen (Thomson und Rutherford, 1896; Thomson, 1924). Auf Grundlage von Thomsons Theorie wurden Parametrisierungen entwickelt, die makroskopische Größen wie die Temperatur und den Druck enthielten, so etwa die Formel von Israël (1957). Für Standardbedingungen (1013 hPa, 273 K) ist von einem Wert von $1{,}7 \cdot 10^{-6}\ cm^{-3}\ s^{-1}$ für α auszugehen (Lenz, 1932; Israël, 1957; Bates, 1982). In den 1970er Jahren haben Gringel et al. (1978), Rosen und Hofmann (1981) und Morita (1983) Ballonmessungen durchgeführt, bei denen sie gleichzeitig die Ionisierungsrate und die elektrische Mobilität bzw. Ionenkonzentration gemessen haben, um daraus α für einen Bereich zwischen 10 und 45 km Höhe abzuleiten. Oberhalb von 10 km Höhe weist α einen abnehmenden Trend auf. Für die Troposphäre ist davon auszugehen, dass α etwa konstant bleibt, wobei hier genaue Beobachtungen aus Feldmessungen fehlen. Auf den oben genannten Ballonmessungen basieren weitere Parametrisierungen, wie etwa die von Arijs et al. (1983) und Brasseur und Chatel (1983); die Monte-Carlo-Simulation von Bates (1982) stimmt mit den Beobachtungen überein. Außerdem wurden in Zauner-Wieczorek et al. (2022b) Theorien, die die Anhaftung von Ionen an Aerosolpartikel beschreiben wie etwa die Theorie von Hoppel und Frick (1986), auf die Ion-Ion-Rekombination angewandt, indem für das Aerosolpartikel angenommen wurde, dass es so groß wie ein Ion und einfach geladen sei. Die verschiedenen

Theorien und Parametrisierungen wurden für die Bedingungen der US-Standardatmosphäre mit den Feld- und Modelldaten sowie den Labordaten von Franchin et al. (2015) verglichen. Keine der Theorien konnte für den betrachteten Höhenbereich von 0–50 km die Daten vollumfassend reproduzieren. Für 0–20 km bzw. 0–22 km empfehlen sich jeweils die Parametrisierungen von Israël (1957) und Brasseur und Chatel (1983); für den Bereich von 10–25 km die höhenabhängige Parametrisierung von Bates (1985); oberhalb von 25 km die Formel von Smith und Adams (1982) und oberhalb von 30 km die Theorie von Hoppel und Frick (1986). Der Ion-Ion-Rekombinationskoeffizient findet zum Beispiel Anwendung bei der Berechnung der Anzahlkonzentration der gasförmigen Schwefelsäure aus Messungen von Nitrat- und Hydrogensulfat-Ionen in der Atmosphäre, wie von Zauner-Wieczorek et al. (2022a) für Messdaten der CAFE-EU/BLUESKY-Kampagne beschrieben.

Die Messkampagne CAFE-EU/BLUESKY fand vom 16. Mai bis 9. Juni 2020 über Westeuropa während der Lockdowns in vielen Ländern bei reduziertem Luft- und Straßenverkehr und industrieller Produktion statt. Die Forschungsflugzeuge HALO und Falcon vom Deutschen Zentrum für Luft- und Raumfahrt (DLR) waren mit Instrumenten ausgestattet, die zahlreiche Spurengase (u.a. NO_x, O_3, SO_2, H_2SO_4, $OH^{\cdot}$), Aerosolparameter (u.a. Konzentration, chemische Zusammensetzung, Größenverteilung) sowie meteorologische und physikalische Parameter (u.a. Temperatur, Druck, Windgeschwindigkeit, Strahlung) gemessen haben. Die Flüge haben einen Bereich von Spanien bis vor die Küste Irlands abgedeckt, mit Fokus auf urbanen Agglomerationen, kontinentalem Hintergrund, Ausfluss hochreichender konvektiver Wolken und der maritimen Grenzschicht. In Voigt et al. (2022) wurden die Details der Kampagne und Instrumentierung sowie die wichtigsten Ergebnisse beschrieben. Über dem Großraum Frankfurt konnte ein Rückgang von reaktiven Stickstoffverbindungen (NO_y) von 40–70 % und von Kohlenstoffmonoxid von 20–40 % im Vergleich zu 1994–2005 beobachtet werden. Auch NO_x-Messungen des Nadir-Scanning-UV/VIS-Spektrometers GOME-2 auf dem MetOp-Satelliten zeigen eine globale Reduktion von NO_x um 12 % und bis zu 55 % über urbanen Ballungsräumen im Vergleich zum Zeitraum 2015–2019. Diese Reduktionen sind neben veränderten meteorologischen Rahmenbedingungen auf die verringerten Emissionen von Luftfahrt, Transport auf der Straße und Industrie zurückzuführen. Simulationen mit dem MECO(n)-Modell zeigten außerdem eine Reduktion von bis zu 10 % für O_3, bis zu 13 % für CO und bis zu 34 % für NO_y für ein Lockdown-Szenario im Vergleich zu einem Business-as-usual-Szenario. Der NO_y-Rückgang war hauptsächlich den verringerten Emissionen beim Transport in der Luft und auf der Straße zuzuordnen. Darüber hinaus wurde am 1. Juni 2020 eine Reduktion des CO-Mischungsverhältnisses über der Po-Ebene im Vergleich zur

HYSPLIT-Simulation festgestellt, bei der keine Emissionsreduktion implementiert war. Schwefeldioxid wies in der Stratosphäre erhöhte Hintergrundwerte auf, die auf den Vulkanausbruch des Raikoke im Jahr 2019 zurückzuführen sind.

Neben den Spurengasen wurden auch Aerosolpartikel während CAFE-EU/BLUESKY untersucht. Unterhalb von 5 km war die Aerosolmassenkonzentration von Aerosolpartikeln mit einem Durchmesser $\leq 1\,\mu m$ (PM1) um einen Faktor 2–3 niedriger als bei früheren Messkampagnen über Europa. Die Masse von Black Carbon war durch Lockdown-Effekte um bis zu 40 % reduziert. Die Konzentration von Aerosolpartikeln > 18 nm war zwischen 4–11 km um 30–70 % reduziert im Vergleich zu 2005–2015. Außerdem konnte eine Verringerung der aerosolbasierten optischen Dicke von 40 % im Vergleich zu 2015–2019 festgestellt werden. Das Spektrum der nach unten gerichteten spektralen Irradianz für einen solaren Zenithwinkel von 45° war während CAFE-EU/BLUEKSY zu kürzeren Wellenlängen verschoben, wodurch die Farbe des Himmels vom menschlichen Auge als blauer wahrgenommen wurde. Darüber hinaus führte die starke Verringerung des Luftverkehrs zu einer geringeren Contrail-Cirrus-Bedeckung und damit zu einer verringerten cirrusbasierten optischen Dicke.

Während CAFE-EU/BLUESKY wurden mithilfe der Ionenquelle *Switchable corona-powered ion source* (SCORPION), die an ein Flugzeit-Massenspektrometer (TOF-MS) gekoppelt und auf HALO installiert war u.a. Schwefelsäure (H_2SO_4), C_2-Amine (z.B. Dimethylamin, DMA, $(CH_3)_2NH$) und Methansulfonsäure (MSA, CH_3SO_3H) gemessen. Diese Ergebnisse werden an anderer Stelle veröffentlicht. Die SCORPION-Quelle ist eine neu entwickelte Ionenquelle, die auf dem Prinzip der chemischen Ionisation durch Corona-Entladung basiert. Massenspektrometer können geladene Moleküle nach ihrem Masse-zu-Ladungs-Verhältnis trennen und detektieren. Um neutrale Moleküle nachzuweisen, müssen diese in einer Ionenquelle zunächst ionisiert werden. Neben der klassischen, „harten“ Elektronenstoß- oder der „weicheren“ Elektrospray-Ionisierung stellt die chemische Ionisation eine weitere Methode dar, um Analyten „weich“, also möglichst ohne Fragmentierung zu ionisieren. Im Falle der SCORPION-Quelle wird gasförmige Salpetersäure durch Corona-Entladung zu Nitrationen und -clustern ($(HNO_3)_{0–2}NO_3^-$) ionisiert. Diese Reagenzionen können wiederum neutrale Analytmoleküle durch Ladungstransfer oder Adduktbildung ionisieren. Das SCORPION-System verfügt über einige speziell an den Einsatz im Flugzeug angepasste Eigenschaften. So ist der Fluss durch die Einlassleitung hoch, um den verlustreichen Kontakt zu den Wänden zu minimieren. Ein automatisiertes Druckstufensystem bewirkt einen konstanten Druck von 200 hPa in der Ionenquelle trotz unterschiedlicher Außendrücke. Zudem wird durch ein

Gegenstromprinzip im Bauteil der Coronaentladung verhindert, dass reaktive Nebenprodukte in die Ionen-Molekül-Reaktionszone gelangen, wo sie mit den Analyten reagieren und so die Messergebnisse verfälschen könnten.

Neben der Konfiguration im chemischen Ionisationsmodus kann das SCORPION-TOF-MS aber auch im *atmospheric pressure interface* (APi) Modus betrieben werden, d.h. die Coronaspannung wird ausgeschaltet und damit die Bildung von Reagenzionen gestoppt; natürliche Ionen können so gemessen werden. Die Ergebnisse dieser Messungen während CAFE-EU/BLUESKY für den Höhenbereich 4,7–13,4 km sind in Zauner-Wieczorek et al. (2022a) beschrieben. Es wurden übereinstimmend mit der Literatur die nitratbasierten Ionen $(HNO_3)_{0–2}NO_3^-$ und die sulfatbasierten Ionen $(H_2SO_4)_{0–1}HSO_4^-$ und $(HNO_3)HSO_4^-$ im negativen Modus sowie protoniertes Pyridin ($H^+(C_5H_5N)$) im positiven Modus detektiert. Die Zählraten der nitratbasierten Ionen wiesen einen positiven Trend mit der Höhe auf, während die sulfatbasierten Ionen keinen signifikanten Trend zeigten. Das Maximum des protonierten Pyridins zeigte sich zwischen 4,6–8,5 km Höhe. Aus dem Verhältnis der nitratbasierten und sulfatbasierten Ionen konnte unter Zuhilfenahme der Parametrisierung des Ion-Ion-Rekombinationskoeffizienten (vgl. Zauner-Wieczorek et al., 2022b) die Anzahlkonzentration von gasförmiger Schwefelsäure bestimmt werden. In der Höhenklasse von 8,7–9,2 km wurde die höchste durchschnittliche Konzentration von $7{,}8 \cdot 10^5$ cm^{-3} festgestellt. Darüber zeigte sich ein abnehmender Trend mit durchschnittlich nur noch $1{,}9 \cdot 10^5$ cm^{-3} in der obersten Höhenklasse von 13,4 km. Zudem wurde beim Flug durch eine Mischphasenwolke auf 5,3 km Höhe bei 261 K Außentemperatur ein Ereignis von erhöhter Ionenzählrate (insbesondere nitratbasierte Ionen), Partikelkonzentration (Partikel < 100 nm) und relativer Luftfeuchte aufgezeichnet werden. Dieses Ereignis kann womöglich durch den balloeketrischen Effekt (Christiansen, 1913) beim Zerplatzen von flüssigen Wolkentröpfchen auf der Oberfläche des Flugzeugs oder des Einlasses erklärt werden.

Die CAFE-EU/BLUESKY-Kampagne stellte eine einzigartige Möglichkeit dar, Luftschadstoffe während einer Zeit massiv reduzierter Emissionen durch die Industrie und den Transport in der Luft und auf der Straße zu messen. Die Untersuchung natürlicher Ionen und der daraus abgeleiteten Schwefelsäurekonzentration stellen die ersten Messungen in der oberen Troposphäre und unteren Stratosphäre dar, die seit fast drei Jahrzehnten durchgeführt wurden.

Durch diese Dissertation wurde somit ein Beitrag zur Atmosphärenwissenschaft geleistet, um die chemischen Prozesse in der Atmosphäre besser zu verstehen, die letztendlich auch auf die menschliche Gesundheit, Ökosysteme und das Klima wirken.

Table of content

1 Motivation

Humans have left an impact on their surroundings ever since. Commencing with the Industrial Revolution, when the enormous exploitation of fossil fuels became a central part of the upcoming new economic system in the Global North – Capitalism –, the impacts of this grew to geological scales because the activity of humans not only affected their direct surroundings and had a short temporal effect, but also global and permanent effects, e.g. the addition to the natural greenhouse effect by the continuous emission of carbon dioxide to the atmosphere through fossil fuel burning. In 1856, the greenhouse effect of carbon dioxide was first described by Eunice Foote (who has only received credit for this discovery recently; Foote, 1856), however, it has taken societies more than 150 years to grasp the full impact of their behaviour, namely that global warming leads to extreme weather conditions, hot temperatures, and a rise in sea level that makes vast areas uninhabitable and causes the extinction of numerous species (IPCC AR6 Working Group I, 2021). In addition, land use change has resulted in desertification and loss in biodiversity and air pollutants such as particulate matter, sulfur dioxide, or nitrogen dioxide that have adverse health effects on humans and cause a decreased average life expectancy especially in industrialised regions (World Health Organization, 2016). These are further example of the detrimental effects caused by the expansive and intensive economic activities of humans, especially in the societies of the Global North.

In order to understand these impacts, research in various disciplines is necessary to uncover the related mechanisms and processes. This research should be conducted not for the sake of research itself, but for the production of knowledge from which societies and especially vulnerable groups can benefit. With regards to climate change and air pollution, atmospheric scientists need to investigate the chemical and physical mechanisms that lead to adverse climate or pollution effects. This is inevitable should societies wish to preserve and enhance the safety and well-being of all people and ecosystems.

This dissertation seeks to contribute a small piece to the vast puzzle of atmospheric sciences. During the first COVID-19 lockdown in Europe, the emissions of some pollutants were cut enormously, especially in the aviation and ground-based travel sector and the manufacturing industry. One focus of this work is, thus, to investigate the effects of the lockdown on certain air pollutants during the Chemistry of the Atmosphere Field Experiment in Europe (CAFE-EU)/BLUEKSY measurement campaign such as nitrogen oxides, sulfur dioxide, ozone, and particulate matter which can have severe adverse health effects especially in urban areas. Moreover, climate change, as a global and long-term phenomenon, is fuelled by different chemical species and their respective emission processes. Aerosol particles have an overall cooling effect on the climate (Bellouin et al., 2020) and the knowledge of their formation and their effects on the climate is important in order to tailor the responses of politics and societies on climate change mitigation and adaptation. Therefore, another focus of this work is to investigate the concentrations and spatial distribution of a precursor gas for aerosol nucleation – sulfuric acid – in order to broaden the data set that, eventually, chemical and climate models can be based on, especially in the free troposphere and lower stratosphere where field data of the precursor gases are scarce. A third focus is on the atmospheric ions that influence many atmospheric processes such as ion-induced aerosol nucleation. Many theories have been developed to describe the recombination of gas-phase ions. Therefore, in this dissertation, these theories are compared to find favourable approaches for atmospheric conditions.

The topics of this dissertation address different short- and long-term processes that affect the climate as well as local air quality. Ultimately, these pieces are interrelated and are part of the huge puzzle of atmospheric science that needs to be solved for the benefit of present and future societies.

2 Introduction

2.1 Constituents of the atmosphere

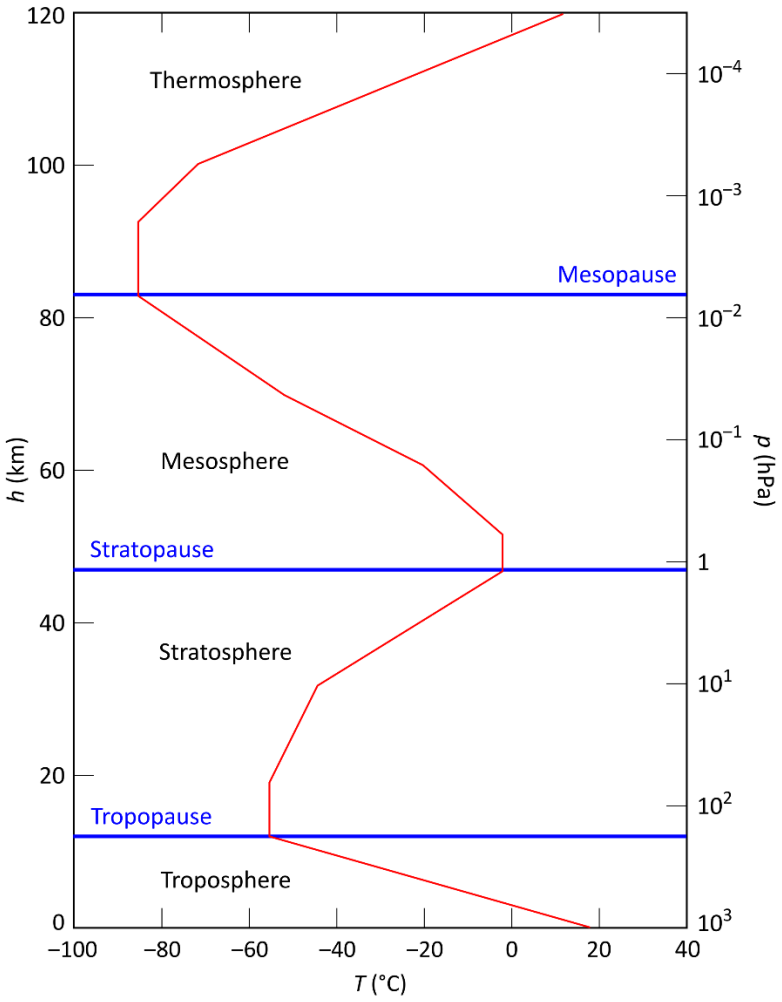

Figure 1: Layers of the atmosphere and temperature trends (red line) after Seinfeld and Pandis (2016).

The Earth is surrounded by a layer of gases, the atmosphere, which is held by the Earth's gravity. Due to the decreasing gravitational effect with increasing altitude, the density of the atmosphere and, therefore, also the pressure are the greatest at the surface and continuously decrease with increasing altitude. The atmosphere can be divided into several layers with certain characteristics. From 0 km to approximately 12 km altitude, the troposphere is characterised by

a decreasing trend of temperature and a turbulent, vertically well-mixed air mass. The border to the next sphere, the stratosphere, is called the tropopause (TP); this is higher at the equator (ca. 17 km) and lower at the poles (ca. 6 km), while its height is furthermore dependent on the season. At the TP, the temperature decrease ceases and is inverted further in the stratosphere which ranges up to an altitude of 45–55 km; this is where the stratopause lies. The above-lying mesosphere is characterised by a negative temperature gradient up to the mesopause at approximately 80–90 km altitude. Above the mesopause, the thermosphere follows with a positive temperature gradient; the thermosphere ends at the thermopause at approximately 500 km altitude. Above the thermopause, the exosphere represents the outermost layer of the Earth's atmosphere, ranging up to approximately 10,000 km (Seinfeld and Pandis, 2016). Figure 1 shows the layers of the atmosphere up to an altitude of 120 km and the corresponding temperature trends.

The atmosphere's main constituents are nitrogen (N_2, 78 %), oxygen (O_2, 21 %), and argon (Ar, 0.9 %). The content of water vapour (H_2O) is highly variable and generally decreases with increasing altitude. Close to the ground, a mixing ratio of up to 3 % is possible. There is an almost endless number of trace gases that add up to < 1 % of the atmosphere (Seinfeld and Pandis, 2016), however, these can have a big impact on meteorology, the climate, ecosystems, and human health. Of these trace gases, the so-called greenhouse gases (GHGs) have experienced the greatest attention in public discussion because of their relevance to the climate. Without GHGs, life on Earth, as we know it, would not be possible because they ensure that the average surface temperature on our planet is +15 °C. Without the naturally occurring GHGs, of which H_2O and carbon dioxide (CO_2) are the most important, the temperature would be –18 °C on average and the majority of the Earth would be uninhabitable. However, the ever-increasing anthropogenic emissions of CO_2, methane (CH_4), and nitrous oxide (N_2O) fuel the greenhouse effect causing the global mean surface temperature to rise continuously. The global mean temperature increased by 1.1 K between 1850–1900 and the 2010s; the global mean mixing ratio of CO_2 rose from 280 ppm in pre-industrial times to more than 410 ppm today. Depending on the emission scenario, the global mean temperature will rise by another 0.4 to 4.4 K by 2081–2100. This global warming leads to irrevocable changes of geophysical and biological cycles, extreme weather conditions, and the rising of the sea level, amongst other effects (IPCC AR6 Working Group I, 2021). Moreover, some trace gases can have more direct adverse health effects, for instance, due to irritation and damage of the respiratory tract or due to the pollution of the biosphere.

Some trace gases with low volatilities have the potential to form aerosol particles from the gas phase. Apart from these, aerosol particles can also be emitted as such into the atmosphere. Aerosol particles form part of the mixture of the air, which is only regarded on a first approximation as a mixture of gases. Besides neutral gases and particles, gas-phase ions are also part of the atmosphere. In the following subchapters, some important chemical species in the atmosphere are introduced that were measured during the CAFE-EU/BLUEKSY measurement campaign, which was aimed to investigate the effect of the COVID lockdown on atmospheric pollutants, trace gases, aerosol particles, and atmospheric ions (see Sect. 3.2). Trace gases that are either responsible for urban air pollution (NO_x, SO_2, CO) or participate in the formation of aerosol particles (H_2SO_4) are introduced in Sect. 2.1.1, followed by aerosol particles in Sect. 2.1.2, while atmospheric ions will be described in Sect. 2.1.3.

2.1.1 Trace gases

In the atmosphere there exist numerous trace gases. In this chapter, some of the most relevant trace gases that were measured during the CAFE-EU/BLUESKY campaign are introduced with respect to their formation and emission, their impact on atmospheric chemistry, and their environmental relevance; these gases include nitrogen oxides, sulfur dioxide, sulfuric acid, and carbon monoxide.

Nitrogen oxides (NO_x)

The nitrogen oxides NO and NO_2 are typically referred to as NO_x. The main sources of NO_x in the troposphere are anthropogenic sources (total: 37.5 Tg N a^{-1}) of which fossil fuel combustion and industrial processes (28.3 Tg N a^{-1}) are the most dominant, along with biomass burning and biofuel burning (5.5 Tg N a^{-1}) and agriculture (3.7 Tg N a^{-1}). The natural sources of NO_x (total: 11.3 Tg N a^{-1}) are lightning (4 Tg N a^{-1}) and soils (7.3 Tg N a^{-1}) (Seinfeld and Pandis, 2016), while the main sink is wet deposition (Bliefert, 2002).

There exists a photochemical equilibrium between NO_2 and NO under participation of O, O_2, and O_3 according to Reactions (R1) to (R3) (Bliefert, 2002):

$$NO_2 + h\nu\ (\lambda < 420\ \text{nm}) \rightarrow NO + O \quad \text{(R1)}$$

$$O + O_2 + M \rightarrow O_3 + M \quad \text{(R2)}$$

$$O_3 + NO \rightarrow O_2 + NO_2 \quad \text{(R3)}$$

Both NO and NO_2 are toxic gases, although atmospheric NO has no significant health effects due to its low concentration in the atmosphere. NO_2, on the other hand, is very water soluble, forming nitric acid, HNO_3, with water. In the respiratory system, therefore, NO_2 is converted to HNO_3 which causes irritation of the mucous membrane, coughing, pulmonary oedema, and eventually death. NO_2 also adversely affects certain animals and plants, even at low mixing ratios (Bliefert, 2002).

NO_x play a crucial role in atmospheric chemistry. Tropospheric ozone, O_3, is mainly produced via the reaction of peroxides (HO_2 and RO_2) with NO. Only 10–20 % of tropospheric ozone originates from the stratosphere (Seinfeld and Pandis, 2016). Thus, local concentrations of tropospheric ozone are influenced by the NO_x concentration. High NO_x levels can lead to high (and potentially harmful) ozone levels. Summer smog, also called photochemical smog or Los Angeles smog, is characterised by high levels of ozone and is formed when high levels of UV light, NO_x, and volatile organic compounds (VOCs) coincide, e.g. in large cities during sunny days in summer (Haagen-Smit, 1952; Sillman et al., 1990).

The source of stratospheric NO_x, on the other hand, is the photodissociation of N_2O (see Reactions (R4) and (R5)) which has a longer lifetime than the reactive nitrogen oxide species NO_y and can, therefore, be transported from the troposphere into the stratosphere (Seinfeld and Pandis, 2016). NO_y is the sum of NO_x and all of their oxidation products in the atmosphere, including HNO_3, nitrous acid (HONO), the nitrate radical ($NO_3^{\cdot}$), dinitrogen pentoxide (N_2O_5), and peroxyacetyl nitrate (PAN, $CH_3C(O)OONO_2$) (Seinfeld and Pandis, 2016).

$$N_2O + h\nu \rightarrow N_2 + O(^1D) \quad \text{(R4)}$$

$$N_2O + O(^1D) \rightarrow 2\ NO \quad \text{(R5)}$$

NO_x contributes to the catalytical depletion mechanism of stratospheric ozone (see Reactions (R6) and (R7)) (Seinfeld and Pandis, 2016; Crutzen, 1970; Johnston, 1971):

$$NO + O_3 \rightarrow NO_2 + O_2 \quad \text{(R6)}$$

$$NO_2 + O \rightarrow NO + O_2 \quad \text{(R7)}$$

Sulfur dioxide (SO_2)

Sulfur dioxide is a toxic gas whose main sources in the atmosphere are anthropogenic. The global emission of SO_2 is estimated to be 64.2 Tg S a^{-1}, of which fossil fuel combustion and industry are responsible for the largest part (56.3 Tg S a^{-1}), followed by volcanoes

(6.6 Tg S a^{-1}) and biomass burning (1.3 Tg S a^{-1}) (Lee et al., 2011). Background mixing ratios are 20–50 ppt in the marine boundary layer and up to 1 ppb for continental air masses, while urban levels can be as high as several hundred ppb. The sinks of SO_2 are wet and dry deposition. Its atmospheric lifetime is around 1 week, while the tropospheric lifetime is 2 days (Seinfeld and Pandis, 2016). SO_2 can be oxidised to sulfate and sulfuric acid in the liquid phase (through O_3 and H_2O_2) and gas phase, respectively (Seinfeld and Pandis, 2016). SO_2 and sulfate particles are responsible for the so-called London smog or winter smog that causes severe respiratory diseases that may become fatal, as was the case in London in 1952, when thousands of people died (Bliefert, 2002). The wet deposition of SO_2 lowers the pH value of the rain leading to acid rain, acidification of lakes and soils, and damage to foliage (Bliefert, 2002). The global emissions of SO_2 have reduced since the 1980s by means of the desulfurisation of fossil fuels and waste gases in combustion processes (Bliefert, 2002).

Sulfuric acid (H_2SO_4)

Sulfuric acid, H_2SO_4, is the oxidation product of sulfuric compounds such as SO_2 and carbonyl sulfide, OCS. In the gas phase, the oxidation of SO_2 with the hydroxyl radical $OH^{\cdot}$ is dominant (see Reactions (R8) to (R10)) (Stockwell and Calvert, 1983; Jayne et al., 1997). The hydroxyl radical is formed from the photodissociation of O_3 to $O(^1D)$ and O_2 and the subsequent reaction of $O(^1D)$ with H_2O to $OH^{\cdot}$ (Seinfeld and Pandis, 2016). As ozone photolysis requires sunlight, $OH^{\cdot}$ and H_2SO_4 are, thus, formed during daytime only. Typical orders of magnitude for the number concentrations of sulfuric acid in the troposphere are 10^5 cm^{-3} during nighttime and 10^6 to 10^7 cm^{-3} during daytime, while in the lower stratosphere, they are in the order of 10^5 cm^{-3} during daytime (Clarke et al., 1999; Weber et al., 1999; Fiedler et al., 2005; Arnold, 2008; Kürten et al., 2016; Berresheim et al., 2000).

$$SO_2 + OH^{\cdot} + M \rightarrow HSO_3^{\cdot} + M \quad \text{(R8)}$$

$$HSO_3^{\cdot} + O_2 \rightarrow HO_2^{\cdot} + SO_3 \quad \text{(R9)}$$

$$SO_3 + 2\,H_2O \rightarrow H_2SO_4 + H_2O \quad \text{(R10)}$$

In the stratosphere, OCS is the most important precursor to sulfuric acid and sulfate because OCS has a lifetime of approximately 7 years in the troposphere and is, thus, the only sulfur compound that is transported to the stratosphere in an appreciable amount. The only exception is SO_2 that is occasionally directly injected into the stratosphere through strong volcanic eruptions (Seinfeld and Pandis, 2016). In the stratosphere, OCS is photolysed and transformed

to SO_2 (Crutzen, 1976), which then undergoes further oxidation to sulfuric acid as described above. The main sources of OCS are emissions of OCS and the precursors carbon disulfide, CS_2, and dimethyl sulfide (DMS), $(CH_3)_2S$, from the oceans (279 Gg S a^{-1}) and anthropogenic sources of OCS and CS_2 (180 Gg S a^{-1}). The main sinks are the uptake by plants (238 Gg S a^{-1}) and soils (130 Gg S a^{-1}) as well as the reaction with $OH^{\cdot}$ (94 Gg S a^{-1}) (Seinfeld and Pandis, 2016).

Carbon monoxide (CO)

Carbon monoxide is a toxic gas whose sources to the atmosphere are direct emissions (1,230–1,400 Tg CO a^{-1}) and in-situ oxidation (1,450–1,550 Tg CO a^{-1}) in approximately equal parts. The sources of direct emissions are mainly anthropogenic via biomass burning (700 Tg CO a^{-1}) and fossil fuel burning (650 Tg CO a^{-1}), while natural sources (200 Tg CO a^{-1}) only account for a smaller proportion. The precursors for the in-situ oxidation are mainly methane, isoprene, and industrial hydrocarbons (Seinfeld and Pandis, 2016). The atmospheric lifetime of CO is 1 to 4 months (IPCC AR6 Working Group I, 2021). The sinks of CO are the reaction with $OH^{\cdot}$ in the troposphere (2,050 Tg CO a^{-1}) and, to a much smaller extent, the uptake by soils (250 Tg CO a^{-1}) and the photochemical depletion in the stratosphere (107 Tg CO a^{-1}) (Bliefert, 2002). The tropospheric mixing ratio of CO is approximately 100 ppb in the northern and approximately 50 ppb in the southern hemisphere (Bliefert, 2002). Since 2000, the global burden of CO has decreased (IPCC AR6 Working Group I, 2021).

2.1.2 Aerosol particles

As a first approximation, the atmosphere can be considered as a mixture of gases, however, it also contains airborne particles in the size range from 1 nm to 50 µm. Thus, technically speaking, the atmosphere is an aerosol, i.e. a mixture of gases and particulate matter that is suspended in the air. The suspended particles are called aerosol particles (Seinfeld and Pandis, 2016).

One can distinguish primary and secondary aerosol particles based on their source. Primary aerosol particles are emitted as such into the atmosphere; examples of natural sources of primary aerosol particles are mineral dust, pollen, and sea salt. Soot and tyre wear particles are examples of anthropogenic origin. On the other hand, secondary particles are formed via condensation of low volatile gases on existing aerosol particles or in situ from the gas phase in a process called new particle formation (NPF). In this process, gas molecules of substances with low volatilities cluster together as shown in Figure 2. The volatility describes the eagerness of

a compound to be in the vapour phase. This is dependent on the compound-specific evaporation enthalpy and the temperature (Donahue et al., 2011). The volatility of a compound can be classified along the spectrum of the vapour saturation concentration into discrete volatility bins based on the volatility basis set (VBS) as performed for organic compounds (Donahue et al., 2011; Donahue et al., 2012; Schervish and Donahue, 2020). Generally speaking, atmospheric trace gases with large volatilities contribute to chemical reactions in the gas and liquid phase, whereas gases with low volatilities tend to interact with aerosol particles or change their aggregation state to the solid or liquid phase.

The aforementioned initial cluster can grow in size through condensation of additional molecules or shrink by the re-evaporation of molecules (see Figure 2). Once the critical size of approximately 1 nm is reached, the re-evaporation ceases and it is defined as an aerosol particle. Further particle growth is possible through further condensation of vapours on the existing particle or through coagulation of two or more particles (Seinfeld and Pandis, 2016). Aerosol particles can be characterised by their size or chemical composition. For their characterisation by particle size, different modes are defined: the nucleation mode (< 10 nm in diameter), the Aitken mode (10–100 nm), the accumulation mode (0.1–2.5 µm), and the coarse mode (> 2.5 µm) (Seinfeld and Pandis, 2016).

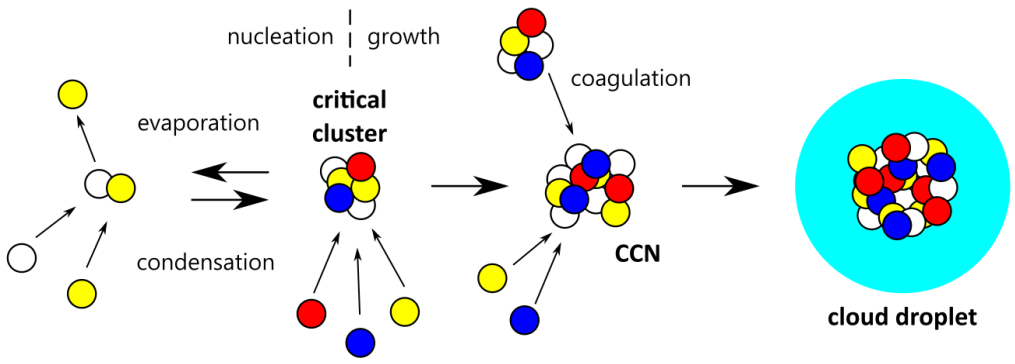

Figure 2: Scheme of new particle formation and growth after Kirkby (2007). CCN – cloud condensation nucleus.

Depending on their size and chemical composition, aerosol particles can act as cloud condensation nuclei (CCN), enabling water vapour to condense onto them and form liquid cloud droplets. The homogeneous nucleation of water vapour, i.e. the condensation on its own, is only possible for a supersaturation of approximately 6, i.e. when the vapour pressure of water exceeds the saturation vapour pressure by a factor of 6 (Seinfeld and Pandis, 2016). Such values are never observed in the atmosphere where the relative humidity barely exceeds a few per cent above 100 %. Heterogeneous nucleation, the condensation on a foreign substance, is already

observed below 100 %. This is because the saturation vapour pressure can be lower for mixtures than for the pure substances.

Some of the most important chemical systems for new particle formation are the systems of an acid, water, and a base. Nucleation-inducing acids comprise sulfuric acid, iodic acid, and nitric acid, while ammonia and several amines such as dimethyl amine are examples of bases known for their contribution to nucleation. Furthermore, in purely biogenic systems, particle formation is observed by highly oxygenated organic molecules (HOMs) (e.g. Hoppel, 1987; Kirkby et al., 2011; Almeida et al., 2013; Chen et al., 2015; Kirkby et al., 2016; Kürten et al., 2016; Tröstl et al., 2016; Kürten et al., 2018; Simon et al., 2020; Wang et al., 2020; He et al., 2021; van Rooy et al., 2021; Wang et al., 2022).

Aerosol particles also affect the optical thickness of the atmosphere. The optical thickness, or optical depth, τ, is defined as the path from the Earth's surface (or the position of the observer) to the top of the atmosphere (TOA) in which radiation experiences Rayleigh and Mie scattering by aerosol particles and absorption by gases. For the absorption of gases, it is defined following the Lambert–Beer–Bougouer law, according to Eq. (1) (Liou, 1992):

$$\tau = \int_{z_0}^{z_{\mathrm{TOA}}} k(z) \cdot \rho(z)\, \mathrm{d}z, \tag{1}$$

where z is the altitude, k is the absorption coefficient, and ρ is the air density. The aerosol optical thickness (AOT) can be defined likewise. Larger aerosol concentrations lead to a stronger scattering of the sunlight, thus affecting the irradiance reaching the Earth's surface and shifting the wavelength of the light; observations of the change in AOT during the CAFE-EU/BLUESKY campaign will be further discussed in Sect. 4.1.2 (Voigt et al., 2022).

Aerosol particles have numerous effects on meteorological systems, the climate, the biosphere, and the human body. Thus, aerosol particles play a crucial role in the formation of clouds and, subsequently, in the local and global water cycles (e.g. Jardine et al., 2015; Li et al., 2022). Due to their influence on cloud formation and cloud properties, and because of the direct reflection of sunlight, aerosol particles have a significant influence on the radiative forcing and, thus, on the climate (IPCC AR6 Working Group I, 2021). In total, aerosol particles and their changes to optical cloud properties have a negative radiative forcing and, thus, a cooling effect on the climate. The largest uncertainties in climate models, however, result from the uncertainties in the quantification of the aerosol effects on the radiative forcing (IPCC AR6 Working Group I, 2021). Therefore, further research is necessary to improve the climate models so that societies can cope better with climate change and tailor their mitigation and adaptation strategies.

The impact of aerosol particles on human health is also significant. Particulate matter does not only affect the respiratory system, causing diseases such as pneumonia and lung cancer, but small aerosol particles can also enter the cardiovascular system through uptake in the alveoli and cause diseases including stroke or ischaemic heart disease (Lelieveld et al., 2019). Air pollution is estimated to decrease the average life expectancy in Europe by 2.2 years (Lelieveld et al., 2019) and in northern China by 5.5 years (Chen et al., 2013). Therefore, stronger measures to decrease the indoor and ambient burden of particulate matter in populated regions need to be taken.

Apart from sulfuric acid which was mentioned earlier, a number of other precursor gases contribute to NPF and secondary aerosol formation such as methanesulfonic acid (MSA), HOMs, ammonia, or amines, to name but a few. MSA, CH_3SO_3H, is an oxidation product of dimethyl sulfide, DMS, along with SO_2 (Hatakeyama et al., 1982; Shen et al., 2022; van Rooy et al., 2021). DMS is emitted mostly from the oceans (Seinfeld and Pandis, 2016) and, thus, MSA-rich air is a proxy for a marine origin of air masses. HOMs are a class of molecules that originate from volatile compounds such as terpenes or sesquiterpenes and have undergone an autoxidation process that has led to an increase in oxygen atoms in the molecules and, thereby, a decrease in volatility (Ehn et al., 2012; Crounse et al., 2013; Ehn et al., 2014). Ammonia, NH_3, is mainly emitted from agriculture, including animal husbandry, while other sources of NH_3 include industry, vehicles and volatilisation from soils and oceans (Behera et al., 2013). As a base, ammonia can stabilise nucleation clusters that contain water and acids (Kirkby et al., 2011). Amines are derivatives of ammonia with the formula NR_3, where R can be alkyl or aryl groups or a hydrogen atom. Amines in the atmosphere originate from anthropogenic sources, such as animal husbandry, industrial emissions, and composting, and from natural sources such as biodegradation (Ge et al., 2011). As bases, amines can contribute to NPF, similar to NH_3 (Almeida et al., 2013; Kürten et al., 2016).

2.1.3 Atmospheric ions

In the previous subchapters, the neutral constituents of the atmosphere, namely gases and aerosol particles, were discussed. The atmosphere, moreover, contains charged species: ions in the gas phase and charged aerosol particles.

The main source of ionisation in the lower part of the atmosphere, i.e. in the troposphere and stratosphere, are galactic cosmic rays (GCRs). These “rays” are, in fact, mostly protons and α particles, also called primary particles. These are modulated by the 11-year cycle of solar

activity and are partly deflected by the Earth's magnetic field. However, the part that is able to penetrate the Earth's atmosphere induces showers of secondary particles consisting of pions, muons, and neutrinos, amongst others, upon collision with an air molecule (Bazilevskaya et al., 2008). The primary and secondary particles are able to ionise the air molecules, yielding N^+, N_2^+, O^+, O_2^+, and electrons. The latter quickly react with oxygen, forming O^- and O_2^-. These initial cations and anions experience further reactions that ultimately lead to the ion clusters $(HNO_3)_n(H_2O)_mNO_3^-$ and $H^+(H_2O)_n(B)_m$, amongst others, where B are bases such as methanol, acetone, ammonia, or pyridine (Viggiano and Arnold, 1995; Shuman et al., 2015). A more detailed description of the atmospheric ion chemistry is given in the introductory section of the research article "Mass spectrometric measurements of ambient ions during CAFE-EU/BLUESKY" (see Sect. 4.3.3) (Zauner-Wieczorek et al., 2022a). Close to the ground, the decay of the radioisotope ^{222}Rn emitted from the soil is an additional sources of ionisation as well as lightning (Viggiano and Arnold, 1995). Above the stratosphere, solar energetic particles (SEPs) contribute to the ionisation of atmospheric compounds (Bazilevskaya et al., 2008).

The sinks of atmospheric ions are their mutual neutralisation, also called recombination, and the attachment of ions to aerosol particles. The latter process is predominant in regimes with large concentrations of aerosol particles, i.e. especially in the lower part of the troposphere. In the upper part of the troposphere and above, the ion–ion recombination is predominant. An exhaustive review on the history of the research on the ion–ion recombination coefficient α, its theories and parameterisation is presented in the review paper "The ion–ion recombination coefficient α: comparison of temperature- and pressure-dependent parameterisations for the troposphere and stratosphere" (see Sect. 4.1.1 and 4.3.1) (Zauner-Wieczorek et al., 2022b). This review was motivated by the need for a pressure- and temperature-dependent parameterisation of α in order to derive the number concentration of gaseous sulfuric acid from the measurements of nitrate and hydrogen sulfate ions during the CAFE-EU/BLUESKY campaign (see Sect. 4.1.3 and 4.3.3) (Zauner-Wieczorek et al., 2022a).

Ambient ions affect several atmospheric processes such as the propagation of radio waves (Basu et al., 1985), the slight conductivity of the atmosphere that enables thunderstorms (Harrison, 2011), or the ion-induced nucleation (IIN) of aerosol particles (Hirsikko et al., 2011). The first observation of an enhancement of aerosol particle concentrations during an event of increased atmospheric ion production by SEPs was reported by Shumilov et al. (1996). Yu and Turco (2000) enunciated the concept of the IIN, stating that newly formed molecular clusters can be thermodynamically favoured if ions are involved. Thereafter, the importance of ions in

NPF has been shown in several studies (e.g. Kazil and Lovejoy, 2004; Curtius et al., 2007; Kazil et al., 2008; Kirkby et al., 2016).

2.2 Mass spectrometry

A powerful method to identify analytes by their mass is mass spectrometry. The first mass spectrometer was developed by J. J. Thomson (Thomson, 1912, 1913). In his vacuum apparatus, he deflected the anions produced by a cathode with a magnet and detected them with a Faraday cup, separated by their mass-to-charge ratio, *m*/*z* (Maher et al., 2015). Mass spectrometers consist of three main parts: the ion source, the mass analyser, and the detector. As detectors, electron multipliers, Faraday cups, and microchannel plate detectors (MCPs) are used (Maher et al., 2015).

There are four main types of mass analysers. Firstly, the sector field mass analyser uses a magnetic field to deflect the ions (Maher et al., 2015). Secondly, a quadrupole mass analyser, developed by Paul and Steinwedel (1953), uses an electrical field to deflect the ion (Maher et al., 2015). Thirdly, time-of-flight (TOF) mass spectrometers, first described by Stephens (1946) and Wolff and Stephens (1953), use the *m*/*z*-dependent time of an ion to travel from one point of the analyser to the detector for identification, based on Eq. (2) (Maher et al., 2015):

$$t = \frac{d}{\sqrt{2Ue}}\sqrt{\frac{m}{z}}, \tag{2}$$

where *t* is the time of flight, *d* is the flight distance, *U* is the potential difference, and *e* is the elementary charge. Fourthly, there are a number of ion traps using different techniques to both trap and analyse ions of a certain *m*/*z* (Maher et al., 2015).

An ion source is necessary to ionise the neutral analytes of interest in order to be able to detect them with a mass spectrometer. However, it is possible to detect ambient ions and ion clusters without an ion source. This measurement mode is today referred to as the atmospheric pressure interface (APi) mode. In fact, the first mass spectrometric application to detect atmospheric species were measurements of atmospheric ions, first reported by Johnson et al. (1958) for the mesosphere and ionosphere. In the course of time, the APi measurements were expanded to the stratosphere and troposphere. More details about the history of atmospheric ion measurements are given in the introductory part of the research article “Mass spectrometric measurements of ambient ions and estimation of gaseous sulfuric acid in the free troposphere and lowermost stratosphere during the CAFE-EU/BLUESKY campaign” (see Sect. 4.3.3) (Zauner-Wieczorek

et al., 2022a). Junninen et al. (2010) were the first to perform APi measurements with a TOF-MS, identifying numerous species by virtue of the much higher mass resolution compared to a quadrupole MS.

From 1985 onwards, neutral analytes in the atmosphere could be measured by coupling a chemical ionisation (CI) source to the mass spectrometer (Arnold and Hauck, 1985). There are various ionisation techniques that are often divided into soft and hard ionisation techniques. The classical hard ionisation technique is electron ionisation; here, an electron impacts the analyte causing the loss of an electron from the analyte and, thus, produces the positively charged molecular ion. Due to the high energies involved, the molecule usually fragments yielding several fragment ions in the mass spectrum (Märk and Dunn, 1985). Among the soft techniques, electrospray ionisation (ESI) and CI are some of the most commonly used. In classical ESI, the analyte is solved, a high voltage is applied to the solution, and the analyte ions are sprayed from the tip of a capillary (Kebarle and Verkerk, 2009). Moreover, there are other forms of electrospray techniques in which the gaseous analyte is extracted into electrosprayed solvent droplets (extractive ESI, EESI) (Lopez-Hilfiker et al., 2019), or chemically ionised by electrosprayed reagent ions (electrospray chemical ionisation, ESCI) (Zhao et al., 2017; Zauner-Wieczorek, 2018; Zhao, 2019; Sayed, 2021). In chemical ionisation, a reagent ion is provided that ionises the analytes by charge transfer or adduct formation. The primary ionisation of the reagent can occur with different techniques, such as radioactive sources or a corona discharge (Kürten et al., 2011). In the latter method, a high voltage is applied to a corona needle, which results in a discharge and the subsequent reagent ion formation. Since reactive side products like $OH^{\cdot}$ can be produced in this process, a sheath flow must be provided to keep the reactants away from the analytes. Such an ion source was first described by Eisele and Tanner (1993). There is a wide range of reagent ions used nowadays that are able to ionise different classes of analytes, depending on the possible chemical reactions between the reagent ion and the analyte. The ionisation can occur either by clustering/adduct formation, ligand exchange, or charge transfer/proton transfer (Hyttinen et al., 2018).

provides an overview of selected reagent ions in the negative mode. In Sect. 3.1, a corona-powered nitrate-based CI source is described that was developed for aircraft-borne measurements of low volatile nucleation precursors.

Table 1: Overview of negative reagent ions and their respective detectable analytes.

Reagent ion	Analytes	References
Br^- (bromide)	HIO_3, HOI, I_2, HO_2, H_2SO_4, oxygenated VOCs	Sanchez et al., 2016, Hyttinen et al., 2018, Wang et al., 2021
CF_3O^- (trifluoro-methanolate)	HNO_3, $ClONO_2$, N_2O_5, HCl, SO_2, HI, H_2SO_4, H_2O, H_2O_2, organic acids	Huey et al., 1996, Crounse et al., 2006, Hyttinen et al., 2018
CH_3–CH_2OH–COO^- (lactate)	HOMs	Berndt et al., 2016a, Berndt et al., 2016b, Hyttinen et al., 2018
CH_3–CO–COO^- (pyruvate)	HOMs	Berndt et al., 2016a
CH3–COO^- (acetate)	Less oxidised organics, HOMs, organic acids	Yatavelli et al., 2012, Chhabra et al., 2015, Brophy and Farmer, 2016, Berndt et al., 2016a, Berndt et al., 2016b, Hyttinen et al., 2017, Hyttinen et al., 2018
CO_3^- (carbonate)	SO_2, H_2SO_4	Seeley et al., 1997, Jost et al., 2003, Salcedo et al., 2004
I^- (iodide)	$ClNO_3$, NO_3, N_2O_5, HNO_3, PAN, PAA, SO2, HCl, HOCl, $ClNO_2$, Cl_2, Br_2, $BrNO_2$, BrCl, polar or acidic VOCs, oxygenated VOCs	Huey et al., 1996, Lee et al., 2014, Lee et al., 2018, Hyttinen et al., 2018, Dörich et al., 2021
NO_3^- (nitrate)	H_2SO_4, MSA, HIO_3, HOMs (> 4 O atoms), C_2 amines	Eisele and Tanner, 1993, Viggiano et al., 1997, Berresheim et al., 2000, Berndt et al., 2016a, Berndt et al., 2016b, Hyttinen et al., 2018
SF_6^- (sulfur hexafluoride)	H_2SO_4, SO_3, SO_2, HNO_3, $ClONO_2$, N_2O_5, HCl, O_3, Cl_2, Cl_2O, HOCl, CF_2O, CF_3CFO, Br_2O, $BrNO_3$, HOBr	Huey et al., 1996

3 Methods

3.1 SCORPION-TOF-MS

Measuring low volatile vapours at different altitudes from on board an aeroplane is a challenging undertaking for several reasons. On the one hand, low volatile vapours adhere to the inlet walls easily; thus, sampling at cruise speed needs a sophisticated sampling system with optimised aerodynamics and minimised turbulence and wall losses. On the other hand, the varying pressure at different flight altitudes poses a challenge for instruments that require a constant pressure in the inlet system.

In order to measure nucleation precursors such as sulfuric acid, MSA, or dimethylamine (DMA) in an altitude range of 0–14.5 km, the Switchable CORona-Powered ION source (SCORPION) was developed at the Goethe University Frankfurt which was then coupled to a high-resolution time-of-flight mass spectrometer (TOF-MS) (*Tofwerk AG*). Subsequently, this instrumentation was prepared for installation on board the High Altitude Long Range research aircraft (HALO). The system consists of an outside sampling system, a connecting tube, a pressure stage, the ion source, and the mass spectrometer. The sampling of the air masses is realised by using the LiF-OH inlet developed by the Forschungszentrum Jülich (Broch, 2011). This inlet system is designed to reduce wall losses and was initially developed for measuring the reactive hydroxyl radical. During the CAFE-EU/BLUESKY campaign (see Sect. 3.2), the LiF-OH inlet system was attached on top of the aircraft in the front third. A brief description of the system follows. Attached to the LiF-OH inlet system is a 1.7 m long stainless-steel tube of 25 mm outer diameter that is bent twice coplanarly by 90° and 270°, respectively. It is designed to minimise wall losses by ensuring a laminar flow at high flow rates (10–30 slpm, depending on the altitude). The inlet line is connected to the pressure stage by a stainless-steel bellow tube. The pressure stage is an aluminium cylinder that contains two critical orifices in the flow direction. In front of the first orifice, the inlet pressure is measured by a pressure sensor. There, five tubes, which lead to a blower, are connected equidistantly around the cylinder; the blower ensures a high flow rate through the inlet line. The critical orifice of 1.4 mm diameter is at the tip of a

cone that is pointed towards the inlet line; the critical orifice allows only the core air mass of the inlet line to enter the mid-pressure stage, where the pressure is monitored by another pressure controller. In this second stage, two tubes are connected to an IDP-3 dry scroll pump (*Agilent Technologies Inc.*), regulated by an automated control valve (*MKS Instruments Inc.*). The valve is opened fully at ground level but is closed completely at maximum flight altitude in order to maintain the pressure close to the aimed ion source pressure of 200 hPa. Behind the second critical orifice, which is identical to the first one, lays the ion source. Here, a constant pressure of 200 hPa is necessary to ensure a comparable ionisation throughout the whole flight. The pressure influences the reaction of the reagent ions with the analytes in the ion source, therefore, in order to use a constant calibration factor for all flight altitudes, the pressure in the ion source must stay constant. To supply the reagent to the ion source, an external reagent reservoir within the instrument rack is utilised. This reservoir holds a bottle of aqueous HNO_3 solution (65–70 % in H_2O, ultra-high purity). A flow of synthetic air from a gas bottle within the instrument rack can take up the solved HNO_3 into the gas phase; this HNO_3 is then injected into the ion source in front of the corona needle.

The ion source consists of two main areas. The ion–molecule reaction (IMR) region, also called the drift tube (DT), is attached to the mid-pressure stage on the upper side and to the mass spectrometer interface on the lower side. In the upper region, there are the two ion production blocks installed perpendicularly to the DT and to each other, respectively. The ion production region is built cylindrically inside and contains the corona needle at the outer point, followed by the ion source exhaust port, the reagent ion inlet port, the metal-ring cascade, and, closest to the DT, the air inlet port. This design ensures a gas flow away from the IMR towards the corona needle; any contaminant gases that are produced through the corona discharge are sucked away into the exhaust without reaching the analytes with which they could interfere. Through the reagent ion inlet port, the HNO_3-enriched air is injected into the ion production region where it is ionised by the corona discharges. The voltage applied to the needle is between –2000 and –3500 V. The ions are guided towards the IMR through a voltage applied to the metal ring cascade. This cascade consists of five stainless steel rings that are connected by resistors so that a decreasing electrical field is yielded along this cascade. When the ions reach the IMR, they mix with the sample flow and react with the analytes along the DT. On the bottom of the DT, an exhaust sucks the sampled air with a rate of approximately 2.7 slpm through the IMR/DT.

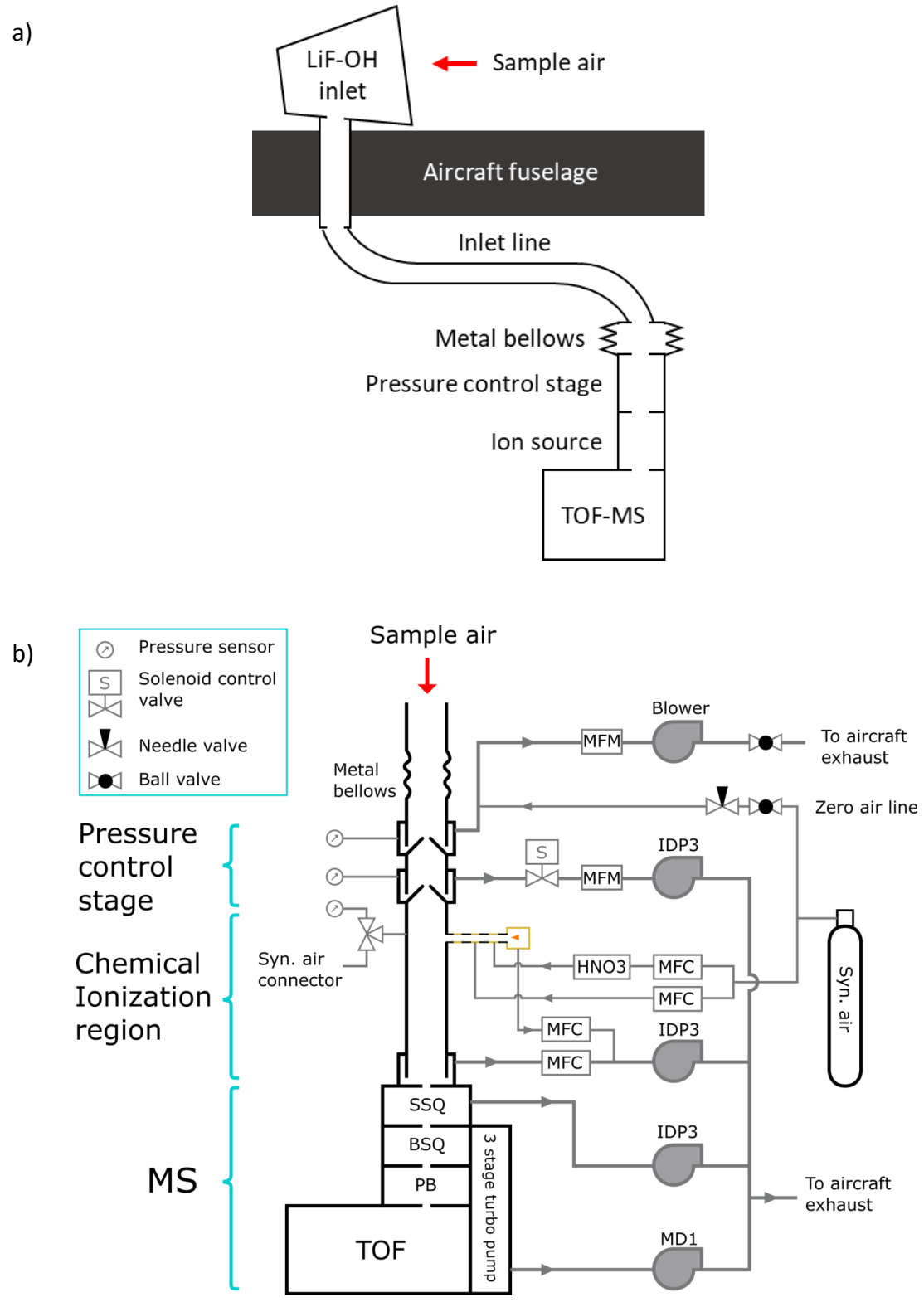

Figure 3: Scheme of the SCORPION-TOF-MS. a) Overview scheme of the inlet system, inlet line and SCORPION-TOF-MS. b) Detailed scheme of the pressure stage, SCORPION source, and TOF-MS by Heinritzi et al. (in preparation). BSQ – big segmented quadrupole, IDP3 and MD1 – pumps, MFC – mass flow controller, MFM – mass flow meter, MS – mass spectrometer, SSQ – small segmented quadrupole, syn. air – synthetic air, TOF – time-of-flight chamber.

Ultimately, a flow of 0.16 slpm sampled gas is sucked into the mass spectrometer through a pinhole of 0.3 mm diameter. The mentioned flow rates are regulated by mass flow controllers

(MFCs) (*MKS Instruments Inc.*). In order to perform background measurements during the flight, the internal synthetic air gas bottle can be connected to the five blower tubes in front of the first critical orifice of the pressure control stage by opening a manual valve. This zero air can overflow the inlet line when the aircraft is at maximum flight altitude and the inlet flow is, therefore, minimal. The setup is shown schematically in Figure 3. A photo of the SCORPION-TOF-MS installed on board the HALO is depicted in Figure 4 and a photo of the HALO in Figure 5.

Figure 4: Photo of the SCORPION-TOF-MS installed on board the HALO. The black line in the upper left corner is the inlet line covered by thermal insulation.

Figure 5: Photo of the HALO. The white arrow indicates the LiF-OH inlet.

3.2 CAFE-EU/BLUESKY campaign

The first COVID lockdowns in most European countries in spring 2020 resulted in reduced road, air traffic, and industrial emissions (Guevara, 2020). Furthermore, there was a subjective perception that the sky appeared bluer than usual. To take advantage of this unique situation of reduced anthropogenic emissions, the airborne measurement campaign CAFE-EU/BLUESKY was conducted between 16 May and 9 June 2020 at the German Aerospace Center (DLR) at the airport base Oberpfaffenhofen (OBF) in Bavaria, Germany, employing the two research aircraft Falcon (D-CMET), a modified Dassault Falcon 20-E5, and the HALO (D-ADLR), a modified Gulfstream G 550.

The instrumentation was capable of detecting a wide span of atmospherically relevant trace gases, aerosol parameters, and meteorological conditions. On board the HALO, there were instruments to measure NO_x, CO, O_3, H_2SO_4, MSA, C_2 amines, and the aerosol particle composition, number, and size distribution, while on board the Falcon, NO_y, O_3, CO, and the aerosol particle size distribution were measured, amongst others. A detailed overview of all instruments and their references is provided in the research article “Cleaner Skies during the COVID-19 Lockdown” (see Sect. 4.1.2 and 4.3.2) by Voigt et al. (2022).

The measurement flights were performed in Western Europe covering an area between Ireland and Spain, up to altitudes of 14.5 km with HALO and 12 km with the Falcon. HALO performed one test flight and eight measurement flights and the Falcon performed twelve measurement flights (on nine days) and one test flight. Through low approaches at airports, vertical profiles in urban regimes could be sampled, while low flight legs above the Atlantic Ocean and the Mediterranean Sea allowed for the investigation of maritime air masses. Measurements on flight legs perpendicular to the standard flight routes of transatlantic aircraft on the North Atlantic Tracks (NAT) were performed to analyse aircraft-related emissions and the outflows of cumulonimbus clouds were also probed. Figure 6 shows the map of the altitude-resolved flight tracks of all eight HALO measurement flights. The foci of flight nos. 01–03 were the measurements above Germany and adjacent countries, while the foci of flight nos. 04–05 were the NAT measurements and of flight nos. 06–08, the measurements above the Mediterranean Sea and adjacent countries. More details on the flights of both aircraft are summarised by Voigt et al. (2022).

The results of the CAFE-EU/BLUESKY campaign are discussed in more detail in Sect. 4.1.2. Additional results from the campaign were, and will be, published in the special issue “BLUESKY atmospheric composition measurements by aircraft during the COVID-19

lockdown in spring 2020" in *Atmospheric Chemistry and Physics* (https://acp.copernicus.org/articles/special_issue1170.html).

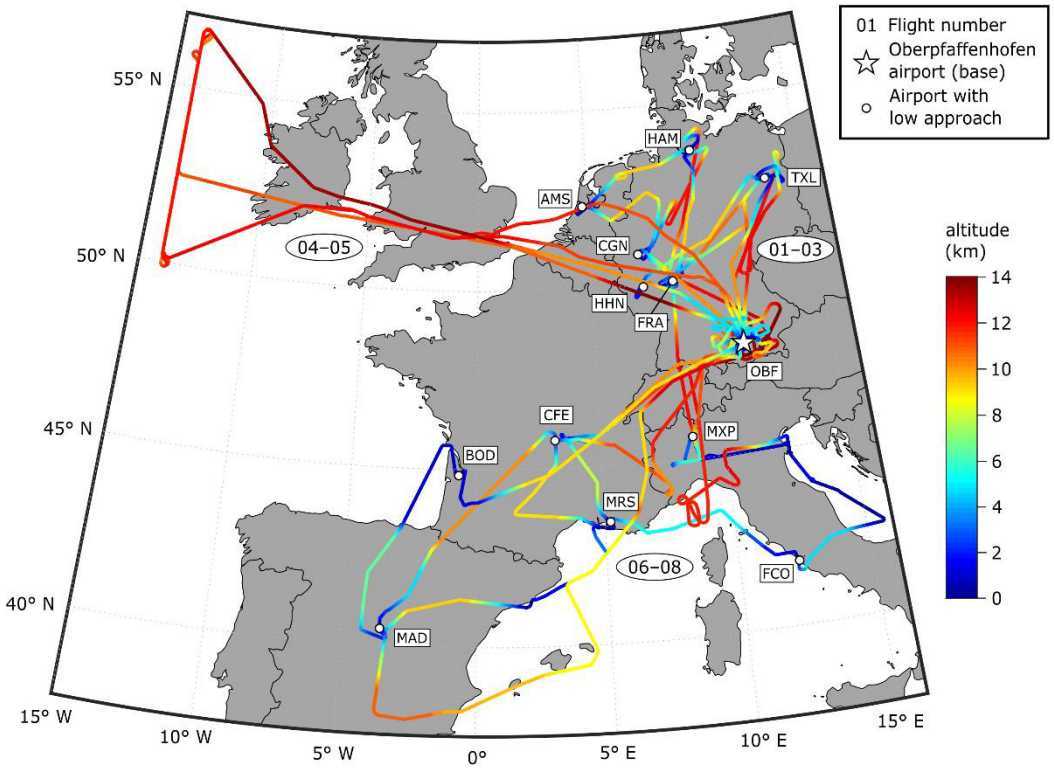

Figure 6: Map of the flight tracks of HALO (Zauner-Wieczorek et al., in prep.). The colour code indicates the cruise altitude and the circles show the airports where low approaches were performed. National border data are taken from Greene et al. (2019).

4 Publications

4.1 Summary of the publications

4.1.1 Summary of "The ion–ion recombination coefficient α"

The review article "The ion–ion recombination coefficient α: comparison of temperature- and pressure-dependent parameterisations for the troposphere and stratosphere" addresses the history and the different theories and parameterisations used to determine the ion–ion recombination coefficient α for different temperature and pressure regimes. This is necessary when α is used for conditions other than pressures and temperatures close to standard conditions (i.e. ground level conditions), e.g. when applied to upper tropospheric or stratospheric conditions.

The ion–ion recombination coefficient α is defined as the reaction coefficient of the recombination, i.e. the mutual neutralisation of an anion and a cation in the gas phase. One can distinguish two mechanisms: the binary (or two-body) and the ternary (or three-body) recombination. In the binary mechanism, the two ions recombine upon collision, while in the ternary reaction, a third body is involved that acts as a collision body in order to dissipate excess (kinetic) energy that would prevent the two ions from recombining. The process of "trapping" one of the ions by initial collision is also called three-body trapping. In the atmosphere, the ternary mechanism is predominant between ground level and approximately 25 km altitude; here, the density of the air is sufficiently high to make the collision with the third body probable. Above approximately 40 km, binary recombination is predominant because the density of the air is lower and collision bodies are too scarce to overweigh the binary process. Many theories and parameterisations account for one or both of the processes; the sum of both is called total recombination.

Thomson and Rutherford (1896) were the first to describe the ion–ion recombination coefficient and introduced Eq. (3) that describes the temporal change in the number concentration of gas-phase ions n:

$$\frac{\mathrm{d}n}{\mathrm{d}t} = q - \alpha n^2 - L, \tag{3}$$

where t is the time, q is the ion production rate, and L is the loss rate to the electrodes in the experimental setup used by Thomson and Rutherford (1896). Assuming steady-state conditions ($\mathrm{d}n/\mathrm{d}t = 0$) and a negligible loss rate in the experimental setup, one can derive α simply from the ratio of the ion production rate and the squared ion concentration (Eq. (4)). This simple equation has been used in numerous lab and field experiments.

$$\alpha = \frac{q}{n^2}. \tag{4}$$

Thomson's theory is based on thermodynamic considerations. The recombination occurs when an anion and a cation each collide with a neutral molecule within the ion–ion trapping distance d_T and subsequently recombine. At the distance d_T, the Coulomb potential energy and the thermal energy of motion of the ions are equal. The resulting Eq. (5) is:

$$d_\mathrm{T} = \frac{e^2}{4\pi \cdot \varepsilon_0 \cdot 1.5\, k_\mathrm{B} T}, \tag{5}$$

where e is the elementary charge, ε_0 is the vacuum permittivity, k_B is the Boltzmann constant, and T is the temperature. The definition of the ion–ion trapping distance is the foundation of many theories and differs significantly among the different approaches.

Opposed to Thomson's thermodynamic approach, Langevin (1903) presented a theory that is based on the speeds of the ions in an electrical field. Between the 1900s and the 1940s, many laboratory experiments were conducted to determine α for various pressure and temperature conditions. The values for standard conditions did not differ greatly and were close to $1.7 \cdot 10^{-6}$ cm^3 s^{-1}. This value holds true to date (Lenz, 1932; Israël, 1957; Bates, 1982). The experiments showed that for sub-atmospheric pressures, the Thomson theory with $p^{0.5\ldots1}$ and $T^{-1.5}$ dependencies applies, while for super-atmospheric pressures, the Langevin theory with p^{-1} and T^{1} dependencies holds true. In order to use the Thomson theory with macroscopic parameters as input, several parameterisations were developed, e.g. the one by Israël (1957) (Eqs. (6) to (8)):

$$\alpha = 1.95 \cdot 10^{-6} \cdot \left(\frac{273}{T}\right)^{1.5} \cdot \varepsilon_\mathrm{T}, \text{ with} \tag{6}$$

$$\varepsilon_\mathrm{T} = 1 - \frac{4}{x'^4} \cdot [1 - e^{-x'} \cdot (x' + 1)]^2, \text{ and} \tag{7}$$

$$x' = 0.810 \cdot \left(\frac{T_0}{T}\right)^2 \cdot \left(\frac{p}{p_0}\right) \cdot \frac{\lambda_{\mathrm{air}}}{\lambda_{\mathrm{ion}}}, \quad (8)$$

where ε_T is the ratio of successful recombinations per collision, the index 0 indicates standard conditions, λ_{air} is the mean free path of the surrounding air, λ_{ion} is the mean free path of the ion, and the ratio $\lambda_{air} \cdot \lambda_{ion}^{-1} = 3$.

In the 1960s and 70s, lab experiments with more sophisticated methods and instruments led to new theories and advanced parameterisations. Hickman (1979) developed a complex potential model that describes the binary recombination coefficient in dependence of T, the reduced ion mass, m_{red}, and the electron affinity of the negative ion, EA; this was later refined by Miller et al. (2012). A breakthrough in the application of α to different altitudes came with the field measurements performed by Gringel et al. (1978), Rosen and Hofmann (1981), and Morita (1983). These researchers measured the ion production rate q and the number concentration of positive ions simultaneously (however, Gringel et al. just assumed q from past measurements) and derived α with Eq. (5) and another method based on the ion mobilities for altitudes of 3 km up to 45 km. However, the measurements below 10 km were erroneous, because the aerosol sink reaches the same order of magnitude as the recombination sink and, therefore, it cannot be neglected any more, thus making Eq. (5) invalid. In general, α has a decreasing trend with increasing altitude above 10 km. Nevertheless, these field data boosted the development of parameterisations of which some were solely dependent on the altitude h and some were dependent on T and p, while considering both the binary and ternary recombination. One such parameterisation was presented by Brasseur and Chatel (1983) (Eq. (9)):

$$\alpha = 6 \cdot 10^{-8} \cdot \left(\frac{300}{T}\right)^{0.5} + 6 \cdot 10^{-26} \cdot [\mathrm{M}] \cdot \left(\frac{300}{T}\right)^4, \text{ with} \quad (9)$$

$$[\mathrm{M}] = 7.243 \cdot 10^{18} \cdot \left(\frac{p}{T}\right), \quad (10)$$

where [M] is the number concentration of atmospheric molecules. The first term in Eq. (9) accounts for the binary recombination and the second term accounts for the ternary process. Furthermore, Bates (1982) presented a Monte Carlo simulation of α for the altitude range of 0–40 km that confirmed the laboratory data for the ground level and the measured field data for higher altitudes.

The ion–aerosol attachment coefficient that describes the attachment of an ion to a charged or uncharged aerosol particle can also be applied to the recombination of two ions when assuming the radius of the “aerosol particle” to be of ionic size and a single charge of the aerosol particle.

In this way, the binary theory of Fuchs (1963) and the ternary theory of Hoppel and Frick (1986) can be applied to the ion–ion recombination. It should be noted, however, that Hoppel and Frick's theory needs the input of a known α for standard conditions in order to be able to calculate the ion–ion trapping distance. When supplying this information, however, one can determine α for different temperature and pressure conditions at different altitudes. Furthermore, Filippov's (1993) theory of the ionic charging of small aerosol particles in dependence of the Knudsen number can be used to express the ion–ion recombination coefficient as a function of the Knudsen number.

Since 1985, until very recently, no further developments of the theories or parameterisations of the ion–ion recombination coefficient applied to atmospheric conditions have been conducted. Lately, Tamadate et al. (2020) presented a hybrid continuum-molecular dynamics (MD) simulation of the recombination of NH_4^+ and NO_2^- in He at 300 K under different pressures. Such simulations can account for physical (T, p) and chemical (gas and ion compositions) features and are, therefore, a promising approach to be investigated further. Furthermore, Franchin et al. (2015) reported laboratory values for α at standard pressure and a temperature range of 218 to 293 K.

After introducing the theories and parameterisations, the predicted α values were compared to the field data of Gringel et al. (1978), Rosen and Hofmann (1981), and Morita (1983) and the model data of Bates (1982) as shown in Figure 7, using the conditions of the US Standard Atmosphere for an altitude range of 0–50 km. Furthermore, they were compared to the laboratory data of Franchin et al. (2015). Although there is no theory or parameterisation that reproduces the field, model, and lab data equally well for all conditions, some favourable parameterisations were identified for different altitude ranges. Between 0 and 20 km altitude, Israël's (1957) parameterisation shows the best agreement with field and model data, while between 0 and 22 km altitude, Brasseur and Chatel's (1983) formula agrees sufficiently well and, furthermore, proves to be the best for reproducing the laboratory data by Franchin et al. (2015). For altitudes between 10 and 25 km, Bates's (1985) altitude-dependent parameterisation is favourable, while above 25 km, the parameterisations of Smith and Adams (1982) (h dependent) and Arijs et al. (1983) (p and T dependent) yield the closest agreement to the field data. Above altitudes of 30 km, Hoppel and Frick's (1986) theory reproduces the field data most accurately, however, one has to bear in mind that the data coverage above 35 km remains scarce.

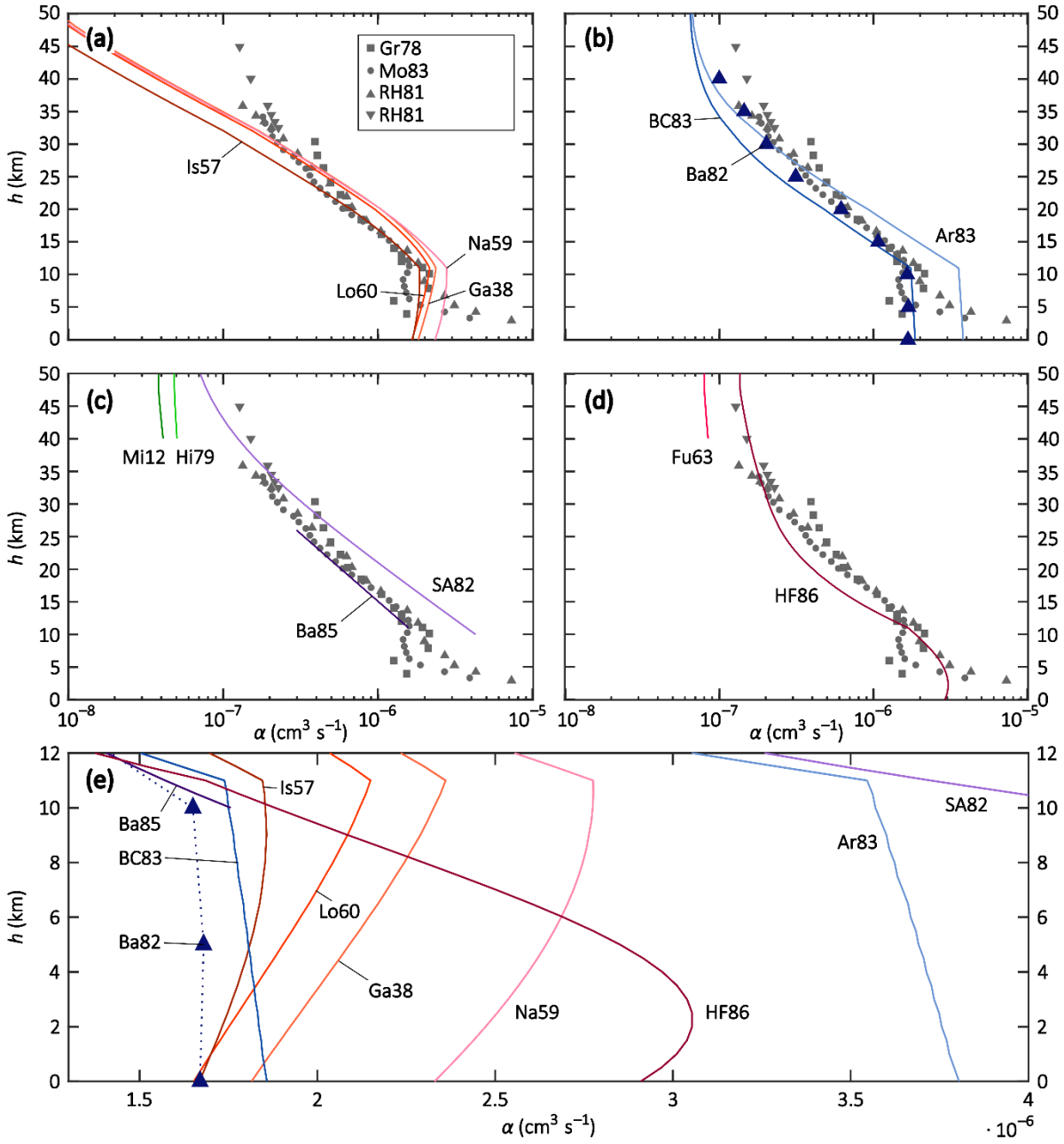

Ar83	Arijs et al., 1983	Hi79	Hickman, 1979
Ba82	Bates, 1982	Is57	Israël, 1957
Ba85	Bates, 1985	Lo60	Loeb, 1960
BC83	Brasseur and Chatel, 1983	Mi12	Miller et al., 2012
Fu63	Fuchs, 1963	Mo83	Morita, 1983
Ga38	Gardner, 1938	Na59	Natanson, 1959
Gr78	Gringel et al., 1978	RH81	Rosen and Hofmann, 1981
HF86	Hoppel and Frick, 1986	SA82	Smith and Adams, 1982

Figure 7: Comparison of different theories and parameterisations with respect to their predicted α in dependence of the altitude h, adapted after Zauner-Wieczorek et al. (2022b).

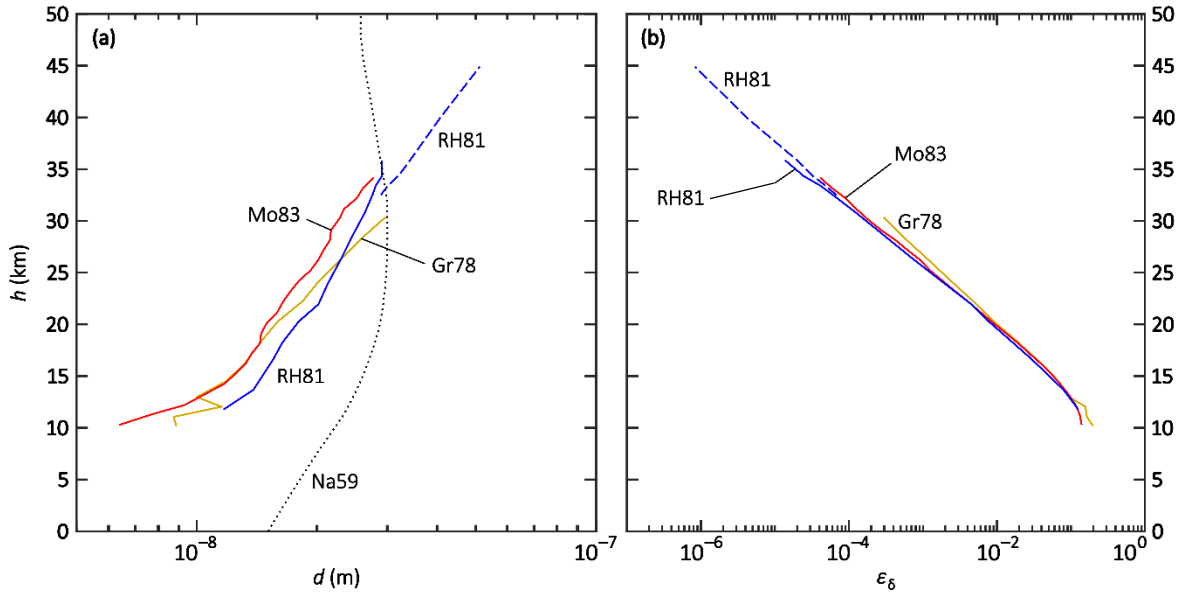

Figure 8: Altitude plots of the (a) numerically determined ion–ion trapping radius d and (b) analytically determined limiting sphere probability ε_δ, each for the field data set of Gringel et al. (1978) (Gr78), Rosen and Hofmann (1981) (RH81), and Morita (1983) (Mo83). The dotted curve in panel (a) shows d_N after Natanson's theory (Na59). Adapted after Zauner-Wieczorek et al. (2022b).

A central part in the ternary process of the recombination of two ions is the trapping of one ion by a third body. This trapping is accounted for in some theories by the three-body trapping distance, also called the ion–ion trapping distance d. Thomson's d_T is given in Eq. (6), while Hoppel and Frick (1986) assume a constant d irrespective of the pressure. Natanson (1959) introduced a definition of α that aims to unify Thomson's and Langevin's approaches. In Zauner-Wieczorek et al. (2022b), Natanson's formula was solved for d numerically using the Newton–Raphson method by using the α values from Gringel et al. (1978), Rosen and Hofmann (1981), and Morita (1983). The resulting d values are depicted in Figure 8 (a) and show a decadic logarithmic trend with increasing altitude and can be expressed by Eq. (11). Moreover, using a multivariate fit for T and p, Eq. (12) expresses the temperature and pressure dependence of d:

$$d(h) = 10^{\frac{h-(468\pm15)}{58.5\pm2.0}}, \tag{11}$$

$$d(T,p) = (1.9 \pm 0.3) \cdot 10^{-8} \cdot \left(\frac{T}{T_0}\right)^{1.9\pm0.4} \cdot \left(\frac{p}{p_0}\right)^{-0.19\pm0.02}. \tag{12}$$

Moreover, the collision probability in the limiting sphere, ε_δ, a parameter that is necessary in Filippov's (1993) equation, was determined by analytically solving the equation for the conditions of the standard atmosphere with the input values of α from Gringel et al. (1978), Rosen and Hofmann (1981), and Morita (1983). The resulting values for ε_δ are shown in Figure

8 (b) and can be expressed by Eq. (13) in dependence of the altitude. A multivariate fit for T and p, however, did not yield meaningful results.

$$\varepsilon_\delta(h) = 10^{\frac{h-(7.0\pm0.2)}{-(6.18\pm0.06)}}. \quad (13)$$

Thus, while this review article has introduced the most important theories of the recombination of two ions and compared the available theories and parameterisations with field, lab, and model data for atmospheric conditions, it must be concluded that there is no single theory that agrees perfectly with the known values in all altitude ranges. It is reasonable to assume that α is more or less constant in the troposphere and decreases with altitude above an altitude of 10 km. The ground-level value of α is $1.7 \cdot 10^{-6}$ cm^3 s^{-1}. For future research, more field data and model simulations are necessary; moreover, MD simulations offer a promising new approach to determine α for various chemical and physical systems.

4.1.2 Summary of "Cleaner Skies during the COVID-19 Lockdown"

The research article "Cleaner Skies during the COVID-19 Lockdown" by Voigt et al. (2022) provides an overview of the CAFE-EU/BLUESKY campaign, its instrumentation, and the most important results. The campaign aimed to investigate the changes in airborne pollutants and the blueness of the sky during the COVID lockdowns in most European countries; CAFE-EU/BLUESKY took place between 16 May and 9 June 2020, performing 20 measurement flights with the two research aircraft Falcon and HALO over Europe and the Atlantic Ocean. The twelve research flights with the Falcon were performed on nine days between 19 May and 2 June 2020 mainly in Germany, northern Italy, and offshore Ireland with flight tracks perpendicular to the NAT. The eight research flights with HALO were performed between 23 May and 9 June 2020 covering Germany, the NAT, and parts of southern Europe including the Mediterranean Sea. Some flights of HALO and the Falcon were performed on the same day to ensure the comparability of data.

The instrumentation on board HALO included the measurement of H_2SO_4, MSA, C_2 amines, atmospheric ions (CI-APi-TOF); peroxyacyl nitrates (PANs) (iodide-CIMS); non-methane VOCs (NMVOCs) (GC-MS); oxidised VOCs (OVOCs) (PTR-MS); hydroperoxides (TRIHOP); NO_x, CO (NOAH/ATTILA); submicron aerosol particle composition (C-TOF-AMS); the aerosol number and size distribution (UHSAS, OPC); CCN, black carbon (BC) (CCN-rack); O_3 (FAIRO); the actinic flux density (HALO-SR); the pressure, temperature, wind, humidity, and aircraft speed, position, and altitude (BAHAMAS); and the H_2O mixing

ratio (SHARC). On board the Falcon, instrumentation was installed to measure NO_y (NO_y chemiluminiscence detector); O_3 (UV absorption photometer); CO_2, CH_4, CO (cavity ring down instrument); HNO_3, HONO, SO_2, HCl (AIMS); gas phase H_2O (frost point and TDL hygrometer); the aerosol size distribution, shape, and polarisation (CPCs, OPCs, PSAP, PCASP-100X, CAS-DPOL/CIP, UHSAS); and the temperature, wind, meteorological and aircraft state parameters (Meteorological Sensor System). For the flight planning, the global model EMAC was used in its nudged version. Comparisons after the campaign revealed good agreement with an emission-reduced scenario.

The mixing ratios of NO_y and CO in the lower and middle troposphere in the Frankfurt area (Germany) were found to be reduced compared to previous years (see Figure 9). The vertical profile at Frankfurt measured by the Falcon on 28 May 2020 showed a reduction of NO_y by 40–70 % and of CO by 20–40 % compared to the 11-year averaged measurements from passenger aircraft at Frankfurt airport via the Measurement of Ozone and Water Vapor by Airbus In-Service Aircraft (MOZAIC) at the same time of the year. There was no significant difference observed for O_3 concentrations. These results are supported by data from the nadir-scanning spectrometer Global Ozone Monitoring Experiment 2 (GOME-2) on board the Meteorogical Operational satellite B (MetOp-B), as shown in Figure 10; the global reduction of NO_2 during the CAFE-EU/BLUESKY period was 12 %, with maximum reductions of up to 55 % in large cities and urban agglomerations compared to 2015–2019. The reductions in NO_x and CO can be explained, in parts, by the prevailing meteorological conditions on the day of measurement and, on the other hand, by emission reductions. Additional simulations with the MECO(n) model showed that the COVID lockdown led to reductions in O_3 of up to 10 %, in CO of up to 13 %, and in NO_y of up to 34 % when compared to a business-as-usual scenario. The reductions in NO_y are mainly due to reduced land transport emissions close to the ground and reduced aircraft emissions at altitudes above 10 km. Moreover, for the Po Valley (Italy), a reduction in CO mixing ratios of up to 30 % was observed on 1 June 2020 compared to the Hybrid Single Particle Lagrangian Integrated Trajectory model (HYSPLIT) simulations in which no reductions in traffic and industry emissions were implemented.

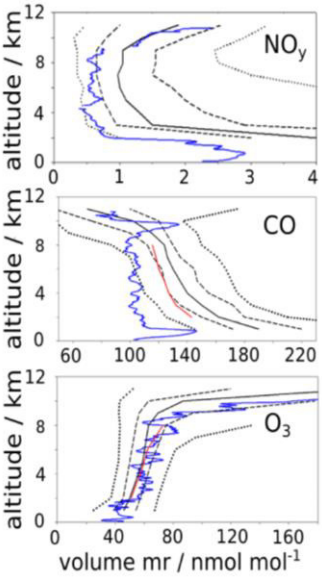

Figure 9: Vertical profiles of the volume mixing ratios of NO_y, CO, and O_3 during CAFE-EU/BLUESKY on 28 May 2020 in the Frankfurt area (blue lines) compared to MOZAIC data from 1994–2005 (median: black lines; 5th, 25th, 75th, and 95th percentiles: black dotted lines) and averaged IAGOS data from spring 2016–2019 (red lines), adapted after Voigt et al. (2022).

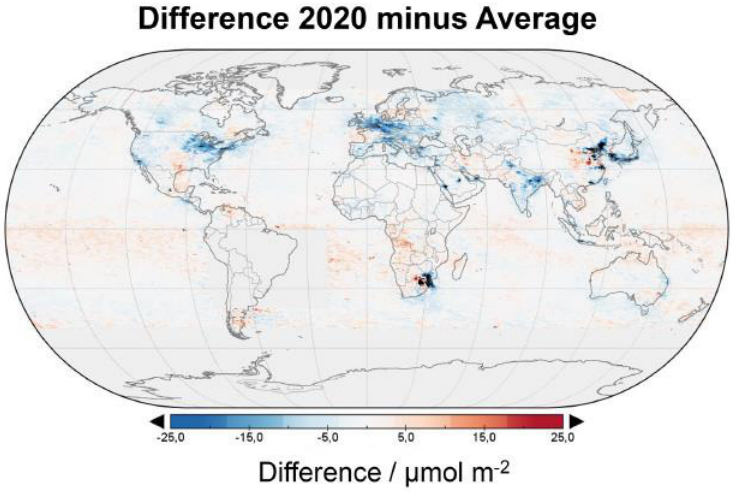

Figure 10: Difference in the tropospheric NO_2 between 2020 and the baseline mean 2015–2019 during the BLUESKY period, observed by GOME-2 on board the MetOp satellite. Adapted after Voigt et al. (2022).

The background concentrations of SO_2 observed in the continental upper troposphere and lower stratosphere (UTLS) during the campaign were in the upper range compared to measurements in summer 2004 (ITOP campaign) and summer 2008 (CONCERT campaign). The concentrations in the aircraft flight corridors, on the other hand, were reduced compared to 2008 due to reduced air traffic. The mass concentrations of sulfate particles were reduced in the lower troposphere compared to previous campaigns in Europe (EMeRGe-EU in summer 2017 and CAFE-Africa in summer 2018) due to reduced anthropogenic emissions, while they were enhanced in the stratosphere due to the persistent effect of the Raikoke volcanic eruption in June 2019.

Below an altitude of 5 km, the concentration of particulate matter with a diameter of ≤ 1 µm (PM1) was reduced by a factor of up to 2–3 during the CAFE-EU/BLUESKY campaign when compared to the values from the CAFE-Africa and EMeRGe-EU campaigns; this is consistent with the chemical species detected: organic matter, sulfate, nitrate, and ammonium, as Figure 11 shows. In addition, organic matter mass was also reduced above 5 km altitude. Combined with EMAC simulations, a 40 % reduction in black carbon mass was observed due to the lockdown effects. The aerosol number concentration of particles > 18 nm was reduced by 30–70 % between 4 and 11 km altitude during CAFE-EU/BLUESKY compared to the IAGOS-CARIBIC data for May and June between 2005 and 2015.

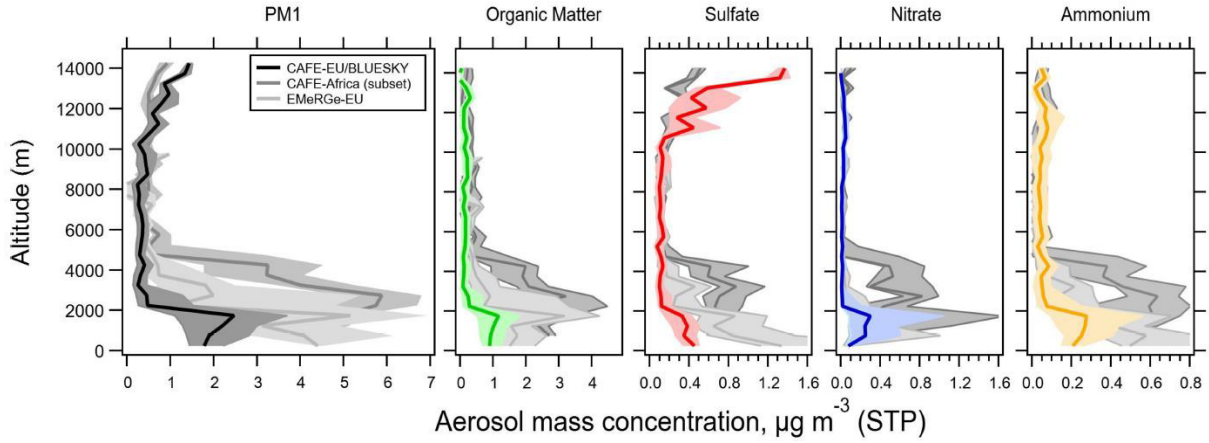

Figure 11: Vertical profiles of the aerosol mass concentration of PM1, organic matter, sulfate, nitrate, and ammonium during CAFE-EU/BLUESKY (colours) compared to the European data subset of CAFE-Africa (dark grey) and EMeRGe-EU (light grey), taken from Voigt et al. (2022).

The sky over Western Europe appeared bluer than usual during the lockdown period in 2020. This perception was investigated by using simulations of the atmospheric radiative transfer model UVSPEC using altitude-resolved aerosol optical thickness (AOT) data as an input. The AOT data were provided by the Moderate Resolution Imaging Spectroradiometer (MODIS) on board the Terra and Aqua satellites. The median AOT for Europe for the period 23 May to 9 June 2020 was 0.156 at 0.55 µm and 0.247 for the same period in the years 2015–2019 (see Figure 12 (a)); this corresponds to a reduction of 40 % in AOT. Furthermore, the spectrum of the diffuse component of downward directed spectral irradiances for a solar zenith angle (SZA) of 45° was shifted towards shorter wavelengths for the CAFE-EU/BLUESKY campaign (see Figure 12 (b)); this resulted in a bluer colour of the sky as perceived by the human eye (see Figure 12 (c) to (e)).

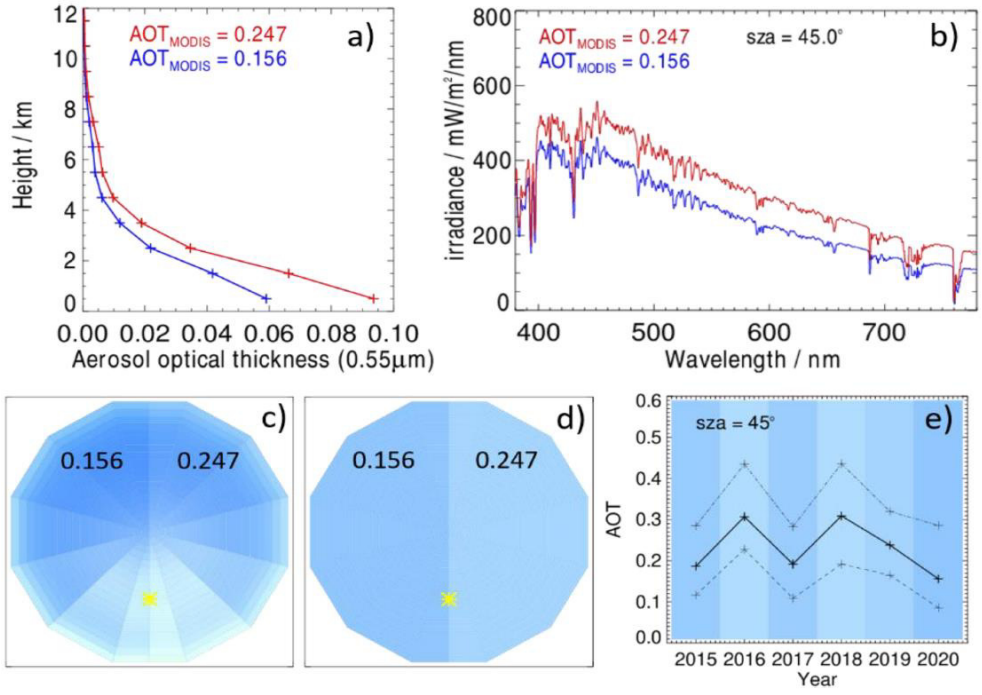

Figure 12: The blue sky during BLUESKY. (a) Altitude profile of the aerosol optical thickness (AOT) in 2020 (blue) and 2015–2019 (red). (b) Irradiance versus wavelength for 2020 (blue) and 2015–2019 (red) at a solar zenith angle (sza) of 45°. (c) and (d) Sky colours as perceived by the human eye (left: 2020; right: 2015–2019). (e) Evolution of the AOT and sky colour in the years 2015–2020. Taken from Voigt et al. (2022).

The reduced air traffic also led to reduced contrail cirrus cover and contrail optical thickness during the campaign period. Moreover, the reduction in the extinction and depolarisation ratio of cirrus clouds below –50 °C was observed and may have potentially been caused by the reduced air traffic.

The CAFE-EU/BLUESKY campaign offers a unique dataset on the changes in trace gases, aerosol particles, and clouds during the COVID lockdown in Europe, contributing to a better understanding of anthropogenic influences on the atmosphere.

4.1.3 Summary of "Mass spectrometric measurements of ambient ions during CAFE-EU/BLUESKY"

In the research article "Mass spectrometric measurements of ambient ions and estimation of gaseous sulfuric acid in the free troposphere and lowermost stratosphere during the CAFE-EU/BLUESKY campaign" by Zauner-Wieczorek et al. (2022a), results of the APi-TOF-MS measurements during the CAFE-EU/BLUESKY campaign are presented. The measurements took place between 30 May and 09 June 2020 in an altitude range of 4.7–13.5 km for a total of 6 hours in the negative mode and 0.6–12.7 km for a total of 1.4 hours in the positive mode above Western Europe.

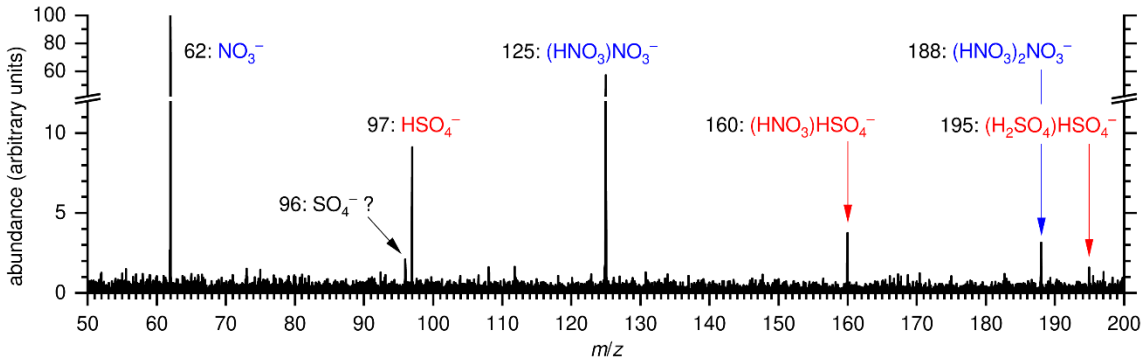

Figure 13: Average mass spectrum (6 hours) recorded during the measurements in the negative APi mode during CAFE-EU/BLUESKY, taken from Zauner-Wieczorek et al. (2022a).

In agreement with the literature, NO_3^-, $(HNO_3)NO_3^-$, $(HNO_3)_2NO_3^-$ (called nitrate core ions), HSO_4^-, $(HNO_3)HSO_4^-$, and $(H_2SO_4)HSO_4^-$ (called hydrogen sulfate core ions) were identified. Figure 13 shows the average mass spectrum recorded during the negative APi measurements. The peak at $m/z = 96$ could possibly be assigned to SO_4^-, however, it does not agree to the exact mass of SO_4^- perfectly. As Figure 14 (a) to (c) shows, the measured count rates were significantly increased above the tropopause (10–11 km) for NO_3^- and $(HNO_3)NO_3^-$, while there was no clear trend observed for HSO_4^-. From the ratio of nitrate and hydrogen sulfate core ions, the number concentration of gaseous sulfuric acid was inferred according to Eq. (14) (Arnold and Qiu, 1984):

$$[H_2SO_4] = \frac{1}{k \cdot t_{rec}} \cdot \ln\left(1 + \frac{CR(HSO_4^-)}{CR(NO_3^-)}\right), \quad (14)$$

where k is the reaction rate constant of the reaction $H_2SO_4 + NO_3^- \rightarrow HSO_4^- + HNO_3$, t_{rec} is the ion–ion recombination lifetime and CR is the sum of count rates of the respective core ion family. The resulting number concentrations of H_2SO_4 were in the order of 10^5 cm^{-3}: the maximum average value was observed in the altitude bin of 8.7–9.2 km ($7.8 \cdot 10^5$ cm^{-3}), whereas the lowest average value was found in the highest altitude bin, i.e. 13.4 km ($1.9 \cdot 10^5$ cm^{-3}), as Figure 14 (d) shows. The scarce literature suggests that the concentration of H_2SO_4 decreases above 8 km which is in accordance with these findings. Furthermore, the proof of principle was reported for measurements in the positive APi mode and protonated pyridine ($H^+(C_5H_5N)$) was detected unambiguously, where its largest abundance was observed in an altitude range of between 4.6 and 8.5 km.

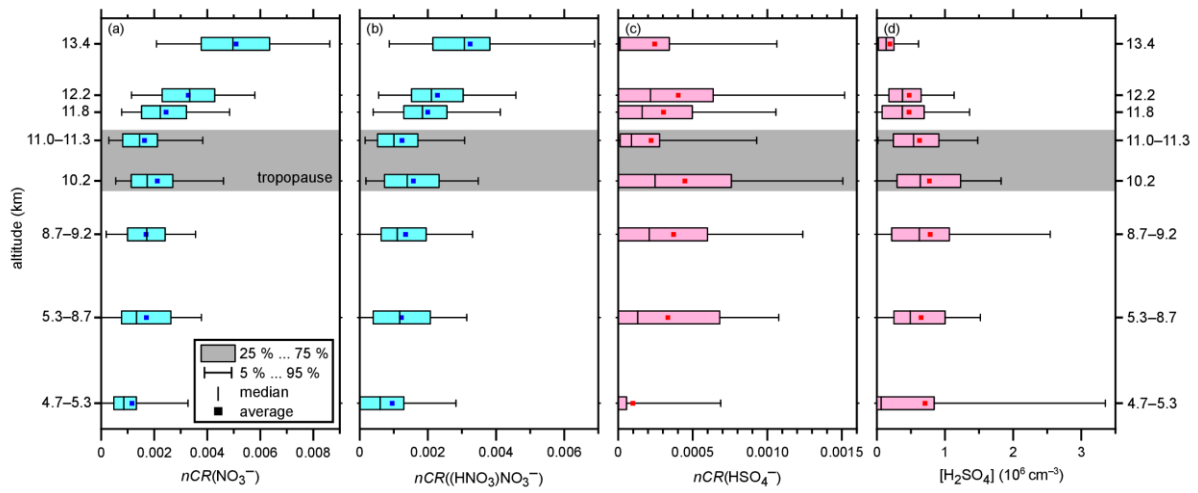

Figure 14: Vertical profiles of the normalised count rates nCR of (a) NO_3^-, (b) $(HNO_3)NO_3^-$, and (c) HSO_4^- and (d) vertical profile of the number concentration of gaseous sulfuric acid, taken from Zauner-Wieczorek et al. (2022a).

During a measurement flight above the Mediterranean Sea offshore Italy at 5.3 km altitude and 261 K ambient temperature, simultaneous increases in total and nitrate ion count rates, particle concentration (in the size range < 100 nm) of nitrate and organics, and relative humidity occurred for 30 seconds during an in-cloud measurement. Since mixed-phase clouds are mostly liquid at a temperature of 261 K, it is hypothesised that this event was caused by the shattering of water droplets on the surface of the aircraft or inlet system due to the balloelectric effect (Christiansen, 1913).

In this publication, the first measurements of atmospheric ions in the UTLS with a TOF-MS was reported, providing not only qualitative information on the distribution of nitrate and hydrogen sulfate ions, but also quantitative information on the number concentration of gaseous sulfuric acid. This information had, until then, only been reported twice in the literature for the UTLS (Heitmann and Arnold, 1983; Möhler and Arnold, 1992).

4.2 Contribution to the publications

The research article “Mass spectrometric measurements of ambient ions and estimation of gaseous sulfuric acid in the free troposphere and lowermost stratosphere during the CAFE-EU/BLUESKY campaign” is based on measurements with the TOF-MS during the CAFE-EU/BLUESKY campaign. I participated in the preparation and performance of the measurements, analysed the APi-TOF-MS data, and subsequently designed and wrote the manuscript except for chapter 2.1.

The review article “The ion–ion recombination coefficient α: comparison of temperature- and pressure-dependent parameterisations for the troposphere and stratosphere” is an independent research project of mine, which was motivated by the requirement to find a suitable formulation for calculating the ion–ion recombination coefficient for different altitudes. I designed the study, brought together and revised the literature, and coded the theories and parameterisations for the comparison except for the theories of Natanson, Fuchs, Hoppel and Frick, and Filippov. The calculation of the data points in chapter 8 (Fig. 4; Table B1) were not performed by me. I wrote the manuscript except for chapter 6 and parts of chapter 5.

The research article “Cleaner Skies during the COVID-19 Lockdown” provides an overview of the CAFE-EU/BLUESKY campaign and highlights the most important results. I contributed to the preparation and conduction of the measurements with the SCORPION-TOF-MS and participated as an instrument operator during one of the scientific flights. I analysed the SCOPRION-TOF-MS data yielding the sulfuric acid data shown in the publication.

4.3 Publications

4.3.1 The ion–ion recombination coefficient α

Atmos. Chem. Phys., 22, 12443–12465, 2022
https://doi.org/10.5194/acp-22-12443-2022

Atmospheric Chemistry and Physics
Open Access
EGU

Review article

The ion–ion recombination coefficient α: comparison of temperature- and pressure-dependent parameterisations for the troposphere and stratosphere

Marcel Zauner-Wieczorek, Joachim Curtius, and Andreas Kürten

Institute for Atmospheric and Environmental Sciences, Goethe University Frankfurt am Main, Frankfurt am Main, 60629, Germany

Correspondence: Marcel Zauner-Wieczorek (zauner-wieczorek@iau.uni-frankfurt.de) and Andreas Kürten (kuerten@iau.uni-frankfurt.de)

Received: 21 September 2021 – Discussion started: 3 November 2021
Revised: 4 July 2022 – Accepted: 18 August 2022 – Published: 22 September 2022

Abstract. Many different atmospheric, physical, and chemical processes are affected by ions. An important sink for atmospheric ions is the reaction and mutual neutralisation of a positive and negative ion, also called ion–ion recombination. While the value for the ion–ion recombination coefficient α is well-known for standard conditions (namely $1.7 \times 10^{-6}\,\mathrm{cm^3\,s^{-1}}$), it needs to be calculated for deviating temperature and pressure conditions, especially for applications at higher altitudes of the atmosphere. In this work, we review the history of theories and parameterisations of the ion–ion recombination coefficient, focussing on the temperature and pressure dependencies as well as the altitude range between 0 and 50 km. Commencing with theories based on J. J. Thomson's work, we describe important semi-empirical adjustments as well as field, model, and laboratory data sets, followed by short reviews of binary recombination theories, model simulations, and the application of ion–aerosol theories to ion–ion recombination. We present a comparison between theories, parameterisations, and field, model, and laboratory data sets to conclude favourable parameterisations. While many theories agree well with field data above an altitude of approximately 10 km, the nature of the recombination coefficient is still widely unknown between Earth's surface and an altitude of 10 km. According to the current state of knowledge, it appears reasonable to assume an almost constant value for the recombination coefficient for this region, while it is necessary to use values that are adjusted for pressure and temperature for altitudes above 10 km. Suitable parameterisations for different altitude ranges are presented and the need for future research, be it in the laboratory or by means of modelling, is identified.

1 Introduction

Earth's atmosphere is not only a neutral mixture of gases, but also contains gas-phase ions that are crucial to the phenomena of atmospheric electricity. They play a central role in meteorological processes in thunderstorms (Sagalyn et al., 1985), maintaining the global atmospheric electrical circuit (Harrison, 2004), the formation of aerosol particles with the ion-induced nucleation mechanism (Hirsikko et al., 2011), and the propagation of radio waves in the ionosphere (Basu et al., 1985), to name but a few processes. It is thus important to understand the production and loss of atmospheric ions. There are several sources of ions in the atmosphere, of which ionisation by galactic cosmic rays (GCRs) is the most important (Bazilevskaya et al., 2008). Close to the ground, ionisation by the radioactive decay of radon as well as lightning are additional sources of atmospheric ions (Viggiano and Arnold, 1995). Further, minor sources of ionisation in the atmosphere include solar cosmic rays (also called solar energetic particles, SEPs) and magnetospheric electrons (Bazilevskaya et al., 2008). The two important sinks for atmospheric ions are the reaction of a positive ion and negative ion, the so-called recombination, as well as the condensation of ions onto aerosol particles (Viggiano and Arnold, 1995).

Published by Copernicus Publications on behalf of the European Geosciences Union.

The ion–ion recombination coefficient α describes the reaction rate of the recombination of a positive and negative ion in the gas phase; its unit is $cm^3\,s^{-1}$, which is used throughout this work unless noted otherwise. There are two important recombination mechanisms: binary recombination, in which two ions of opposite sign recombine upon collision, and ternary recombination, in which one of the ions first collides with a neutral gas molecule, i.e. the third body, to dissipate energy in order to recombine successfully with the second ion. Hence, the latter process is also called three-body trapping. When both the binary and ternary processes are included in a theory or parameterisation, it is called total recombination. While ion–ion recombination concerns the recombination of atomic or molecular ions or small molecular ion clusters, ion–aerosol attachment regards the interaction between an ion and a charged or neutral aerosol particle. Typically, aerosol particles are defined to have a size of 1 nm or bigger. As the ion–aerosol attachment coefficient depends on the size of the aerosol particle, the ion–ion recombination coefficient can be viewed as a special case of the former if the "aerosol particle" is considered to have ionic size and is singly charged.

In this work, we focus on ion–ion recombination and summarise the history and fundamentals of the theory behind it in Sect. 2, followed by a description of the theories of the binary ion–ion recombination process in Sect. 3. In Sect. 4, we discuss the field and laboratory measurements and subsequent semi-empirical parameterisations of ion–ion recombination. We focus on the applicability of the theory to atmospheric conditions, especially for the troposphere and stratosphere, i.e. in an altitude range of 0–50 km. We describe the application of ion–aerosol theories to the ion–ion recombination in Sect. 5, followed by an overview of numerical simulations in Sect. 6. Thereafter, we compare the available parameterisations and theories with field data, laboratory data, and a model simulation for the atmospheric altitude range of 0–50 km in Sect. 7. The determination of the three-body trapping sphere radius and the collision probability in the limiting sphere (a concept used in different theories) can be found in Sect. 8. Finally, we conclude the applicability of the discussed theories to atmospheric conditions and identify the demand for future research in Sect. 9. To improve the readability, we adhere to the conventionally used units of hPa and atm for pressure, $cm^3\,s^{-1}$ for the recombination rate and related quantities, eV for the electron affinity, and km for the atmospheric altitude; otherwise, we use the SI units.

2 The fundamental theories

The theoretical foundation of the recombination of gaseous ions was laid down by J. J. Thomson and Ernest Rutherford. The theory based on their approach is referred to as the Thomson theory in the literature. In their work "On the Passage of Electricity of Gases exposed to Röntgen Rays", Thomson and Rutherford (1896) discuss, for the first time, the sources and sinks of ions in the gas phase. In their experimental setup, the source of ions are X-rays, while the sinks are the recombination of negative and positive ions as well as losses to the electrodes. They describe the temporal change of the number concentration of ions n according to Eq. (1):

$$\frac{\mathrm{d}n}{\mathrm{d}t} = q - \alpha n^2 - L, \tag{1}$$

where t is the time, q is the ion production rate, and L is the loss rate to the electrodes. This formula already includes the assumption that the number concentrations of negative and positive ions, n_- and n_+, are approximately equal and, therefore, the product $n_- n_+$ can be simplified to n^2. They conclude that when the electrode current is small ($L \approx 0$) and the system is in a steady state ($\mathrm{d}n/\mathrm{d}t = 0$), the number concentration of gas-phase ions can be calculated in a simple way (Eq. 2):

$$n^2 = \frac{q}{\alpha}. \tag{2}$$

As per today's convention, q is the production rate for ion pairs so that n in Eqs. (1) and (2) must be specified to be either n_+ or n_-, not to be confused with $n_{\mathrm{total}} = n_+ + n_-$. Equation (2) can be rearranged to determine α when the ion pair production rate and the number concentration of positive or negative ions are known. A few years later, in 1906, the Nobel Prize in Physics was awarded to J. J. Thomson for his studies on the electrical conductivity of gases.

Soon after Thomson and Rutherford's publication, several experiments to determine the ion–ion recombination coefficient were pursued by different scientists. It was shown that α is dependent on the chemical composition of the surrounding gas, as well as on the temperature and pressure. Here, we focus on experiments in air. Many of these first approaches have been reviewed by Lenz (1932), who himself had developed a sophisticated experimental setup in order to control losses due to diffusion and deposition on walls. It is remarkable that even during this time, the determined values of α are similar to the one used today and have not changed significantly since then. For standard conditions, i.e. 273.15 K and 1013 hPa, Thirkill (1913) determined a value of $1.7 \times 10^{-6}\,cm^3\,s^{-1}$, while Thomson (1924) determined a value of $2.0 \times 10^{-6}\,cm^3\,s^{-1}$. Lenz (1932) reported $(1.7 \pm 0.1) \times 10^{-6}\,cm^3\,s^{-1}$ for the conditions of 291.15 K and 1013 hPa. The value for α used nowadays is $1.6 \times 10^{-6}\,cm^3\,s^{-1}$ (e.g. Franchin et al., 2015) and is taken from Israël (1971) (which is the English translation of the first edition in German: Israël, 1957). In addition, Gardner (1938) reported the value of $2.1 \times 10^{-6}\,cm^3\,s^{-1}$ for pure oxygen, 1013 hPa, and 298.15 K. Sayers (1938) reported a value of $2.3 \times 10^{-6}\,cm^3\,s^{-1}$, while Nolan (1943), who has also reviewed previous works, concluded $1.4 \times 10^{-6}\,cm^3\,s^{-1}$. Within a particular uncertainty range, these values do agree

quite well and no further ado appears to be necessary to discuss this value. However, the values for α differ tremendously when temperatures are lower than 273.15 K and pressures are lower than 1013 hPa, as Lenz (1932) has already shown. Loeb (1960) pointed out that before the 1950s, measurement techniques were not sophisticated enough and gases not pure enough to be able to determine the ion–ion recombination accurately. In any case, a correct value for α is crucial for the analysis of field data and the calculations of atmospheric models at higher altitudes in the atmosphere where the temperatures and pressures are different from those at ground level. This calls for a good understanding of the mechanisms involved in ion–ion recombination and a solid parameterisation of α.

In a later work, Thomson (1924) explains his theory in more detail and provides a kinetic derivation of the recombination coefficient. In his approach, recombination occurs when the two oppositely charged ions each collide with a neutral molecule of the surrounding gas within a certain sphere d_T around the respective ions. It is defined as the sphere in which the ions of opposite signs experience Coulomb attraction (Loeb, 1960); thus, it can be derived from equalising the Coulomb potential energy, $e^2(4\pi\varepsilon_0 d_\mathrm{T})^{-1}$, and the thermal energy of motion from the surrounding molecules and ions in the absence of an electrical field, $1.5\,k_\mathrm{B}T$ (Loeb, 1960), as shown in Eq. (3):

$$d_\mathrm{T} = \frac{e^2}{4\pi\cdot\varepsilon_0\cdot 1.5 k_\mathrm{B}T}, \tag{3}$$

where e is the elementary charge, ε_0 is the vacuum permittivity, k_B is the Boltzmann constant, and T is the temperature. Loeb (1960) stresses that the pre-factor value of 1.5 for the thermal energy is debated, ranging from 1 (Tamadate et al., 2020b), 1.5 (Thomson, 1924), and 2.4 (Natanson, 1959a) to 6 (Loeb and Marshall, 1929), amongst others. Loeb and Marshall (1929) approximate the radius d_T to be in the order of 10 nm when the value of $6\,k_\mathrm{B}T$ is used for the thermal energy. Thus, a rough estimate of 10–60 nm for d_T can be derived from different Thomsonian theories.

Thomson deduced that α is dependent on the average speeds of the positive and negative ion, v_+ and v_-, respectively, according to Eq. (4) for low pressures and Eq. (5) for high pressures:

$$\alpha = 2\pi\cdot\left(v_+^2+v_-^2\right)^{0.5}\cdot d_\mathrm{T}^3\cdot\left(\frac{1}{\lambda_+}+\frac{1}{\lambda_-}\right), \tag{4}$$

where the pressure is low, i.e. $d_\mathrm{T}\lambda_\mathrm{ion}^{-1}$ is small, λ_+ and λ_- are the mean free paths of the positive and negative ions, respectively, and λ_ion is the mean free path of one ion.

$$\alpha = 2\pi\cdot\left(v_+^2+v_-^2\right)^{0.5}\cdot d_\mathrm{T}^2, \tag{5}$$

where the pressure is high, i.e. $d_\mathrm{T}\lambda_\mathrm{ion}^{-1}$ is large. From these equations, Thomson (1924) deduced that the recombination coefficient is proportional to the pressure for low pressures (because of the sum of the reciprocal mean free paths of the ions), whereas it is independent of the pressure for high pressures. This was supported by the measurements of Thirkill (1913) who found α to be proportional to the pressure throughout the measurement range of approximately 200–1000 hPa. Thus, the pressure regime of 1013 hPa and below is included in the low-pressure scenario. The transition pressure from the low-pressure to the high-pressure regime is clearly above 1013 hPa, and thus beyond the concern of atmospheric application. The temperature dependence is given as $\alpha\sim T^{-2.5}$ for low pressures and $\alpha\sim T^{-1.5}$ for high pressures because $d\sim T^{-1}$ and $v_{+,-}\sim T^{0.5}$ (Thomson, 1924). Hence, the recombination coefficient decreases with rising temperature for pressures below 1013 hPa. For the troposphere, this leads to a somewhat counterbalancing effect on α for increasing altitudes when both the temperature and pressure drop simultaneously.

Another approach to explain the recombination of ions was introduced by Langevin (1903a, b) whose ansatz is based on the speeds of ions in an electrical field, as opposed to the later thermodynamic approach of Thomson. To account for the effectiveness of collisions of a negative and positive ion with regard to recombination, Langevin introduced the ratio of successful recombinations per collision, ε_L, which is included in the formula that he proposed to determine α (Eq. 6); this probability is of empirical nature and was not further defined by a formula:

$$\alpha = \frac{e}{\varepsilon_0}\cdot(\mu_+ + \mu_-)\cdot\varepsilon_\mathrm{L}, \tag{6}$$

where μ_+ and μ_- are the ion mobilities of the positive and negative ions, respectively, defined by Eq. (7a) and (7b):

$$v_+ = \mu_+\cdot\left(E+\frac{e}{4\pi\cdot\varepsilon_0\cdot r^2}\right), \tag{7a}$$

$$v_- = -\mu_-\cdot\left(E+\frac{e}{4\pi\cdot\varepsilon_0\cdot r^2}\right), \tag{7b}$$

where E is the external electrical field and $e(4\pi\varepsilon_0 r^2)^{-1}$ is the electrical field produced by the ions. Here, r is the distance between the two ions of opposite charge (Langevin, 1903a). The consideration of the recombination efficiency leads to an adapted term for the recombination sink (Langevin, 1903a) shown in Eq. (8):

$$\frac{\mathrm{d}n_\pm}{\mathrm{d}t} = -\frac{e}{\varepsilon_0}\cdot(\mu_+ + \mu_-)\cdot\varepsilon_\mathrm{L}\cdot n_+\cdot n_-. \tag{8}$$

Langevin (1903b) further determined the pressure (p) dependence of ε_L (and thus of α). For 1013 hPa, $\varepsilon_\mathrm{L}=0.27$ and $\varepsilon_\mathrm{L}\sim p^2$ (and thus $\alpha\sim p^2$) for pressures below 1013 hPa. However, this is in contrast to Thomson (1924) who stated that $\alpha\sim p$ for low pressures. Loeb and his colleagues later argued that the assumptions made by Langevin to calculate ε_L

are based on incorrect, sometimes even antithetical assumptions. They even stated that this correction factor was only introduced to make the experimental results fit the theoretical ones. The application of the Langevin theory is only considered valid for very high pressures (above approximately 10 atm) (Loeb and Marshall, 1929; Gardner, 1938; Loeb, 1960) and is therefore not within the focus of this work.

Loeb and Marshall (1929) further advanced and refined the Thomson theory; they introduced a probability term, similar to Langevin, for collisions leading to recombination, extending Eq. (5) to a more refined Eq. (9):

$$\alpha = \pi \cdot d_{\mathrm{T}}^2 \cdot \left(v_+^2 + v_-^2\right)^{0.5} \cdot \left[1 - \frac{\lambda_{\mathrm{ion}}^2}{2d_{\mathrm{T}}^2} \cdot \left(1 - \mathrm{e}^{-2d_{\mathrm{T}}/\lambda_{\mathrm{ion}}} \cdot \left(\frac{2d_{\mathrm{T}}}{\lambda_{\mathrm{ion}}} + 1\right)\right)\right]^2. \quad (9)$$

In subsequent works, the ratio of the doubled collision sphere radius and the mean free path of the ion, $2d_{\mathrm{T}} \cdot \lambda_{\mathrm{ion}}^{-1}$, is often denoted as x. With a number of assumptions and simplifications, and together with validation from experimental work, Gardner (1938) summarised the previous findings and advanced them to a set of equations (Eqs. 10–13) that contain macroscopic quantities that are more accessible for direct observation:

$$\alpha = 1.9 \times 10^{-5} \cdot \left(\frac{T_0}{T}\right)^{1.5} \cdot \left(\frac{1}{m_{\mathrm{ion}}}\right)^{0.5} \cdot \varepsilon_{\mathrm{T}}, \quad (10)$$

where

$$\varepsilon_{\mathrm{T}} = 2w_{\mathrm{T}} - w_{\mathrm{T}}^2, \quad (11)$$

$$w_{\mathrm{T}} = 1 - 2 \cdot \frac{\left[1 - e^{-x'} \cdot \left(x' + 1\right)\right]}{x'^2}, \quad (12)$$

and

$$x' = 0.810 \cdot \left(\frac{T_0}{T}\right)^2 \cdot \left(\frac{p}{p_0}\right) \cdot \frac{\lambda_{\mathrm{air}}}{\lambda_{\mathrm{ion}}}, \quad (13)$$

where T_0 is the temperature at standard conditions (i.e. 273.15 K), m_{ion} is the ion mass in Da, ε_{T} is the recombination probability upon collision, p_0 is the pressure at standard conditions (i.e. 1013.25 hPa), λ_{air} is the mean free path of the surrounding air, and the ratio $\lambda_{\mathrm{air}} \cdot \lambda_{\mathrm{ion}}^{-1} = 5$. Here, x is no longer defined by the ratio of d_{T} and λ_{ion}, but as a function of T, p, and the ratio $\lambda_{\mathrm{air}} \cdot \lambda_{\mathrm{ion}}^{-1}$, and hence denoted as x'. Importantly, Loeb and Marshall (1929) also discuss the limitations of their approach. Firstly, the exact masses of the ions are unknown since clustered ions and ions from impurities in the sample gas can also occur. This has a non-negligible effect on the value of the recombination coefficient. They argue that this circumstance could be the reason for the variation of results among different authors. Apart from the difference in ion mass, the property of free electron pairs in the surrounding gas may also influence the recombination (Loeb and Marshall, 1929). Secondly, based on the observation that the measured α value is much smaller than the calculated one at low temperatures, they discuss whether the presumed power of -1.5 for the T dependence might be inaccurate.

A detailed overview of the different theories and their experimental validations can be found in Loeb (1960) (second edition of Loeb, 1955) where he discusses ion–electron and ion–ion recombination. For the latter, cases of α, particle- or X-ray-induced ion production that feature a non-uniform spatial ion distribution are also described. Until the beginning of the 1980s, it was hypothesised that, in general, ions are not uniformly distributed in the atmosphere because the ions are produced along the GCR paths and diffusion may not be sufficiently fast. Bates (1982) showed that ions are mixed fast enough in the atmosphere so that the assumption of a uniform ion concentration of the "volume recombination" theories, described in the following discussion, is valid. Table 1 provides a selection of recombination theories discussed in detail by Loeb (1960). Above atmospheric pressure, the Langevin theory is applied. Loeb subclassifies it, firstly, to the range of 20–100 atm, where there is no diffusional approach of the ions towards each other because they are already within the Coulomb attractive radius d_{T} and, secondly, to the range of 2–20 atm (called the Langevin–Harper theory), where the initial distance of the ions r_0 is greater than d_{T}; hence they first have to diffuse towards each other. The subsequent collision inside d_{T} is almost certain because of the high pressure. For the pressure range of 0.01–1013 hPa, i.e. for the lower and middle atmosphere, the Thomson theory is applicable. Here, the initial distance of the ions is greater than d_{T} and the mean free path λ_{ion}; therefore, a random diffusive approach is necessary. Within d_{T}, the collision probability ε_{T} is less than 1. Below 0.01 hPa, i.e. in the ionosphere, the collision probability becomes almost 0, and thus the collision is governed by the collision cross section. For super-atmospheric pressures (i.e. in the Langevin regime), α is dependent on p^{-1} and proportional to T. In the regime where the Thomson theory should be applicable (i.e. from 0.01 to 1013 hPa), α is dependent on $T^{-1.5}$. The pressure dependence of α is different in various Thomsonian theories; while Thomson (1924) stated a proportional dependence (see Eq. 4), it varies in the parameterisations of Gardner (1938), Israël (1957), and Loeb (1960) (see Eqs. 10, 14, 15, respectively, with Eqs. 11–13): for approximately 500–1000 hPa, α is dependent on $p^{0.5}$ and below 500 hPa, it approaches p^1. In the cross-section regime (i.e. < 0.01 hPa), α is independent of the pressure and dependent on $T^{-0.5}$.

A detailed derivation of all theories and the above-mentioned equations is given in Loeb (1960). In his work, the only variation in the Thomson parameterisation for α from the one presented by Gardner (1938) is the first factor in the formula for the recombination coefficient, as shown in Eq. (14):

Table 1. Selection of ion–ion recombination theories described in detail by Loeb (1960), where d_T is the radius of mutual Coulomb attraction between the two ions of opposite charge, r_0 is the initial distance of the two ions, and λ_{ion} is the mean free path of one ion.

Theory	Pressure range	Conditions	p and T dependence	Description
Langevin	20–100 atm	$d_T > r_0 > \lambda_{ion}$	p^{-1}, T^1	Both ions inside d_T, no diffusive approach
Langevin–Harper	1–20 atm	$r_0 > d_T > \lambda_{ion}$	p^{-1}, T^1	Diffusion towards d_T, collision inside d_T certain
Thomson	0.01–1013 hPa	$r_0 > d_T \approx \lambda_{ion}$	$p^{0.5...1}$, $T^{-1.5}$	Random diffusive approach, finite collision probability ε_T
Collision cross section	< 0.01 hPa	$\lambda_{ion} > r_0 > d_T$	no p dep., $T^{-0.5}$	Collision probability $\varepsilon_T \approx 0$, collision driven by cross section (ionosphere)

$$\alpha = 1.73 \times 10^{-5} \cdot \left(\frac{273}{T}\right)^{1.5} \cdot \left(\frac{1}{m_{ion}}\right)^{0.5} \cdot \varepsilon_T. \tag{14}$$

Israël (1957) further altered this parameterisation by including the few experimental data available at that time into his parameterisation. In the derivation of the formula, he used the value of $1.6 \times 10^{-6}\,cm^3\,s^{-1}$ for α for "normal conditions". However, he neither included a reference for this nor specified the normal conditions. These were probably 273.15 K and 1013.25 hPa. Furthermore, he stated that the recombination of small negative and small positive ions are accompanied by the recombination of small and big ions as well as small ions with neutrals, so that a whole equation system of recombination rates would result. He proposed the slightly altered parameterisation of the small-ion recombination that no longer includes the ion mass according to Eq. (15):

$$\alpha = 1.95 \times 10^{-6} \cdot \left(\frac{273}{T}\right)^{1.5} \cdot \varepsilon_T. \tag{15}$$

Contrary to previous authors, Israël used the value $\lambda_{air} \cdot \lambda_{ion}^{-1} \approx 3$ for air; Gardner (1938) and Loeb (1960) used the value of 5. Note that in Israël's work, there is a typing error in the formula of ε_T: instead of $\varepsilon_T = 1 - \frac{4}{x'^4} \cdot [1 - e^{-x'} \cdot (x'+1)]^2$, the fraction in front of the brackets was erroneously given as $\frac{4}{x'^2}$.

Natanson (1959a) (English translation of the original in Russian: Natanson, 1959b) developed a theory to unify Thomson's (low pressure) and Langevin's (high pressure) approaches; this formula is given in Eq. (16), assuming two ions of identical mass:

$$\alpha = \frac{\pi \cdot d_N^2 \cdot v_{rel} \cdot \varepsilon_N \cdot \left[1 + \frac{e^2 \cdot \lambda}{4\pi \cdot \varepsilon_0 \cdot d_N \cdot (d_N + \lambda) \cdot k_B T}\right] \cdot \exp\left(\frac{e^2}{4\pi \cdot \varepsilon_0 \cdot (d_N + \lambda) \cdot k_B T}\right)}{1 + \frac{\pi \cdot \varepsilon_0 \cdot d_N^2 \cdot v_{rel} \cdot \varepsilon_N \cdot k_B T}{e^2 \cdot D} \cdot \left[1 + \frac{e^2 \cdot \lambda}{4\pi \cdot \varepsilon_0 \cdot d_N \cdot (d_N + \lambda) \cdot k_B T}\right] \cdot \left[\exp\left(\frac{e^2}{4\pi \cdot \varepsilon_0 \cdot (d_N + \lambda) \cdot k_B T}\right) - 1\right]}, \tag{16}$$

with

$$d_N = \frac{\lambda}{2} \cdot \left[\sqrt{1 + \frac{5e^2}{12\pi \cdot \varepsilon_0 \cdot k_B T \cdot \lambda}} - 1\right], \tag{17}$$

$$v_{rel} = \sqrt{\frac{8 \cdot k_B T}{\pi \cdot m_{red}}}, \tag{18}$$

$$\varepsilon_N = 2w_N - w_N^2, \tag{19}$$

$$w_N = 1 - \frac{2}{x_N^2} \cdot \left[1 - e^{-x_N} \cdot (x_N + 1)\right], \tag{20}$$

and

$$x_N = \frac{2 \cdot d_N}{\lambda}, \tag{21}$$

where d_N is the ion–ion trapping distance, v_{rel} is the mean relative thermal speed of the ions, ε_N is the probability that one ion collides with a gas molecule while the other ion is at a distance $< d_N$ (also named "absorption coefficient"), D is the diffusion coefficient, and m_{red} is the reduced mass in kg. Note that the use of x_N depends on Natanson's d_N in Eq. (20), which is otherwise identical to Eq. (12); D is the sum of D_+ and D_-, the diffusion coefficients of the positive and negative ion, respectively. Tamadate et al. (2020b) suggested exchanging $v_{rel} \cdot D^{-1}$ with the reciprocal of the ion–ion mean free path, λ^{-1}, in the first fraction of the denominator in Eq. (16), based on the definition of λ in Eq. (22):

$$\lambda = D \cdot v_{rel}^{-1} = (D_+ + D_-) \cdot \left(\frac{\pi \cdot m_{red}}{8 \cdot k_B T}\right)^{0.5}, \tag{22}$$

where D_+ and D_- are calculated according to Eq. (23a) and (23b), respectively:

$$D_+ = D_{+,0} \cdot \frac{p_0}{p} \cdot \left(\frac{T}{T_0}\right)^{1.75}, \tag{23a}$$

and

$$D_- = D_{-,0} \cdot \frac{p_0}{p} \cdot \left(\frac{T}{T_0}\right)^{1.75}, \tag{23b}$$

with

$$D_{+/-,0} = \frac{\mu_0 \cdot k_B T_0}{e}, \tag{24}$$

where $D_{+,0}$ and $D_{-,0}$ are the reference diffusivities calculated from the reference ion mobility at standard pressure ($p_0 = 1013.25$ hPa) and standard temperature ($T_0 = 273.15$ K), μ_0, given by López-Yglesias and Flagan (2013) as $\mu_0 = 1.35 \times 10^{-4}\,\mathrm{m^2\,V^{-1}\,s^{-1}}$ for the ion mass of 90 Da. The temperature dependence of 1.75 for $D_{+,-}$ is taken from Tang et al. (2014). Note that López-Yglesias and Flagan (2013) use T^2 and the Chapman–Enskog theory predicts $T^{1.5}$ (Chapman and Cowling, 1960).

In the course of time, additional sinks for atmospheric ions, other than the ion–ion recombination process, have been discussed. Lenz (1932) explained the strong deviations observed between several experimentally derived values for α by the authors' negligence of losses due to their experimental setups, for example, by wall losses. In addition, the attachment of ions to aerosol particles suspended in the surrounding gas has been found to cause problems in the quantification of α, especially in field studies performed in the atmosphere (Rosen and Hofmann, 1981; Morita, 1983), while Franchin et al. (2015), who conducted chamber experiments, included the aerosol sink and wall losses to their calculations. Furthermore, one has to bear in mind that the capabilities of the instruments and the purity of the gases were less advanced before the 1950s (Loeb, 1960). Therefore, results obtained before that time need to be considered with caution. Nevertheless, the theory of ion–ion recombination experienced more advances in the following decades as discussed in the next sections.

3 Binary ion–ion recombination

In the previous section, the theories and parameterisations that concern the total ion–ion recombination, i.e. the combination of binary and ternary processes, were discussed. Commencing in the late 1970s, several groups examined the binary and ternary processes, respectively, in more detail. Hickman (1979) developed an approach to determine the binary recombination coefficient, α_2. Based on a complex potential model, the neutralisation of two ions of opposite sign is determined by an electron transfer from the negative to the positive ion. While the two ions approach one other, the electron transfer can occur when the potential curve of the initial state crosses at least one of the potential curves of the final states. In the semi-empirical Eq. (25), α_2 depends on the temperature T, the reduced mass m_{red}, and the electron affinity EA of the negative ion, i.e. its electron detachment energy:

$$\alpha_2 = 5.35 \times 10^{-7} \cdot \left(\frac{T}{300}\right)^{-0.5} \cdot m_{red}^{-0.5} \cdot \mathrm{EA}^{-0.4}, \tag{25}$$

where m_{red} is in Da and EA is in eV. Due to the mass and electron affinity dependencies, the recombination coefficient can vary by 1 order of magnitude or more, e.g. from $(49 \pm 20) \times 10^{-8}\,\mathrm{cm^3\,s^{-1}}$ for $NO^+ + O^-$ to $(4.1 \pm 0.4) \times 10^{-8}\,\mathrm{cm^3\,s^{-1}}$ for $CClF_2^+ + Cl^-$ (Hickman, 1979). The temperature dependence is $T^{-0.5}$; the mass dependence of $m_{red}^{-0.5}$ is in accordance to Gardner (1938) and Loeb (1960). The dependence on the electron affinity is unique compared to the other approaches.

Several experiments were performed to test this deduction. A recent approach was reported by Miller et al. (2012), who used the variable electron and neutral density attachment mass spectrometry (VENDAMS) method, utilising a flowing afterglow/Langmuir probe (FALP) apparatus. This method is limited to atomic cations from noble gases. Miller et al. (2012) determined the rate coefficients of neutralisation reactions of several anions, among them SF_{4-6}^-, NO_3^-, and Br_2^-, with Ar^+ and Kr^+ at conditions of 300–550 K and a helium buffer gas number concentration of typically $3.2 \times 10^{16}\,\mathrm{cm^{-3}}$ (i.e. 1.3 hPa at 300 K). They also summarised previous works. The resulting binary ion–ion recombination coefficients were found to be in the range of $2.5\text{–}5.6 \times 10^{-8}\,\mathrm{cm^3\,s^{-1}}$ at 300 K, showing decreasing values for higher temperatures, with a typical uncertainty of $5 \times 10^{-9}\,\mathrm{cm^3\,s^{-1}}$ (Miller et al., 2012). Shuman et al. (2014b) later pointed out that the rate coefficients involving Ar^+ should be increased uniformly by $4 \times 10^{-9}\,\mathrm{cm^3\,s^{-1}}$. Miller et al. (2012) fitted the data to the parameterisation developed by Hickman (1979), resulting in adapted exponents for T, m_{red}, and EA, as shown in Eqs. (26) and (27):

$$\alpha_2 = (3.2 \pm 1.4) \times 10^{-8} \cdot \left(\frac{T}{300}\right)^{-1.1 \pm 0.2} \cdot m_{red}^{-0.01 \pm 0.09} \cdot \mathrm{EA}^{-0.04 \pm 0.23} \tag{26}$$

for diatomic anions and

$$\alpha_2 = (2.8 \pm 1.0) \times 10^{-7} \cdot \left(\frac{T}{300}\right)^{-0.9 \pm 0.2} \cdot m_{red}^{-0.5 \pm 0.1} \cdot \mathrm{EA}^{-0.13 \pm 0.04} \tag{27}$$

for polyatomic anions.

Later, the mutual neutralisation reactions of di- and polyatomic cations with the halide anions Cl^-, I^-, and Br^- were also studied (Shuman et al., 2014a). The cations were produced by transferring the charge from Ar^+ to neutral species such as O_2, NO, or CF_4. It was found that the binary ion–ion recombination coefficients are primarily governed by the chemical nature of the system (i.e. the locations of the curve crossings) for systems with the recombination of two monoatomic ions, while the physical nature of the system (e.g. the relative velocity of the ions) becomes dominant for systems with more than four or five atoms. For the latter, a good description of the rate constants is given by $2.7 \times 10^{-7} m_{red}^{-0.5} (T/300)^{-0.9}$ (Shuman et al., 2014a), thus agreeing with the previous findings given in Eq. (27). In addition, experiments with heavier molecular ions such as

$C_{10}H_8^+$, WF_5^+, and $C_6F_{11}^+$ support these findings (Wiens et al., 2015).

While most research in the field has been carried out on the recombination process itself, some works have also been devoted to study the product formation. For instance, Shuman et al. (2010) investigated the different product channels of the recombination of SF_{4-6}^- with Ar^+. Besides simple electron transfer reactions, the elimination of F atoms was also observed.

Subsequently, further parameterisations of the total ion–ion recombination coefficient based on laboratory experiments and field measurements in the troposphere and stratosphere were developed, as will be discussed in the next section.

4 Field and laboratory measurements and semi-empirical parameterisations

In the late 1970s, Smith and Church (1977) investigated the different influences of binary and ternary collisions on the recombination coefficient. They determined the recombination rates of NO^+ and NO_2^- in an experimental setup for different temperatures and pressures typical for the atmosphere and inferred the binary (α_2) and ternary (α_3) recombination rates for different altitudes using helium as the carrier gas. They found that above 30 km, where air is less dense, the binary recombination is dominant, while below 30 km, where air is denser and three-body collisions are more likely, the ternary recombination is more important. For ground level, they determined a rather high value of $\alpha_3 = 3 \times 10^{-6}\,\mathrm{cm^3\,s^{-1}}$. Interestingly, the total ion–ion recombination rate is almost constant throughout the whole troposphere according to their work. The value only decreases above 10 km, until an altitude of about 50 km. With regard to the temperature, they determined a dependency of $T^{-0.4}$ from their data for the binary recombination. For the ternary recombination, they expected a dependency of $T^{-2.5}$ to T^{-3}, while Fisk et al. (1967) even determined $T^{-4.1}$ in a recombination experiment with Tl_2I^+ and TlI_2^-. Smith and Church (1977) have inferred an equation for the binary recombination from further experiments (Eq. 28), which was later adapted by Bates (1982) (Eq. 29):

$$\alpha_2 = 6.8 \times 10^{-7} \cdot T^{-0.4}, \tag{28}$$

and

$$\alpha_2 = 5 \times 10^{-8} \cdot \left(\frac{300}{T}\right)^{0.5}. \tag{29}$$

Furthermore, Smith and Adams (1982) presented a parameterisation valid for the altitude range of 10–60 km based on the laboratory measurements of binary recombination with the FALP technique. The resulting parameterisation is simple because it only depends on the altitude and contains two terms that represent the ternary and binary recombination, respectively, as Eq. (30) shows:

$$\alpha = 1.63 \times 10^{-5} \cdot e^{-\frac{h}{7.38}} + 5.25 \times 10^{-8}, \tag{30}$$

where h is the altitude in km. Johnsen et al. (1994) later disputed their results because they found that the ion-collecting probes, as used by Smith and Adams, are not suitable to obtain data on ion–ion recombination coefficients in flowing-afterglow studies.

Bates (1982) criticised that the binary and ternary recombination rates had been erroneously considered to be additive in previous works, stating that both processes are not independent of each other. Instead of the binary recombination rate α_2, he defined the enhancement due to the binary channel, $\Delta\alpha_2$, and calculated α_3, $\Delta\alpha_2$, and the resulting total recombination coefficient, α, in a Monte Carlo (MC) simulation for altitudes between 0 and 40 km. Interestingly, Smith, Church, Adams, and Bates have never cited the works of Israël (1957) or Lenz (1932). It seems that the two latter authors have been overlooked, probably because they published their works in German (however, Israël's textbook was translated into English in 1971). This is especially remarkable since Bates (1982) determined α to be $1.67 \times 10^{-6}\,\mathrm{cm^3\,s^{-1}}$ at ground level, which is in striking agreement with Israël (1957) ($1.6 \times 10^{-6}\,\mathrm{cm^3\,s^{-1}}$) and Lenz (1932) ($(1.7 \pm 0.1) \times 10^{-6}\,\mathrm{cm^3\,s^{-1}}$). Instead, Bates referred to Sayers (1938) ($2.3 \times 10^{-6}\,\mathrm{cm^3\,s^{-1}}$) and Nolan (1943) ($1.4 \times 10^{-6}\,\mathrm{cm^3\,s^{-1}}$), whom he regarded as the first experimenters to quantitatively and accurately determine α.

At the start of the 1980s, science was in urgent need of correct and altitude-resolved values for the recombination coefficient. Arnold and Fabian (1980) presented a method to calculate the concentration of gaseous sulfuric acid from measured concentration ratios of the ambient HSO_4^- and NO_3^- ions. The recombination coefficient, which describes the sink for ions, forms part of the formula (see Arnold and Qiu, 1984, for a more detailed derivation). Until the early 1980s, this method was the only way to determine the concentration of trace gases, such as sulfuric or nitric acid, in the different layers of the atmosphere.

The need for an experimental investigation in the atmosphere was answered by Gringel et al. (1978), Rosen and Hofmann (1981), and Morita (1983). Gringel et al. (1978) conducted balloon-borne measurements of the air conductivity between 4 and 25 km over northern Germany in August and October 1976. From the measured air conductivity, σ, the calculated altitude-corrected ion mobility, μ, and the mean of formerly measured ionisation rates, they determined the ion–ion recombination coefficients for different altitudes according to Eqs. (31) and (32):

$$\alpha = \frac{q \cdot e^2 \cdot \mu^2}{\sigma^2}, \tag{31}$$

where

$$\mu = \mu_0 \cdot \frac{p_0}{p} \cdot \frac{T}{T_0}, \quad (32)$$

with $\mu_0 = 1.3 \times 10^{-4}\,\mathrm{m^2\,V^{-1}\,s^{-1}}$. The altitude-resolved values for q are the means of three independent measurements between the 1930s and the 1970s, although q varies with the 11-year solar cycle which casts doubt on the validity of the values in the calculations.

On the other hand, both Rosen and Hofmann (1981) and Morita (1983) measured the positive ion number concentration n_+ directly along with the ionisation rate q in a concerted measurement campaign. Thus, Rosen and Hofmann's data, being available earlier than Morita's, were considered to be the most reliable data at that time because they measured the relevant parameters simultaneously (Arijs, 1983). Applying Eq. (2), they calculated α for different altitude levels. Additionally, for altitudes above 32 km, they used the alternative method given in Eq. (31) to calculate α. The derived data points followed a profile suggested by a theory that accounted for both binary and ternary recombination. The data points derived with Eq. (31) fit the theoretical predictions better. However, below 9 km, the derived values for the ion–ion recombination were unexpectedly large. As the authors themselves wrote, in the troposphere, the losses of ions due to aerosol particle attachment have to be taken into account, otherwise the loss due to ion–ion recombination is overestimated when using Eq. (2); this is why only the values above 9 km are reliable. Nevertheless, these measurements have led to further adjustments of the parameterisations, such as the ones by Arijs et al. (1983) and Brasseur and Chatel (1983). Arijs et al. (1983) presented a formula that contains two terms, accounting for binary and ternary reactions, as shown in Eq. (33):

$$\alpha = 6 \times 10^{-8} \cdot \left(\frac{300}{T}\right)^{0.5} + 1.25 \times 10^{-25} \cdot [\mathrm{M}] \cdot \left(\frac{300}{T}\right)^{4}, \quad (33)$$

where [M] is the number density of air molecules in $\mathrm{cm^{-3}}$ (representing the pressure dependence), given by Eq. (34):

$$[\mathrm{M}] = 7.243 \times 10^{18} \cdot \left(\frac{p}{T}\right). \quad (34)$$

Independently, Brasseur and Chatel (1983) proposed a very similar formula that only differs in the factor of the ternary recombination term (Eq. 35):

$$\alpha = 6 \times 10^{-8} \cdot \left(\frac{300}{T}\right)^{0.5} + 6 \times 10^{-26} \cdot [\mathrm{M}] \cdot \left(\frac{300}{T}\right)^{4}. \quad (35)$$

Due to the T^{-1} dependence of [M], the ternary recombination coefficient ultimately shows a T^{-5} dependence in Arijs et al. (1983) and Brasseur and Chatel (1983), which is even stronger than previously discussed. The temperature dependence of $T^{-0.5}$ in the binary term is in agreement with Hickman (1979) (but not with the more recent parameterisation of Miller et al. (2012) that describes a $T^{-0.9}$ dependence). The pressure dependence of α is p^1 in the ternary terms in Eqs. (33) and (35) through the linear p dependence of [M] (see Eq. 34). A proportional pressure dependence is also observed in some Thomsonian theories (see Sect. 2).

Parallel to Rosen and Hofmann, Morita (1983) conducted atmospheric field measurements and also found reasonable results for altitudes above 6 km; however, for the above-mentioned reason, strong disagreement of the observed results from the theoretically expected ones below 6 km was found. Bates (1985) synthesised his earlier model results (see Sect. 6) and the measurements by Morita to define another parameterisation that is merely dependent on the altitude, as shown in Eq. (36):

$$\alpha = 5.33 \times 10^{-6} \cdot e^{-0.111 \cdot h}, \quad (36)$$

which is valid for the range of 10–25 km. Below 10 km, α is expected to be constant at $1.7 \times 10^{-6}\,\mathrm{cm^3\,s^{-1}}$.

More recently, Franchin et al. (2015) reported experimental data for the recombination coefficient for atmospheric conditions. They have examined the dependency of α on the temperature, relative humidity (RH), and the number concentrations of sulfur dioxide [SO_2] and ozone [O_3] in a series of chamber experiments. Their experimental setup did not allow for pressures below 1013 hPa, therefore, it is not directly possible to derive new insights with regard to processes in the upper troposphere or stratosphere. However, they did show that α is dependent on RH; with increasing RH, the recombination coefficient decreases. At 70 % RH, α is $2.0 \times 10^{-6}\,\mathrm{cm^3\,s^{-1}}$, which is within the known range of uncertainty; however, for 7 % RH, it is as high as $8.1 \times 10^{-6}\,\mathrm{cm^3\,s^{-1}}$ (both at 293.15 K). They convincingly explain this by an increase in ion sizes with increasing RH. With a higher humidity, more water ligands are added to the ion cluster, and thus its size and mass increase while its mobility decreases. This effect could not be reproduced quantitatively by any theory (Franchin et al., 2015). Their data also revealed the temperature dependence of α: at 293.15 K, the value was $(2.3 \pm 0.7) \times 10^{-6}\,\mathrm{cm^3\,s^{-1}}$ and, at 218.15 K, it was $(9.7 \pm 1.2) \times 10^{-6}\,\mathrm{cm^3\,s^{-1}}$ (both at 40 % RH). Unfortunately, the standard deviations of the data points are large, thus any temperature dependence derived from the four data tuples is inaccurate in itself. Nevertheless, we derived a temperature dependence of T^{-3} from their data. This is in a similar order of magnitude to the findings of Smith and Church (1977) ($T^{-2.5}$ to T^{-3}) and is still comparable to Arijs et al. (1983) and Brasseur and Chatel (1983) (both teams: T^{-5}) for the ternary recombination, considering that ternary recombination is the predominant process at atmospheric pressure. Besides this, the recombination coefficient was found to be independent of [O_3] and [SO_2].

After 1985, no further improvements of the parameterisation for direct application in the atmosphere have been made. One reason could be that the need for this value has become less urgent, since, from that year, trace gases could be

measured directly in their neutral forms (Arnold and Hauck, 1985). In addition, most of the parameterisations were in good accordance for the altitude range of 10–40 km (Arijs, 1983) so that no further improvement appeared to be necessary. As yet, for the troposphere, experimental validation of the parameterisations remains open until this day. The best estimate available is the assumption that α remains constant between 0 and 10 km due to the cancellation of the opposing temperature and pressure effects. However, theories concerning the ion–aerosol attachment have been further developed. The most important theories and their applicability to the ion–ion recombination will be discussed in the next section.

5 Application of ion–aerosol theories

Apart from ion–ion recombination, the analogous process of ion–aerosol attachment was further studied as well. For instance, Natanson (1960a) (English translation of the original in Russian: Natanson, 1960b) expanded his approach to the attachment of ions to particles. In general, the ion–ion recombination can be considered as a special case of the ion–aerosol attachment, i.e. when the radius of the aerosol particle is reduced to ionic sizes. While in many ion–ion recombination theories, the concept of the three-body collision radius, or trapping radius, d, can be found, many ion–aerosol theories additionally use the concept of the limiting sphere, δ. The limiting sphere and its radius are defined slightly differently depending on the theory. With Fuchs (1963), it is defined as a concentric sphere around the particle with the radius $\delta_F = r_p + \lambda'$, where r_p is the particle radius and λ' is "the mean distance from the surface of the particle at which the ions collide for the last time with gas molecules before striking this surface" (Fuchs, 1963). Notably, λ' is not equal to the mean free path of one ion, λ_{ion}, or the ion–ion mean free path, λ. Hoppel and Frick (1986) define it as the sum of the ion–aerosol three-body trapping sphere and the ion–ion mean free path (see Eq. 44). Transferred to the ion–ion recombination, the limiting sphere can be defined as the sum of the ion–ion three-body trapping distance and one mean free path (see Eq. 45), as depicted in Fig. 1.

In Fig. 1a, an ion (white circle) approaches the ion in the centre (black circle) which has the opposite charge. The approaching ion experiences its last collision with a neutral gas molecule approximately one mean free path away from the trapping sphere (i.e. on the surface of the limiting sphere according to Hoppel and Frick's definition). When entering the limiting sphere, the white ion collides with another neutral gas molecule on the surface of the trapping sphere. This process is also called three-body trapping, because the gas molecule, which is the third body, "traps" the white ion inside the trapping sphere of the centre ion. However, not all of these collisions lead to the recombination of the two ions. The probability for an ion to collide with a neutral gas

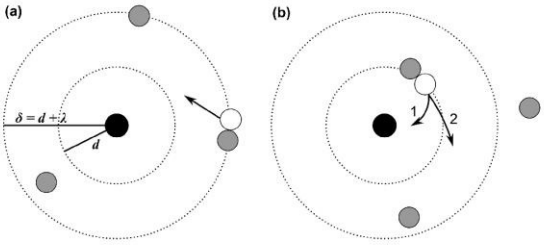

Figure 1. Schematic representation of the limiting sphere, based on Hoppel and Frick (1986), López-Yglesias and Flagan (2013), and Tamadate et al. (2020b). The black circle in the centre represents an ion and the white circle represents an ion of opposite sign, while the grey circles represent neutral gas molecules. The inner dotted circle with the radius d is the ion–ion trapping sphere, while the outer dotted circle with the radius $\delta = d + \lambda$ describes the limiting sphere. The spheres are defined differently in various theories; this schematic representation depicts the theory of Hoppel and Frick (1986). **(a)** The approaching white ion experiences its last collision with a neutral gas molecule outside the ion–ion trapping sphere, here, one mean free path away from the surface of the trapping sphere. **(b)** The white ion collides with another neutral gas molecule, this time leading to it entering the trapping sphere, i.e. being "trapped". In case 1, it collides and subsequently recombines with the black ion of opposite sign. In case 2, no ion–ion collision and recombination occur and the white ion leaves the trapping sphere.

molecule is accounted for in many theories. Two possible outcomes of the third-body collision are shown as cases 1 (collision) and 2 (non-collision) in Fig. 1b.

Tamadate et al. (2020b) provided a comprehensive review of those theories and their application to the ion–ion recombination in the introductory part of their work. For the sake of completeness and to identify the potential of these approaches for their application to the lower atmosphere, the most important concepts and formulae are given in the following paragraphs.

In Fuchs's theory, outside the limiting sphere, continuum equations are used, whereas inside the sphere, kinetic theory is applied because steady-state, rather than equilibrium conditions, are valid (Fuchs, 1963; Hoppel and Frick, 1986). Coulomb as well as image forces are taken into account in this theory, but no third-body processes. The radius δ_F of the limiting sphere is given in Eq. (37) (Fuchs, 1963), based on considerations by Wright (1960):

$$\delta_F = \frac{r_{coll}^3}{\lambda^2} \cdot \left[\frac{1}{5} \cdot \left(1 + \frac{\lambda}{r_{coll}}\right)^5 - \frac{1}{3} \cdot \left(1 + \frac{\lambda^2}{r_{coll}^2}\right) \cdot \left(1 + \frac{\lambda}{r_{coll}}\right)^3 + \frac{2}{15} \cdot \left(1 + \frac{\lambda^2}{r_{coll}^2}\right)^{2.5} \right], \quad (37)$$

where r_{coll} is the collision radius, which is the sum of both ion radii (originally, the particle radius r_p).

Although Fuchs (1963) did not provide a formula for α himself, Tamadate et al. (2020b) have used Fuchs's approach to derive the ion–ion recombination coefficient, shown in Eqs. (38) to (40):

$$\alpha = \frac{(D_+ + D_-)\cdot e^2}{\varepsilon_0 \cdot k_B T \cdot \left[1 - \exp\left(\frac{-e^2}{4\pi\cdot\varepsilon_0\cdot k_B T\cdot \delta_F}\right)\right]} \cdot \left(1 + \frac{(D_+ + D_-)\cdot e^2}{\alpha_\delta \cdot \varepsilon_0 \cdot k_B T \cdot \left[\exp\left(\frac{e^2}{4\pi\cdot\varepsilon_0\cdot k_B T\cdot \delta_F}\right) - 1\right]}\right)^{-1}, \quad (38)$$

where

$$\alpha_\delta(r_{coll}) = \pi \cdot r_{coll}^2 \cdot \left(\frac{8 k_B T}{\pi \cdot m_{red}}\right)^{0.5} \cdot \gamma(r_{coll}), \quad (39)$$

and

$$\gamma(r_{coll}) = 1 + \frac{e^2}{4\pi \cdot \varepsilon_0 \cdot k_B T} \cdot \left(\frac{1}{r_{coll}} - \frac{1}{\delta_F}\right), \quad (40)$$

where α_δ is the ion–ion collision rate coefficient at the limiting sphere surface.

However, there are two main problems with the theory of Fuchs (1963). Firstly, it ignores the three-body trapping, i.e. collisions of the two ions (or the ion and the particle) with neutral gas molecules (Hoppel and Frick, 1986; Tamadate et al., 2020b). Hoppel and Frick (1986) showed that Fuchs's theory would lead to an ever-growing underestimation of the attachment coefficient for decreasing particle radii (e.g. $4.4 \times 10^{-7}\,cm^3\,s^{-1}$ for a 1 nm radius) due to the negligence of the three-body trapping. Three-body trapping becomes increasingly more relevant for aerosol particles approaching ionic sizes (or when two ions recombine) and when the pressure is relatively high, as is the case in the lower atmosphere. Secondly, an ion entering the limiting sphere of another ion with the opposite sign does not follow the thermal equilibrium distribution; instead, the equilibrium ion drift velocity, $v = \mu E$, in the direction of the ion in the centre of the limiting sphere needs to be considered (Gopalakrishnan and Hogan, 2012; Tamadate et al., 2020b).

Similarly, Tamadate et al. (2020b) derived α using the theory of Filippov (1993), who had examined the ionic charging of small aerosol particles with respect to the Knudsen number, which was also based on the considerations of Fuchs (1963). Tamadate et al. (2020b) presented Eq. (41) that defines the ion–ion recombination coefficient and which already includes the collision probability for ions entering the limiting sphere, ε_δ, and is independent of α_δ:

$$\alpha = \frac{4\pi \cdot (D_+ + D_-)\cdot \delta \cdot \Psi_\delta}{1 - \exp(-\Psi_\delta)} \cdot \left[1 + \left(\frac{\pi}{2}\right)^{0.5} \cdot \frac{2 - \varepsilon_\delta}{\varepsilon_\delta} \cdot Kn_\delta \cdot \frac{\Psi_\delta}{\exp(\Psi_\delta) - 1}\right]^{-1}, \quad (41)$$

with

$$\Psi_\delta = \frac{e^2}{4\pi \cdot \varepsilon_0 \cdot k_B T \cdot \delta}, \quad (42)$$

and

$$Kn_\delta = \left(\frac{m_{red}}{k_B T}\right)^{0.5} \cdot \frac{D_+ + D_-}{\delta}, \quad (43)$$

where Ψ_δ is the ratio of Coulomb and thermal energy at the limiting sphere surface and Kn_δ is the Knudsen number for the limiting sphere. To obtain ε_δ, Tamadate et al. (2020b) performed molecular dynamics (MD) simulations that will be described in the next section.

Subsequent to Fuchs, Hoppel and Frick (1986) developed a theory for ion–aerosol attachment based on Natanson (1960a), Keefe et al. (1968), and Hoppel (1977) that uses the limiting sphere approach and includes image forces and three-body trapping.

Hoppel and Frick (1986) defined limiting sphere radii for both effects as well as for their combination, which indicate the maximum distance for which the ions would recombine with a particle given the respective effect(s). Since the collisions with a third body (i.e. a gas molecule) only occur with a certain probability within the limiting sphere, this probability needs to be taken into account in a similar way as in the Thomson theory. Hoppel and Frick (1986) show that image forces are not relevant for the case of ion–ion recombination or for ion–particle attachment when the particle diameter is small (< 40 nm). For this condition, they define the limiting sphere radius, δ_{HF}, as the sum of the ion–aerosol three-body trapping distance, d_{ia}, and the ion–ion mean free path according to Eq. (44):

$$\delta_{HF} = d_{ia} + \lambda. \quad (44)$$

The value for the attachment coefficient of a singly charged particle smaller than 2 nm in radius and an ion of opposite sign reported by Hoppel and Frick (1986) approaches $1.3 \times 10^{-6}\,cm^3\,s^{-1}$, and thus approaches the ion–ion recombination coefficient itself. Therefore, by applying Eq. (44) to ion–ion recombination, one can derive Eq. (45) where the ion–aerosol trapping sphere d_{ia} is replaced by the ion–ion trapping sphere d_{HF} (see also Tamadate et al., 2020b):

$$\delta_{HF} = d_{HF} + \lambda. \quad (45)$$

In the following discussion we want to briefly outline how the Hoppel and Frick method is used to determine the ion–aerosol attachment coefficients. Their method does not provide any means of accurately calculating the ion–aerosol trapping distance from theory. Therefore, they adopt the theory by Natanson (1959a) to derive the ion–ion trapping distance from a measured ion–ion recombination coefficient and certain ion properties (they take the value of $\alpha = 1.4 \times 10^{-6}\,cm^3\,s^{-1}$ from Nolan, 1943). The value of the

ion–ion trapping sphere distance can then be used to calculate the ion–aerosol trapping sphere distance. Since the method by Hoppel and Frick (1986) was explicitly developed to determine ion–aerosol attachment coefficients, it is not directly suitable to determine ion–ion recombination coefficients. One important application for the Hoppel and Frick theory is the calculation of equilibrium charge distribution of aerosols as a function of the particle diameter. The knowledge of the charged fractions (as a function of diameter and the number of elementary charges) are important for aerosol size distribution measurements with differential mobility analysers after the aerosol is "neutralised" by passing a strong ion source with high concentrations of bipolar ions (e.g. Wang and Flagan, 1990). The fact that the method by Hoppel and Frick (1986) does not include any means of calculating the ion–aerosol or the ion–ion trapping distance directly was also discussed by Tamadate et al. (2020b). They highlight that the effect of changing pressure and temperature on the trapping distance is not taken into account. Nevertheless, López-Yglesias and Flagan (2013) have improved some approximations made by Hoppel and Frick (1986) and developed a model to calculate the ion–aerosol attachment for aerosol particles of different sizes and charges. The amendment of using Maxwellian speed distributions for the ion and the colliding gas molecule instead of fixed average speeds led to the most significant of the deviations from Hoppel and Frick's model.

Tamadate et al. (2020b) provided a set of formulae in order to calculate the ion–ion recombination rate after Hoppel and Frick, also using Eq. (38). However, the ion–ion collision rate coefficient α_δ at distance δ is defined differently for Hoppel and Frick, and is given in Eq. (46). Here, the ion–ion collision rate α_δ is not directly dependent on the collision radius r_{coll} (cf. Eq. 39), but on the ion–ion trapping distance d_{HF}. Furthermore, the additional probability factor for ions entering the trapping sphere, ε_d, is introduced to the ion–ion collision rate:

$$\alpha_\delta(d_{\mathrm{HF}}) = \pi \cdot d_{\mathrm{HF}}^2 \cdot \left(\frac{8 k_{\mathrm{B}} T}{\pi \cdot m_{\mathrm{red}}}\right)^{0.5} \cdot \gamma(d_{\mathrm{HF}}) \cdot \varepsilon_d, \tag{46}$$

with

$$\gamma(d_{\mathrm{HF}}) = 1 + \frac{e^2}{4\pi \cdot \varepsilon_0 \cdot k_{\mathrm{B}} T} \cdot \left(\frac{1}{d_{\mathrm{HF}}} - \frac{1}{\delta_{\mathrm{F}}}\right), \tag{47}$$

$$\varepsilon_d = 1 - \frac{\lambda^2}{2 \cdot d_{\mathrm{HF}}^2} \cdot \left(1 - \exp\left(\frac{-2 \cdot d_{\mathrm{HF}} \cdot \cos\theta}{\lambda}\right) \cdot \left(1 + \frac{2 \cdot d_{\mathrm{HF}}}{\lambda} \cdot \cos\theta\right)\right), \tag{48}$$

$$\theta = \sin^{-1}\left(\frac{b}{d_{\mathrm{HF}}}\right), \tag{49}$$

and

$$b = r_{\mathrm{ion}} \cdot \sqrt{1 + \frac{e^2}{32 \cdot k_{\mathrm{B}} T \cdot \varepsilon_0} \cdot \left(\frac{1}{r_{\mathrm{coll}}} - \frac{1}{d_{\mathrm{HF}}}\right)}, \tag{50}$$

where θ is the critical angle to enter the trapping sphere and b is the critical collision parameter (Tamadate et al., 2020b). Again, to obtain a value for α, one needs to know the given trapping sphere radius, d_{HF}. However, to determine d_{HF}, Hoppel and Frick used a known ion–ion recombination coefficient. This circular logic arises because we divert their theory that is meant to determine ion–aerosol attachment processes to ion–ion recombination processes. Nevertheless, it can be tested to calculate α for different altitudes of the atmosphere by keeping a constant value for d_{HF} while varying T and p.

6 Numerical simulations

Tamadate et al. (2020b) highlight the fact that there is no single calculation approach that yields accurate ion–ion recombination rates for a wide range of pressures, temperatures, gas compositions, and ion chemical compositions. This deficiency motivated their development of a so-called hybrid continuum–MD approach. This method couples the limiting sphere method, when the two ions are sufficiently far apart from each other and their motion is controlled by diffusion, with MD simulations that model the ion motions within a critical distance δ. The calculations are applied to a system where NH_4^+ and NO_2^- ions recombine in helium at 300 K under varying pressure. Collisions between the ions and neutral gas molecules are taken into account. Excellent agreement is found when the model results are compared with the laboratory measurements at two different pressures (Lee and Johnsen, 1989). The equation for calculating the ion–ion recombination coefficient (Eq. 41) is derived from Filippov (1993). For their test case, Tamadate et al. (2020b) show that the limiting sphere distance suggested by Fuchs (1963) (δ_{F}, see Eq. 37) can be used as the initial distance between the two ions when the MD simulations commence. For larger distances, the calculated recombination rates do not change, demonstrating that the proposed method is independent of the choice of the limiting sphere radius, as long as it is sufficiently large. The quantity that is determined by the simulations is the probability, ε_δ, that a successful collision occurs when the initial speeds of the ions in 3D are drawn from probability density functions based on Boltzmann distributions. A collision is defined as being successful if the distance between the two ions gets smaller than a threshold value, whereas it is not successful if the distance eventually exceeds δ_{F}. Especially for low pressures (and correspondingly large δ_{F}), ε_δ can become very small, hence it requires many simulations for achieving results with small statistical errors. The MD simulations require, in addition, Lennard-Jones parameters and partial charges on atoms as input variables. In a separate publication, Tamadate et al. (2020a) apply their continuum–MD approach to a system where positively charged polyethylene glycol ions (1 to 7 charges, mass of 4600 Da) recombine with NO_2^- ions in nitrogen.

The comparison between the experimentally determined recombination rates and the calculated ones indicates that they agree within a factor of 2. These results show that the hybrid continuum–MD approach is well suited to yield accurate ion–ion recombination rates for a wide range of applications and conditions, including studies of the different layers of the atmosphere.

Numerical simulations using MC methods have been another powerful tool for gaining insights into ion–ion recombination or ion–particle attachment rates and their dependencies on parameters such as gas pressure and temperature. In contrast to the MD simulations, the ion–ion and the ion–neutral interactions are generally much more simplified, e.g. the collisions with neutral gas molecules are treated by the use of random numbers for the collision frequencies, energies, and angles. In the majority of cases, the collisions are treated as elastic, while spherical geometry is assumed for the collision partners. The first MC calculations to include three-body trapping were conducted by Feibelman (1965), who found good agreement with a measured recombination rate. Later, MC simulations studied the recombination in oxygen for varying pressure from zero pressure, i.e. for the binary condition, up to approximately 1000 hPa where ternary recombination is clearly dominant (Bates and Mendaš, 1978). The results showed that the ion–ion recombination rates peak between 1000 and 2000 hPa, as expected from theory. Besides the pressure dependence of the recombination rate, Bardsley and Wadehra (1980) also studied the temperature dependence using MC simulations. The results indicate a dependence stronger than T^{-3} for low pressures and a strongly reduced temperature dependence for pressures above approximately 5000 hPa. Bates (1982) reported ion–ion recombination rates calculated with an MC model for the atmospheric conditions ranging between 0 and 40 km altitude, which agree well when compared to the values from the balloon measurements (see Sect. 7.1). Filippov (1993) developed an MC model for the charging of aerosol particles. The numerical results show fairly good agreement with the measured values in the range of 5 and 80 nm when using either air or helium as the neutral gas.

7 Comparison of the parameterisations and theories

In Table 2, all theories, parameterisations, field and laboratory data sets, and model results discussed in the previous sections are listed for a better overview. In the following sections, they will be addressed by the abbreviations listed in Table 2. In order to determine the most suitable single formula to determine the ion–ion recombination coefficient for different altitudes, we compare the above-mentioned parameterisations and theories to the field, laboratory, and model data.

7.1 Comparison to field and model data

In a first step, the parameterisations and theories were compared to the field and model data. The temperature, pressure and air density data of the US Standard Atmosphere were used here (National Oceanic and Atmospheric Administration et al., 1976). Furthermore, we used the parameters $m_{\mathrm{ion}} = m_+ = m_- = 90\,\mathrm{Da}$, $\mu_0 = 1.35 \times 10^{-4}\,\mathrm{m^2\,V^{-1}\,s^{-1}}$ (López-Yglesias and Flagan, 2013), $d_{\mathrm{HF}} = 18\,\mathrm{nm}$ for HF86 (the proposed value of Hoppel and Frick (1986) for an ion of 90 Da, assuming an ion–ion recombination coefficient of $1.7 \times 10^{-6}\,\mathrm{cm^3\,s^{-1}}$), and EA = 3.94 eV (Weaver et al., 1991). r_{coll} was calculated according to Eq. (A1). The results are plotted in Fig. 2. Here, the y axes represent the altitude h and the x axes represent the ion–ion recombination coefficient α. In Fig. 2a to d, the field measurements Gr78, RH81, and Mo83 are shown for better comparability. Note that the data are inaccurate below 10 km. For RH81, there are two data sets for altitudes above 32 km: one is calculated based on Eq. (2), the other one is based on Eq. (31). One should bear in mind that these data sets, which were determined with similar methods, may also suffer from systematic errors such as losses inside the instrument that were not accounted for; however, these remain the most reliable data from field measurements available to this day. The challenge for the theories and parameterisations is to accurately determine the ion–ion recombination coefficient for the different regimes: the ternary recombination regime between 0 and approximately 25 km, the transition regime between 25 and approximately 40 km, and the binary recombination regime above 40 km. Note that the binary theories (i.e. Fu63, Hi79, and Mi12) are therefore only plotted above 40 km altitude.

In Fig. 2a, the Thomsonian theories (Ga38, Lo60, Is57, and Na59) are depicted. In Fig. 2b, the semi-empirical adjustments to the Thomson theory (Ar83 and BC83) as well as the MC simulation (Ba82) are shown and in Fig. 2c, the binary complex potential models (Hi79 and Mi12) as well as the solely altitude-dependent parameterisations (SA82 and Ba85) are plotted. Figure 2d shows Fu63 and HF86, the ion–aerosol attachment theories that are applied to the ion–ion recombination. Figure 2e provides an overview of the most relevant theories and data sets for an altitude range of up to 12 km with a linear x scale, whereas the other subplots use a logarithmic x scale.

The Thomsonian theories (Ga38, Lo60, Is57, and Na59; see Fig. 2a and e) all show a similar behaviour; from ground level up to 11 km (tropopause), the α value slightly increases, and above 11 km, it decreases more strongly. Above 16 km, Ga38, Na59, and Lo60 yield almost the same values, while Is57 yields lower values throughout the stratosphere. Close to the ground, Ga38, Lo60, and Is57 predict α values identical or close to $1.7 \times 10^{-6}\,\mathrm{cm^3\,s^{-1}}$, whereas it is slightly elevated for Na59. Comparing these theories to the field data, Is57 shows a striking agreement in the altitude range of 11–

Table 2. List of all theories, parameterisations, data sets, and models used for comparison.

Study	Abbr.	Formula (for parameterisations)/range (for data sets)	
Theories and parameterisations			
Gardner (1938)	Ga38	$\alpha = 1.9 \times 10^{-5} \cdot \left(\frac{273}{T}\right)^{1.5} \cdot \left(\frac{1}{m_{\mathrm{ion}}}\right)^{0.5} \cdot \varepsilon_{\mathrm{T}}(Tp)$	Eqs. (10) to (13)
Loeb (1955, 1960)	Lo60	$\alpha = 1.73 \times 10^{-5} \cdot \left(\frac{273}{T}\right)^{1.5} \cdot \left(\frac{1}{m_{\mathrm{ion}}}\right)^{0.5} \cdot \varepsilon_{\mathrm{T}}(Tp)$	Eqs. (14) and (11) to (13)
Israël (1957, 1971)	Is57	$\alpha = 1.95 \times 10^{-6} \cdot \left(\frac{273}{T}\right)^{1.5} \cdot \varepsilon_{\mathrm{T}}(Tp)$	Eqs. (15) and (11) to (13)
Natanson (1959a)	Na59	$\alpha = \frac{\pi \cdot d_{\mathrm{N}}^2 \cdot v_{\mathrm{rel}} \cdot \varepsilon_{\mathrm{N}} \cdot \left[1 + \frac{e^2 \cdot \lambda_{\mathrm{ion}}}{4\pi \cdot \varepsilon_0 \cdot d_{\mathrm{N}} \cdot (d_{\mathrm{N}} + \lambda_{\mathrm{ion}}) \cdot k_{\mathrm{B}} T}\right] \cdot \exp\left(\frac{e^2}{4\pi \cdot \varepsilon_0 \cdot (d_{\mathrm{N}} + \lambda_{\mathrm{ion}}) \cdot k_{\mathrm{B}} T}\right)}{1 + \frac{\pi \cdot \varepsilon_0 \cdot d_{\mathrm{N}}^2 \cdot v_{\mathrm{rel}} \cdot \varepsilon_{\mathrm{N}} \cdot k_{\mathrm{B}} T}{e^2 \cdot D} \cdot \left[1 + \frac{e^2 \cdot \lambda_{\mathrm{ion}}}{4\pi \cdot \varepsilon_0 \cdot d_{\mathrm{N}} \cdot (d_{\mathrm{N}} + \lambda_{\mathrm{ion}}) \cdot k_{\mathrm{B}} T}\right] \cdot \left[\exp\left(\frac{e^2}{4\pi \cdot \varepsilon_0 \cdot (d_{\mathrm{N}} + \lambda_{\mathrm{ion}}) \cdot k_{\mathrm{B}} T}\right) - 1\right]}$	Eqs. (16) to (21)
Hickman (1979)	Hi79	$\alpha_2 = 5.35 \times 10^{-7} \cdot \left(\frac{T}{300}\right)^{-0.5} \cdot m_{\mathrm{red}}^{-0.5} \cdot \mathrm{EA}^{-0.4}$	Eq. (25)
Miller et al. (2012)	Mi12	$\alpha_2 = 2.8 \times 10^{-7} \cdot \left(\frac{T}{300}\right)^{-0.9} \cdot m_{\mathrm{red}}^{-0.5} \cdot \mathrm{EA}^{-0.13}$	For polyatomic anions, Eq. (27)
Smith and Adams (1982)	SA82	$\alpha = 1.63 \times 10^{-5} \cdot e^{-\frac{h}{7.38}} + 5.25 \times 10^{-8}$	Valid from 10 to 60 km, Eq. (30)
Arijs et al. (1983)	Ar83	$\alpha = 6 \times 10^{-8} \cdot \left(\frac{300}{T}\right)^{0.5} + 1.25 \times 10^{-25} \cdot [\mathrm{M}] \cdot \left(\frac{300}{T}\right)^{4}$	Eqs. (33) and (34)
Brasseur and Chatel (1983)	BC83	$\alpha = 6 \times 10^{-8} \cdot \left(\frac{300}{T}\right)^{0.5} + 6 \times 10^{-26} \cdot [\mathrm{M}] \cdot \left(\frac{300}{T}\right)^{4}$	Eqs. (35) and (34)
Bates (1985)	Ba85	$\alpha = 5.33 \times 10^{-6} \cdot e^{-0.111 \cdot h}$	Valid from 10 to 25 km, Eq. (36)
Fuchs (1963)	Fu63	$\alpha = \frac{\frac{(D_+ + D_-) \cdot e^2}{\varepsilon_0 \cdot k_{\mathrm{B}} T \cdot \left[1 - \exp\left(\frac{-e^2}{4\pi \cdot \varepsilon_0 \cdot k_{\mathrm{B}} T \cdot \delta_{\mathrm{F}}}\right)\right]}}{1 + \frac{(D_+ + D_-) \cdot e^2}{\alpha_\delta \cdot \varepsilon_0 \cdot k_{\mathrm{B}} T \cdot \left[\exp\left(\frac{e^2}{4\pi \cdot \varepsilon_0 \cdot k_{\mathrm{B}} T \cdot \delta_{\mathrm{F}}}\right) - 1\right]}}$	Eqs. (38) to (40) and (37)
Hoppel and Frick (1986)	HF86	see Fu63	Eqs. (38), (37) and (46) to (50)
Field data			
Gringel et al. (1978)	Gr78	α derived from measurements of q and σ at 4–30 km	
Rosen and Hofmann (1981)	RH81	α derived from measurements of q and n_+ at 2–36 km and of q and σ at 32–45 km	
Morita (1983)	Mo83	α derived from measurements of q and n_+ at 3–35 km	
Laboratory data			
Franchin et al. (2015)	Fr15	$\alpha(T)$ for RH = const. and α(RH) for T = const.; $\alpha \sim T^{-3}$ (approximately)	
Model data			
Bates (1982)	Ba82	Monte Carlo simulation of α_3, $\Delta\alpha_2$ and α for 0–40 km in 5 km steps	

22 km. However, none of the theories predict the slower decrease and asymptotic approach towards a constant value due to the binary recombination predominating over the ternary process. Apparently, the binary process is not sufficiently taken into account in these theories, thus, their validity is limited to the altitude range of 0–22 km. However, within this range, the parameterisation of Is57 yields the most promising results.

The MC simulation Ba82 (see Fig. 2b and e) reproduces the ground-level value of 1.7×10^{-6} cm^3 s^{-1} and yields almost constant values for 0, 5, and 10 km altitudes, while decreasing above 10 km, reproducing the field data with re-

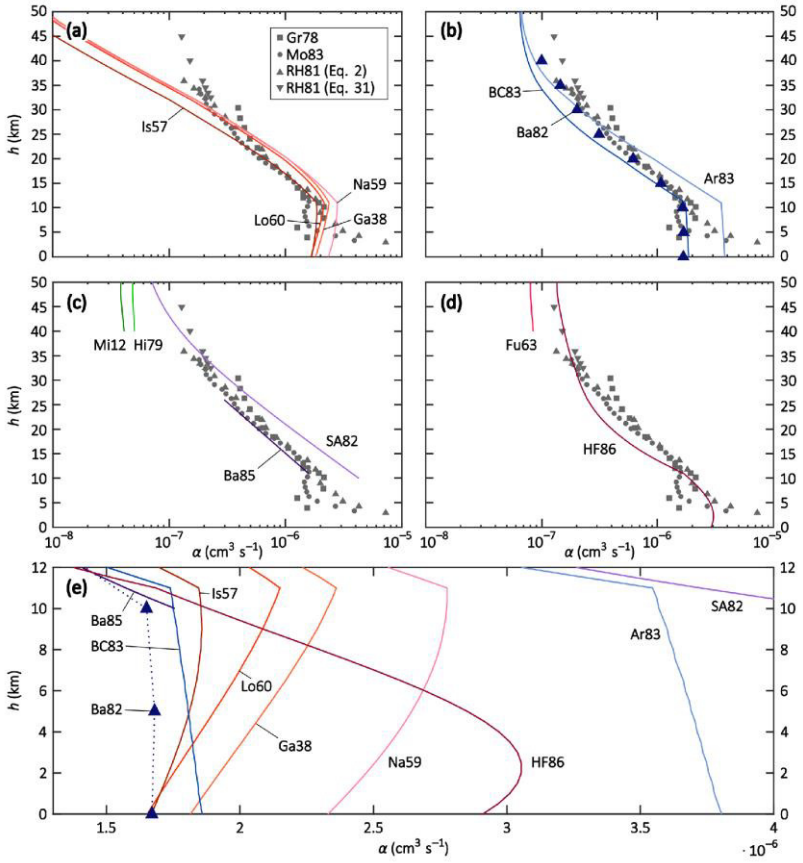

Figure 2. Altitude profiles of theories and parameterisations (solid lines), field data (grey symbols), and model simulations (purple triangles) of the recombination coefficient α for conditions of the US Standard Atmosphere. Panels **(a–d)** depict altitude profiles up to 50 km with a logarithmic x axis; the field data are depicted in all panels for better comparability. Panel **(e)** shows altitude profiles up to 12 km with a linear x axis. The meanings of the labels are listed in Table 2. See text for more details.

markable agreement. The semi-empirical parameterisations Ar83 and BC83 (see Fig. 2b and e) contain both a binary and a ternary recombination term and were developed to reproduce the data set of RH81; BC83 does so between 11 and approximately 20 km, while Ar83 reproduces the data set between approximately 20 and 35 km. Moreover, BC83 predicts a ground-level value of $1.9 \times 10^{-6}\,\mathrm{cm^3\,s^{-1}}$ for α, which is much closer to the expected value than that of $3.8 \times 10^{-6}\,\mathrm{cm^3\,s^{-1}}$ by Ar83. Close to 50 km, both parameterisations approach a similar value because their binary term is identical and becomes increasingly more dominant at higher altitudes. The strong deviations, especially in the troposphere, show that small changes in the prefactor of the ternary term can have substantial effects on the resulting recombination coefficient. For altitudes above 25 km, Ar83 can be chosen to parameterise the ion–ion recombination coefficient because it reproduces the field data sufficiently well. It is worth noting that BC83 and Ar83 both have a strong temperature dependence of T^{-5}, while the Thomsonian theories have a much weaker temperature dependence of $T^{-1.5}$, although they do still yield similar results in the troposphere.

The solely altitude-dependent empirical parameterisations SA82 and Ba85 (see Fig. 2c and e) are valid from 10 to 60 km and from 10 to 25 km, respectively. The Ba85 parameterisation, indeed, reproduces the field data of RH81 well within this range, while Sa82 overestimates the recombination coefficient below an altitude of 30 km but fits the field data reasonably well between 32 and 45 km; this is because it features the slower decrease of α for increasing altitudes above 30 km where the binary recombination process predominates. Given their solely empirical nature and their limited validity ranges, these two parameterisations appear to be

useful in applications where only information about the altitude is available but knowledge of the temperature or pressure is lacking.

The two binary theories Hi79 and Mi12 (see Fig. 2c, only shown above 40 km altitude) yield lower recombination coefficients than the field data while still being in the same order of magnitude as SA82, Ar83, and BC83. However, as the data coverage is scarce above 35 km altitude, it is difficult to compare these theories to the field data and draw appropriate conclusions.

The two ion–aerosol attachment theories Fu63 and HF86 (see Fig. 2d and e), when applied to the ion–ion recombination process, do not reproduce the field measurements. While Fu63 only accounts for the binary recombination process and is therefore only shown in the binary regime, i.e. above 40 km altitude, it yields reasonable results with values for α that are only slightly lower compared to the field data. On the other hand, HF86 yields results that are in the correct order of magnitude within the troposphere; however, the α value of $2.9 \times 10^{-6}\,\mathrm{cm^3\,s^{-1}}$ at ground level is higher than expected. Within the stratosphere, one can observe the increasing dominance of the binary recombination process in HF86 with increasing altitude since the curve approaches a constant value, as seen in other theories discussed above. The recombination coefficient is in excellent agreement with the field data above 30 km altitude, however, it is underestimated between 15 and 25 km. One possible source for these inaccuracies could be the assumption of a constant value of 18 nm for the ion–ion trapping sphere radius d_{HF}; in other theories, this value is dependent on T and/or p. An altitude-dependent trapping distance may improve the performance of HF86 (see Sect. 8).

In summarising the intercomparison, it becomes obvious that there is no theory that can accurately reproduce the known ground-level value for the recombination coefficient α as well as the field data between 10 and 45 km altitude. Within the troposphere, it is reasonable to assume that the recombination coefficient remains almost constant due to the counterbalancing temperature and pressure effects. In the stratosphere, on the other hand, it decreases, although the decline lessens in the upper stratosphere, approaching an almost constant value at the top of the stratosphere. For altitudes between 0 and 22 km, the Thomsonian parameterisation Is57 most accurately reproduces the ground-level data and the field data. The semi-empirical parameterisation BC83 yields similar results in this altitude range, although it misses the exact values slightly. The Thomsonian theories and the semi-empirical parameterisations show similar results to each other in the troposphere despite having very different temperature dependencies in the ternary term. Between 10 and 25 km, Ba85 reproduces the field data of RH81 accurately, however, its application is limited because it is only dependent on h and does not contain physical information about the p and T dependencies. Above this altitude range, the picture is more complicated. Field data coverage above 35 km is sparse, hence it is difficult to judge the performance of the different theories and parameterisations. Based on the available field data, HF86 shows the best performance, followed by Ar83 and SA82, although both parameterisations come with certain constraints: the ternary term of Ar83 has a weak performance below 25 km; SA82 is solely dependent on h and contains no physical information about T and p, similar to Ba85. This intercomparison ultimately shows that the question regarding an accurate parameterisation or theory of the recombination coefficient α for the troposphere and stratosphere is not yet solved and further research is necessary in the future.

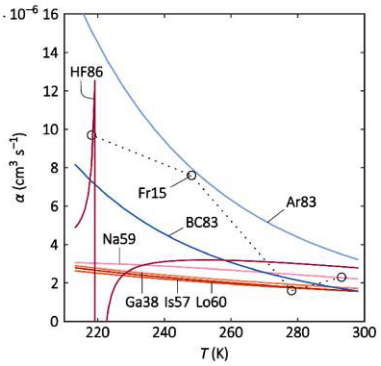

Figure 3. Parameterisations and theories (solid lines) and laboratory data (circles; dotted lines to guide the eye) of the recombination coefficient α versus T for the temperature range of 213–298 K. The meanings of the abbreviated labels are listed in Table 2.

7.2 Comparison to laboratory data

In a second step, the parameterisations and theories are compared to the constant-pressure (1013.25 hPa assumed) and temperature-dependent (218.15–293.15 K) data set reported by Franchin et al. (2015). Here, only theories and parameterisations are used that include the temperature as a parameter and account for the ternary recombination mechanism (i.e. Ga38, Is57, Na59, Lo60, Ar83, BC83, and HF86). Parameterisations that predict α based solely on the altitude or only describe the binary recombination mechanism are therefore excluded (i.e. Fu63, Hi79, SA82, Ba85, and Mi12). We used the same parameters as in the previous subsection. The result of the intercomparison is shown in Fig. 3. For Fr15, there is a general trend towards higher recombination coefficient values for lower temperatures, although the fluctuation is comparably strong. One should be mindful of the possible sources of error from wall losses in the aerosol chamber and sampling-line losses of the Neutral cluster and Air Ion Spectrometer (NAIS), the instrument used to determine the mobility distribution of the ions from which the ion–ion recombination rate could be derived. The reported uncertainties for α can be as high as 30 % (Franchin et al., 2015).

All theories and parameterisations agree within a reasonable range at ground-level temperatures (270–300 K). This is especially the case for the Thomsonian theories Ga38, Is57, Na59, and Lo60; in Ga38, Is57, and Lo60, almost the same values are yielded throughout the considered temperature range. However, the Thomsonian theories differ tremendously from the semi-empirical parameterisations (Ar83 and BC83) for tropopause temperatures (around 220 K). The weaker temperature dependence ($T^{-1.5}$) of the group – Ga38, Is57, Na59, and Lo60 – results in a negligible increase of α with decreasing temperatures. The laboratory data of Fr15, on the other hand, show a stronger T dependence (around T^{-3}) that is best reproduced by Ar83 and BC83. These parameterisations assume a T^{-5} dependence for the ternary recombination that is dominant at ground-level pressure; BC83 appears to reproduce the data points slightly better than Ar83. For 278 and 293 K, HF86 is in the same range as Fr15, although it yields much lower values for 248 K compared to Fr15. However, HF86 shows an unexpected behaviour below 230 K, with fluctuating α values that can even become negative. This feature occurs at different temperatures, depending on the input chosen for the ion masses.

In summary, all considered theories and parameterisations can reproduce the laboratory data for warm temperatures (270 and 300 K), while only BC83 and Ar83 can reproduce the α values for colder temperatures (218 and 248 K) because their temperature dependence is more similar to the temperature trend in Fr15. The Thomsonian theories (Ga38, Lo60, Is57, and Na59) only show a weak reaction to reducing temperatures, while HF86 displays an unexpected behaviour within the temperature range considered here.

Franchin et al. (2015) have additionally used the model by López-Yglesias and Flagan (2013) to simulate the ion–ion recombination coefficient for the discussed temperature range. This model describes the ion–aerosol attachment coefficient, although it can also be applied to the special case of two ions recombining. However, the model is unable to reproduce the measured data in the low-temperature regime (Franchin et al., 2015).

8 Determination of the ion–ion trapping distance and the collision probability in the limiting sphere

As discussed in the previous section, the ion–ion trapping sphere radius d is an important parameter in the process of the ion–ion recombination. It is connected with the recombination rate α according to Eq. (16) (Natanson, 1959a). In order to find the values for the ion–ion trapping radius as a function of pressure and temperature from the measured ion–ion recombination rates (Rosen and Hofmann, 1981; Morita, 1983; Gringel et al., 1978), the equation needs to be solved for d_N. Since this cannot be done analytically, it is performed numerically using the Newton–Raphson method. The results are listed in Table B1 and shown in Fig. 4a as an altitude plot, where each data point for d is based on the measured α. Only α values above 10 km are considered due to the erroneous determination of the ion–ion recombination coefficient below 10 km, as discussed previously. The values for the temperature and pressure are taken from the US Standard Atmosphere (National Oceanic and Atmospheric Administration et al., 1976). The reference value for the electrical mobilities, μ_0, for the conditions of 288.15 K and 1013.25 hPa is $1.3 \times 10^{-4}\,\mathrm{m^2\,V^{-1}\,s^{-1}}$ for Gr78 and Mo83, whereas $1.5 \times 10^{-4}\,\mathrm{m^2\,V^{-1}\,s^{-1}}$ is used for the RH81 data set. The mobility values, μ, were adjusted for temperature and pressure according to Eq. (32), with a reference temperature of $T_0 = 288.15$ K. For the calculations, it is further assumed that the masses are 90 Da for both the positive and negative ions (see Sect. 7).

All data sets yield similar results for d (see Fig. 4a). The resulting values of d show an increasing trend with altitude; this trend is approximately linear for a logarithmic x axis. A linear fit of all data points using a logarithmic x axis yields the altitude-dependent parameterisation given in Eq. (51) and a multivariate fit is performed to determine the T and p dependencies (see Eq. 52):

$$d(h) = 10^{\frac{h-(468\pm15)}{58.5\pm2.0}}. \tag{51}$$

$$d(T,p) = (1.9\pm0.3)\times10^{-8}\cdot\left(\frac{T}{T_0}\right)^{1.9\pm0.4}\cdot\left(\frac{p}{p_0}\right)^{-0.19\pm0.02}. \tag{52}$$

It is not possible to extrapolate the parameterisations beyond the input data range of 10–45 km. Especially in the troposphere, the temperature trend is opposite to the one in the stratosphere, while the pressure trend is the same. Thus, a conclusion for the altitude range of 0–10 km cannot be drawn from these calculations. Furthermore, the significance of the pressure- and temperature-dependent fit is limited because the temperature only changes by approximately 15 % between 10 and 45 km altitude which could lead to imprecise results in the temperature dependence.

The gained values for the altitude-dependent Eq. (51) are 15 nm for 10 km, 22 nm for 20 km, and 57 nm for 44 km. The values for the temperature- and pressure-dependent Eq. (52) are similar: 17 nm for 10 km, 21 nm for 20 km, and 59 nm for 44 km. These results are in contrast to the values calculated for Na59 according to Eq. (17) (see Fig. 4a). Natanson's trapping distance d_N is 15 nm at 0 km altitude, 22 nm at 10 km, and 29 nm at 20 km, reaching a maximum of 30 nm at 30 km; above this altitude, d_N decreases again, with a value of 27 nm at 44 km. For HF86 on the other hand, d_{HF} is assumed to be constant at 18 nm. The divergence of the numerical determination presented here, the calculation according to Natanson's formula, and the constant value of Hoppel and Frick highlight that the determination of d is anything but trivial;

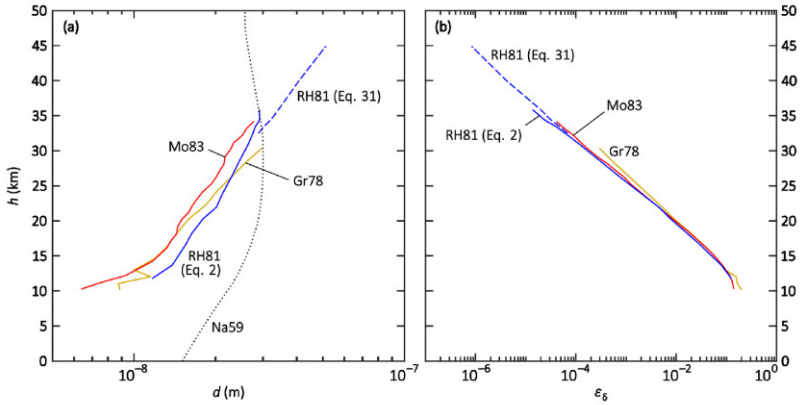

Figure 4. Altitude plots of the **(a)** numerically determined ion–ion trapping radius d and **(b)** analytically determined limiting sphere collision probability ε_δ, each for the field data sets of Gringel et al. (1978) (Gr78, yellow), Rosen and Hofmann (1981) (RH81, blue), and Morita (1983) (Mo83, red). Additionally, the dotted curve (Na59) in panel **(a)** shows d_N after Eq. (17) (Natanson, 1959a).

further research has to be conducted to determine the ion–ion trapping distance for theories that use this parameter in their formulae.

The formula used in Eq. (41) by Filippov (1993) and Tamadate et al. (2020b) to determine the ion–ion recombination coefficient is generally valid. Other theories, experiments, or models, therefore, only need to determine the collision probability for ions entering the limiting sphere, ε_δ, in order to be compared with other theories or data sets. To be able to validate the determined values with the field data, ε_δ is calculated by analytically solving Eq. (41) for ε_δ and using the balloon-borne ion–ion recombination rates mentioned above as the input variable. The results are listed in Table B1 and are shown in the altitude plot in Fig. 4b. All data sets yield similar results and show a decreasing trend for increasing altitudes. With a logarithmic x axis, this trend is linear and can be described by the parameterisation given in Eq. (53):

$$\varepsilon_\delta(h) = 10^{\frac{h-(7.0\pm0.2)}{-(6.18\pm0.06)}}. \tag{53}$$

For the above-mentioned reasons, this parameterisation is only valid between 10 and 45 km. For instance, ε_δ is 0.33 for 10 km altitude, 7.9×10^{-3} for 20 km, and 1.0×10^{-6} for 44 km. The multivariate fit for T and p does not yield a satisfactory parameterisation for ε_δ; the deviation from the initially determined values can be as high as 1 order of magnitude for higher altitudes, therefore, the T- and p-dependent parameterisation is omitted.

9 Conclusion and outlook

The history of theoretical and empirical approaches to quantify the ion–ion recombination coefficient α and its parameterisations have been reviewed. The parameterisations and theories have been compared to field and laboratory data and to a model calculation of α with a focus on temperature and pressure dependence and their applicability to the troposphere and stratosphere, i.e. from 0 to 50 km altitude. For standard conditions (i.e. 273.15 K, 1013 hPa), the value of 1.7×10^{-6} cm^3 s^{-1} is recommended to be used. Evidence is strong that this value is accurate because several authors have derived it independently from both laboratory measurements and model calculations. As of today's knowledge, it is the best assumption to use a nearly constant value for altitudes between 0 and 10 km; this is due to the roughly counterbalancing effects of temperature and pressure on the recombination coefficient. Above 10 km, however, a temperature- and pressure-dependent parameterisation must be used to account for the decreasing value of the ion–ion recombination coefficient. The parameterisation of Israël (1957) shows the best agreement with the field and model data of α for the altitude range of 0–22 km. Between 0 and 20 km, the parameterisation by Brasseur and Chatel (1983) also yields good results and, furthermore, it reproduces the recent laboratory measurements the most faithfully. Between 10 and 25 km, the altitude-dependent parameterisation of Bates (1985) reproduces the field data accurately, while for altitudes above 25 km, the parameterisations of Smith and Adams (1982) and Arijs et al. (1983) show the closest resemblance to the field data, although it is difficult to judge this for altitudes above 35 km because of the sparse data coverage above this altitude. Above 30 km altitude, the theory of Hoppel and Frick (1986) shows an excellent agreement with the (sparse) field data.

However, the understanding of the processes in ion–ion recombination is far from complete. Binary and ternary recombination mechanisms both play a role; however, their specific temperature and pressure dependencies are not fully resolved up to the present day. Additionally, the ion–ion re-

combination is influenced by the mobilities and masses of the ions. Moreover, this work only focussed on the recombination in air; additional gases can be investigated in future studies. More experiments and state-of-the-art model simulations, including MD simulations, are needed to determine the ion–ion recombination coefficient in dependence of temperature, pressure, ion masses, and ion mobilities. This is crucial in order to accurately calculate the recombination loss of ions for the diverse ambient conditions we observe in our atmosphere.

Appendix A: Calculation of the collision radius

They collision radius r_{coll} is defined as the sum of the radii of the positive and the negative ion, $r_+ + r_-$, respectively. These can be calculated in dependence of the masses of the two ions, the temperature, and the pressure, according to Eqs. (A1) to (A4) (López-Yglesias and Flagan, 2013):

$$r_+ = -r_{\mathrm{gas}} + 0.5 \cdot \sqrt{3 \cdot \sqrt{1 + \frac{m_+}{m_{\mathrm{gas}}}} \cdot \frac{v_+ \cdot k_{\mathrm{B}} T}{8 \cdot p \cdot D_+}}, \tag{A1}$$

$$v_+ = \sqrt{\frac{8 \cdot k_{\mathrm{B}} T}{\pi \cdot m_+}}, \tag{A2}$$

$$r_{\mathrm{gas}} = \left(\frac{m_{\mathrm{gas}} \cdot k_{\mathrm{B}} T}{16\pi^2 \cdot \eta^2} \right)^{0.25}, \tag{A3}$$

$$\eta = \eta_0 \cdot \frac{T_0 + S_{\mathrm{C}}}{T + S_{\mathrm{C}}} \cdot \left(\frac{T}{T_0} \right)^{1.5}, \tag{A4}$$

where r_{gas} is the radius of the gas molecule, m_+ is the mass of the positive ion in kg, m_{gas} is the mass of the gas molecule in kg, η is the viscosity of the gas, η_0 is the viscosity of the gas at standard temperature, and S_C is the Sutherland's constant. Accordingly, r_- can be calculated by replacing m_+ for m_-, v_+ for v_-, and D_+ for D_-, respectively. Here, $T_0 = 298.15$ K, for m_{gas}, we assumed 29 Da, for η_0, we used 1.827×10^{-5} Pa s (López-Yglesias and Flagan, 2013), and for S_C, we used 113 K (Chapman and Cowling, 1960).

Appendix B: Values for the ion–ion trapping distance and the collision probability in the limiting sphere

Table B1. Numerically calculated values for the ion–ion trapping distance, d, and analytically calculated values for the collision probability in the limiting sphere, ε_δ, for the reported field data of the ion–ion recombination coefficient, α, taken from Gringel et al. (1978), Rosen and Hofmann (1981), and Morita (1983). The data for T and p are taken from the US Standard Atmosphere (National Oceanic and Atmospheric Administration et al., 1976). For details, see Sect. 8.

h (km)	α ($cm^3\,s^{-1}$)	T (K)	p (hPa)	d (m)	ε_δ
Gringel et al. (1978)					
10.2	2.14×10^{-6}	223	265	1.63×10^{-8}	1.99×10^{-1}
11.1	1.93×10^{-6}	217	227	1.60×10^{-8}	1.64×10^{-1}
12.0	2.06×10^{-6}	217	194	1.90×10^{-8}	1.57×10^{-1}
13.0	1.42×10^{-6}	217	166	1.65×10^{-8}	9.45×10^{-2}
14.5	1.27×10^{-6}	217	131	1.83×10^{-8}	6.64×10^{-2}
16.1	1.05×10^{-6}	217	102	1.94×10^{-8}	4.06×10^{-2}
18.4	7.82×10^{-7}	217	71.1	2.05×10^{-8}	1.81×10^{-2}
20.3	6.37×10^{-7}	217	52.8	2.18×10^{-8}	9.18×10^{-3}
22.3	5.73×10^{-7}	219	38.6	2.46×10^{-8}	4.74×10^{-3}
24.1	4.95×10^{-7}	221	29.3	2.65×10^{-8}	2.44×10^{-3}
26.3	4.44×10^{-7}	223	20.9	2.98×10^{-8}	1.14×10^{-3}
28.3	4.06×10^{-7}	225	15.4	3.31×10^{-8}	5.74×10^{-4}
30.4	3.92×10^{-7}	227	11.3	3.77×10^{-8}	2.94×10^{-4}
Rosen and Hofmann (1981) (Eq. 2)					
11.8	1.81×10^{-6}	217	200	1.88×10^{-8}	1.26×10^{-1}
13.7	1.54×10^{-6}	217	149	2.08×10^{-8}	7.91×10^{-2}
16.6	1.04×10^{-6}	217	94.2	2.20×10^{-8}	2.96×10^{-2}
18.2	8.41×10^{-7}	217	73.3	2.27×10^{-8}	1.64×10^{-2}
20.3	6.79×10^{-7}	217	52.8	2.43×10^{-8}	7.71×10^{-3}
21.9	6.27×10^{-7}	218	41.1	2.67×10^{-8}	4.53×10^{-3}
23.9	4.89×10^{-7}	220	30.2	2.78×10^{-8}	1.97×10^{-3}
26.4	3.75×10^{-7}	223	20.6	2.97×10^{-8}	7.17×10^{-4}
28.5	3.03×10^{-7}	225	15.0	3.14×10^{-8}	3.07×10^{-4}
30.8	2.45×10^{-7}	227	10.6	3.36×10^{-8}	1.23×10^{-4}
32.5	2.05×10^{-7}	230	8.25	3.50×10^{-8}	6.10×10^{-5}
33.4	1.84×10^{-7}	232	7.24	3.56×10^{-8}	4.08×10^{-5}
34.3	1.63×10^{-7}	235	6.08	3.68×10^{-8}	2.44×10^{-5}
35.9	1.34×10^{-7}	239	5.13	3.67×10^{-8}	1.37×10^{-5}

Table B1. Continued.

h (km)	α ($cm^3\,s^{-1}$)	T (K)	p (hPa)	d (m)	ε_δ
Rosen and Hofmann (1981) (Eq. 31)					
32.5	2.28×10^{-7}	230	8.25	3.66×10^{-8}	6.78×10^{-5}
33.4	2.16×10^{-7}	232	7.24	3.81×10^{-8}	4.79×10^{-5}
34.5	2.05×10^{-7}	235	6.08	4.06×10^{-8}	3.07×10^{-5}
35.9	1.94×10^{-7}	239	5.13	4.30×10^{-8}	1.98×10^{-5}
40.0	1.51×10^{-7}	250	2.87	5.10×10^{-8}	4.14×10^{-6}
44.9	1.28×10^{-7}	264	1.53	6.35×10^{-8}	8.37×10^{-7}
Morita (1983)					
10.3	1.54×10^{-6}	222	255	1.28×10^{-8}	1.40×10^{-1}
11.3	1.59×10^{-6}	217	217	1.44×10^{-8}	1.31×10^{-1}
12.2	1.57×10^{-6}	217	188	1.60×10^{-8}	1.16×10^{-1}
13.2	1.43×10^{-6}	217	161	1.70×10^{-8}	9.27×10^{-2}
14.3	1.31×10^{-6}	217	135	1.82×10^{-8}	7.10×10^{-2}
15.2	1.18×10^{-6}	217	117	1.89×10^{-8}	5.43×10^{-2}
16.2	1.05×10^{-6}	217	100	1.95×10^{-8}	3.95×10^{-2}
17.2	9.01×10^{-7}	217	85.8	1.98×10^{-8}	2.74×10^{-2}
18.2	7.99×10^{-7}	217	73.3	2.03×10^{-8}	1.94×10^{-2}
19.1	6.77×10^{-7}	217	63.7	2.03×10^{-8}	1.32×10^{-2}
20.1	5.91×10^{-7}	217	54.4	2.06×10^{-8}	8.98×10^{-3}
21.2	5.32×10^{-7}	218	45.8	2.16×10^{-8}	5.99×10^{-3}
22.2	4.69×10^{-7}	219	39.2	2.21×10^{-8}	4.00×10^{-3}
23.2	4.22×10^{-7}	220	33.6	2.29×10^{-8}	2.70×10^{-3}
24.2	3.86×10^{-7}	221	28.8	2.38×10^{-8}	1.85×10^{-3}
25.2	3.63×10^{-7}	222	24.4	2.52×10^{-8}	1.26×10^{-3}
26.2	3.42×10^{-7}	223	21.2	2.62×10^{-8}	9.08×10^{-4}
27.2	3.08×10^{-7}	224	18.2	2.70×10^{-8}	6.07×10^{-4}
28.1	2.85×10^{-7}	225	15.9	2.78×10^{-8}	4.28×10^{-4}
29.1	2.45×10^{-7}	226	13.7	2.79×10^{-8}	2.73×10^{-4}
30.3	2.24×10^{-7}	227	11.5	2.92×10^{-8}	1.73×10^{-4}
31.1	2.08×10^{-7}	228	10.2	2.99×10^{-8}	1.26×10^{-4}
32.2	2.05×10^{-7}	229	8.63	3.21×10^{-8}	8.91×10^{-5}
33.2	1.87×10^{-7}	232	7.45	3.32×10^{-8}	5.86×10^{-5}
34.2	1.81×10^{-7}	234	6.45	3.52×10^{-8}	4.10×10^{-5}

Appendix C: Nomenclature

b	Critical collision parameter, in m
d	Ion–ion trapping distance or trapping sphere radius, in m
d_{ia}	Three-body trapping distance in ion–aerosol attachment (after Hoppel and Frick), in m
$d_{\mathrm{HF,N}}$	Ion–ion trapping distance (after Hoppel and Frick, Natanson), in m
d_{T}	Ion–ion trapping distance, radius of the collision sphere around each ion, or radius of mutual Coulomb attraction between two ions of opposite charge (after Thomson), in m
D	Diffusion coefficient, sum of D_+ and D_-, in $\mathrm{m^2\,s^{-1}}$
$D_{+,-}$	Diffusion coefficient of the positive, negative ion, in $\mathrm{m^2\,s^{-1}}$
$D_{+/-,0}$	Diffusion coefficient of the positive/negative ion at standard temperature and pressure, in $\mathrm{m^2\,s^{-1}}$
D_{ion}	Diffusion coefficient of one ion, in $\mathrm{m^2\,s^{-1}}$
e	Electron charge, 1.602177×10^{-19} C
E	External electrical field, in $\mathrm{V\,m^{-1}}$
EA	Electron affinity, in eV
h	Altitude, in km
k_{B}	Boltzmann constant, $1.380649 \times 10^{-23}\,\mathrm{J\,K^{-1}}$
$Kn_{\,\delta}$	Knudsen number for the limiting sphere
L	Loss rate to the electrodes, in $\mathrm{cm^{-3}\,s^{-1}}$
[M]	Number density of air molecules, in $\mathrm{cm^{-3}}$
$m_{+,-}$	Mass of the positive, negative ion, in Da (unless noted otherwise)
m_{gas}	Molecular mass of the gas, in kg
m_{ion}	Ion mass, in Da (unless noted otherwise)
m_{red}	Reduced mass, in kg (unless noted otherwise)
n	Number concentration of ions in the gas phase, in $\mathrm{cm^{-3}}$
$n_{+,-}$	Number concentration of the positive, negative ions in the gas phase, in $\mathrm{cm^{-3}}$
n_{total}	Number concentration of the sum of negative and positive ions in the gas phase, in $\mathrm{cm^{-3}}$
p	Pressure, in hPa
p_0	Standard pressure, 1013.25 hPa
q	Ion pair production rate, in $\mathrm{cm^{-3}\,s^{-1}}$
r	Distance of the two ions, in m
r_0	Initial distance of the two ions, in m
r_{coll}	Collision radius, sum of the radii of the positive and negative ions, in m
r_{gas}	Radius of the gas molecule, in m
r_{p}	Particle radius, in m
RH	Relative humidity, in %
S_C	Sutherland's constant, 113 K for air
t	Time, in s
T	Temperature, in K
T_0	Standard temperature, 273.15 K
v	Equilibrium ion drift velocity, in $\mathrm{m\,s^{-1}}$
$v_{+,-}$	Mean thermal speed of the positive, negative ion, in $\mathrm{m\,s^{-1}}$
v_{rel}	Relative thermal speed of two ions, in $\mathrm{m\,s^{-1}}$
$w_{\mathrm{T,N}}$	Function of x (used in Thomson theory and Natanson's theory)
x	Function of d_{T} and λ_{ion} (used in Thomson theory)
x'	Function of T and p (used in Thomson theory)
x_{N}	Function of d_{N} and λ_{ion} (used in Natanson's theory)
α	Ion–ion recombination coefficient, in $\mathrm{cm^3\,s^{-1}}$
α_2	Binary ion–ion recombination coefficient, in $\mathrm{cm^3\,s^{-1}}$
α_3	Ternary ion–ion recombination coefficient, in $\mathrm{cm^3\,s^{-1}}$
α_δ	Ion–ion collision rate coefficient at distance δ (limiting sphere surface), in $\mathrm{m^3\,s^{-1}}$
γ	Function of r_{coll} or d_{HF} (used for the theories of Fuchs and Hoppel and Frick)
δ	limiting sphere radius, in m

δ_F	Limiting sphere radius of Fuchs, in m
δ_{HF}	Limiting sphere radius of Hoppel and Frick, in m
$\Delta\alpha_2$	Enhancement to the ion–ion recombination coefficient due to the binary channel, in $cm^3\ s^{-1}$
ε_0	Vacuum permittivity, 8.854188×10^{-12} A s V^{-1} m^{-1}
ε_d	Probability factor for ions entering the trapping sphere
$\varepsilon_{L,T}$	Ratio of successful recombinations per collision (after Langevin, Thomson)
ε_N	Ion–gas molecule collision probability, also named "adsorption coefficient" (after Natanson)
ε_δ	Collision probability for ions entering the limiting sphere
η	Viscosity of a gas, in Pa s
η_0	Viscosity of air at 298.15 K, 1.827×10^{-5} Pa s
θ	Critical angle to enter the trapping sphere
λ	Ion–ion mean free path, in m
$\lambda_{+,-}$	Mean free path of the positive, negative ion, in m
λ_{air}	Mean free path of air, in m
λ_{ion}	Mean free path of one ion, in m
λ'	Mean distance of the last collision of a particle with a gas molecule before striking the limiting sphere surface (after Fuchs), in m
μ	Ion mobility, in $m^2\ V^{-1}\ s^{-1}$
$\mu_{+,-}$	Ion mobility of the positive, negative ion, in $m^2\ V^{-1}\ s^{-1}$
μ_0	Ion mobility at standard temperature and pressure, in $m^2\ V^{-1}\ s^{-1}$
σ	Electrical conductivity of the air, in S m^{-1}
Ψ_δ	Ratio of Coulomb and thermal energy at distance δ (limiting sphere surface)

Data availability. The data shown in the figures are available on the data repository Zenodo: https://doi.org/10.5281/zenodo.7044018 (Zauner-Wieczorek et al., 2022).

Author contributions. MZW designed the study, surveyed the literature and compared the parameterisations, models and data sets. MZW and AK modelled the parameterisations and theories. MZW, AK, and JC discussed the results. MZW and AK wrote the manuscript; JC provided input for revision before submission.

Competing interests. The contact author has declared that none of the authors has any competing interests.

Disclaimer. Publisher's note: Copernicus Publications remains neutral with regard to jurisdictional claims in published maps and institutional affiliations.

Acknowledgements. We thank the three anonymous referees for their valuable feedbacks.

Financial support. Marcel Zauner-Wieczorek is funded by the Heinrich Böll Foundation. This open-access publication was funded by the GRADE Center Sustain of Goethe University Frankfurt.

Review statement. This paper was edited by Veli-Matti Kerminen and reviewed by three anonymous referees.

References

Arijs, E.: Positive and negative ions in the stratosphere, Ann. Geophys., 1, 149–160, 1983.

Arijs, E., Nevejans, D., Ingels, J., and Frederick, P.: Positive ion composition measurements between 33 and 20 km altitude, Ann. Geophys., 1, 161–166, 1983.

Arnold, F. and Fabian, R.: First measurements of gas phase sulphuric acid in the stratosphere, Nature, 283, 55–57, https://doi.org/10.1038/283055a0, 1980.

Arnold, F. and Hauck, G.: Lower stratosphere trace gas detection using aircraft-borne active chemical ionization mass spectrometry, Nature, 315, 307–309, https://doi.org/10.1038/315307a0, 1985.

Arnold, F. and Qiu, S.: Upper stratosphere negative ion composition measurements and inferred trace gas abundances, Planet. Space Sci., 32, 169–177, https://doi.org/10.1016/0032-0633(84)90151-X, 1984.

Bardsley, J. N. and Wadehra, J. M.: Monte Carlo Simulation of Three-Body Ion-Ion Recombination, Chem. Phys. Lett., 72, 477–480, https://doi.org/10.1016/0009-2614(80)80335-6, 1980.

Basu, S., Buchau, J., Rich, F. J., Weber, E. J., Field, E. C., Heckscher, J. L., Kossey, P. A., Lewis, E. A., Dandekar, B. S., McNamara, L. F., Cliver, E. W., Millman, G. H., Aarons, J., Klobuchar, J. A., and Mendillo, M. F.: Chapter 10. Ionospheric radio wave propagation, in: Handbook of geophysics and the space environment, edited by: Jursa, A. S., Air Force Geophysics Laboratory, US Air Force, https://www.cnofs.org/Handbook_of_Geophysics_1985/pdf_menu.htm (last access: 1 September 2022), 1985.

Bates, D. R.: Recombination of small ions in the troposphere and lower stratosphere, Planet. Space Sci., 30, 1275–1282, https://doi.org/10.1016/0032-0633(82)90101-5, 1982.

Bates, D. R.: Ion-ion recombination in an ambient gas, Adv. Atom. Mol. Phys., 20, 1–39, https://doi.org/10.1016/S0065-2199(08)60264-X, 1985.

Bates, D. R. and Mendaš, I.: Ionic Recombination in an Ambient Gas. II. Computer Experiment with Specific Allowance for Binary Recombination, Proc. R. Soc. Lond. A, 359, 287–301, https://www.jstor.org/stable/79596 (last access: 1 September 2022), 1978.

Bazilevskaya, G. A., Usoskin, I. G., Flückiger, E. O., Harrison, R. G., Desorgher, L., Bütikofer, R., Krainev, M. B., Makhmutov, V. S., Stozhkov, Y. I., Svirzhevskaya, A. K., Svirzhevsky, N. S., and Kovaltsov, G. A.: Cosmic Ray Induced Ion Production in the Atmosphere, Space Sci. Rev., 137, 149–173, https://doi.org/10.1007/s11214-008-9339-y, 2008.

Brasseur, G. and Chatel, A.: Modelling of stratospheric ions: a first attempt, Ann. Geophys., 1, 173–185, https://orfeo.kbr.be/bitstream/handle/internal/6155/Brasseur%281983f%29.pdf?sequence=1&isAllowed=y (last access: 1 September 2022), 1983.

Chapman, S. and Cowling, T. G.: The mathematical theory of non-uniform gases: An account of kinetic theory of viscosity, thermal conduction, and diffusion in gases, 2nd edn., 2. repr., Cambridge University Press, Cambridge, 1960.

Feibelman, P. J.: Numerical Study of the Three-Body Ion-Ion Recombination Rate, J. Chem. Phys., 42, 2462–2470, https://doi.org/10.1063/1.1696317, 1965.

Filippov, A. V.: Charging of Aerool in the Transition Regime, J. Aerosol Sci., 24, 423–436, https://doi.org/10.1016/0021-8502(93)90029-9, 1993.

Fisk, G. A., Mahan, B. H., and Parks, E. K.: Gaseous Ion Recombination Rates. IV, J. Chem. Phys., 47, 2649–2658, https://doi.org/10.1063/1.1712281, 1967.

Franchin, A., Ehrhart, S., Leppä, J., Nieminen, T., Gagné, S., Schobesberger, S., Wimmer, D., Duplissy, J., Riccobono, F., Dunne, E. M., Rondo, L., Downard, A., Bianchi, F., Kupc, A., Tsagkogeorgas, G., Lehtipalo, K., Manninen, H. E., Almeida, J., Amorim, A., Wagner, P. E., Hansel, A., Kirkby, J., Kürten, A., Donahue, N. M., Makhmutov, V., Mathot, S., Metzger, A., Petäjä, T., Schnitzhofer, R., Sipilä, M., Stozhkov, Y., Tomé, A., Kerminen, V.-M., Carslaw, K., Curtius, J., Baltensperger, U., and Kulmala, M.: Experimental investigation of ion–ion recombination under atmospheric conditions, Atmos. Chem. Phys., 15, 7203–7216, https://doi.org/10.5194/acp-15-7203-2015, 2015.

Fuchs, N. A.: On the stationary charge distribution on aerosol particles in a bipolar ionic atmosphere, Geofisica Pura e Applicata, 56, 185–193, https://doi.org/10.1007/BF01993343, 1963.

Gardner, M. E.: The Recombination of Ions in Pure Oxygen as a Function of Pressure and Temperature, Phys. Rev., 53, 75–83, https://doi.org/10.1103/PhysRev.53.75, 1938.

Gopalakrishnan, R. and Hogan, C. J. J.: Coulomb-influenced collisions in aerosols and dusty plasmas, Phys. Rev. E, 85, 26410, https://doi.org/10.1103/PhysRevE.85.026410, 2012.

Gringel, W., Käselau, K. H., and Mühleisen, R.: Recombination rates of small ions and their attachment to aerosol particles, Pure Appl. Geophys., 116, 1101–1113, https://doi.org/10.1007/BF00874674, 1978.

Harrison, R. G.: The global atmospheric electrical circuit and climate, Surv. Geophys., 25, 441–484, https://doi.org/10.1007/s10712-004-5439-8, 2004.

Hickman, A. P.: Approximate scaling formula for ion–ion mutual neutralization rates, J. Chem. Phys., 70, 4872–4878, https://doi.org/10.1063/1.437364, 1979.

Hirsikko, A., Nieminen, T., Gagné, S., Lehtipalo, K., Manninen, H. E., Ehn, M., Hõrrak, U., Kerminen, V.-M., Laakso, L., McMurry, P. H., Mirme, A., Mirme, S., Petäjä, T., Tammet, H., Vakkari, V., Vana, M., and Kulmala, M.: Atmospheric ions and nucleation: a review of observations, Atmos. Chem. Phys., 11, 767–798, https://doi.org/10.5194/acp-11-767-2011, 2011.

Hoppel, W. A.: Ion-Aerosol Attachment Coefficients and the Diffusional Charging of Aerosols, in: Electrical Processes in Atmospheres: proceedings of the 5. Internat. Conference on Atmospheric Electricity, Garmisch-Partenkirchen, Germany, 2–7 September 1974, edited by: Dolazek, H. and Reiter, R., Steinkopff, Darmstadt, 60–69, ISBN 3798504350, 1977.

Hoppel, W. A. and Frick, G. M.: Ion–Aerosol Attachment Coefficients and the Steady-State Charge Distribution on Aerosols in a Bipolar Ion Environment, Aerosol Sci. Tech., 5, 1–21, https://doi.org/10.1080/02786828608959073, 1986.

Israël, H.: Atmosphärische Elektrizität: Teil 1. Grundlagen, Leitfähigkeit, Ionen, Akademische Verlagsgesellschaft Geest & Portig K.G., Leipzig, 1957.

Israël, H.: Atmospheric Electricity: Volume I. Fundamentals, Conductivity, Ions, 2nd edn., Israel Program for Scientific Translations Ltd, Jerusalem, 1971.

Johnsen, R., Shun'ko, E. V., Gougousi, T., and Golde, M. F.: Langmuir-probe measurements in flowing-afterglow plasmas, Phys. Rev. E, 50, 3994–4004, https://doi.org/10.1103/PhysRevE.50.3994, 1994.

Keefe, D., Nolan, P. J., and Scott, J. A.: Influence of Coulomb and Image Forces on Combination in Aerosols, P. Roy. Irish Acad. A, 66, 17–29, https://www.jstor.org/stable/20488658 (last access: 1 September 2022), 1968.

Langevin, M. P.: Recombinaison et mobilités des ions dans les gaz, Ann. Chim. Phys., 433–530, https://gallica.bnf.fr/ark:/12148/bpt6k34928d/f431.item, (last access: 1 September 2022), 1903a.

Langevin, M. P.: Sur la loi de recombinaison des ions, C. R. Hebd. Acad. Sci., 177–179, https://gallica.bnf.fr/ark:/12148/bpt6k6262249w/f25.item, (last access: 1 September 2022), 1903b.

Lee, H. S. and Johnsen, R.: Ion–ion recombination studies in ambient helium and argon at atmospheric densities, J. Chem. Phys., 90, 6328–6334, https://doi.org/10.1063/1.456349, 1989.

Lenz, E.: Die Wiedervereinigung von Ionen in Luft bei niederen Drucken, Z. Phys., 76, 660–678, https://doi.org/10.1007/BF01341939, 1932.

Loeb, L. B.: Basic Processes of Gaseous Electronics, University of California Press, Berkeley, https://doi.org/10.1525/9780520348936, 1955.

Loeb, L. B.: Basic Processes of Gaseous Electronics, 2nd edn., revised, University of California Press and Cambridge University Press, Berkeley, Los Angeles and London, 1960.

Loeb, L. B. and Marshall, L. C.: The Theory of Recombination of Gaseous Ions, J. Frankl. Inst., 208, 371–388, https://doi.org/10.1016/S0016-0032(29)91182-0, 1929.

López-Yglesias, X. and Flagan, R. C.: Ion–Aerosol Flux Coefficients and the Steady-State Charge Distribution of Aerosols in a Bipolar Ion Environment, Aerosol Sci. Tech., 47, 688–704, https://doi.org/10.1080/02786826.2013.783684, 2013.

Miller, T. M., Shuman, N. S., and Viggiano, A. A.: Behavior of rate coefficients for ion-ion mutual neutralization, 300–550 K, J. Chem. Phys., 136, 204306, https://doi.org/10.1063/1.4720499, 2012.

Morita, Y.: Recent measurements of electrical conductivity and ion pair production rate, and the ion-ion recombination coefficient derived from them in the lower stratosphere, J. Geomagn. Geoelectr., 35, 29–38, https://doi.org/10.5636/jgg.35.29, 1983.

Natanson, G. L.: The Theory of Volume Recombination of Ions, Journal of Technical Physics, 4, 1263–1269, 1959a.

Natanson, G. L.: The Theory of Volume Recombination of Ions, Zhurnal Tekhnicheskoi Fiziki, 29, 1373–1380, 1959b (in Russian).

Natanson, G. L.: On the Theory of the Charging of Amicroscopic Aerosol Particles as a Result of Capture if Gas Ions, Journal of Technical Physics, 5, 538–551, 1960a.

Natanson, G. L.: On the Theory of the Charging of Amicroscopic Aerosol Particles as a Result of Capture if Gas Ions, Zhurnal Tekhnicheskoi Fiziki, 30, 573–588, 1960b (in Russian).

National Oceanic and Atmospheric Administration, National Aeronautics and Space Administration, and United States Air Force: U.S. Standard Atmosphere, 1976, U.S. Government Printing Office, Washington, D.C., https://ntrs.nasa.gov/api/citations/19770009539/downloads/19770009539.pdf, (last access: 1 September 2022), 1976.

Nolan, P. J.: The Recombination Law for Weak Ionisation, P. Roy. Irish Acad. A, 49, 67–90, https://www.jstor.org/stable/20488452 (last access: 1 September 2022), 1943.

Rosen, J. M. and Hofmann, D. J.: Balloon-borne measurements of electrical conductivity, mobility, and the recombination coefficient, J. Geophys. Res.-Oceans, 86, 7406–7410, https://doi.org/10.1029/JC086iC08p07406, 1981.

Sagalyn, R. C., Burke, H. C., and Fitzgerald, D. R.: Chapter 20. Atmospheric electricity, in: Handbook of geophysics and the space environment, edited by: Jursa, A. S., Air Force Geophysics Laboratory, US Air Force, https://www.cnofs.org/Handbook_of_Geophysics_1985/pdf_menu.htm (last access: 1 September 2022), 1985.

Sayers, J.: Ionic recombination in air, Proc. R. Soc. Lond. A, 169, 83–101, https://doi.org/10.1098/rspa.1938.0196, 1938.

Shuman, N. S., Miller, T. M., Hazari, N., Luzik, E. D., and Viggiano, A. A.: Kinetics following addition of sulfur fluorides to a weakly ionized plasma from 300 to 500 K: rate constants and product determinations for ion-ion mutual neutralization and thermal electron attachment to SF5, SF3, and SF2, J. Chem. Phys., 133, 234304, https://doi.org/10.1063/1.3520150, 2010.

Shuman, N. S., Wiens, J. P., Miller, T. M., and Viggiano, A. A.: Kinetics of ion-ion mutual neutralization: halide anions with polyatomic cations, J. Chem. Phys., 140, 224309, https://doi.org/10.1063/1.4879780, 2014a.

Shuman, N. S., Miller, T. M., Johnsen, R., and Viggiano, A. A.: Mutual neutralization of atomic rare-gas cations (Ne^+, Ar^+, Kr^+, Xe^++)) with atomic halide anions (Cl^-, Br^-, I^-), J. Chem. Phys., 140, 44304, https://doi.org/10.1063/1.4862151, 2014b.

Smith, D. and Adams, N. G.: Ionic recombination in the stratosphere, Geophys. Res. Lett., 9, 1085–1087, https://doi.org/10.1029/GL009i009p01085, 1982.

Smith, D. and Church, M. J.: Ion-ion recombination rates in the earth's atmosphere, Planet. Space Sci., 25, 433–439, https://doi.org/10.1016/0032-0633(77)90075-7, 1977.

Tamadate, T., Higashi, H., Hogan, C. J., and Seto, T.: The charge reduction rate for multiply charged polymer ions via ion-ion recombination at atmospheric pressure, Phys. Chem. Chem. Phys., 22, 25215–25226, https://doi.org/10.1039/d0cp03989f, 2020a.

Tamadate, T., Higashi, H., Seto, T., and Hogan, C. J., J.: Calculation of the ion-ion recombination rate coefficient via a hybrid continuum-molecular dynamics approach, J. Chem. Phys., 152, 94306, https://doi.org/10.1063/1.5144772, 2020b.

Tang, M. J., Cox, R. A., and Kalberer, M.: Compilation and evaluation of gas phase diffusion coefficients of reactive trace gases in the atmosphere: volume 1. Inorganic compounds, Atmos. Chem. Phys., 14, 9233–9247, https://doi.org/10.5194/acp-14-9233-2014, 2014.

Thirkill, H.: On the recombination of the ions produced by Röntgen rays in gases and vapours, Proc. R. Soc. Lond. A, 88, 477–494, https://doi.org/10.1098/rspa.1913.0046, 1913.

Thomson, J. J.: XXIX. Recombination of gaseous ions, the chemical combination of gases, and monomolecular reactions, The London, Edinburgh, and Dublin Philosophical Magazine and Journal of Science, 47, 337–378, https://doi.org/10.1080/14786442408634372, 1924.

Thomson, J. J. and Rutherford, E.: XL. On the passage of electricity through gases exposed to Röntgen rays, The London, Edinburgh, and Dublin Philosophical Magazine and Journal of Science, 42, 392–407, https://doi.org/10.1080/14786449608620932, 1896.

Viggiano, A. A. and Arnold, F.: Ion Chemistry and Composition of the Atmosphere, in: Handbook of Atmospheric Dynamics. Volume 1. Atmospheric Electricity, edited by: Volland, H., CRC Press, Boca Raton, London, Tokyo, 1–25, ISBN 0849386470, 1995.

Wang, S. C. and Flagan, R. C.: Scanning Electrical Mobility Spectrometer, Aerosol Sci. Tech., 13, 230–240, https://doi.org/10.1080/02786829008959441, 1990.

Weaver, A., Arnold, D. W., Bradforth, S. E., and Neumark, D. M.: Examination of the 2A'2 and 2E" states of NO_3 by ultraviolet photoelectron spectroscopy of NO_3^-, J. Chem. Phys., 94, 1740–1751, https://doi.org/10.1063/1.459947, 1991.

Wiens, J. P., Shuman, N. S., and Viggiano, A. A.: Dissociative recombination and mutual neutralization of heavier molecular ions: $C_{10}H_8^+$, WF_5^+, and $C_nF_m^+$, J. Chem. Phys., 142, 114304, https://doi.org/10.1063/1.4913829, 2015.

Wright, P. G.: On the Discontinuity Involved in Diffusion Across an Interface (The Δ of Fuchs), Discuss. Faraday Soc., 30, 100–112, https://doi.org/10.1039/df9603000100, 1960.

Zauner-Wieczorek, M., Curtius, J., and Kürten, A.: Data set for "The ion–ion recombination coefficient α: comparison of temperature- and pressure-dependent parameterisations for the troposphere and stratosphere", Zenodo [data set], https://doi.org/10.5281/zenodo.7044018, 2022.

4.3.2 Cleaner Skies during the COVID-19 Lockdown

BAMS Article

Cleaner Skies during the COVID-19 Lockdown

Christiane Voigt, Jos Lelieveld, Hans Schlager, Johannes Schneider, Joachim Curtius, Ralf Meerkötter, Daniel Sauer, Luca Bugliaro, Birger Bohn, John N. Crowley, Thilo Erbertseder, Silke Groß, Valerian Hahn, Qiang Li, Mariano Mertens, Mira L. Pöhlker, Andrea Pozzer, Ulrich Schumann, Laura Tomsche, Jonathan Williams, Andreas Zahn, Meinrat Andreae, Stephan Borrmann, Tiziana Bräuer, Raphael Dörich, Andreas Dörnbrack, Achim Edtbauer, Lisa Ernle, Horst Fischer, Andreas Giez, Manuel Granzin, Volker Grewe, Hartwig Harder, Martin Heinritzi, Bruna A. Holanda, Patrick Jöckel, Katharina Kaiser, Ovid O. Krüger, Johannes Lucke, Andreas Marsing, Anna Martin, Sigrun Matthes, Christopher Pöhlker, Ulrich Pöschl, Simon Reifenberg, Akima Ringsdorf, Monika Scheibe, Ivan Tadic, Marcel Zauner-Wieczorek, Rolf Henke, and Markus Rapp

ABSTRACT: During spring 2020, the COVID-19 pandemic caused massive reductions in emissions from industry and ground and airborne transportation. To explore the resulting atmospheric composition changes, we conducted the BLUESKY campaign with two research aircraft and measured trace gases, aerosols, and cloud properties from the boundary layer to the lower stratosphere. From 16 May to 9 June 2020, we performed 20 flights in the early COVID-19 lockdown phase over Europe and the Atlantic Ocean. We found up to 50% reductions in boundary layer nitrogen dioxide concentrations in urban areas from GOME-2B satellite data, along with carbon monoxide reductions in the pollution hot spots. We measured 20%–70% reductions in total reactive nitrogen, carbon monoxide, and fine mode aerosol concentration in profiles over German cities compared to a 10-yr dataset from passenger aircraft. The total aerosol mass was significantly reduced below 5 km altitude, and the organic aerosol fraction also aloft, indicative of decreased organic precursor gas emissions. The reduced aerosol optical thickness caused a perceptible shift in sky color toward the blue part of the spectrum (hence BLUESKY) and increased shortwave radiation at the surface. We find that the 80% decline in air traffic led to substantial reductions in nitrogen oxides at cruise altitudes, in contrail cover, and in resulting radiative forcing. The light extinction and depolarization by cirrus were also reduced in regions with substantially decreased air traffic. General circulation–chemistry model simulations indicate good agreement with the measurements when applying a reduced emission scenario. The comprehensive BLUESKY dataset documents the major impact of anthropogenic emissions on the atmospheric composition.

KEYWORDS: Cirrus clouds; Aerosols/particulates; Air pollution; Atmospheric composition; Measurements; COVID-19

https://doi.org/10.1175/BAMS-D-21-0012.1
Corresponding author: Christiane Voigt, christiane.voigt@dlr.de
In final form 21 March 2022

AFFILIATIONS: Voigt, Hahn, and Tomsche—Deutsches Zentrum für Luft- und Raumfahrt, Oberpfaffenhofen, and Johannes Gutenberg-Universität, Mainz, Germany; **Lelieveld, Schneider, Crowley, Pozzer, Williams, Dörich, Edtbauer, Ernle, Fischer, Harder, Holanda, Krüger, Martin, C. Pöhlker, Pöschl, Reifenberg, Ringsdorf, and Tadic**—Max-Planck-Institut für Chemie, Mainz, Germany; **Schlager, Meerkötter, Sauer, Bugliaro, Erbertseder, Groß, Li, Mertens, Schumann, Bräuer, Dörnbrack, Giez, Jöckel, Marsing, Matthes, Scheibe, and Henke**—Deutsches Zentrum für Luft- und Raumfahrt, Oberpfaffenhofen, Germany; **Curtius, Granzin, Heinritzi, and Zauner-Wieczorek**—Goethe-Universität Frankfurt, Frankfurt, Germany; **Bohn**—Forschungszentrum Jülich, Jülich, Germany; **M. L. Pöhlker**—Max-Planck-Institut für Chemie, Mainz, and Leipzig Institut für Meteorologie, Universität Leipzig, and Leibniz Institut für Troposphärenforschung, Leipzig, Germany; **Zahn**—Karlsruhe Institut für Technologie, Karlsruhe, Germany; **Andreae**—Max-Planck-Institut für Chemie, Mainz, Germany, and Scripps Institution of Oceanography, University of California, San Diego, La Jolla, California; **Borrmann and Kaiser**—Johannes Gutenberg-Universität, and Max-Planck-Institut für Chemie, Mainz, Germany; **Grewe and Lucke**—Deutsches Zentrum für Luft- und Raumfahrt, Oberpfaffenhofen, Germany, and Faculty of Aerospace Engineering, Delft University of Technology, Delft, Netherlands; **Rapp**—Deutsches Zentrum für Luft- und Raumfahrt, Oberpfaffenhofen, and Ludwig-Maximilians-Universität, Munich, Germany

Regulations to limit the spread of the COVID-19 pandemic led to substantial changes in human life, industrial productivity, and mobility, which caused reductions in emissions from industry and ground and airborne transportation (Venter et al. 2020). Hence, the lockdown period offered the unique opportunity to directly measure the effects of reduced pollution emissions on atmospheric composition and thereby challenge our understanding of the anthropogenically perturbed chemical and physical environment (Kroll et al. 2020). The different starting times and types of regulations from the national governments as well as the different chemical and physical processing and hence lifetimes of the emissions caused regionally different evolutions of atmospheric concentrations of individual species. This leads to major uncertainties in the quantitative estimate of emission changes needed to establish emission inventories (Forster et al. 2020). For example, there have been efforts to derive trends in ground transportation in many countries from searches in web-based map platforms (Le Quéré et al. 2020). Guevara et al. (2021) estimated the reduction in primary emissions from different source sectors, such as energy and manufacturing industries and traffic sectors, based on publicly available data [with further data in Copernicus (2020) and Guevara et al. (2020)]. Extrapolating previous emissions to a 2020 business as usual scenario, they derive an average 33% emission reduction of nitrogen oxides (NO_x) in Europe and similar but less reduction for other pollutants (Fig. 1). The transport and the industry sectors were affected differently from lockdown restrictions, with the highest per-sector emission reductions in aviation, whereas the highest total reduction was attributable to road transport (up to about 70% of all sectors, depending on pollutant). Le et al. (2020) compared satellite observations of particulate matter ($PM_{2.5}$), nitrogen dioxide (NO_2), sulfur dioxide (SO_2), and ozone (O_3) during the lockdown in China to prelockdown observations. While reductions in $PM_{2.5}$, NO_2, and SO_2 agree with the trend expected from reduced emissions from transport and industry, enhancements in $PM_{2.5}$ in the Beijing area could only be explained by taking the appropriate meteorology into account. The impact of meteorology, pollution, and other factors on the boundary layer composition and on $PM_{2.5}$ is discussed in many studies (e.g., Chen et al. 2020; Dhaka et al. 2020; Hallar et al. 2021; Karle et al. 2021; Solimini et al. 2021). These

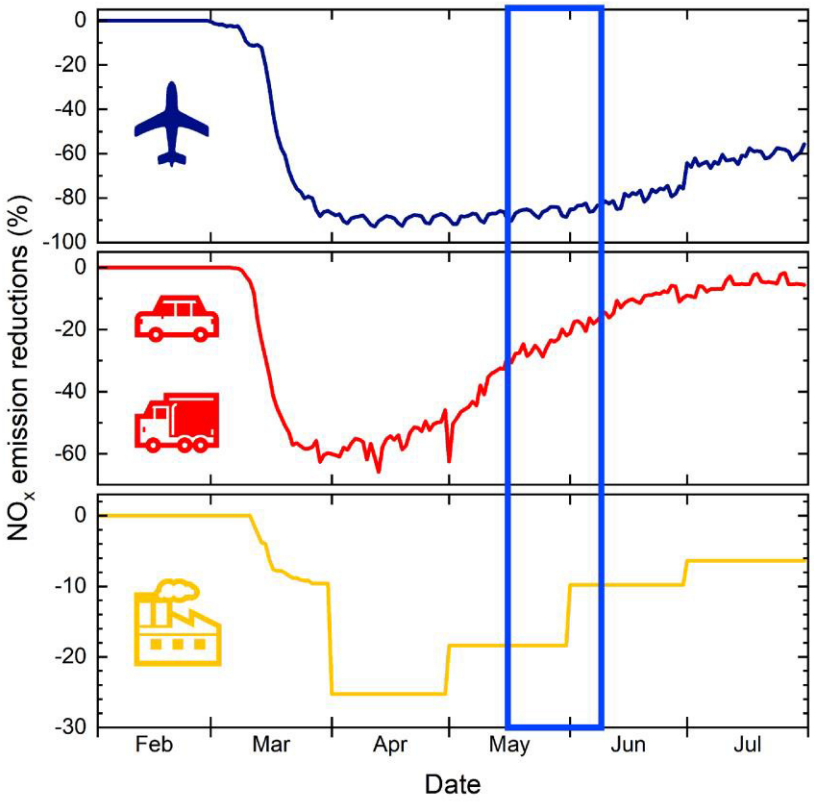

Fig. 1. Percentage change of nitrogen oxide (NO_x) emissions in the aviation (blue), road transport (red), and industry (yellow) sectors in early 2020, compared to a business-as-usual scenario, for the European Union and the United Kingdom. The BLUESKY period was from 16 May to 9 Jun 2020 indicated by the blue box. Emission reduction factors are taken from https://atmosphere.copernicus.eu/covid-data-download [last accessed: 30 Sep 2021; detailed description in Guevara et al. (2020)]. The underlying method has been developed by Guevara et al. (2021).

studies emphasize the need for comprehensive atmospheric composition measurements from the boundary layer to the stratosphere in different parts of the world in order to determine and better understand atmospheric composition changes caused by human activities and distinguish the anthropogenic impact from natural factors.

Travel restrictions resulted in more than 80% reductions in air traffic worldwide during the early lockdown phase (Guevara et al. 2021), and aviation experienced significantly stronger reductions compared to other transport sectors. While air traffic generally recovered within a year in Asia and America, European air traffic lagged behind and showed a significant decrease throughout summer 2020 with a slight recovery toward the end of the year (see Fig. 2). One year after the initial lockdown, European air traffic was still reduced by about 30% compared to pre-COVID-19 levels.

Aircraft emit carbon dioxide (CO_2), nitrogen oxides (NO_x), water vapor (H_2O), and aerosols. The aircraft emissions can modify cirrus clouds and lead to the formation of contrails in cold and humid areas at cruise altitudes (Lee et al. 2010). The recent, comprehensive assessment of air traffic effects on the atmosphere (Lee et al. 2021) shows that aviation up to 2018 contributed about 3.5% to the total anthropogenic effective radiative forcing, with about one-third coming from its CO_2 emissions and two-thirds resulting from the non-CO_2 effects. In fact, the major contributor to effective radiative forcing from aviation is caused by contrail cirrus (57%) (Burkhardt et al. 2018; Lee et al. 2021). The effects of aviation generated aerosol on natural

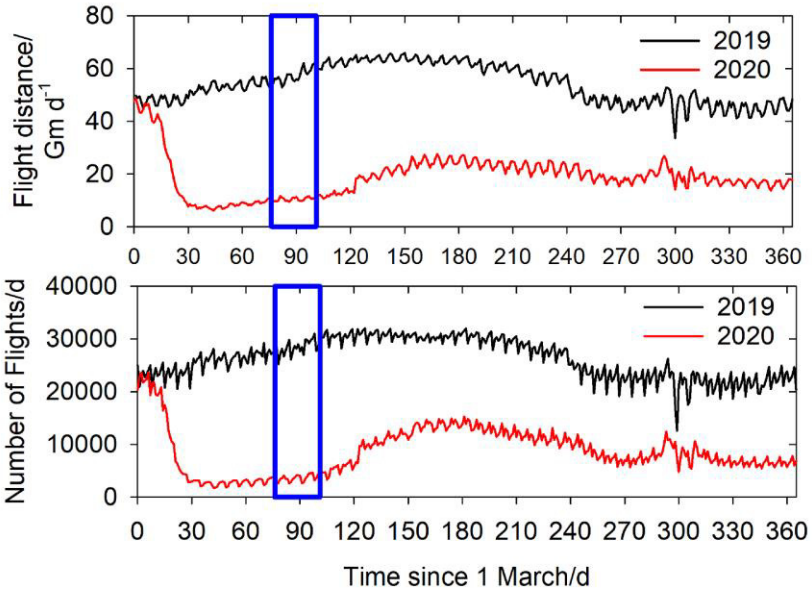

Fig. 2. Flight distance and number of flights over Europe since 1 Mar 2020 (red) and 1 Mar 2019 (black) from EUROCONTROL and NATS. The BLUESKY period was from 16 May to 9 Jun 2020 indicated by the blue box.

clouds remains uncertain (Lee et al. 2021). Properties of contrail cirrus have been measured from aircraft (Heymsfield et al. 2010; Voigt et al. 2010, 2017, 2021; Schumann et al. 2017; Bräuer et al. 2021a,b) and satellites (Minnis et al. 2013; Vázquez-Navarro et al. 2015). These observations were used to evaluate the Contrail Cirrus Prediction model (COCIP) (Schumann 2012; Schumann et al. 2017), with which the radiative forcing from contrail cirrus can be calculated. Reduced contrail cirrus optical thickness and radiative forcing caused by diminished air traffic over Europe has been calculated for a 9-month period in 2020 (Schumann et al. 2021a). Significant reductions in seasonal and regional effective radiative forcing from contrail cirrus caused by reduced air traffic emissions during the lockdown 2020 were also found by Gettelman et al. (2021), while the annual mean effective radiative forcing was less affected. Also, the difficulty in separating the impact of meteorology from the reduced aircraft emissions impact on cloud properties induces considerable uncertainties in the calculations (Schumann et al. 2021b). Quaas et al. (2021) used satellite-based cloud retrievals in regions more and less affected by air traffic to derive changes in the aviation impact on cirrus clouds in 2020. Recent studies (Urbanek et al. 2018; Li and Groß 2021) also suggest changes in optical cirrus properties (extinction, depolarization) caused by aged air traffic emissions. Still, many research questions remain with respect to the derivation of changes in cirrus properties and radiative forcing for reduced air traffic in 2020.

Combined, these challenges motivated the BLUESKY mission (www.dlr.de/content/en/articles/news/2020/02/20200522_bluesky-examines-the-atmosphere-during-the-coronavirus-lockdown.html), with the objective to advance our understanding of the anthropogenic impact on atmospheric composition by acquiring a unique dataset on trace gas, aerosol, and cloud properties measured in the early lockdown phase over central Europe and the northern Atlantic flight corridor. Two aircraft were equipped for the BLUESKY campaign: the High-Altitude and Long-Range Research Aircraft (HALO), a Gulfstream 550 with a range of about 8,000 km and 14.5 km cruise altitude (Tadic et al. 2021; Voigt et al. 2017), and the DLR Falcon with 3,000 km range and up to 12 km cruise altitude (Voigt et al. 2011). For BLUESKY, the aircraft were equipped with instruments that measure long- and short-lived

trace gases, aerosol, and cloud properties. The aircraft measurements were combined with satellite data of tropospheric NO_2 column densities from the Global Ozone Monitoring Experiment 2 (GOME-2; Munro et al. 2016) and *Sentinel-5P*/Tropospheric Monitoring Instrument (TROPOMI; Veefkind et al. 2012), and with cloud data retrieved from the SEVIRI Imager on the Meteosat Second Generation (MSG) satellite, as well as the Cloud–Aerosol Lidar with Orthogonal Polarization (CALIOP) on the *Cloud–Aerosol Lidar and Infrared Pathfinder Satellite Observations* (*CALIPSO*) (Winker et al. 2010). The measurements were also used to evaluate the global chemistry climate model EMAC (Jöckel et al. 2010) and the global–regional chemistry–climate model MECO(n) (Kerkweg and Jöckel 2012a,b; Mertens et al. 2016).

Due to travel restrictions, BLUESKY was conducted out of the home base in Oberpfaffenhofen (48°5′N, 11°17′E) in southern Germany. The observations were performed in May and June 2020 during the early COVID-19 lockdown phase in Europe. This paper describes the aircraft instrumentation and the campaign strategy supported by satellite and modeling activities, as well as first results and highlights from the BLUESKY mission.

Aircraft preparation and instrumentation

During the first days of the lockdown, we developed the idea to deploy the two aircraft HALO and Falcon to measure the atmospheric composition changes during the COVID-19 lockdown. This required adaptation of the Falcon instrumentation to the new science goals by adding instruments to measure O_3 and NO_y, which are expected to be influenced by anthropogenic emissions. For HALO, the payload that was planned for the mission CAFE-Brazil, originally scheduled for May 2021, was used for the BLUESKY mission. The preparation of both aircraft was performed under special health, distance, and safety regulations, as there was no COVID-19 vaccine available at that time. Instrument certification mainly was done from home, and remote access to instruments was promoted; thereby, instrument automatization was advanced for future campaigns. The flights were performed with a minimum crew and with the same personnel to minimize contacts; see Fig. 3.

Also, the scientific payloads of the two aircraft were complementary. The HALO payload included a comprehensive set of trace gas and aerosol instruments and the Falcon was equipped with a smaller trace gas and aerosol payload and in addition included cloud probes. Basic meteorological sensor systems to measure meteorological parameters and humidity were operated on both aircraft. The aircraft instrumentations for BLUESKY are described in more detail below.

HALO instrumentation

The heavily instrumented HALO aircraft focused on the detection of short- and long-lived trace gases as well as aerosol properties and composition (Fig. 4 and Table 1). To this end, several mass spectrometers were operated on HALO: The chemical ionization–atmospheric pressure interface time-of-flight (CI-APITOF) mass spectrometer was deployed to measure nucleating vapors such as sulfuric acid, methanesulfonic acid, highly oxygenated organic molecules, and naturally occurring ions.

The thermal dissociation iodide–chemical–ionization mass spectrometer (I-CIMS) (Slusher et al. 2004; Dörich et al. 2021) monitors peroxyacetylnitric anhydride (PAN), peroxypropylnitric anhydride (PPN), and other species. A proton transfer time of flight mass spectrometer system monitors several volatile organic compounds (Derstroff et al. 2017) including species like isoprene and monoterpenes, acetonitrile, acetone, and methanol. The gas chromatography mass spectrometer (GC-MS) system collects and separates volatile organic components (VOCs) by gas chromatography and detects them with a quadrupole mass spectrometer with a time resolution of 3.5 min (Bourtsoukidis et al. 2017). The instrument provides information on

Fig. 3. The BLUESKY experiment was performed with the High-Altitude and Long-Range Research Aircraft (HALO) and the DLR research aircraft Falcon in the early COVID-19 lockdown phase from 16 May to 9 Jun 2020. (top) The instrumentation and the cabin crew of the Falcon.

organohalogen compounds such as methyl chloride, selected alkanes, alkenes, aromatics, and alkyl nitrates as well as isopropylnitrate (IPN).

Measurements of NO and NO_2 were made with the Nitrogen Oxides Analyzer for HALO (NOAH) instrument, a modified instrument from ECO-Physics (Hosaynali Beygi et al. 2011). The Airborne Tropospheric Tracer In situ Laser Absorption (ATTILA) spectrometer measured CO and methane (CH_4) using dual quantum cascade midinfrared laser absorption spectroscopy. The hydrogen oxide radicals OH and HO_2 were measured with the Hydroxyl Radical measurement Unit (HORUS) instrument (Marno et al. 2020) based on the laser-induced fluorescence technique. The Tracer In situ quantum cascade laser absorption spectrometer/Hydrogen and Organic Peroxide (TRIHOP) monitor consists of an infrared-laser absorption spectrometer (Schiller et al. 2008) for in situ measurements of formaldehyde (HCHO) and a dual-enzyme monitor (Hottmann et al. 2020) for the detection of hydrogen peroxides H_2O_2 and ROOH.

In addition, the aerosol composition was measured using a compact time-of-flight aerosol mass spectrometer (C-ToF-AMS; Drewnick et al. 2005; Schmale et al. 2010; Schulz et al. 2018). The C-ToF-AMS analyzes aerosol particles in a diameter range of approximately 50–800 nm and provides quantitative mass concentrations of organic matter, sulfate, nitrate, and ammonium. For aircraft operation, it is equipped with a constant pressure inlet that ensures a steady mass flow and operation pressure of the aerodynamic lens. The Fast Aerosol Size Distribution (FASD) system contains a condensation particle counter (CPC) battery, an Ultra-High Sensitivity Aerosol Spectrometer (UHSAS) instrument, and an optical particle size spectrometer. The CCN-Rack includes a cloud condensation nuclei (CCN) counter (Holanda et al. 2020),

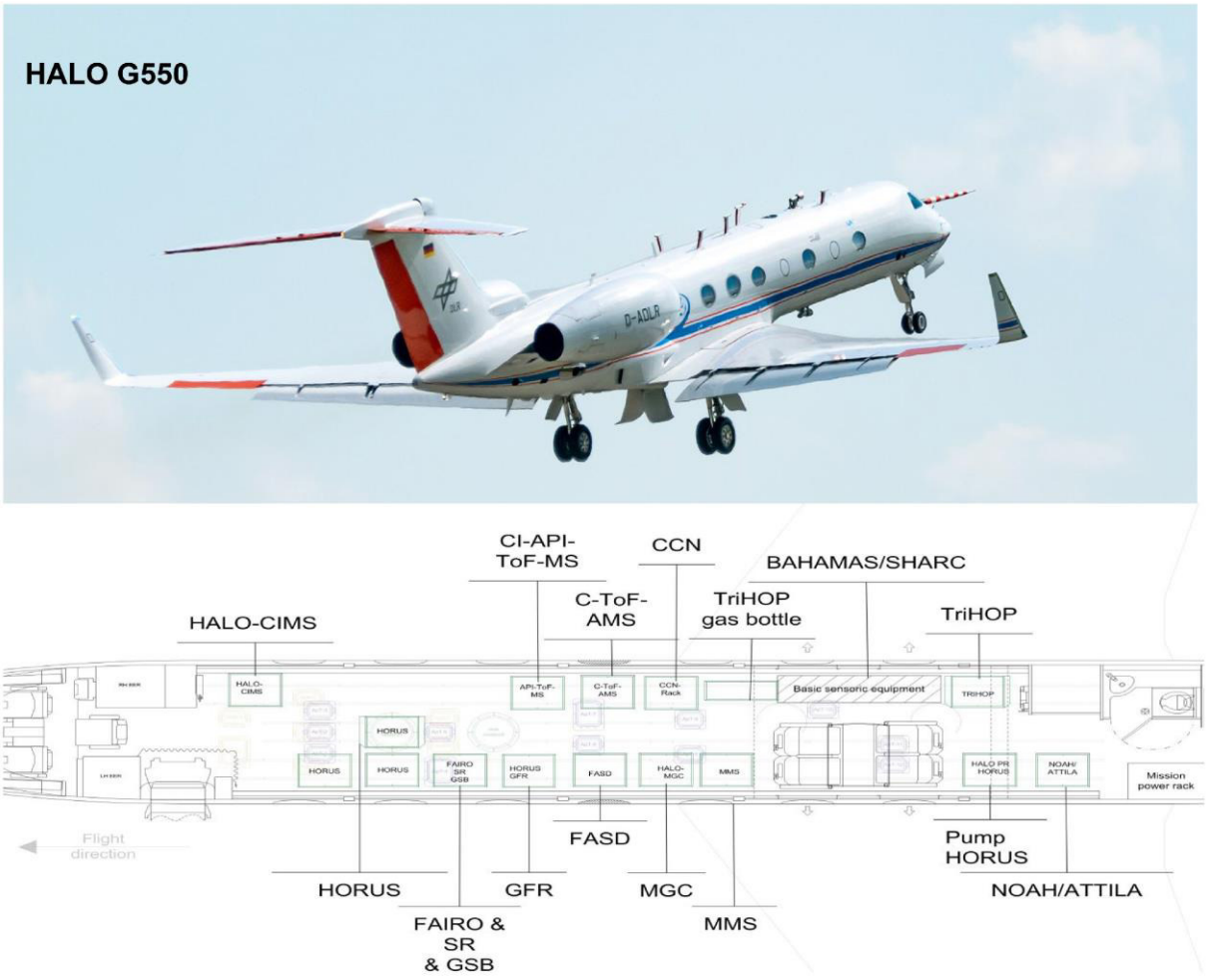

Fig. 4. (top) Photo and (bottom) cabin layout of the comprehensive trace gas and aerosol instrumentation of HALO during BLUESKY.

a single-particle soot photometer (SP2; Krüger et al. 2022; Holanda et al. 2020), and an impaction aerosol sampler with the aim to analyze the physical properties and the chemical composition of aerosol particles. Near isokinetic aerosol sampling was achieved with the HALO Aerosol Submicron Inlet (HASI) mounted on the fuselage outside of the aircraft boundary layer (Andreae et al. 2018).

Finally, upward and downward spectral actinic flux densities in the range 280–650 nm were measured by combinations of CCD spectroradiometers and optical receivers on the aircraft top and bottom fuselage (Bohn and Lohse 2017), and O_3 was measured with the Fast Airborne Ozone (FAIRO) instrument by a combination of two techniques: a UV photometer and a chemiluminescence detector (Zahn et al. 2012).

Falcon instrumentation

The Falcon instrumentation (Fig. 5 and Table 2) included aircraft tracers, stratospheric and tropospheric tracers and, in addition, a dedicated aerosol and cloud payload. The sum of gas-phase reactive nitrogen species (NO_y) was sampled through a rear-facing inlet tube and detected as NO by chemiluminescence after reduction of the reactive odd-nitrogen

Table 1. HALO instrumentation for BLUESKY. A comprehensive set of instruments or long- and short-lived trace gases and aerosol properties was integrated.

Instrument	Measured property, range	Principal investigator, institution	References
CI-API-ToF MS	H_2SO_4, $(CH_3)SO_3H$, VOCs, clusters, C2 amines, naturally occurring ions	J. Curtius, GU Frankfurt	—
I-CIMS	PAN/PAA/PPN peroxypropionylnitrate	J. Crowley, MPIC	Phillips et al. (2013)
GC-MS	NMVOC, e.g., isopropylnitrate (IPN)	J. Williams, MPIC	Bourtsoukidis et al. (2017)
PTR-MS	OVOC	J. Williams, MPIC	Edtbauer et al. (2020)
TRIHOP	Total hydroperoxides, H_2O_2, HCHO	H. Fischer, MPIC	Hottmann et al. (2020), Schiller et al. (2008)
NOAH/ATTILA	NO, NO_2/CH_4, CO	H. Fischer, MPIC	Tadic et al. (2021)
HORUS	OH/HO_2	H. Harder, MPIC	Marno et al. (2020)
C-ToF-AMS	Submicron aerosol particle composition (nonrefractory)	J. Schneider, MPIC	Drewnick et al. (2005), Schmale et al. (2010), Schulz et al. (2018)
FASD (CPCs, UHSAS, OPC)	Aerosol number and size distribution	M. Pöhlker, MPIC	
CCN-Rack (CCNC, SP2, impactor)	CCN, BC, aerosol impactor	M. Pöhlker/U. Pöschl, MPIC	Andreae et al. (2018), Holanda et al. (2020), Krüger et al. (2022)
FAIRO	O_3	A. Zahn, KIT	Zahn et al. (2012)
HALO-SR	Actinic flux density, 280–650 nm	B. Bohn, FZJ	Bohn and Lohse (2017)
BAHAMAS	Pressure, temperature, wind, humidity, TAS, aircraft position, altitude	A. Giez, DLR	—
SHARC	H_2O mixing ratio (gas phase)	A. Giez, DLR	—

compounds in a heated gold converter (Ziereis et al. 2022). O_3 was measured using an UV photometer (Schulte and Schlager 1996; Ziereis et al. 2000). CO, CH_4, and CO_2 were measured by cavity ring down spectroscopy (Klausner et al. 2020). The instruments were calibrated using standard mixtures which can be traced back to reference standards of the National Institute of Standards and of Global Atmosphere Watch. The accuracies of the measurements are 15% for NO_y and CO, 5% for O_3, 0.1% for CH_4, and 0.02% for CO_2. The atmospheric chemical ionization mass spectrometer (AIMS) uses SF_5^- reagent ions for the detection of upper tropospheric and stratospheric concentrations of gaseous SO_2, hydrogen chloride (HCl), nitric acid (HNO_3), and chlorine nitrate ($ClONO_2$) (Voigt et al. 2014; Jurkat et al. 2016, 2017; Marsing et al. 2019).

Water vapor distribution was measured with the accurate frost point hygrometer CR2 (Voigt et al. 2010; Kaufmann et al. 2014; Heller et al. 2017) and the liquid or ice water content with the tunable diode laser water vapor analyzer (WARAN) instrument (Kaufmann et al. 2018). Aerosol number concentrations were detected with a set of CPCs with different cutoff diameters of 5, 18, and 50 nm facilitated by different temperature settings and diffusion screen separators (Fiebig et al. 2005; Feldpausch et al. 2006) and a Particle Soot Absorption Photometer (PSAP) measuring aerosol optical properties at three wavelengths of 467, 530, and 660 nm (Virkkula et al. 2005; Virkkula 2010).

Two additional aerosol instruments and two cloud probes were installed in wing stations on the Falcon, including the cloud, aerosol, and precipitation probe (CAPS) (Baumgardner et al. 2004; Voigt et al. 2017) and the cloud and aerosol spectrometer with polarization (CAS-DPOL) (Baumgardner et al. 2004; Taylor et al. 2019; Kleine et al. 2018), as well as two optical particle spectrometers, the UHSAS and Passive Cavity Aerosol Spectrometer Probe (PCASP) (Voigt et al. 2021).

BLUESKY flight strategy and scope

After approximately 6 weeks of aircraft and payload preparation, the Falcon took off for the first instrument test flight on 16 May 2020. The first HALO instrument test flight followed 5 days later.

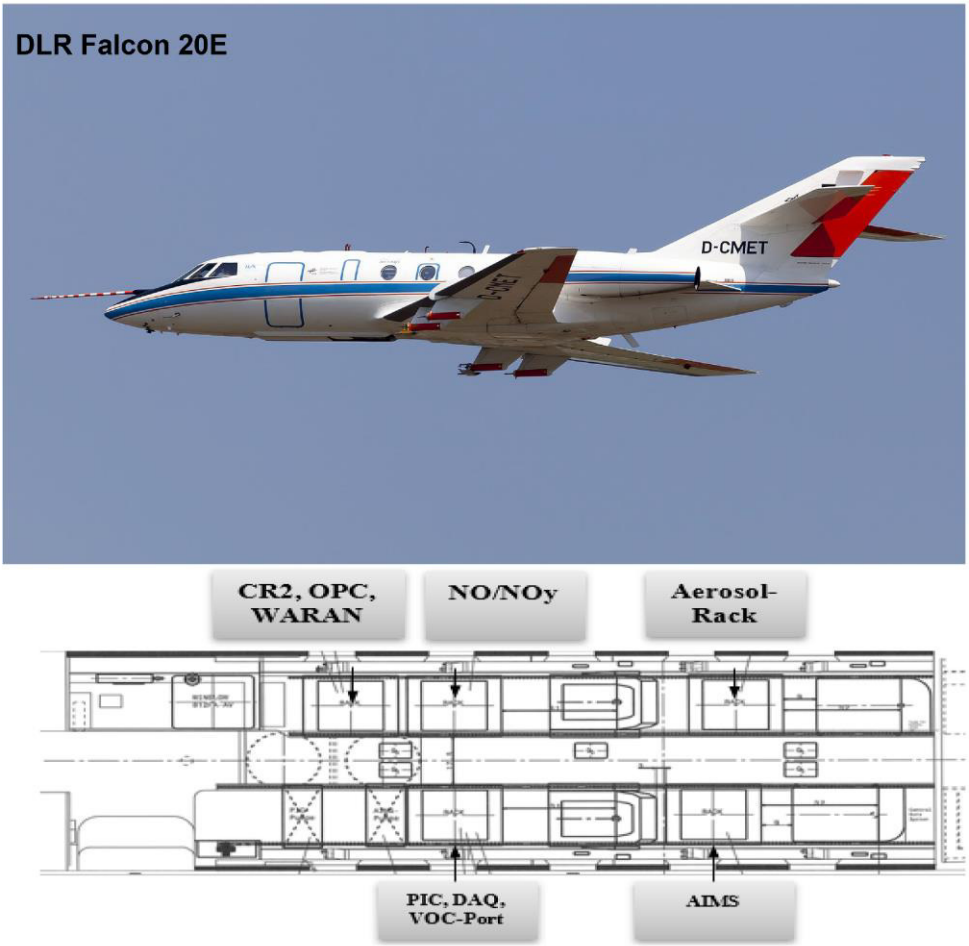

Fig. 5. (top) Photo and (bottom) cabin layout of the trace gas, aerosol, and cloud instrumentation of the DLR Falcon 20 E during BLUESKY.

Both aircraft flew five missions together, then the Falcon had to return for maintenance while HALO continued with three more mission flights until 9 June 2020. Altogether 20 flights were performed during BLUESKY, 12 with the Falcon and 8 with HALO, albeit with different flight lengths of up to 2,860 km with the Falcon and up to 6,734 km with HALO, see also Table 3.

Extensive measurements were performed over Germany, western Europe, and the Atlantic from 13°E to 14°W and from 38° to 55°N as shown in Fig. 6. During survey flights, many profiles of atmospheric composition were made near large cities.

The strict travel restrictions led to strongly reduced air traffic and the DLR research aircraft were for the first time allowed to perform low-approach maneuvers down to 3 m altitude above ground at large international passenger airports like Frankfurt, Berlin-Tegel, and Milan, as well as Amsterdam, Barcelona, Madrid, Marseille, and Rome.

Many profiles were measured near large cities and the composition of the atmosphere was probed from the boundary layer to the lower stratosphere. We also measured spatially highly resolved data of a multitude of trace species in the upper troposphere and lower stratosphere, in order to investigate changes in atmospheric composition caused mainly by aviation. Observations of the reactive nitrogen and ozone distributions in the northern Atlantic flight corridor and over Europe were performed. According to Eurocontrol, during normal operation in 2019, up to 25,000

Table 2. Falcon instrumentation for BLUESKY. A suite of advanced trace gas, aerosol, and cloud probes was integrated into the cabin and wing stations.

Instrument	Measured property, range	Principal investigator, institution	References
NO_y chemiluminescence detector	NO_y, aircraft tracer, 5 ppt–60 ppb	Schlager, DLR	Schulte and Schlager, (1996), Ziereis et al. (2000, 2021)
UV absorption photometer	O_3	Schlager, DLR	Schlager et al. (1997)
Cavity ring down instrument	CO_2, CH_4, CO	Schlager, DLR	Klausner et al. (2020)
AIMS chemical ionization mass spectrometer	HNO_3, HONO, SO_2, HCl, 5 ppt to 5 ppbv	Voigt, Jurkat, DLR	Voigt et al. (2014), Jurkat et al. (2016, 2017)
CR2, Frostpoint hygrometer	H_2O, gas phase water, 1–1,000 ppm	Heller, DLR	Voigt et al. (2010), Heller et al. (2017)
WARAN, TDL hygrometer	H_2O, total water, 50–40,000 ppm	Heller, DLR	Voigt et al. (2011), Kaufmann et al. (2018)
Aerosol rack with CPCs, OPCs, PSAP	Size distribution of total and nonvolatile aerosol, 4 nm–2 μm, absorption	Sauer, DLR	Fiebig et al. (2005), Voigt et al. (2021)
Meteorological Sensor System	Temperature, u and v wind components, meteorological and aircraft state parameters	Mallaun, DLR	
AIMS, HNO_3, SO_2, HCl mass spectrometer	H_2O, gas-phase water, 1–500 ppm	Voigt/Kaufmann, DLR	Jurkat et al. (2017), Marsing et al. (2019)
CAS-DPOL Cloud and Aerosol Spectrometer	Particle size distribution, polarization, 0.6–50 μm	Voigt, DLR	Voigt et al. (2011), Kleine et al. (2018), Voigt et al. (2021)
CAS-DPOL/CIP (CAPS) Cloud and Aerosol Spectrometer	Particle size distribution, shape, polarization, CAS 0.6–50 μm; CIP 15–960 μm	Voigt, DLR	Voigt et al. (2017), Kleine et al. (2018)
PCASP-100X Passive Cavity Aerosol Spectrometer Probe	Aerosol size distribution, 0.12–3.5 μm	Sauer, DLR	Voigt et al. (2017)
UHSAS Ultra-High-Sensitivity Aerosol Spectrometer	Dry particle size distribution 60–1,000 nm	Sauer, DLR	Voigt et al. (2017)

flights were performed per day in Europe (Fig. 2). The number of flights was greatly reduced, by more than 80%, in the early lockdown phase and gradually recovered to a reduction of about 30% in summer 2021. This also allowed investigation of aviation induced changes in properties of cirrus cloud as observed from satellite. A third specific focus was the effect of shutdown on strongly populated industrial areas like the Ruhr area in Germany and the Milan region in Italy. In both of them, NO_2 levels were strongly enhanced, as urban emissions are captured in a river valley and therefore the exchange with the free-tropospheric air masses is reduced. Satellite observations of tropospheric NO_2 from GOME-2 and TROPOMI are presented in the next section.

Tropospheric NO_2 changes in early lockdown phase during BLUESKY 2020

Tropospheric NO_2 is a representative short-lived tracer for anthropogenic emissions from transport, industrial processes, and energy production (Müller et al. 2022). While the transport sector and in particular diesel engines are often the prevailing source of nitrogen dioxide in the boundary layer, there are also natural emissions from soil (Lu et al. 2021) and lightning (Pérez-Invernón et al. 2022) that can contribute to the boundary layer NO_2 concentrations. Here we use satellite observations from the GOME-2 (Munro et al. 2016) and the TROPOMI (Veefkind et al. 2012) instruments to motivate the BLUESKY campaign, to give a general overview on the changes of the short-lived tracer NO_2 and to support the planning of individual flight tracks. TROPOMI aboard *Sentinel-5 Precursor* (2017 to the present) is a nadir-scanning spectrometer with an equator crossing time at 1330 local solar time and daily global coverage. Retrievals of tropospheric NO_2 vertical column densities have a spatial resolution of 3.5 km × 5.5 km (van Geffen et al. 2019). Each orbit (level 2 products of version 1.2) was sampled onto a grid of 0.01° × 0.01° longitude–latitude resolution to enable a consistent averaging and data

Table 3. Overview of the BLUESKY flights of Falcon and HALO. Flight number, date, scope, target region, and flight duration are given. The Falcon flights extend from the surface to 12 km altitude and the HALO flights to 14 km altitude.

Flight No.	Date	Takeoff (UTC)	Landing (UTC)	Scope and target region	Length (km)
Falcon0	16 May 2020	0855	1145	Allgäu, Munich area	1,490
F1	19 May 2020	1045	1505	Survey of Germany, boundary layer Ruhr area: Düsseldorf, Hohenpeißenberg, Munich	2,265
F2	21 May 2020	0820	1230	Survey Germany, profiles near Berlin, Hamburg, Frankfurt, Munich	2,259
F3	22 May 2020	1030	1445	Survey Germany: Berlin, Hamburg, Köln, Frankfurt, Munich	2,227
F4	23 May 2020	0850	1130	Survey Germany: profile Berlin, Hamburg	1,508
F5	23 May 2020	1230	1540	Survey Germany, Ruhr area: Hamburg, Köln, Frankfurt, Munich	1,644
F6	26 May 2020	0950	1420	Boundary layer Milano, Italy, Switzerland, Munich	2,262
F7	28 May 2020	0740	1145	Survey Germany: Berlin, Hamburg, Frankfurt, Munich	2,145
F8	30 May 2020	0705	1120	Transfer Ireland, intercomparison HALO, North Atlantic flight tracks (NAT)	2,764
F9	30 May 2020	1210	1650	Shannon, NAT tracks, Munich, Hohenpeissenberg	2,860
F10	1 Jun 2020	0940	1355	Boundary layer Milano, Italy, Switzerland, Munich	2,097
F11	2 Jun 2020	0655	1115	Transfer Ireland, intercomparison HALO, NAT tracks, Shannon	2,798
F12	2 Jun 2020	1205	1620	Shannon, NAT tracks, intercomparison Munich	2,816
HALO 0	21 May 2020	1331	1622	TRA Allgäu, Munich area	1,404
H1	23 May 2020	0806	1439	Berlin, Frankfurt, Hamburg, Köln, Munich area	4,077
H2	26 May 2020	0759	1549	Berlin, Frankfurt, boundary layer Milan, Munich area	4,412
H3	28 May 2020	0804	1515	Berlin, Frankfurt, Hahn, Hamburg, Amsterdam, Köln, Munich area	3,874
H4	30 May 2020	0740	1622	NAT tracks	6,734
H5	2 Jun 2020	0726	1535	NAT tracks	6,436
H6	4 Jun 2020	0801	1620	France (Clermont-Ferrand, Marseille), Mediterranean Sea, Italy (Rome, Adriatic Sea, Milano)	4,738
H7	6 Jun 2020	0757	1537	France (Clermont-Ferrand, Marseille), Spain (Madrid, Barcelona)	4,374
H8	9 Jun 2020	0758	1535	France (Bordeaux, Marseille), Spain (Madrid, Mallorca)	4,652

comparison (Müller et al. 2022). Although observations from TROPOMI currently exhibit the highest spatial resolution to study regional effects on the atmospheric composition the data are available from April 2018 onward only and not yet suitable to examine longer-term variability.

To better analyze the deviation of tropospheric NO_2 levels in 2020 from previous years, GOME-2 data were examined from 2015 to 2020. GOME-2 aboard *MetOp-B* (2012 to the present) is a nadir-scanning spectrometer, which measures at around 0930 local solar time equator crossing time and has a ground pixel size of 80 km × 40 km (Munro et al. 2016). Level 2 offline products of version 4.8 were sampled onto a grid of 0.25° × 0.25° geographical resolution.

Long-term analyses of global satellite data show that NO_2 pollution can vary strongly from year to year due to weather conditions (Zhou et al. 2012; Georgoulias et al. 2019). To reduce this source of variability and uncertainty, observations from GOME-2B for 2020 are compared to the mean from 2015 to 2019 as reference (Fig. 7). For each year the BLUESKY period was considered accordingly. Although the multiannual mean provides a better statistical baseline to quantify possible lockdown effects in 2020, the 3-week sampling period is still short regarding meteorological variability Reductions in tropospheric NO_2 are evident throughout Europe, the United States, and Asia (Fig. 7). The global mean values for the BLUESKY period suggest a 12% reduction in global NO_2 in 2020 with respect to the 2015–19 average. Large cities and conurbations show the highest reductions in NO_2 of up to 55%.

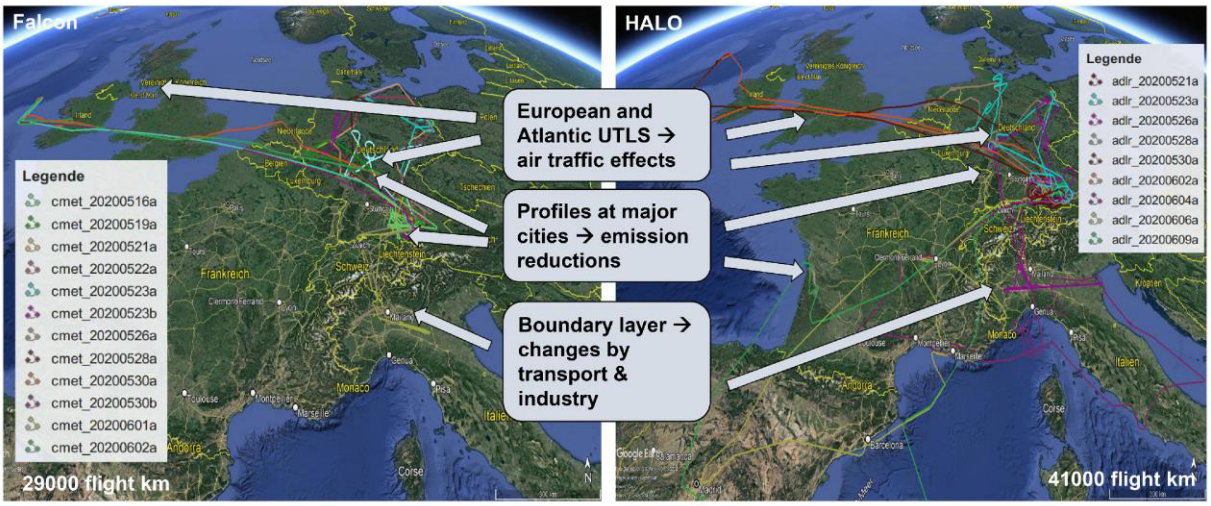

Fig. 6. Scope and flight path of HALO and Falcon during BLUESKY. In order to probe the atmospheric composition during the COVID-19 lockdown, 41,000 km were flown by HALO and 29,000 km by the Falcon from 16 May to 9 Jun 2020.

In Germany, the measures to limit the spread of the coronavirus started with strong social restrictions and a first lockdown on 22 March 2020. On 15 April 2020, the German government decided to gradually reopen public life. In terms of NO_2 levels, a strong reduction was detected from 22 March to 15 April 2020, and from 15 April the NO_2 levels increased gradually (Erbertseder and Loyola 2020).

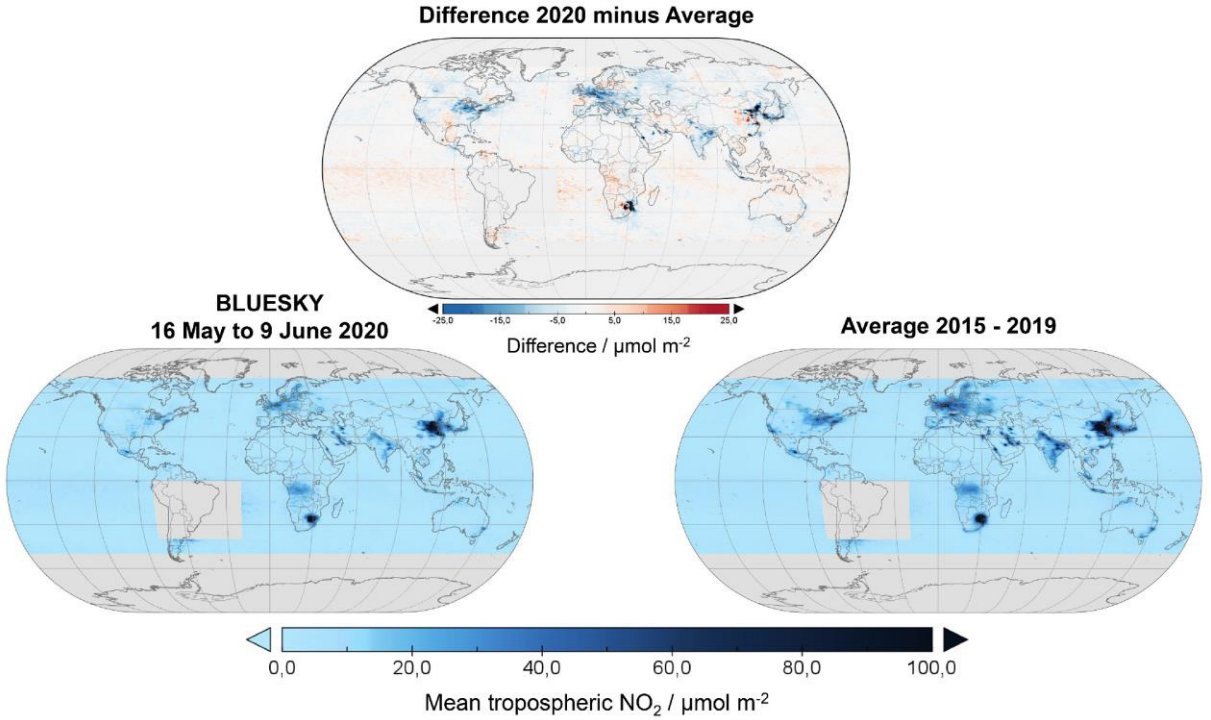

Fig. 7. (top) Differences in tropospheric NO_2 between 2020 and the baseline mean 2015–19 during the BLUESKY period from 16 May to 9 Jun 2020 as observed by MetOp/GOME-2B. (bottom) The averages for the corresponding periods. The area of the South Atlantic anomaly covering large parts of South America is masked.

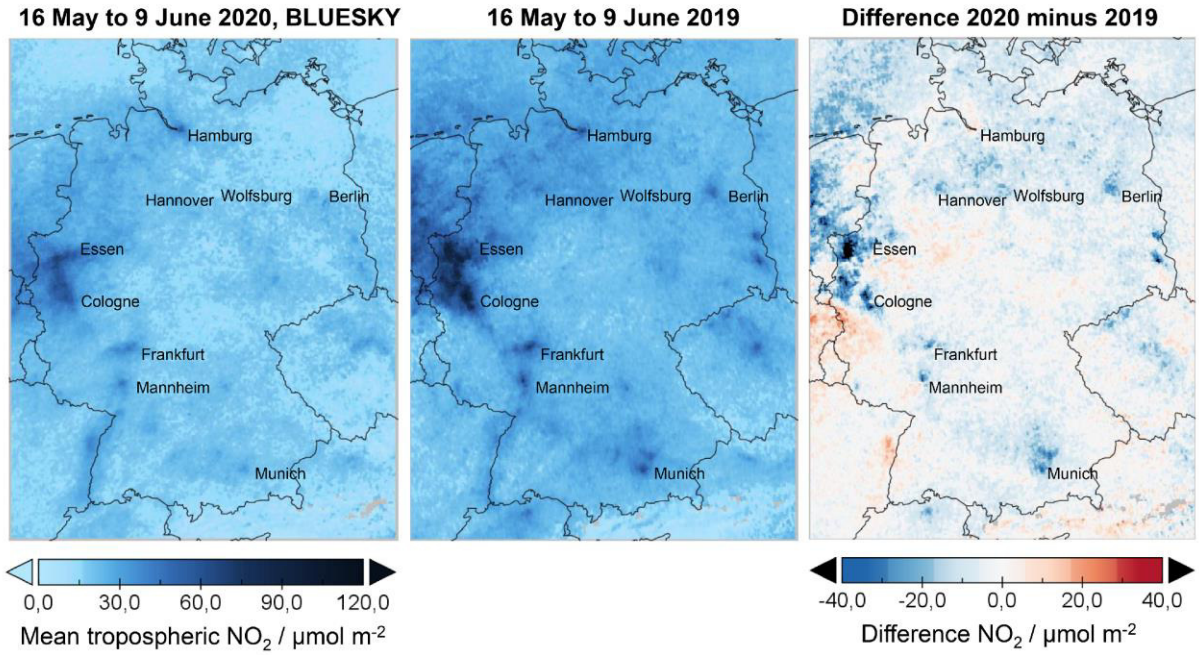

Fig. 8. Mean tropospheric NO_2 vertical column densities over Germany for (left) 2020 and (center) 2019 averaged over the BLUESKY period from 16 May to 9 Jun. The means were derived from *Sentinel-5P*/TROPOMI level 2 data. (right) The difference of 2020 minus 2019.

Tropospheric NO_2 densities monitored by *Sentinel-5P*/TROPOMI overpasses in 2019 and 2020 were used to support the flight planning. Figure 8 shows mean tropospheric NO_2 densities for 2020 and 2019 averaged over the respective BLUESKY period from 16 May to 9 June 2020. For the selected area, the mean NO_2 values are 26.8 ± 8.9 μmol m^{-2} and 31.7 ± 11.2 μmol m^{-2} for 2020 and 2019, respectively. The reduction in 2020 is evident throughout Germany and corresponds to an overall decrease of tropospheric NO_2 in 2020 by about 15%. The decrease is pronounced in the Ruhr area and in urban areas such as Cologne, Frankfurt, Munich, and Berlin with reductions between 21% and 38%, attributable to strongly reduced road traffic and industrial production, but also to lower NO_2 levels in 2020 before the lockdown and meteorological conditions that are not further disentangled here. A detailed analysis of the lockdown effects on tropospheric NO_2 and their statistical significance considering source attributions of different sectors (Petit et al. 2021; Feng et al. 2021; Putaud et al. 2021), adjustments to multiannual trend effects (Bekbulat et al. 2020), or corrections for meteorological influences (Zhou et al. 2012; Goldberg et al. 2020) is out of scope of this paper. However, the presented findings are in the range of more detailed studies that consider wind corrections and adjustments to trend effects, but focus on different periods of the lockdown (e.g., Liu et al. 2020; Goldberg et al. 2020).

Highlights from the BLUESKY mission

We briefly present first results from the BLUESKY mission and show tropospheric profiles of trace species and aerosol affected by anthropogenic emissions, investigate the blue color of the sky and address effects from reduced air traffic on cirrus.

Reduced reactive nitrogen and carbon monoxide in Frankfurt city profiles and in the industrial boundary layer. Profiles taken over Frankfurt can be compared to climatological datasets measured by instrumented in-service passenger aircraft starting or landing in Frankfurt.

Figure 9 shows vertical profiles of NO_y, CO, and O_3 mixing ratios measured in the Frankfurt area by the Falcon on 28 May 2020 and related model results. The profiles are compared to median profiles derived from a climatology of 11 years of Measurement of Ozone and Water Vapor by Airbus In-Service Aircraft (MOZAIC) measurements at the same time of year (Petzoldt 2010). The MOZAIC dataset includes over 3,000 vertical profiles over Frankfurt covering a multitude of different meteorological situations in the same season. For comparison, average vertical profiles of CO and O_3 sampled by In-service Aircraft for a Global Observing System (IAGOS) in March–May during 2016–19 over Frankfurt at altitudes between 2 and 8 km (Clark et al. 2021) are also shown.

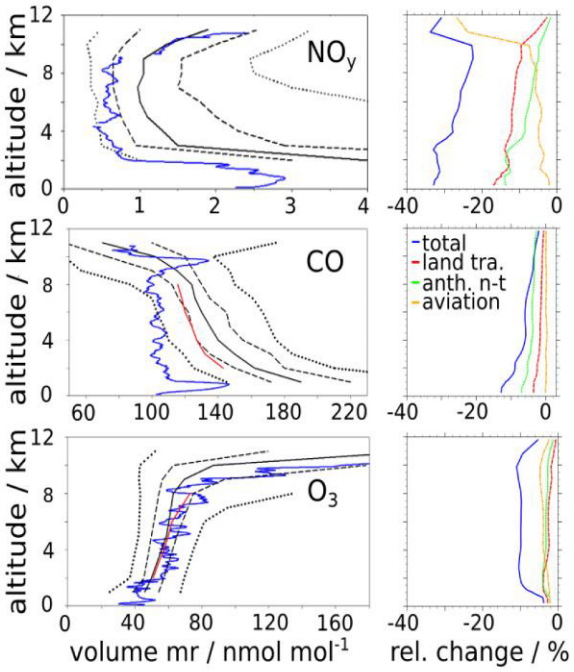

Fig. 9. (left) Vertical profiles of (top) NO_y, (middle) CO, and (bottom) O_3 measured during BLUESKY on 28 May 2020 in the Frankfurt area (blue lines), medians (black solid lines), and 5th, 25th, 75th, and 95th percentiles (black dotted lines) of Frankfurt profile data in spring from a climatology of MOZAIC data sampled from 1994 to 2005 (Petzoldt 2010) and average CO and O_3 profiles over Frankfurt from IAGOS (red lines) for spring 2016–19 (Clark et al. 2021). (right) Vertical profiles of the relative changes (%) for (top) NO_y, (middle) CO, and (bottom) O_3 between the COVID-19 and the business-as-usual simulation over the Frankfurt area at 1000 UTC 28 May. The blue line shows the total change, and red, green, and orange indicate the changes attributed to the emission categories land transport (land tra.), anthropogenic nontraffic (anth. n-t), and aviation, respectively.

The measured NO_y and CO mixing ratios in the lower and middle troposphere are significantly lower than the median MOZAIC values by 40%–70% and 20%–40%, respectively, and the CO mixing ratios are also lower than the average IAGOS CO profile. The observed O_3 concentrations agree with the median MOZAIC and IAGOS profiles. BLUESKY NO_y and CO concentrations over Frankfurt, however, are close to the 5th percentiles, and only 5% of the MOZAIC data are lower than the BLUESKY profiles. These differences can in part be caused by the meteorological conditions prevailing in May and June 2020 and by COVID-19 emissions reductions.

To better distinguish emission reductions from other factors, we add simulated vertical profiles on the right side of Fig. 9, which show the relative difference between a business as usual simulation and a COVID-19 simulation with a reduced emission scenario [see Mertens et al. (2020) for a full description of the simulations] of NO_y, CO, and O_3 mixing ratio around Frankfurt as simulated by MECO(n). Besides the total difference, the differences attributed to the emission sources land transport, anthropogenic nontraffic, and aviation are shown. In fact, the COVID-19 emission reductions assumed in the model simulations lead to a reduction of O_3 of up to 10%, for CO of up to 13%, and for NO_y of up to 34%. The NO_y reduction near ground are mainly due to reduction of land transport emissions, while reductions above 10 km are mainly attributed to changes of aircraft emissions. This indicates that the observed lower NO_y and CO mixing ratios over Frankfurt can to a large extent be attributed to the reduction

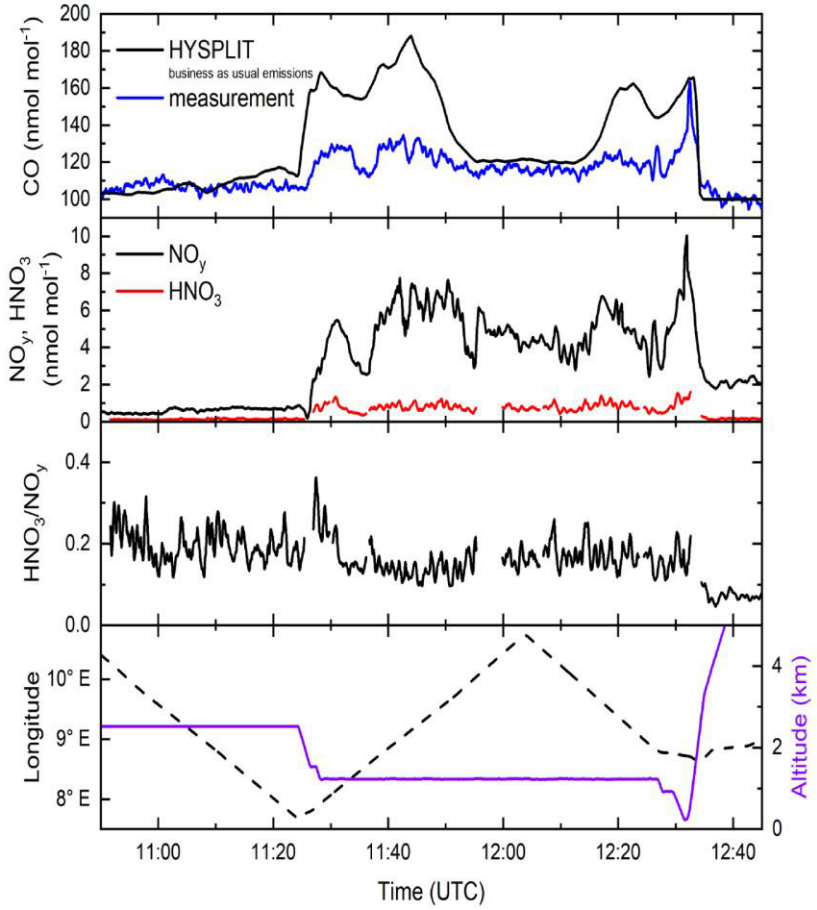

Fig. 10. (top) Falcon measurements of CO volume mixing ratios in the western part of the industrial Po valley near Milan in Italy (blue) on 1 Jun 2020 compared to HYSPLIT simulations with business as usual emissions (black). (middle) Falcon measurements of NO_y and HNO_3 and the relative fraction of HNO_3 in the total gaseous reactive nitrogen budget. (bottom) Longitude (black dashed) and altitude (violet) of the Falcon flight path, indicating the east–west shuttle with vertical steps, terminating in a low approach at the Milan Malpensa airport.

of emissions from the transport sector (land transport and aviation) and to anthropogenic nontraffic COVID-19 emission reductions.

It is interesting to note, that the mixing ratios of the IAGOS average CO profile for the years 2016–19 are about 7% lower than the MOZAIC average profiles for the years 1994–2005, which corresponds to the observed rate of decrease in CO in the Northern Hemispheric troposphere (Clark et al. 2021). There may be a variety of reasons for the simulated 10% O_3 reduction derived by the MECO(n) model for the O_3 profile on 28 May 2020. Uncertainties in the dynamics of the model, temporal or spatial shifts of patterns in the model compared to the observations, uncertainties in the emissions may contribute to this model result. A deeper analysis is required to better assess these deviations using more extensive model simulations as shown in the "Highlights from the BLUESKY mission" section.

Multiple Falcon and HALO flights were also performed in the industrial Po valley in Italy, a pollution hot spot in Europe, where pollution from large cities, e.g., Milan, are trapped in the river valley and by the Alps. As an example, Fig. 10 shows a Falcon measurement transect through the boundary layer in the western part of the Po valley between 46.6°N,

9°E and 45°N, 10.4°E on 1 June 2020, covering the major industrial area of Milan. Measured CO volume mixing ratio are compared to HYSPLIT simulations interpolated to the Falcon flight path. The HYSPLIT simulations are based on the EDGAR emission inventory for CO of the Po valley region with business-as-usual emissions for the year 2017 adjusted to CO observations during the intense HALO measurements in the Italian Po valley during the Effect of Megacities on the transport and transformation of pollutants on the Regional to Global scales (EMERGE) campaign (Andrés Hernández et al. 2022). The observed CO mixing ratios in the major polluted areas during BLUESKY are lower by about 30% compared to the HYSPLIT simulations with no emission reductions for traffic and industry. The HYSPLIT trajectories enable a detailed allocation of emission inventory sources to the observed pollutant concentrations in the boundary layer. In future studies this will also comprise other pollutants such as nitrogen oxides with origins from several sectors. The example in Fig. 10 shows how concentrations of measured NO_y and HNO_3 vary by about one order of magnitude when descending from 2.5 to 1.2 km altitude. Still the HNO_3 relative fraction remains stable, as can be expected from rapid airmass exchange. This instrument performance allows the investigation of the propagation of (reduced) trace gas and aerosol emissions into the free troposphere.

Profiles of other anthropogenic and natural tracers. During BLUESKY, the I-CIMS and GC-MS instruments on board HALO measured two C3-organic nitrates: peroxypropionylnitrate, $CH_3CH_2C(O)OONO_2$, (PPN), and isopropylnitrate, $CH_3CH(ONO_2)CH_3$, (IPN). Both nitrates are formed during the OH-initiated oxidation of propane and are thus closely tied to anthropogenic emissions. PPN is formed subsequent to H-atom abstraction by OH from the CH_3 groups in propane and further oxidation. IPN is formed when the H abstraction takes place at the central C atom from the reaction of the isopropylperoxy radical with NO, albeit at low yield. The vertical profiles of PPN and IPN (Fig. 11, campaign average) indicate maximum values in the boundary layer, which reflects the fact that both are formed in the chemical degradation

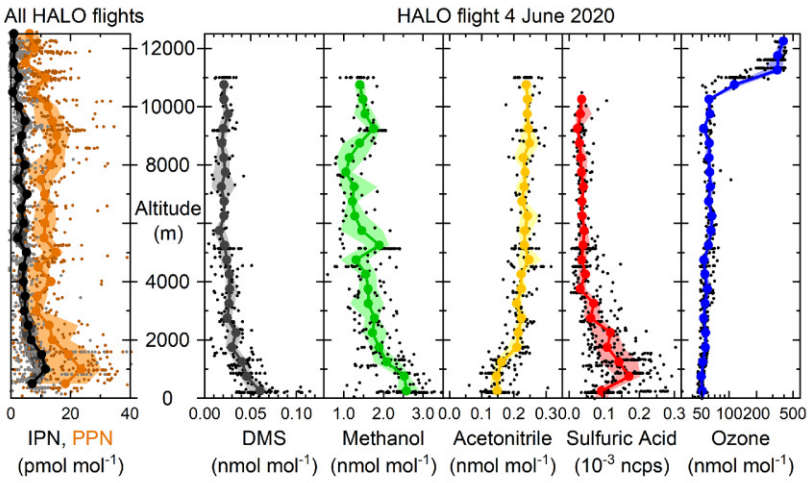

Fig. 11. (left) Vertical profiles of peroxypropionylnitrate [PPN; $CH_3CH_2C(O)OONO_2$] and isopropylnitrate [IPN; $CH_3CH(ONO_2)CH_3$] during all BLUESKY flights measured using the I-CIMS and the GC-MS instruments on HALO. (right) Vertical profiles measured on HALO on 4 Jun 2020 of dimethyl sulfide DMS, methanol, and acetonitrile measured by the GC-MS, gaseous sulfuric acid (H_2SO_4) measured by the CI-API-TOF, and O_3 measured by FAIRO. The flight path on 4 Jun 2020 covered southern Germany, France, Italy, and the Mediterranean. Dots represent individual measurements with 30 s time resolution for H_2SO_4 and O_3 and with 1 min resolution for the GC-MS data; solid lines represent data the median averaged to 500 m altitude bins and the shaded areas represent the corresponding quartiles. H_2SO_4 data are shown as normalized counts per second (NCPS).

of propane emitted during anthropogenic activity at ground level. PPN has a broad, second maximum at around 8 km while IPN decreases quasi monotonically through the free and upper troposphere. The divergence in their vertical profiles can be understood in terms of their chemically different loss processes and different altitude dependent atmospheric lifetimes. PPN is thermally unstable at low altitudes, but reacts only slowly with OH so that its lifetime (mainly controlled by photolysis) is several months at the low temperatures of the upper troposphere. In contrast, IPN is stable with respect to both thermal decomposition and photolysis and is lost mainly by reaction with OH.

Also, organic compounds like acetonitrile and methanol and sulfur species like dimethylsulfide (DMS) were measured by the GC-MS and the PTR-Mass Spectrometer system on board HALO. Figure 11 in addition shows tropospheric concentrations of acetonitrile, methanol, and DMS for the HALO flight on 4 June 2020 over Germany, France, Italy, and the Mediterranean. Stratospheric data were separated and are treated separately in light of extensive ozone tests that were performed in the laboratory following BLUESKY. During HALO flight 6 (violet color in Fig. 6) the aircraft entered the marine boundary layer over the Mediterranean Sea and therefore DMS is enhanced at low altitudes caused by marine emissions of DMS, while acetonitrile is depleted as it is taken up at the sea surface. Methanol, a volatile organic compound of primarily biogenic origin, shows considerable structure caused by cloud outflow.

On the same flight, gaseous sulfuric acid was measured with the newly developed chemical ionization–atmospheric pressure interface time-of-flight mass spectrometer (CI-API-TOF) with a constant pressure inlet by reaction with nitrate ions. The inlet system was designed in a way to enable a high flow rate and to minimize sampling losses of nonvolatile compounds like sulfuric acid and highly oxygenated organic molecules. Low concentrations of gaseous H_2SO_4 were measured in the boundary layer and the free troposphere over central Europe. Here we show count rates respective for H_2SO_4 as the calibration of the pressure dependence of the mass spectrometer signal is ongoing. The data will be used to investigate the budget and the partitioning of the sulfur species, as also SO_2 and sulfate aerosol were measured on Falcon and HALO, respectively.

SO_2 was measured at cruise altitudes in the upper troposphere and lower stratosphere (UTLS) by the AIMS mass spectrometer on board the Falcon in order to investigate the contribution of anthropogenic and natural sources to the UTLS SO_2 budget. In 10–14 km altitude in the midlatitudes, SO_2 has a short life time of 13 ± 2 days (Höpfner et al. 2015). Figure 12 shows the

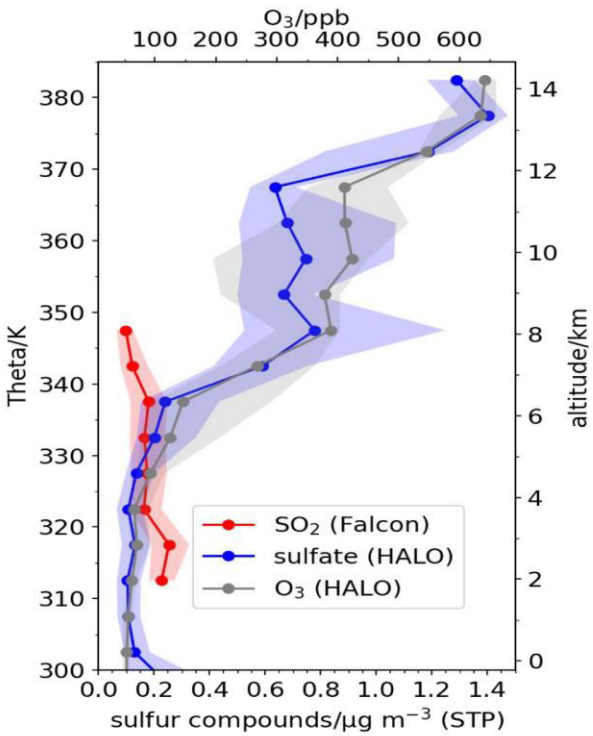

Fig. 12. Profiles of median SO_2 (red), sulfate (blue), and O_3 (gray) concentrations as well as quartiles (shaded) vs potential temperature. The data from all BLUESKY flights are plotted in 5 K bins. SO_2 was measured by AIMS on the Falcon, while sulfate and O_3 were measured on HALO.

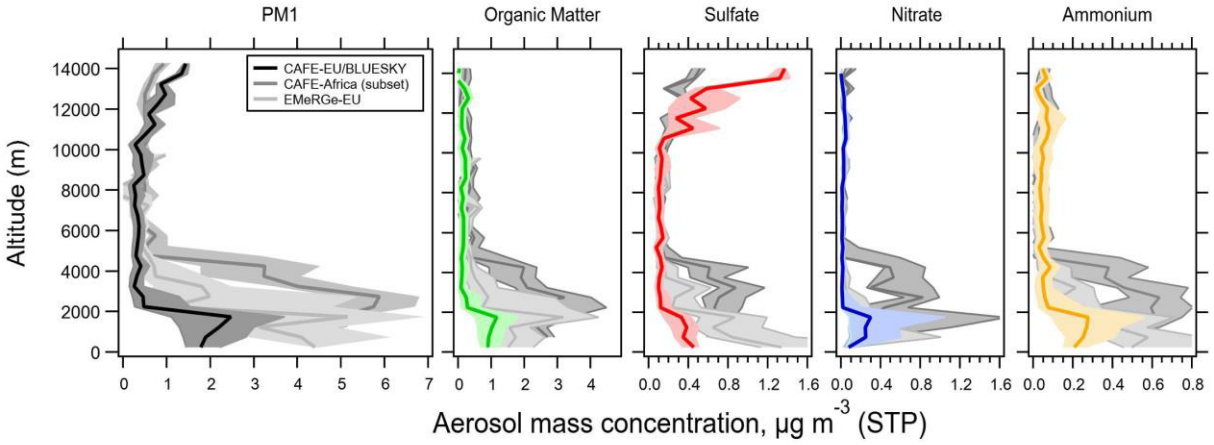

Fig. 13. Vertical profiles of total aerosol mass concentrations (including refractory black carbon) and aerosol mass concentrations of organics, sulfate, nitrate, and ammonium during BLUESKY (black and colors, medians and quartiles). Also shown are data from previous HALO missions over Europe: EMERGE-EU (light gray), conducted in July 2017 in the same area, and CAFE-Africa (gray), conducted between July and September 2018. From CAFE-Africa, only data measured in the same area as the other two missions were used (38°–57°N, 14°W–16°E).

median and quartiles of SO_2 profiles in the UTLS during the entire BLUESKY campaign for flight altitudes between 7.5 and 12.5 km. The maximum height is restricted by the Falcon flight altitude, while the lower limit is caused by a water vapor interference in the SO_2 measurement. The median SO_2 mixing ratio decreases with altitude from around 0.22 to 0.12 $\mu g\ m^{-3}$. SO_2 has been measured at similar altitudes above Europe in previous experiments: During the ITOP campaign in summer 2004, Speidel et al. (2007) reported 0.1 $\mu g\ m^{-3}$ SO_2 for high altitudes (<10.2 km) over Europe as confirmed by stratospheric background SO_2 measurements in August 2008 during CONCERT (Jurkat et al. 2010). Williamson et al. (2021) reported lower SO_2 concentrations over the Northern Hemispheric Pacific during the ATOM mission with values of 0.04 $\mu g\ m^{-3}$ in the upper troposphere and 0.07 $\mu g\ m^{-3}$ in the lower stratosphere. Overall, the BLUESKY SO_2 observations are in the upper range of reported background SO_2 concentrations in the continental UTLS. Nevertheless, the significant reductions in air traffic during the lockdown led to an SO_2 level lower than the 2008 background in aircraft flight corridors of 0.26 $\mu g\ m^{-3}$ (Jurkat et al. 2010). In the stratosphere, the SO_2 concentrations are much smaller than sulfate in aerosol, which is still enhanced from volcanic eruptions (see also Fig. 13).

Reductions of aerosol number concentration and aerosol mass in the troposphere. To study the possible influence of reduced ground and aircraft emissions during lockdown on aerosol mass concentrations, we compared the BLUESKY data to previous datasets obtained over Europe, namely, the EMERGE-EU campaign in July 2017 (Andrés Hernández et al. 2022) and the Chemistry of the Atmosphere–Field Experiment in Africa (CAFE-Africa) test and ferry flights conducted over Europe between July and August 2018. Figure 13 shows medians and quartiles of the parameters measured with the C-TOF-AMS on board HALO. For all four measured species, the concentrations measured in 2020 were lower, while in 2018 they were higher. For organics and sulfate, the EMERGE concentrations in 2017 were significantly higher than in 2020, while nitrate and ammonium show comparable values. Although the variability in the datasets is large, the consistent reductions indicated from the 2020 data for all four aerosol components suggests that they were at least partly due to diminished emissions during the lockdown. By combining our black carbon measurements with EMAC simulations we found a 40% reduction in black carbon mass related to the lockdown effects (Krüger et al. 2022).

For organic aerosol mass, this finding holds also for the free troposphere above 5 km altitude, whereas for sulfate, nitrate, and ammonium the free-tropospheric data are comparable for all three datasets.

A recent model study using the EMAC model with reduced emission scenarios is able to reproduce the observations during the BLUESKY campaign (Reifenberg et al. 2022). Anthropogenic aerosol precursor gases include SO_2, NO_x, and VOCs. Although the emissions reductions had slightly leveled off in May and June compared to April 2020 (Guevara et al. 2021), still the NO_x reduction was highest with about 10%–20%, followed by SO_2 (9%–12%) and VOCs (2%–6%). Ammonia originates mainly from agriculture; therefore, no significant reduction was observed. However, the amount of NH_4 in the aerosol is determined by available acids (HNO_3 and H_2SO_4) to react with NH_3 to ammonium nitrate and sulfate. Direct $PM_{2.5}$ emissions were reduced only by 6%–9%. The finding that the observed differences in aerosol mass concentrations are much larger that the reduction in direct emissions suggests that secondary aerosol formation is the most important aerosol source over Europe. Below 2 km, sulfate and organics show a higher reduction compared to the previous campaigns than nitrate, indicating that the anthropogenic emissions of SO_2 and VOCs play a larger role for secondary aerosol formation than anthropogenic NO_x plays for secondary nitrate formation.

As discussed above, the strong increase of sulfate aerosol above 10 km and the higher sulfate mass concentrations observed in 2020 compared to 2018 may in part be due to the Raikoke volcanic eruption in June 2019 (Muser et al. 2020; de Leeuw et al. 2021), but also other, minor volcanic eruptions are likely to play a role.

Figure 14 shows profiles of fine mode aerosol number concentrations for particle sizes above 18 nm from the Falcon measurements during BLUESKY and the long-term observations from the In-service Aircraft for a Global Observing System–Civil Aircraft for the Regular Investigation of the Atmosphere Based on an Instrument Container (IAGOS-CARIBIC) project. The IAGOS-CARIBIC data shown here only include flights during the months May and June between 2005 and 2015. Profile data are restricted to central Europe between 8.8°W and 28°E and at latitudes between 40° and 66°N.

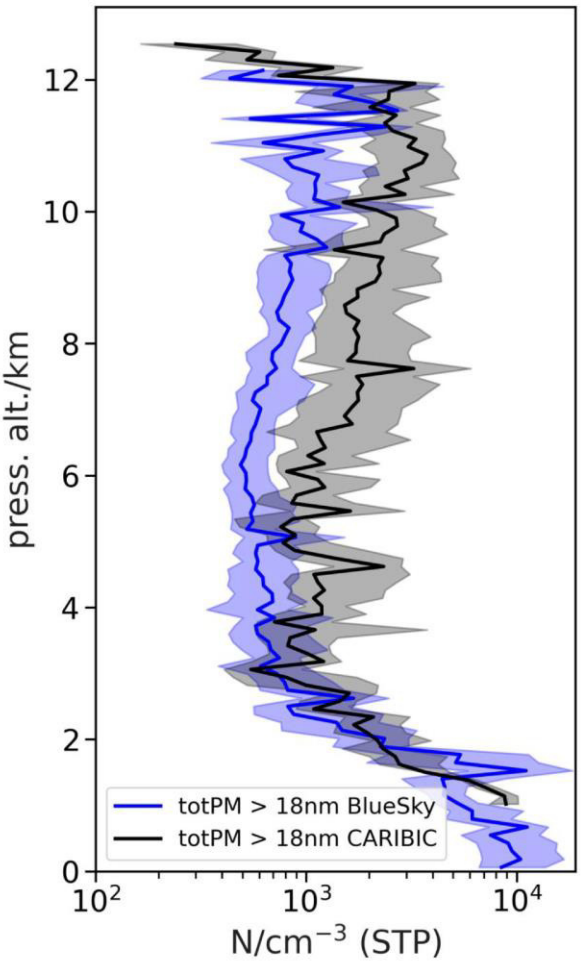

Fig. 14. Profiles of median and quartiles of aerosol number concentration (>18 nm) measured during BLUESKY (blue) in comparison to measurements performed by the CARIBIC-IAGOS project (black) during May and June between 2005 and 2015 in the same region (40°–66°N, 28°E–8.8°W).

The median BLUESKY profile shows a clear reduction of the aerosol number concentration of 30%–70% in the free troposphere above 4 km altitude. At the tropopause above 11 km, the difference becomes less prominent, although the BLUESKY median concentrations are still mostly below the CARIBIC values, even though the IAGOS-CARIBIC data were measured 5– 15 years before BLUESKY with respective lower anthropogenic emissions. It is not possible to quantify an effect in the boundary layer although it has to be kept in mind that the BLUESKY flights represent a larger variety of low-level flights in different areas of Europe and the CARIBIC dataset is composed of primarily the ascents and descents into and out of Frankfurt international airport.

Blue sky during BLUESKY. The solar radiation at Earth's surface reached a maximum during the COVID-19 lockdown period in spring 2020 over western Europe. Van Heerwaarden et al. (2021) found that surface irradiance was highest since 1928 for the area of the Netherlands. Reasons were an overall very low cloud fraction, several exceptionally dry days, and low aerosol optical thickness (AOT). Regardless of whether AOT concentrations are ultimately due to an anthropogenic influence or related to meteorological variability, the subjective impression was that in 2020 the sky appeared in a deeper blue during the lockdown period. To substantiate this perception, we carried out radiative transfer calculations in the cloud-free atmosphere.

Simulations of the atmospheric radiative transfer are based on the 1D radiative transfer model UVSPEC from the program package libRadtran (Mayer and Kylling 2005; Emde et al. 2016). In this study, UVSPEC is used to compute downward-directed spectral radiances and irradiances at the surface in the visible spectral range (380–780 nm) for a cloud-free midlatitude summer standard atmosphere (Anderson et al. 1986). Regarding the aerosol, a model after Fenn et al. (1985) was used, which assumes a rural type for the boundary layer. To examine changes in sky color, calculated spectra are convolved with the spectral sensitivity of the human eye in the red, green, and blue spectral range. A subsequent spectral integration gives RGB color components and enables the representation of the sky color. Input to the model are different vertical distributions of the aerosol optical thickness AOT(z). Profiles close to reality have been generated by scaling a normalized profile of the volume extinction coefficient (Fenn et al. 1985) with a total AOT provided by the Moderate Resolution Imaging Spectroradiometer (MODIS) on board the *Terra* and *Aqua* satellites.

The total aerosol optical thicknesses derived from MODIS data products MOD08_D3 v6.1 (*Terra*) and MYD08_D3 v6.1 (*Aqua*) were statistically analyzed over Germany and Europe. Here we consider the BLUESKY period from 23 May to 9 June 2020 as a reference to the years 2015–19. For 2020 the median total aerosol optical thickness $\mathrm{AOT}_{\mathrm{MODIS}}$ is 0.156 at 0.55 μm, whereas it is 0.247 for the period 2015–19. For comparison, the individual years 2015–19 give an $\mathrm{AOT}_{\mathrm{MODIS}}$ range between 0.187 and 0.309. Also, the statistics for Europe shows a median of 0.156 for the BLUESKY period in 2020 and a range of 0.175 to 0.265 for 2015–19. Vertical profiles of the aerosol optical thickness based on the $\mathrm{AOT}_{\mathrm{MODIS}}$ values of 0.156 and 0.247 are presented in Fig. 15a. Figure 15b shows the spectra of the diffuse component of downward directed spectral irradiances for a solar zenith angle of 45°. Calculating the ratio r of downward irradiances at blue and red wavelengths ($I_{460\mathrm{nm}}/I_{750\mathrm{nm}}$), for example, results in r = 2.4 and r = 2.1 for $\mathrm{AOT}_{\mathrm{MODIS}}$ of 0.156 and 0.247, respectively, indicating a shift of the simulated spectrum toward shorter wavelengths. Figures 15c and 15d reveal that the spectra are associated with a contrast in sky color. Transferring angular resolved radiances and hemispherically integrated irradiances into RGB colors clearly illustrates that in case of a reduced $\mathrm{AOT}_{\mathrm{MODIS}}$ (Figs. 15c and 15d, left halves of circles), the sky appears in a deeper blue color. This result also applies to other solar zenith angles. Figure 15e displays the year-to-year variability of the $\mathrm{AOT}_{\mathrm{MODIS}}$ in the period from 2015 to 2020 highlighted with calculated sky colors. It is obvious that the blue

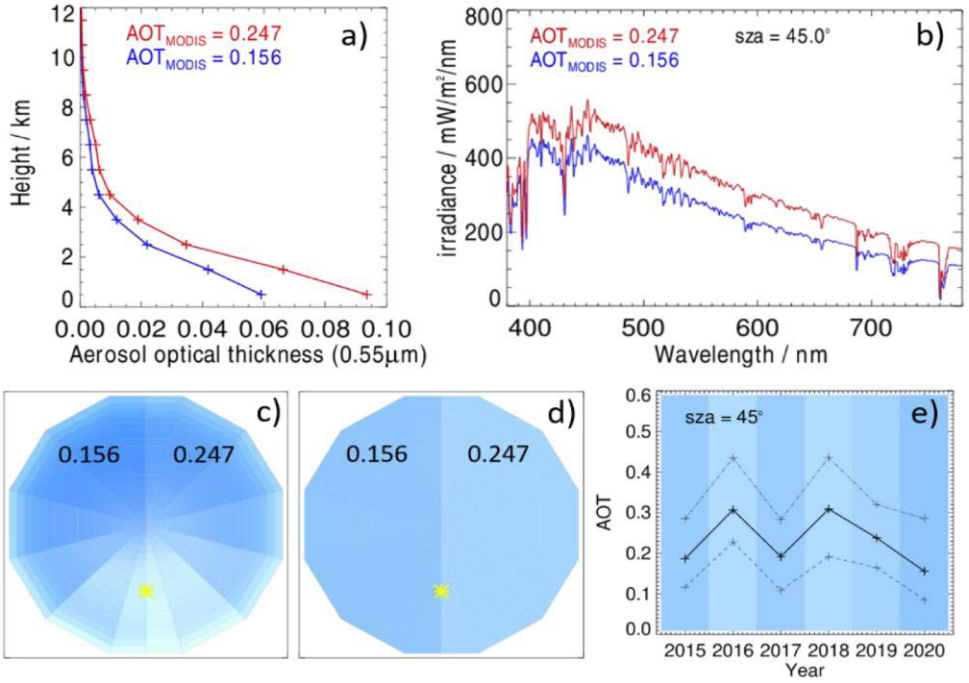

Fig. 15. Blue sky during BLUESKY. (a) Vertical profiles of the aerosol optical thickness at 550 nm scaled to different medians of the total aerosol optical thicknesses AOT_{MODIS} derived from MODIS data covering the area of Germany. Blue: scaled with the median valid for the BLUESKY period in 2020; red: scaled with the median resulting from all BLUESKY periods of the years 2015–19. (b) Spectral distributions of the diffuse component of the downward directed irradiance at the surface for the AOT_{MODIS} as in (a). SZA denotes the solar zenith angle data. (c) Sky colors derived from calculated spectral radiances integrated over the visible spectral range (380–780 nm) convolved with the spectral sensitivity of the human eye. Radiance distributions are displayed relative to the position of the sun (yellow star). Left and right halves of the circles represent colors resulting for AOT_{MODIS} values as indicated. At the center of each circle the viewing zenith angle is 0°. (d) As in (c), but for downward-directed irradiances resulting from an angular integration of the radiances shown in (c) over the upper hemisphere. (e) Year-to-year variability of AOT_{MODIS} for the area of Germany in the period from 2015 to 2020. Dashed and dashed–dotted curves represent minima and maxima of the AOT_{MODIS} within the BLUESKY period of each year.

in 2020 forms a contrast to all previous years, albeit differently pronounced depending on the AOT_{MODIS} differences. Although it is not clear whether changes in the total aerosol optical thickness are mainly due to an anthropogenic or a meteorological influence, the radiative transfer simulations give a clear indication that the lower aerosol optical thickness during the lockdown resulted in a deeper blue color of the sky during BLUESKY compared to the same period in the previous five years. Global model simulations in the "Highlights from the BLUESKY mission" section further investigate the impact of aerosol changes on the radiation budget at the surface.

Effect of pollution on low clouds. To contrast aerosol–cloud interactions in highly polluted regimes against less polluted regimes, intensive measurements of aerosol and clouds were made in the boundary layer over the densely populated Ruhr metropolitan region versus recurrent sampling of the boundary layer over the remote sparsely populated Hohenpeissenberg regions in southern Germany. Further aerosol and cloud measurements were taken above the cities of Berlin, Hamburg, and Munich, during individual arrival and departure routes to and from the respective airports.

Cloud droplet number concentrations (CDNC) in low-level clouds (<2,500 m altitude) were measured with the Cloud and Aerosol Spectrometer (CAS) probe aboard the DLR Falcon and more than 8,000 individual clouds were intercepted. We implemented a cloud threshold considering only droplets larger than 3 μm and with a liquid water content of more than 0.01g m^{-3}, in order to avoid diffuse cloud edges. Only measurements contributed to the remote Hohenpeissenberg statistics from campaign days without a large-scale westerly flow, to avoid an influence of the Munich urban emission plume. Figure 16 shows the cloud droplet number concentrations measured in the remote and the industrial regions. A clear trend is observed between the CDNC in the rural Hohenpeissenberg area with median cloud drop number concentrations of a few tens per cubic centimeters at the lower side of the spectrum and high median CDNC of 385 cm^{-3} in the densely populated Ruhr metropolitan area. The cities of Hamburg (195 cm^{-3}), Berlin (274 cm^{-3}), and Munich (311 cm^{-3}) range in between.

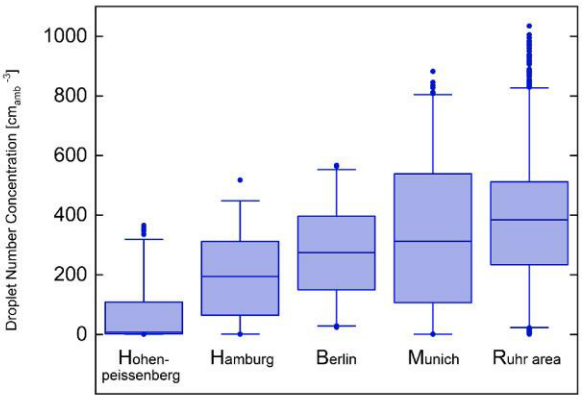

Fig. 16. Statistics of cloud droplet number concentrations (CDNC) in low-level clouds in rural, urban, and industrial regions of Germany during the BLUESKY campaign measured with the CAS on board the Falcon. The figure shows the medians, quartiles, and 1% and 99% percentiles of all cloud intercepts in the different regions. The trend in CDNC number concentration correlates with pollution levels, with lowest CDND in the remote Bavarian Hohenpeissenberg region [number of cloud intercepts (*n*) = 616], intermediate CDNC related to city outflow from Hamburg (*n* = 152), Berlin (*n* = 330), and Munich (*n* = 608) and highest CDNC in the industrial Rhine–Ruhr metropolitan area (*n* = 4,751).

Reduced contrail cirrus cover and radiative impact. The COCIP (Schumann 2012) simulates the life cycle of contrails (Schumann et al. 2017; Schumann and Heymsfield 2017) that form for given aircraft flight track data and numerical weather predictions and computes their local radiative forcing (Schumann 2012). COCIP has been used for mission planning, for simulation of contrail properties comparable with in situ and satellite observations, and for aviation climate impact mitigation studies (Schumann and Graf 2013; Voigt et al. 2017; Teoh et al. 2020; Schumann et al. 2021a). Figure 17 presents example results for 16 April 2020. Travel restrictions in response to COVID-19 caused an 89% decrease in air traffic flight distance over Europe this day. Despite the low air traffic density, MSG/SEVIRI data indicate contrail occurrence on that day, as shown in the optical thickness of ice clouds, derived using the algorithm described in Strandgren et al. (2017), and from brightness temperature differences.

Contrail and cirrus optical thickness (COT) derived from COCIP on that day are shown in the middle panel in Fig. 17, as well as COCIP COT calculated with the same meteorology but with air traffic data from 16 April 2019. Higher contrail cirrus optical thickness is calculated for the factor-of-5-higher air traffic on 16 April 2019. COCIP was also used to calculate the respective positive and negative radiative forcing (RF) from contrail cirrus for both scenarios. The resulting daily net forcing is positive on average in both years. The computed longwave and shortwave RF components locally exceed 1 W m^{-2} in magnitude despite low air traffic in 2020. On 16 April 2020, the contrail RF in the presented area is also strongly reduced to about 20% of its value for the same meteorology but for air traffic data in 2019, implying a significant reduction in RF from contrails due to reduced air traffic in 2020 on that day.

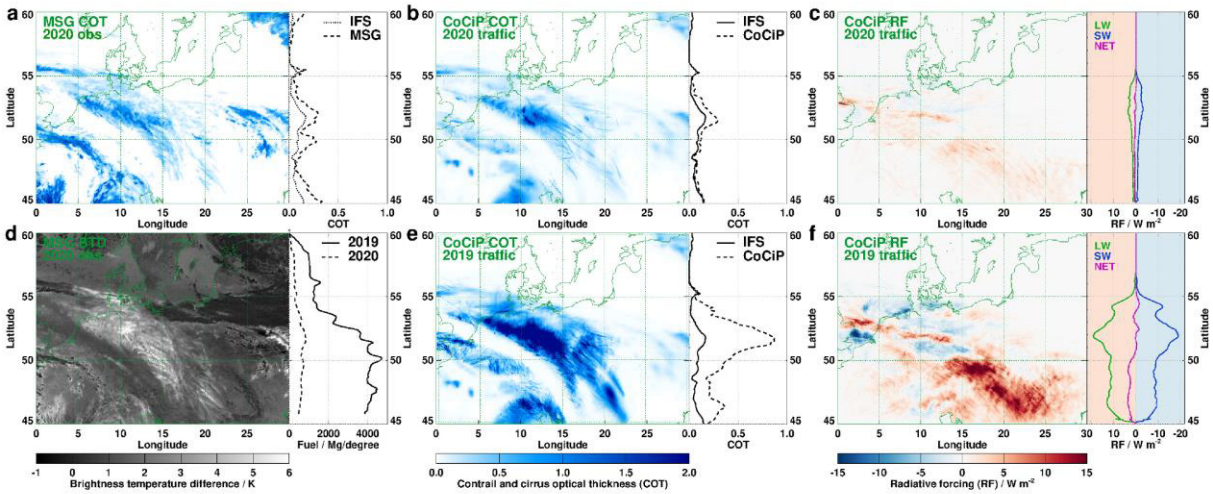

Fig. 17. Cirrus optical thickness derived from (a) MSG/SEVIRI satellite observations and contrail cirrus optical thickness modeled with COCIP for 1000 UTC 16 April 2020 (b) for air traffic of 2020 and (e) for air traffic of 2019, and (d) brightness temperature difference between 10.8 and 12.0 μm channels of MSG/SEVIRI, with color bars. Please notice that all COT plots use the same white–blue color scale depicted below (e). The line diagrams show longitudinal averages of the optical thickness in (a), (b), and (e), and of derived aircraft fuel consumption in (d). The cirrus optical thicknesses are derived from observations (MSG, dashed lines), from ECMWF-IFS numerical weather predictions (IFS, dotted), and from the combined IFS and COCIP model (COCIP, full). The diurnal fuel consumption per degree latitude is derived from EUROCONTROL traffic data (CPR) for 16 April 2019 (full line) and 2020 (dashed). (c),(f) The radiative forcing from contrail cirrus in 2020 and the expected forcing for air traffic in 2019 calculated with COCIP.

Annually averaged changes might be different due to the warming and cooling components of the contrail cirrus forcing (Gettelman et al. 2021). A more detailed discussion of the contrail effects including an uncertainty analysis is given in Schumann et al. (2021a) and the extension to longer time periods is discussed in Schumann et al. (2021b).

Changes in cirrus properties from* CALIPSO *data. Civil aviation may contribute to climate change by inducing contrail cirrus formation and by changing natural cirrus cloud properties (Tesche et al. 2016). Urbanek et al. (2018) showed that cirrus clouds formed in regions highly affected by air traffic have higher mean particle linear depolarization ratios than those formed in pristine regions. To study the effect of reduced aviation on cirrus cloud properties we compared *CALIPSO* satellite measurements of cirrus during the BLUESKY campaign with cirrus data measured at the same time period in the previous years (2010–19). The measurements were performed with CALIOP instrument on board the *CALIPSO* satellite (Winker et al. 2007, 2010; Stephens et al. 2018). CALIOP uses three channels at 1,064 and 532 nm for measuring the total backscatter and the orthogonal component of depolarization. For this study we used the level 2 5 km cloud profile products with a vertical resolution of up to 30 m. To compare the CALIOP cirrus observations with the measurements during the BLUESKY campaign, we analyzed the datasets covering the Falcon cruise area from 50° to 55°N and from 15°W to 5°E as well as latitudes from 45° to 55°N and longitudes from 5° to 15°E. *CALIPSO* passes over the study area three to four times each day resulting in 90 overpasses in the period 16 May–9 June each year. Since all BLUESKY measurements were performed during the day, we only used daytime satellite lidar observations for the intercomparison.

To investigate the changes of cirrus cloud properties as possible consequence of the significantly reduced aviation during the COVID-19 pandemic, we used the particle linear depolarization ratio (PLDR), the extinction coefficients (σ_{ci}), and the calculated effective optical thickness of cirrus clouds ($\tau_{ci} = \int_{r_b}^{r_t} \sigma_{ci}\, dz$, where r_t and r_b are the cloud-top and

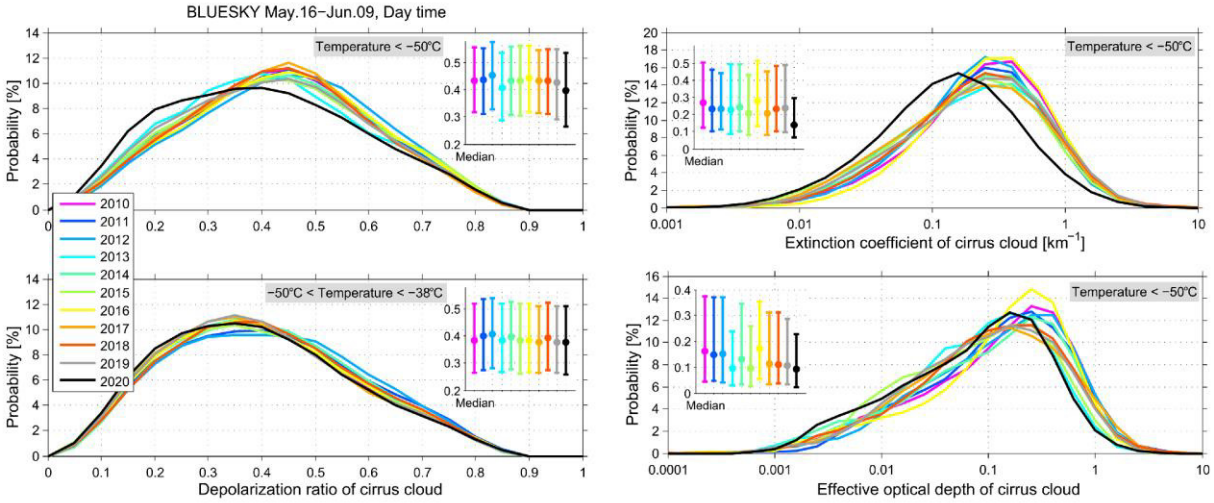

Fig. 18. Comparisons of cirrus cloud properties determined from the lidar measurements of *CALIPSO* in the years 2010–20 over Europe in the period from 16 May to 9 Jun 2020 during BLUESKY. (left) Particle linear depolarization ratios (PLDR) of cirrus clouds determined from the daytime observations at temperatures (top left) below −50°C and (bottom left) between −50°C and −38°C; (top right) extinction coefficient (σ_{ci}) in the cirrus clouds at temperatures colder than −50°C and (bottom right) effective cloud optical depth of cirrus ($\tau_{e,ci}$) at temperatures lower than −50°C. The medians (circles) of PLDR, σ_{ci}, and $\tau_{e,ci}$ of cirrus clouds as well as the quartiles (lower and upper bars, respectively) in years 2010–20 are indicated in the inserted boxes.

cloud-bottom heights of cirrus, respectively). As cirrus cloud properties strongly depend on temperatures (e.g., Urbanek et al. 2018), and as a temperature T of −50°C is one of the threshold conditions for contrail formation (Schumann 1996), we divided the data into two subsets with temperatures from −38° to −50°C and temperatures below −50°C (Li and Groß 2021).

Figure 18 shows the probability density function (PDF) of the PLDR (left) for cirrus clouds at T < −50°C (top panel) and −50° < T < −38°C (bottom panel), as well as of the extinction coefficient (top right) and the effective optical depth (bottom right) for T < −50°C of all cirrus cloud cases measured during the day with CALIOP during the BLUESKY period in the different years. The resulting distributions of cirrus PLDR show a non-Gaussian shape for both temperature ranges with larger values at the lower temperature range (T < −50°C). The PDFs of the PLDR of cirrus clouds in the higher temperature range show almost no deviation from each other, and also the cirrus cloud measurements in 2020 are well within the variability of the previous years. The median of the PLDR distribution is at about 0.35–0.38 for all the years. For the cirrus PLDR at the lower temperature range, the situation looks quite different. The years 2010–19 show only limited variability with a median value between 0.42 and 0.45. However, the PLDR for the cirrus clouds measured during BLUESKY in 2020 show a significantly lower median value of 0.39. The σ_{ci} and τ_{ci} distributions show the same features as PLDR; σ_{ci} and τ_{ci} values for cirrus clouds in 2020 are on average smaller at lower temperatures than in the previous years. The median value of the extinction coefficient for the years 2010–19 varied between 0.20 and 0.26 km^{-1} while it was about 0.14 in 2020. A similar but not as significant picture is found for the cirrus cloud effective optical thickness. Most median values in the years 2010–19 were within a range of 0.10 and 0.16, whereas the median value in 2020 was about 0.09. Low values are, however, also found for cirrus clouds in 2013 and 2015.

Global chemistry–climate modeling. The input and the comparison of measurement data with global models are essential to enhance our understanding of atmospheric processes and their relation to climate. The EMAC atmospheric chemistry–climate model was used

both for forecasting and the postcampaign data analysis. In both cases EMAC was nudged by Newtonian relaxation toward data from the European Centre for Medium-Range Weather Forecasts (ECMWF). The EMAC atmospheric model core is the fifth-generation European Centre Hamburg general circulation model (ECHAM5). For higher resolution in the field campaign region, the forecasts of atmospheric composition were performed with the MECO(n) model, which couples the global EMAC model online with the enhanced resolution regional model COSMO/MESSy, allowing for seamless zooming into regions of interest in the global model context (Kerkweg and Jöckel 2012a,b; Mertens et al. 2016). A continuous analysis simulation is performed from which 5-day forecasts are branched of every 12 h, with nudging toward the ECMWF operational analysis/forecast data. MECO(n) was configured with one refinement ranging from eastern North America to eastern Europe with 0.44° resolution in latitude and longitude. Comprehensive tropospheric gas phase chemistry was calculated as described by Mertens et al. (2016), in addition the source apportionment method by Grewe et al. (2017) and Mertens et al. (2020) was applied. Here, it uses a business as usual air traffic scenario to help identify the regions where large aviation signals onto the NO_y mixing ratios are predicted.

As an example, Fig. 19 shows the NO_y mixing ratios at 250 hPa averaged for 0700–1600 UTC 2 June 2020 and the relative contribution of aviation nitrogen oxide emissions to the NO_y mixing ratios. The model forecast shows regions with relative contributions from air traffic of more than 50% predicted west of Ireland for a business as usual air traffic scenario. The predictions were used to guide both aircraft into regions with aircraft emissions for aviation in 2019, being reduced during the same period in 2020. Accordingly, HALO and Falcon performed measurement flights in the regions west of Ireland (Fig. 19). The NO_x and NO_y measurements on the HALO and the Falcon during their flights into this area show individual spikes in NO_x and NO_y indicating the presence of a few aircraft plumes. In addition, NO_x and NO_y plumes from aircraft flying on 2 June 2020 as well as for air traffic in 2019 were calculated with the COCIP model and folded onto the Falcon and HALO flight paths. Due to reduced air traffic in 2020 only few individual plumes are derived, while calculations for emissions from the denser air traffic in 2019 show many more spikes.

Postcampaign data analysis was also performed with the EMAC model, adopting reduced emissions resulting from the lockdown in Europe as estimated by Guevara et al. (2021). EMAC was nudged toward the ERA-Interim data (Berrisford et al. 2011) to reproduce the observed synoptic weather conditions.

Figure 20 shows a comparison of observed temperature, specific humidity, CO, NO, O_3, and photolysis frequencies $j(NO_2)$ from HALO measurements and EMAC results from simulations with the reduced emission (COVID-19) scenario (Reifenberg et al. 2022). The good agreement between observed and simulated data for temperature, which is a nudged variable and therefore shows the same variance as the ERA-Interim dataset, indicates the quality of the reproduced meteorology. As expected, somewhat larger deviations from the observations are found for unconstrained variables, such as O_3, CO, and NO, although the overall comparison shows a very good agreement of the low-emission scenario simulations with the HALO measurements. In particular, the model is able to reproduce the observed NO, which was strongly reduced in the entire tropospheric column, because of the strong reductions in ground and air traffic (e.g., Schumann et al. 2021a). Furthermore, also parameters which are strongly influenced by parameterizations are satisfactorily represented in the model, such as the photolysis frequency of $j(NO_2)$, whose variability is associated with clouds. In addition, O_3 is in general agreement between model and observations, albeit with modeled O_3 concentrations tending to slightly higher values. The EMAC model has also been used to investigate the impact of reduced emissions on direct and indirect aerosol radiative forcing during COVID-19 lockdown in Europe. Reifenberg et al. (2022) find large differences of selected tracers and aerosol between the reduced emission (COVID-19) scenario and the business as usual scenario at aircraft cruise altitudes in the upper troposphere mainly

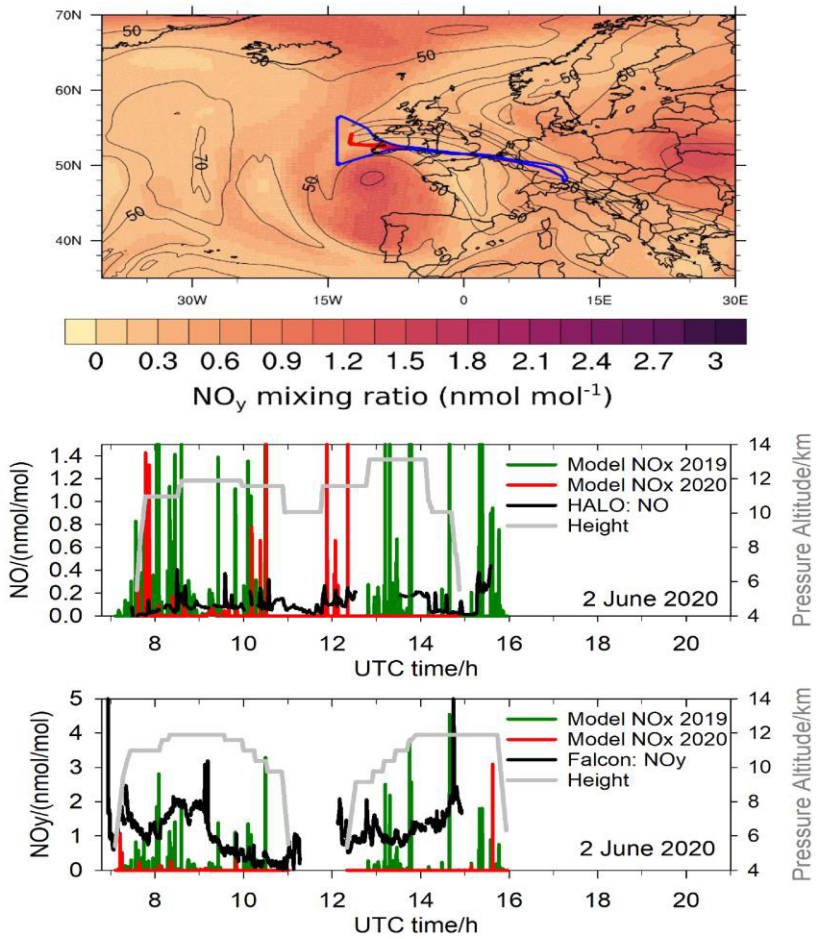

Fig. 19. (top) NO_y mixing ratios (in nmol mol^{-1}) at 250 hPa over Europe averaged from 0700 to 1600 UTC 2 Jun 2020. The black contours show the relative contribution (in %) of aviation emissions to the NO_y mixing ratios for the business as usual scenario using the tagging attribution method. The blue line shows the flight path of HALO, and the red line shows the flight path of the Falcon. The predictions were used to guide the aircraft into regions with expected reduced aircraft emissions. (middle),(bottom) The NO and NO_y data measured on that day by HALO and Falcon, respectively. Individual spikes in NO and NO_y indicate aircraft plumes. The red (green) lines show COCIP contrail model plume NO_x emitted by aircraft on that day in 2020 (red) and on the same day in 2019 (green) folded onto the Falcon and HALO flight paths. The number of plume observations agrees better with the 2020 aircraft scenario.

due to reduced air traffic. In addition, noticeable differences are found in the boundary layer affected mainly by ground transportation and industry. The reduction in aerosol surfaces leads to an increase in incoming solar radiation at the surface during the BLUESKY period (Reifenberg et al. 2022), in addition to the blue sky color.

Conclusions and outlook

From 16 May to 9 June 2020 the HALO and DLR Falcon performed 20 flights over Europe during the early COVID-19 lockdown to investigate the impact of reduced anthropogenic emission on the atmospheric composition during the BLUESKY mission. A comprehensive and unique dataset of trace gases, aerosols, and clouds was measured from the boundary layer to the lower stratosphere and profiles of atmospheric constituents were derived and compared to

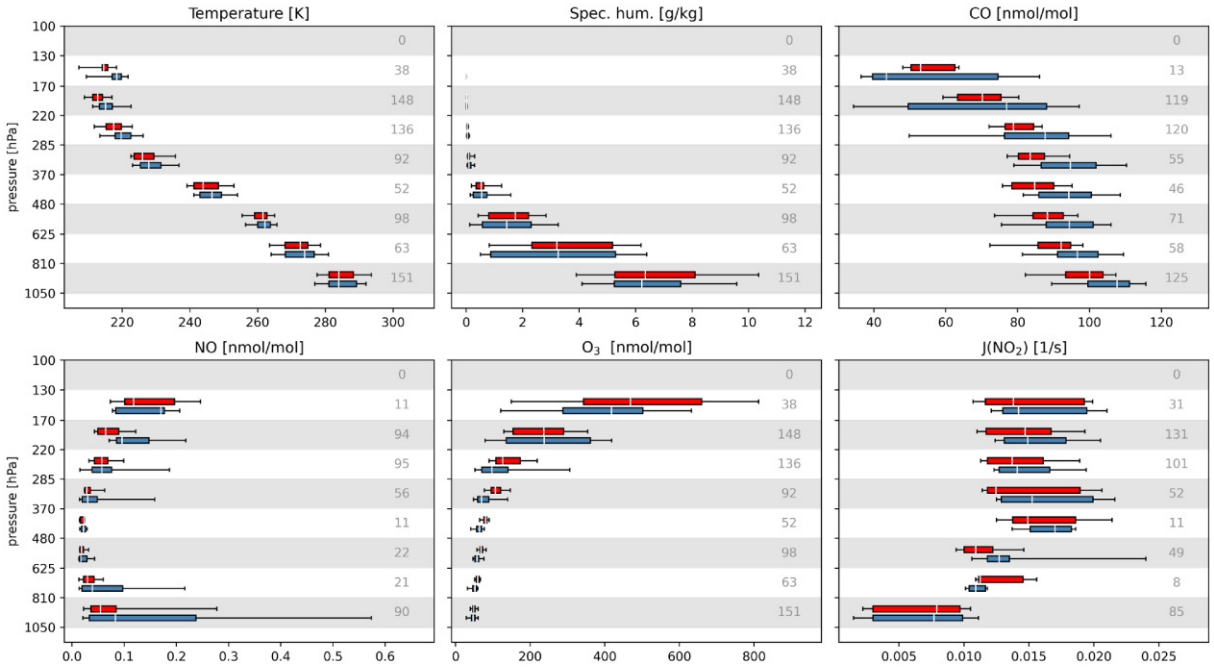

Fig. 20. Vertical distribution of EMAC model results with a reduced emission scenario (red) and BLUESKY aircraft measurements (blue) of trace species and the meteorological variables (temperature and specific humidity), represented by box-and-whisker plots for pressure bins (Reifenberg et al. 2022). The white line marks the median, the box corresponds to lower and upper quartiles, and the whiskers represent the 5th and 95th percentiles. The gray numbers on the right indicate the number of observed and interpolated simulated data points for each pressure bin. Measurements were averaged over 5 min periods to match the time resolution of the model.

measurements in pre-COVID-19 times and to satellite data and models. This paper presents first highlights from BLUESKY:

1) Significant (10%–50%) tropospheric NO_2 reductions were observed over industrialized continental areas as well as in major city outflows during the early lockdown phase, indicated by TROPOMI and GOME satellite data.
2) Tropospheric NO_y and CO profiles over Frankfurt showed significant (20%–70%) reductions on 28 May 2020 compared to the MOZAIC climatology from 2004 to 2015 and to IAGOS measurements from 2016 to 2019. The measured PPN and IPN profiles are in line with reduced anthropogenic influence on atmospheric chemistry. Falcon measurements of CO and NO_y in the industrial boundary layer of the Po valley in Italy show reductions up to 30%.

   EMAC model results confirm the impact of reduced emissions on the NO_y and CO profiles over Frankfurt. A comparison of EMAC results to BLUESKY O_3 data suggests that tropospheric O_3 is in general agreement with the observations, but tends to be slightly elevated compared to the HALO observations during the lockdown phase in Europe.
3) A suite of sulfur species was measured, such as DMS, SO_2, and H_2SO_4 as well as sulfate aerosol, which makes it possible to investigate the sulfur budget in the UTLS. The stratospheric sulfate was still perturbed by the aged emissions from the volcanic Raikoke eruption in June 2019 and by smaller eruptions thereafter.
4) The aerosol fine mode number concentrations and mass were substantially reduced in continental profiles with respect to observations from previous European summer campaigns and from the MOZAIC dataset. In the lower troposphere blow 5 km, we found strong aerosol

mass reductions. For black carbon aerosol, the lockdown-related reduction was as high as 40% (Krüger et al. 2022). Reduced organic aerosol particulates aloft imply that reduced VOC emissions transported from the surface might have led to a reduction of secondary organic aerosol production in the free troposphere.

5) The perceived deeper blue sky during the BLUESKY period in central Europe can be explained by reduced light scattering from aerosol profiles with a 40% lower AOT than usual.
6) Low-level clouds measured in remote parts of Bavaria contained lower cloud droplet number concentrations compared to clouds over large cities and the industrial Ruhr region.
7) The 80% reduced air traffic led to significant reductions in contrail cover, contrail optical thickness and to a reduced, but still positive radiative forcing from contrail cirrus for a case study relating to 16 April 2020. Also, observed reductions in NO_y at cruise altitudes can be explained by simulated reductions in aircraft NO_x emissions.
8) The extinction and the depolarization ratio of cirrus clouds below −50°C measured by CALIOP on daytime between 16 May and 9 June 2020 exhibits reductions at aircraft cruise altitudes above Europe implying a potential effect from reduced aircraft aerosol emissions on cirrus properties.
9) The global model EMAC has been used in its nudged version for flight planning. First postcampaign simulation results indicate good agreement for a scenario with emissions that were reduced during the lockdown period. Reifenberg et al. (2022) derive a higher fraction of incoming solar radiation at the surface for the reduced COVID-19 emission scenario compared to the business as usual simulations, mainly due to reduced aerosol surface areas.

Altogether, BLUESKY provides a comprehensive dataset on trace gases, aerosols, and clouds over Europe, which documents the anthropogenic impact on atmospheric composition and climate.

Acknowledgments. We thank the DLR flight department for support during the campaign and the pilots for excellent flight operations. Support by the Helmholtz Association, the Max-Planck-Society, and by the German Science Foundation DFG within the SPP HALO 1294 under Grants VO1504/5-1, VO1504/7-1, BO1580/5-1, and of the CRC TRR 301/1 TP Change is acknowledged. Also support by the Dr. Hans Messer Foundation and the Heinrich Böll Stiftung is acknowledged. *Sentinel-5P* is a European Space Agency (ESA) mission on behalf of the European Commission (EC). Special thanks to Markus Hermann and Denise Assmann (TROPOS) for providing IAGOS-CARIBIC particle data for aerosol concentration comparisons (www.iagos.org/iagos-caribic). MetOp/GOME-2 level 2 data are provided by DLR in the framework of the EUMETSAT AC-SAF project. The EMAC and MECO(n) simulations have been performed at the German Climate Computing Centre (DKRZ) through support from the Bundesministerium für Bildung und Forschung (BMBF). DKRZ and its scientific steering committee are gratefully acknowledged for providing the HPC and data archiving resources for the project "Multiscale Earth System Chemistry Modelling." The authors thank the NASA Langley Research ASDC and *CALIPSO* science team for making the data available for research.

Data availability statement. Data are available on request at the HALO database at https://halo-db.pa.op.dlr.de/mission/119. The *Sentinel-5P*/TROPOMI level 2 data are freely available via the Copernicus Open Access Hub (https://s5phub.copernicus.eu/).

References

Anderson, G. P., S. A. Clough, F. X. Kneizys, J. H. Chetwynd, and E. P. Shettle, 1986: AFGL atmospheric constituent profiles (0–120 km). Air Force Geophysics Lab Tech. Rep. AFGL-TR-860110, 43 pp.

Andreae, M. O., and Coauthors, 2018: Aerosol characteristics and particle production in the upper troposphere over the Amazon basin. *Atmos. Chem. Phys.*, **18**, 921–961, https://doi.org/10.5194/acp-18-921-2018.

Andrés Hernández, M. D., and Coauthors, 2022: Overview: On the transport and transformation of pollutants in the outflow of major population centres—Observational data from the EMeRGe European intensive operational period in summer 2017. *Atmos. Chem. Phys.*, **22**, 5877–5924, https://doi.org/10.5194/acp-22-5877-2022.

Baumgardner, D., G. Kok, and G. Raga, 2004: Warming of the Arctic lower stratosphere by light absorbing particles. *Geophys. Res. Lett.*, **31**, L06117, https://doi.org/10.1029/2003GL018883.

Bekbulat, B., J. Apte, D. Millet, A. Robinson, K. Wells, and J. Marshall, 2020: $PM_{2.5}$ and ozone air pollution levels have not dropped consistently across the US following societal COVID response. ChemRxiv, https://doi.org/10.26434/chemrxiv.12275603.v2.

Berrisford, P., and Coauthors, 2011: The ERA-Interim archive, version 2.0. ERA Rep. Series 1, 23 pp., www.ecmwf.int/sites/default/files/elibrary/2011/8174-era-interim-archive-version-20.pdf.

Bohn, B., and I. Lohse, 2017: Calibration and evaluation of CCD spectroradiometers for ground-based and airborne measurements of spectral actinic flux densities. *Atmos. Meas. Tech.*, **10**, 3151–3174, https://doi.org/10.5194/amt-10-3151-2017.

Bourtsoukidis, E., F. Helleis, L. Tomsche, H. Fischer, R. Hofmann, J. Lelieveld, and J. Williams, 2017: An aircraft gas chromatograph-mass spectrometer System for Organic Fast Identification Analysis (SOFIA): Design, performance and a case study of Asian monsoon pollution outflow. *Atmos. Meas. Tech.*, **10**, 5089–5105, https://doi.org/10.5194/amt-10-5089-2017.

Bräuer, T., and Coauthors, 2021a: Airborne measurements of contrail ice properties—Dependence on temperature and humidity. *Geophys. Res. Lett.*, **48**, e2020GL092166, https://doi.org/10.1029/2020GL092166.

——, and Coauthors, 2021b: Reduced ice number concentrations in contrails from low-aromatic biofuel blends. *Atmos. Chem. Phys.*, **21**, 16 817–16 826, https://doi.org/10.5194/acp-21-16817-2021.

Burkhardt, U., L. Bock, and A. Bier, 2018: Mitigating the contrail cirrus climate impact by reducing aircraft soot number emissions. *npj Climate Atmos. Sci.*, **1**, 37, https://doi.org/10.1038/s41612-018-0046-4.

Chen, L. A., L. C. Chien, Y. Li, and G. Lin, 2020: Nonuniform impacts of COVID-19 lockdown on air quality over the United States. *Sci. Total Environ.*, **745**, 141105, https://doi.org/10.1016/j.scitotenv.2020.141105.

Clark, H., and Coauthors, 2021: The effects of the COVID-19 lockdowns on the composition of the troposphere as seen by In-service Aircraft for a Global Observing System (IAGOS) at Frankfurt. *Atmos. Chem. Phys.*, **21**, 16 237–16 256, https://doi.org/10.5194/acp-21-16237-2021.

Copernicus, 2020: Emissions changes due to lockdown measures during the first wave of the COVID-19 pandemic in Europe. Accessed 30 September 2021, https://atmosphere.copernicus.eu/emissions-changes-due-lockdown-measures-during-first-wave-COVID-19-pandemic-europe.

de Leeuw, J., and Coauthors, 2021: The 2019 Raikoke volcanic eruption—Part 1: Dispersion model simulations and satellite retrievals of volcanic sulfur dioxide. *Atmos. Chem. Phys.*, **21**, 10 851–10 879, https://doi.org/10.5194/acp-21-10851-2021.

Derstroff, B., and Coauthors, 2017: Volatile organic compounds (VOCs) in photochemically aged air from the eastern and western Mediterranean. *Atmos. Chem. Phys.*, **17**, 9547–9566, https://doi.org/10.5194/acp-17-9547-2017.

Dhaka, S. K., and Coauthors, 2020: $PM_{2.5}$ diminution and haze events over Delhi during the COVID-19 lockdown period: An interplay between the baseline pollution and meteorology. *Sci. Rep.*, **10**, 13442, https://doi.org/10.1038/s41598-020-70179-8.

Dörich, R., P. Eger, J. Lelieveld, and J. N. Crowley, 2021: Iodide CIMS and *m/z* 62: The detection of HNO_3 as NO_3^- in the presence of PAN, peroxyacetic acid and ozone. *Atmos. Meas. Tech.*, **14**, 5319–5332, https://doi.org/10.5194/amt-14-5319-2021.

Drewnick, F., and Coauthors, 2005: A new Time-of-Flight Aerosol Mass Spectrometer (TOF-AMS): Instrument description and first field deployment. *Aerosol Sci. Technol.*, **39**, 637–658, https://doi.org/10.1080/02786820500182040.

Edtbauer, E., C. Stönner, E. Y. Pfannerstill, M. Berasategui, D. Walter, J. N. Crowley, J. Lelieveld, and J. Williams, 2020: A new marine biogenic emission: Methane sulfonamide (MSAM), dimethyl sulfide (DMS), and dimethyl sulfone ($DMSO_2$) measured in air over the Arabian Sea. *Atmos. Chem. Phys.*, **20**, 6081–6094, https://doi.org/10.5194/acp-20-6081-2020.

Emde, C., and Coauthors, 2016: The libRadtran software package for radiative transfer calculations (version 2.0.1). *Geosci. Model Dev.*, **9**, 1647–1672, https://doi.org/10.5194/gmd-9-1647-2016.

Erbertseder, T., and D. Loyola, 2020: Despite weather influence—Corona effect now indisputable. DLR Earth Observation Center, accessed 2 February 2021, www.dlr.de/eoc/en/desktopdefault.aspx/tabid-14195/24618_read-64626.

Feldpausch, P., M. Fiebig, L. Fritzsche, and A. S Petzold, 2006: Measurement of ultrafine aerosol size distributions by a combination of diffusion screen separators and condensation particle counters. *J. Aerosol Sci.*, **37**, 577–597, https://doi.org/10.1016/j.jaerosci.2005.04.009.

Feng, R., and Coauthors, 2021: Quantifying air pollutant variations during COVID-19 lockdown in a capital city in northwest China. *Atmosphere*, **12**, 788, https://doi.org/10.3390/atmos12060788.

Fenn, R. W., and Coauthors, 1985: Optical and infrared properties of the atmosphere. Handbook of geophysics and space environment, Air Force Geophysics Laboratory Doc., www.cnofs.org/Handbook_of_Geophysics_1985/pdf_menu.htm.

Fiebig, M., C. Stein, F. Schröder, P. Feldpausch, and A. Petzold, 2005: Inversion of data containing information on the aerosol particle size distribution using multiple instruments. *J. Aerosol Sci.*, **36**, 1353–1372, https://doi.org/10.1016/j.jaerosci.2005.01.004.

Forster, P. M., and Coauthors, 2020: Current and future global climate impacts resulting from COVID-19. *Nat. Climate. Change*, **10**, 913–919, https://doi.org/10.1038/s41558-020-0883-0.

Georgoulias, A. K., R. J. van der A, P. Stammes, K. F. Boersma, and H. J. Eskes, 2019: Trends and trend reversal detection in 2 decades of tropospheric NO_2 satellite observations. *Atmos. Chem. Phys.*, **19**, 6269–6294, https://doi.org/10.5194/acp-19-6269-2019.

Gettelman, A., C.-C. Chen, and C. G. Bardeen, 2021: The climate impact of COVID-19-induced contrail changes. *Atmos. Chem. Phys.*, **21**, 9405–9416, https://doi.org/10.5194/acp-21-9405-2021.

Goldberg, D. L., S. C. Anenberg, D. Griffin, C. A. McLinden, Z. Lu, and D. G. Streets, 2020: Disentangling the impact of the COVID-19 lockdowns on urban NO^2 from natural variability. *Geophys. Res. Lett.*, **47**, e2020GL089269, https://doi.org/10.1002/essoar.10503396.1.

Grewe, V., E. Tsati, M. Mertens, C. Frömming, and P. Jöckel, 2017: Contribution of emissions to concentrations: the TAGGING 1.0 submodel based on the Modular Earth Submodel System (MESSy 2.52). *Geosci. Model Dev.*, **10**, 2615–2633, https://doi.org/10.5194/gmd-10-2615-2017.

Guevara, M., O. Jorba, H. Petetin, A. Nicodemou, and I. Jiménez, 2020: D8: Scientific content explaining the main outcomes of the project and data analysis. ECMWF Copernicus Rep. CAMS/COP_066, 24 pp., https://atmosphere.copernicus.eu/sites/default/files/2020-12/CAMS_COP_066_2020SC1_D8_202012_v1.pdf.

——, and Coauthors, 2021: Time-resolved emission reductions for atmospheric chemistry modelling in Europe during the COVID-19 lockdowns. *Atmos. Chem. Phys.*, **21**, 773–797, https://doi.org/10.5194/acp-21-773-2021.

Hallar, A. G., and Coauthors, 2021: Coupled air quality and boundary-layer meteorology in western U.S. basins during winter: Design and rationale for a

comprehensive study. *Bull. Amer. Meteor. Soc.*, **102**, E2012–E2033, https://doi.org/10.1175/BAMS-D-20-0017.1.

Heller, R., and Coauthors, 2017: Mountain waves modulate the water vapor distribution in the UTLS. *Atmos. Chem. Phys.*, **17**, 14 853–14 869, https://doi.org/10.5194/acp-17-14853-2017.

Heymsfield, A. J., D. Baumgardner, P. DeMott, P. Forster, K. Gierens, and B. Kärcher, 2010: Contrail microphysics. *Bull. Amer. Meteor. Soc.*, **91**, 465–472, https://doi.org/10.1175/2009BAMS2839.1.

Holanda, B. A., and Coauthors, 2020: Influx of African biomass burning aerosol during the Amazonian dry season through layered transatlantic transport of black carbon-rich smoke. *Atmos. Chem. Phys.*, **20**, 4757–4785, https://doi.org/10.5194/acp-20-4757-2020.

Höpfner, M., and Coauthors, 2015: Sulfur dioxide (SO_2) from MIPAS in the upper troposphere and lower stratosphere 2002–2012. *Atmos. Chem. Phys.*, **15**, 7017–7037, https://doi.org/10.5194/acp-15-7017-2015.

Hosaynali Beygi, Z., and Coauthors, 2011: Oxidation photochemistry in the southern Atlantic boundary layer: Unexpected deviations from photochemical steady state. *Atmos. Chem. Phys.*, **11**, 8497–8513, https://doi.org/10.5194/acp-11-8497-2011.

Hottmann, B., and Coauthors, 2020: Impact of the South Asian monsoon outflow on atmospheric hydroperoxides in the upper troposphere. *Atmos. Chem. Phys.*, **20**, 12 655–12 673, https://doi.org/10.5194/acp-20-12655-2020.

Jöckel, P., and Coauthors, 2010: Development cycle 2 of the Modular Earth Submodel System (MESSy2). *Geosci. Model Dev.*, **3**, 717–752, https://doi.org/10.5194/gmd-3-717-2010.

Jurkat, T., and Coauthors, 2010: Airborne stratospheric ITCIMS measurements of SO_2, HCl, and HNO_3 in the aged plume of Volcano Kasatochi. *J. Geophys. Res.*, **115**, D00L17, https://doi.org/10.1029/2010JD013890.

——, S. Kaufmann, C. Voigt, D. Schäuble, P. Jeßberger, and H. Ziereis, 2016: The airborne mass spectrometer AIMS—Part 2: Measurements of trace gases with stratospheric or tropospheric origin in the UTLS. *Atmos. Meas. Tech.*, **9**, 1907–1923, https://doi.org/10.5194/amt-9-1907-2016.

——, and Coauthors, 2017: Depletion of ozone and reservoir species of chlorine and nitrogen oxide in the lower Antarctic polar vortex measured from aircraft. *Geophys. Res. Lett.*, **44**, GRL55959, https://doi.org/10.1002/2017GL073270.

Karle, N. N., R. M. Fitzgerald, R. K. Sakai, D. W. Sullivan, and W. R. Stockwell, 2021: Multi-scale atmospheric emissions, circulation and meteorological drivers of ozone episodes in El Paso-Juárez airshed. *Atmosphere*, **12**, 1575, https://doi.org/10.3390/atmos12121575.

Kaufmann, S., C. Voigt, P. Jeßberger, T. Jurkat, H. Schlager, A. Schwarzenboeck, M. Klingebiel, and T. Thornberry, 2014: In situ measurements of ice saturation in young contrails. *Geophys. Res. Lett.*, **41**, 702–709, https://doi.org/10.1002/2013GL058276.

——, and Coauthors, 2018: Intercomparison of mid-latitude tropospheric and lower stratospheric water vapor measurements and comparison to ECMWF humidity data. *Atmos. Chem. Phys.*, **18**, 16 729–16 745, https://doi.org/10.5194/acp-18-16729-2018.

Kerkweg, A., and P. Jöckel, 2012a: The 1-way on-line coupled atmospheric chemistry model system MECO(n)—Part 1: Description of the limited-area atmospheric chemistry model COSMO/MESSy. *Geosci. Model Dev.*, **5**, 87–110, https://doi.org/10.5194/gmd-5-87-2012.

——, and ——, 2012b: The 1-way on-line coupled atmospheric chemistry model system MECO(n)—Part 2: On-line coupling with the Multi-Model-Driver (MMD). *Geosci. Model Dev.*, **5**, 111–128, https://doi.org/10.5194/gmd-5-111-2012.

Klausner, T., and Coauthors, 2020: Urban greenhouse gas emissions from the Berlin area: A case study using airborne CO_2 and CH_4 in situ observations in summer 2018. *Elementa*, **8**, 15, https://doi.org/10.1525/elementa.411.

Kleine, J., and Coauthors, 2018: In situ observations of ice particle losses in a young persistent contrail. *Geophys. Res. Lett.*, **45**, 13 553–13 561, https://doi.org/10.1029/2018GL079390.

Kroll, J., C. Heald, C. Cappa, D. Farmer, J. Fry, J. G. Murphy, and A. Steiner, 2020: The complex chemical effects of COVID-19 shutdowns on air quality. *Nat. Chem.*, **12**, 777–779, https://doi.org/10.1038/s41557-020-0535-z.

Krüger, O., and Coauthors, 2022: Black carbon aerosol reductions during COVID-19 confinement quantified by aircraft measurements over Europe. *Atmos. Chem. Phys.*, **22**, 8683–8699, https://doi.org/10.5194/acp-22-8683-2022.

Le, T., Y. Wang, L. Liu, J. Yang, Y. L. Yung, G. Li, and J. H. Seinfeld, 2020: Unexpected air pollution with marked emission reductions during the COVID-19 outbreak in China. *Science*, **369**, 702–706, https://doi.org/10.1126/science.abb7431.

Lee, D. S., and Coauthors, 2010: Transport impacts on atmosphere and climate: Aviation. *Atmos. Environ.*, **44**, 4678–4734, https://doi.org/10.1016/j.atmosenv.2009.06.005.

——, and Coauthors, 2021: The contribution of global aviation to anthropogenic climate forcing for 2000 to 2018. *Atmos. Environ.*, **244**, 117834, https://doi.org/10.1016/j.atmosenv.2020.117834.

Le Quéré, C., and Coauthors, 2020: Temporary reduction in daily global CO_2 emissions during the COVID-19 forced confinement. *Nat. Climate Change*, **10**, 647–653, https://doi.org/10.1038/s41558-020-0797-x.

Li, Q., and S. Groß, 2021: Changes in cirrus cloud properties and occurrence over Europe during the COVID-19-caused air traffic reduction. *Atmos. Chem. Phys.*, **21**, 14 573–14 590, https://doi.org/10.5194/acp-21-14573-2021.

Liu, F., and Coauthors, 2020: Abrupt decline in tropospheric nitrogen dioxide over China after the outbreak of COVID-19. *Sci. Adv.*, **6**, eabc2992, https://doi.org/10.1126/sciadv.abc2992.

Lu, X., and Coauthors, 2021: The underappreciated role of agricultural soil nitrogen oxide emissions in ozone pollution regulation in North China. *Nat. Commun.*, **12**, 5021, https://doi.org/10.1038/s41467-021-25147-9.

Marno, D., and Coauthors, 2020: Calibration of an airborne HO_x instrument using the All Pressure Altitude-based Calibrator for HO_x Experimentation (APACHE). *Atmos. Meas. Tech.*, **13**, 2711–2731, https://doi.org/10.5194/amt-13-2711-2020.

Marsing, A., and Coauthors, 2019: Chlorine partitioning in the lowermost Arctic vortex during the cold winter 2015/2016. *Atmos. Chem. Phys.*, **19**, 10 757–10 772, https://doi.org/10.5194/acp-19-10757-2019.

Mayer, B., and A. Kylling, 2005: Technical note: The libRadtran software package for radiative transfer calculations—Description and examples of use. *Atmos. Chem. Phys.*, **5**, 1855–1877, https://doi.org/10.5194/acp-5-1855-2005.

Mertens, M., A. Kerkweg, P. Jöckel, H. Tost, and C. Hofmann, 2016: The 1-way on-line coupled model system MECO(n)—Part 4: Chemical evaluation (based on MESSy v2.52). *Geosci. Model Dev.*, **9**, 3545–3567, https://doi.org/10.5194/gmd-9-3545-2016.

——, ——, V. Grewe, P. Jöckel, and R. Sausen, 2020: Are contributions of emissions to ozone a matter of scale?—A study using MECO(n) (MESSy v2.50). *Geosci. Model Dev.*, **13**, 363–383, https://doi.org/10.5194/gmd-13-363-2020.

Minnis, P., and Coauthors, 2013: Linear contrail and contrail cirrus properties determined from satellite data. *Geophys. Res. Lett.*, **40**, 3220–3226, https://doi.org/10.1002/grl.50569.

Müller, I., T. Erbertseder, and H. Taubenböck, 2022: Tropospheric NO_2: Explorative analyses of spatial variability and impact factors. *Remote Sens. Environ.*, **270**, 112839, https://doi.org/10.1016/j.rse.2021.112839.

Munro, R., and Coauthors, 2016: The GOME-2 instrument on the MetOp series of satellites: Instrument design, calibration, and level 1 data processing—An overview. *Atmos. Meas. Tech.*, **9**, 1279–1301, https://doi.org/10.5194/amt-9-1279-2016.

Muser, L. O., and Coauthors, 2020: Particle aging and aerosol–radiation interaction affect volcanic plume dispersion: Evidence from the Raikoke 2019 eruption. *Atmos. Chem. Phys.*, **20**, 15 015–15 036, https://doi.org/10.5194/acp-20-15015-2020.

Pérez-Invernón, F. J., and Coauthors, 2022: Quantification of lightning-produced NO_x over the Pyrenees and the Ebro valley by using different TROPOMI-NO_2 and cloud research products. *Atmos. Meas. Tech.*, **15**, 3329–3351, https://doi.org/10.5194/amt-15-3329-2022.

Petit, J.-E., and Coauthors, 2021: Response of atmospheric composition to COVID-19 lockdown measures during spring in the Paris region (France). *Atmos. Chem. Phys.*, **21**, 17 167–17 183, https://doi.org/10.5194/acp-21-17167-2021.

Petzoldt, K., 2010: On the climatology of nitrogen oxides, ozone, and carbon monoxide in the troposphere: An analysis of the MOZAIC data set (in German). Research Centrum Jülich Rep. 4327, 80 pp.

Phillips, G. J., and Coauthors, 2013: Peroxyacetyl nitrate (PAN) and peroxyacetic acid (PAA) measurements by iodide chemical ionisation mass spectrometry: First analysis of results in the boreal forest and implications for the measurement of PAN fluxes. *Atmos. Chem. Phys.*, **13**, 1129–1139, https://doi.org/10.5194/acp-13-1129-2013.

Putaud, J.-P., L. Pozzoli, E. Pisoni, S. Martins Dos Santos, F. Lagler, G. Lanzani, U. Dal Santo, and A. Colette, 2021: Impacts of the COVID-19 lockdown on air pollution at regional and urban background sites in northern Italy. *Atmos. Chem. Phys.*, **21**, 7597–7609, https://doi.org/10.5194/acp-21-7597-2021.

Quaas, J., E. Gryspeerdt, R. Vautard, and O. Boucher, 2021: Climate impact of aircraft-induced cirrus assessed from satellite observations before and during COVID-19. *Environ. Res. Lett.*, **16**, 064051, https://doi.org/10.1088/1748-9326/abf686.

Reifenberg, S. F., and Coauthors, 2022: Impact of reduced emissions on direct and indirect aerosol radiative forcing during COVID-19 lockdown in Europe. *Atmos. Chem. Phys*., https://doi.org/10.5194/acp-2021-1005, in press.

Schiller, C. L., H. Bozem, C. Gurk, U. Parchatka, R. Königstedt, G.W. Harris, J. Lelieveld, and H. Fischer, 2008: Applications of quantum cascade lasers for sensitive trace gas measurements of CO, CH_4, N_2O and HCHO. *Appl. Phys.*, **92B**, 419–430, https://doi.org/10.1007/s00340-008-3125-0.

Schlager, H., and Coauthors, 1997: In situ observations of air traffic emission signatures in the North Atlantic flight corridor. *J. Geophys. Res. Atmos.*, **102**, 10 739–10 750, https://doi.org/10.1029/96JD03748.

Schmale, J., and Coauthors, 2010: Aerosol layers from the 2008 eruptions of Mount Okmok and Mount Kasatochi: In situ upper troposphere and lower stratosphere measurements of sulfate and organics over Europe. *J. Geophys. Res.*, **115**, D00I07, https://doi.org/10.1029/2009JD013628.

Schulte, P., and H. Schlager, 1996: In-flight measurements of cruise altitude nitric oxide emission indices of commercial jet aircraft. *Geophys. Res. Lett.*, **23**, 165–168, https://doi.org/10.1029/95GL03691.

Schulz, C., and Coauthors, 2018: Aircraft-based observations of isoprene-epoxydiol-derived secondary organic aerosol (IEPOX-SOA) in the tropical upper troposphere over the Amazon region. *Atmos. Chem. Phys.*, **18**, 14 979–15 001, https://doi.org/10.5194/acp-18-14979-2018.

Schumann, U., 1996: On conditions for contrail formation from aircraft exhausts. *Meteor. Z.*, **5**, 4–23, https://doi.org/10.1127/metz/5/1996/4.

——, 2012: A contrail cirrus prediction model. *Geosci. Model Dev.*, **5**, 543–580, https://doi.org/10.5194/gmd-5-543-2012.

——, and K. Graf, 2013: Aviation-induced cirrus and radiation changes at diurnal timescales. *J. Geophys. Res.*, **118**, 2404–2421, https://doi.org/10.1002/jgrd.50184.

——, and A. J. Heymsfield, 2017: On the lifecycle of individual contrails and contrail cirrus. *Ice Formation and Evolution in Clouds and Precipitation: Measurement and Modeling Challenges*, *Meteor. Monogr.*, No. 58, Amer. Meteor. Soc., https://doi.org/10.1175/AMSMONOGRAPHS-D-16-0005.1.

——, and Coauthors, 2017: Properties of individual contrails: A compilation of observations and some comparisons. *Atmos. Chem. Phys.*, **17**, 403–438, https://doi.org/10.5194/acp-17-403-2017.

——, L. Bugliaro, A. Dörnbrack, R. Baumann, and C. Voigt, 2021a: Aviation contrail cirrus and radiative forcing over Europe during 6 months of COVID-19. *Geophys. Res. Lett.*, **48**, e2021GL092771, https://doi.org/10.1029/2021GL092771.

——, and Coauthors, 2021b: Air traffic and contrail changes over Europe during COVID-19: A model study. *Atmos. Chem. Phys.*, **21**, 7429–7450, https://doi.org/10.5194/acp-21-7429-2021.

Slusher, D. L., L. G. Huey, D. J. Tanner, F. M. Flocke, and J. M. Roberts, 2004: A thermal dissociation-chemical ionization mass spectrometry (TD-CIMS) technique for the simultaneous measurement of peroxyacyl nitrates and dinitrogen pentoxide. *J. Geophys. Res.*, **109**, D19315, https://doi.org/10.1029/2004JD004670.

Solimini, A., F. Filipponi, D. A. Fegatelli, B. Caputo, C. M. De Marco, A. Spagnoli, and A. R. Vestri, 2021: A global association between COVID-19 cases and airborne particulate matter at regional level. *Sci. Rep.*, **11**, 6256, https://doi.org/10.1038/s41598-021-85751-z.

Speidel, M., R. Nau, F. Arnold, H. Schlager, and A. Stohl, 2007: Sulfur dioxide measurements in the lower, middle and upper troposphere: Deployment of an aircraft-based chemical ionization mass spectrometer with permanent in-flight calibration. *Atmos. Environ.*, **41**, 2427–2437, https://doi.org/10.1016/j.atmosenv.2006.07.047.

Stephens, G., D. Winker, J. Pelon, C. Trepte, D. Vane, C. Yuhas, T. L'Ecuyer, and M. Lebsock, 2018: *CloudSat* and *CALIPSO* within the A-Train: Ten years of actively observing the Earth system. *Bull. Amer. Meteor. Soc.*, **99**, 569–581, https://doi.org/10.1175/BAMS-D-16-0324.1.

Strandgren, J., L. Bugliaro, F. Sehnke, and L. Schröder, 2017: Cirrus cloud retrieval with MSG/SEVIRI using artificial neural networks. *Atmos. Meas. Tech.*, **10**, 3547–3573, https://doi.org/10.5194/amt-10-3547-2017.

Tadic, I., and Coauthors, 2021: Central role of nitric oxide in ozone production in the upper tropical troposphere over the Atlantic Ocean and West Africa. *Atmos. Chem. Phys.*, **21**, 8195–8211, https://doi.org/10.5194/acp-21-8195-2021.

Taylor, J. W., and Coauthors, 2019: Aerosol influences on low-level clouds in the West African monsoon. *Atmos. Chem. Phys.*, **19**, 8503–8522, https://doi.org/10.5194/acp-19-8503-2019.

Teoh, R., U. Schumann, A. Majumdar, and M. E. J. Stettler, 2020: Mitigating the climate forcing of aircraft contrails by small-scale diversions and technology adoption. *Environ. Sci. Technol.*, **54**, 2941–2950, https://doi.org/10.1021/acs.est.9b05608.

Tesche, M., P. Achtert, P. Glantz, and K. J. Noone, 2016: Aviation effects on already-existing cirrus clouds. *Nat. Commun.*, **7**, 12016, https://doi.org/10.1038/ncomms12016.

Urbanek, B., S. Groß, M. Wirth, C. Rolf, M. Krämer, and C. Voigt, 2018: High depolarization ratios of naturally occurring cirrus clouds near air traffic regions over Europe. *Geophys. Res. Lett.*, **45**, 13 166–13 172, https://doi.org/10.1029/2018GL079345.

van Geffen, J. H. G. M., H. J. Eskes, K. F. Boersma, J. D. Maasakkers, and J. P. Veefkind, 2019: TROPOMI ATBD of the total and tropospheric NO_2 data products. KNMI Rep. S5P-KNMI-L2-0005-RP, 86 pp., https://sentinel.esa.int/documents/247904/2476257/Sentinel-5P-TROPOMI-ATBD-NO2-data-products.

van Heerwaarden, C., and Coauthors, 2021: Record high solar irradiance in western Europe during first COVID-19 lockdown largely due to unusual weather. *Nat. Commun. Earth Environ.*, **2**, 37, https://doi.org/10.1038/s43247-021-00110-0.

Vázquez-Navarro, M., H. Mannstein, and S. Kox, 2015: Contrail life cycle and properties from 1 year of MSG/SEVIRI rapid-scan images. *Atmos. Chem. Phys.*, **15**, 8739–8749, https://doi.org/10.5194/acp-15-8739-2015.

Veefkind, J. P., and Coauthors, 2012: TROPOMI on the ESA Sentinel-5 Precursor: A GMES mission for global observations of the atmospheric composition for climate, air quality and ozone layer applications. *Remote Sens. Environ.*, **120**, 70–83, https://doi.org/10.1016/j.rse.2011.09.027.

Venter, Z. S., K. Aunan, S. Chowdhury, and J. Lelieveld, 2020: COVID-19 lockdowns cause global air pollution declines. *Proc. Natl. Acad. Sci. USA*, **117**, 18 984–18 990, https://doi.org/10.1073/pnas.2006853117.

Virkkula, A., 2010: Correction of the calibration of the 3-wavelength Particle Soot Absorption Photometer (3λ PSAP). *Aerosol Sci. Technol.*, **44**, 706–712, https://doi.org/10.1080/02786826.2010.482110.

——, N. C. Ahlquist, D. S. Covert, W. P. Arnott, P. J. Sheridan, P. K. Quinn, and D. J. Coffman, 2005: Modification, calibration and a field test of an instrument for measuring light absorption by particles. *Aerosol Sci. Technol.*, **39**, 68–83, https://doi.org/10.1080/027868290901963.

Voigt, C., and Coauthors, 2010: In-situ observations of young contrails—Overview and selected results from the CONCERT campaign. *Atmos. Chem. Phys.*, **10**, 9039–9056, https://doi.org/10.5194/acp-10-9039-2010.

——, and Coauthors, 2011: Extinction and optical depth of contrails. *Geophys. Res. Lett.*, **38**, L11806, https://doi.org/10.1029/2011GL047189.

——, and Coauthors, 2014: Evolution of CO_2, SO_2, HCl and HNO_3 in the volcanic plumes from Etna. *Geophys. Res. Lett.*, **41**, 2196–2203, https://doi.org/10.1002/2013GL058974.

——, and Coauthors, 2017: ML-CIRRUS: The airborne experiment on natural cirrus and contrail cirrus with the High-Altitude Long-Range Research Aircraft HALO. *Bull. Amer. Meteor. Soc.*, **98**, 271–288, https://doi.org/10.1175/BAMS-D-15-00213.1.

——, and Coauthors, 2021: Cleaner burning aviation fuels can reduce contrail cloudiness. *Nat. Commun. Earth Environ.*, **2**, 114, https://doi.org/10.1038/s43247-021-00174-y.

Williamson, C. J., and Coauthors, 2021: Large hemispheric difference in nucleation mode aerosol concentrations in the lowermost stratosphere at mid- and high latitudes. *Atmos. Chem. Phys.*, **21**, 9065–9088, https://doi.org/10.5194/acp-21-9065-2021.

Winker, D. M., B. H. Hunt, and M. J. McGill, 2007: Initial performance assessment of CALIOP. *Geophys. Res. Lett.*, **34**, L19803, https://doi.org/10.1029/2007GL030135.

——, and Coauthors, 2010: The *CALIPSO* mission: A global 3D view of aerosols and clouds. *Bull. Amer. Meteor. Soc.*, **91**, 1211–1229, https://doi.org/10.1175/2010BAMS3009.1.

Zahn, A., J. Weppner, H. Widmann, K. Schlote-Holubek, B. Burger, T. Kühner, and H. Franke, 2012: A fast and precise chemiluminescence ozone detector for eddy flux and airborne application. *Atmos. Meas. Tech.*, **5**, 363–375, https://doi.org/10.5194/amt-5-363-2012.

Zhou, Y., D. Brunner, C. Hueglin, S. Henne, and J. Staehelin, 2012: Changes in OMI tropospheric NO_2 columns over Europe from 2004 to 2009 and the influence of meteorological variability. *Atmos. Environ.*, **46**, 482–495, https://doi.org/10.1016/j.atmosenv.2011.09.024.

Ziereis, H., H. Schlager, P. Schulte, P. van Velthoven, and F. Slemr, 2000: Distributions of NO, NO_x, and NO_y in the upper troposphere and lower stratosphere between 28° and 61°N during POLINAT 2. *J. Geophys. Res.*, **105**, 3653–3664, https://doi.org/10.1029/1999JD900870.

——, and Coauthors, 2022: Redistribution of total reactive nitrogen in the lowermost Arctic stratosphere during the cold winter 2015/2016. *Atmos. Chem. Phys.*, **22**, 3631–3654, https://doi.org/10.5194/acp-22-3631-2022.

4.3.3 Mass spectrometric measurements of ambient ions during CAFE-EU/BLUESKY

Atmos. Chem. Phys., 22, 11781–11794, 2022
https://doi.org/10.5194/acp-22-11781-2022

Atmospheric Chemistry and Physics
Open Access
EGU

Mass spectrometric measurements of ambient ions and estimation of gaseous sulfuric acid in the free troposphere and lowermost stratosphere during the CAFE-EU/BLUESKY campaign

Marcel Zauner-Wieczorek[1], Martin Heinritzi[1], Manuel Granzin[1], Timo Keber[1], Andreas Kürten[1], Katharina Kaiser[2], Johannes Schneider[2], and Joachim Curtius[1]

[1]Institute for Atmospheric and Environmental Sciences, Goethe University Frankfurt am Main, 60629 Frankfurt am Main, Germany
[2]Particle Chemistry Department, Max Planck Institute for Chemistry, 55128 Mainz, Germany

Correspondence: Marcel Zauner-Wieczorek (zauner-wieczorek@iau.uni-frankfurt.de)

Received: 30 March 2022 – Discussion started: 21 April 2022
Revised: 22 August 2022 – Accepted: 28 August 2022 – Published: 13 September 2022

Abstract. Ambient ions play an important role in atmospheric processes such as ion-induced new particle formation. While there are several studies of ambient ions for different layers of the atmosphere, data coverage for the free troposphere and especially the upper troposphere and lower stratosphere (UTLS) region is scarce. Here, we present the first airborne measurements of ambient ions using a high-resolution atmospheric pressure interface time-of-flight mass spectrometer (HR-APi-TOF-MS) in the free troposphere and lower stratosphere above Europe on board the HALO aircraft during the CAFE-EU/BLUESKY campaign in May and June 2020. In negative measurement mode, we observed nitrate and hydrogen sulfate and their related ion clusters in an altitude range of 4.7 to 13.4 km. The horizontal profiles for those ions reveal an increasing count rate for NO_3^- and $(HNO_3)NO_3^-$ towards higher altitudes but no significant trend for $HSO4^-$. From the count rates of the nitrate (NO_3^-) and hydrogen sulfate (HSO_4^-) core ions, we inferred the number concentration of gaseous sulfuric acid. The lowest average value was found to be 1.9×10^5 cm^{-3} at the maximum altitude bin, i.e. 13.4 km. The highest average value of 7.8×10^5 cm^{-3} was observed in the 8.7–9.2 km altitude bin. During the transit through a mixed-phase cloud, we observed an event of enhanced ion count rates and aerosol particle concentrations that can largely be assigned to nitrate ions and particles, respectively; this may have been caused by the shattering of liquid cloud droplets on the surface of the aircraft or the inlet. Furthermore, we report the proof of principle for the measurement of ambient cations and the identification of protonated pyridine.

1 Introduction

Earth's atmosphere contains not only neutral gases, but also ions in the gas phase that play a crucial role in several atmospheric processes such as ion-induced nucleation of aerosol particles (Hirsikko et al., 2011). For a long time, the measurement of atmospheric ions has been the only means to infer qualitative and quantitative information on the composition of certain neutral compounds of the atmosphere; as an example, the atmospheric concentration of sulfuric acid, one of the most important substances involved in new particle formation (Seinfeld and Pandis, 2006), has historically been determined using ambient ion data.

The most important sources of ionisation from the ground level up to about 50 km altitude are galactic cosmic rays (GCRs) and, close to the Earth's surface, the radioactive decay of radon (Viggiano and Arnold, 1995; Bazilevskaya et al., 2008). GCRs consist mostly of protons and α particles, and these are able to penetrate the Earth's atmosphere. When

Published by Copernicus Publications on behalf of the European Geosciences Union.

their energy is high enough, secondary pions and muons are formed in nuclear–electromagnetic cascades. These secondary pions and muons interact with atmospheric compounds and cause their ionisation (Bazilevskaya et al., 2008). Predominantly, N_2^+, O_2^+, N^+, and O^+ cations are formed along with electrons. The electrons interact rapidly with oxygen, forming O_2^- and O^- (Arijs, 1992; Arnold and Knop, 1987; Shuman et al., 2015; Viggiano and Arnold, 1995). The cations quickly react to NO^+ and subsequently to proton hydrates, i.e. $H^+(H_2O)_n$. The anions react to $(H_2O)_nCO_3^-$ and subsequently to $(H_2O)_nNO_3^-$ (Arijs, 1992; Shuman et al., 2015). As the aforementioned reactions occur so rapidly and the lifetimes of the resulting ion clusters, i.e. $H^+(H_2O)_n$ and $(H_2O)_nNO_3^-$, are relatively long, they can be considered the starting points for the ion chemistry of the stratosphere and troposphere (Shuman et al., 2015; Viggiano and Arnold, 1995). For further details of the ionisation in the atmosphere, the article by Bazilevskaya et al. (2008) provides an overview, whilst, for the ion chemistry of the upper troposphere, Shuman et al. (2015) offer a comprehensive review.

The subsequent negative ion chemistry in the troposphere and stratosphere is comparatively simple. The water–nitrate clusters, $(H_2O)_nNO_3^-$, are able to take up nitric acid or exchange water molecules with nitric acid, yielding clusters of the type $(HNO_3)_m(H_2O)_nNO_3^-$ (Shuman et al., 2015; Viggiano and Arnold, 1995). Acids, HX, with a larger gas-phase acidity than HNO_3 can participate in a charge transfer reaction with NO_3^- and ligand exchange reactions with HNO_3, leading to clusters of the type $(HX)_k(HNO_3)_m(H_2O)_nX^-$. For most of the troposphere and stratosphere, only sulfuric acid (H_2SO_4) fulfils this requirement while being sufficiently abundant (Viggiano and Arnold, 1995). It is only closer to the ground that strong and abundant acids such as malonic acid ($CH_2(COOH)_2$), methanesulfonic acid (CH_3SO_3H), or iodic acid (HIO_3) can also be observed as part of the ion clusters (Ehn et al., 2010; Eisele, 1989a; Frege et al., 2017; Viggiano and Arnold, 1995; He et al., 2021; Beck et al., 2022a). It should be noted that, practically, the only source for HSO_4^- ions and their ion clusters is the reaction of gaseous sulfuric acid with nitrate (clusters) (Viggiano and Arnold, 1995). The direct ionisation of sulfuric acid is negligible. Throughout the troposphere and stratosphere, ion clusters with an NO_3^- core ion are predominant, except for the altitude range of around 35 to 40 km; here, the HSO_4^- core ion family is predominant. However, it is also abundant throughout the whole troposphere and stratosphere, but to a lesser extent than the NO_3^- core ion family (Viggiano and Arnold, 1995).

Knowledge of the abundance of the neutral species HNO_3 and H_2SO_4 in the upper parts of the atmosphere is mainly derived from calculations based on the measurements of the aforementioned ambient ions (Arnold and Fabian, 1980; Heitmann and Arnold, 1983; Arnold and Qiu, 1984). This calculation will be discussed in detail later. Direct measurements of the neutral trace compounds have been few, and their results are only available for a limited part of the atmosphere. Measurements of neutral gaseous sulfuric acid above the boundary layer have been performed at various altitude ranges: 3 to 11 km above the Arctic (Möhler and Arnold, 1992), 0 to 7.5 km in mid-latitudes and polar latitudes (Mauldin et al., 2003), 0 to 6 km above the southern Pacific Ocean (Weber et al., 1999, 2001), 0 to 7 km above the western Pacific Ocean (Weber et al., 2003), and on two mountain research sites in the Alps (Zugspitze, Germany, 2650 m a.s.l., Aufmhoff et al., 2011; Jungfraujoch, Switzerland, 3580 m a.s.l., Bianchi et al., 2016). The reported concentrations of sulfuric acid are high in the boundary layer ($> 10^7\,cm^{-3}$ possible), low in the free troposphere (4×10^5 to $4\times10^6\,cm^{-3}$), and slightly enhanced in the tropopause; however, in the lower stratosphere, the concentrations are lower again (10^5 to $10^6\,cm^{-3}$) according to Möhler and Arnold (1992). The most recent airborne measurements of neutral compounds using a chemical ionisation source in the negative ion mode were performed by our group during the CAFE-EU/BLUESKY campaign in 2020; the results will be presented in detail elsewhere. Early airborne measurements of nitric acid were performed from the 1990s (Hoell et al., 1997, 1999). Iodide-adduct chemical ionisation mass spectrometry (CIMS) is one of the most sensitive methods used nowadays for airborne HNO_3 detection (Lee et al., 2018; Dörich et al., 2021). Measurements in the upper troposphere and lower stratosphere (UTLS) showed that HNO_3 concentrations are low in the free troposphere and enhanced in the stratosphere (Schneider et al., 1998; Schumann et al., 2000; Jurkat et al., 2016).

Positive ion chemistry in the troposphere and stratosphere, on the other hand, involves acetonitrile, pyridine, ammonia, and amines (Viggiano and Arnold, 1995). Bases, B, with higher proton affinities than water, if sufficiently abundant, can react with the proton hydrates via ligand exchange to form clusters of the type $H^+(H_2O)_n(B)_m$. One prominent B compound found throughout the troposphere and stratosphere is acetonitrile (CH_3CN), while around the tropopause, methanol (CH_3OH) and acetone ($(CH_3)_2CO$) also become important, and, in the lower troposphere, ammonia (NH_3), pyridine (C_5H_5N) and several amines are molecules which are found to form clusters of the aforementioned type (Viggiano and Arnold, 1995). Ascending from the ground level towards higher altitudes, the predominant positive core ions are ammonium, protonated pyridine and protonated amines (0–5 km), protonated acetone (5–12 km), protonated acetonitrile (12–30 km), and proton hydrates (> 30 km) (Viggiano and Arnold, 1995).

The first rocket-borne mass spectrometric measurements of atmospheric ions were conducted in the mesosphere and ionosphere (above 64 km) (Johnson et al., 1958; Narcisi and Bailey, 1965; Narcisi et al., 1971; Arnold et al., 1971), leading to the identification of key species such as O^+, O_2^+, H_3O^+, O_2^-, CO_3^-, and NO_3^-, amongst others. In subsequent years, the investigations were extended to lower parts of the atmosphere and included an ever-growing number of identi-

fied ions. Arnold et al. (1977) reported the first rocket-borne measurements in the stratosphere, which were then followed by balloon-borne investigations (Arijs et al., 1978; Arnold et al., 1978; Arnold and Henschen, 1978). By employing mass spectrometers on aircraft, the lower stratosphere and upper troposphere could also be sampled (Heitmann and Arnold, 1983; Arnold et al., 1984). In addition, in the 1980s, Fred Eisele's group performed ground-based experiments in the boundary layer and in the lower free troposphere on mountain research stations (Perkins and Eisele, 1984; Eisele, 1986, 1988, 1989a, b). With all of these studies, measurements of the negative, as well as the positive, ions in the atmospheric range of 0 to more than 100 km altitude have been covered, unravelling a multitude of atmospheric compounds. Nevertheless, these measurements have been few, and questions of the reproducibility and variability of the results cannot be fully resolved. At the beginning of the 1990s, the development of chemical ionisation sources allowed for the direct measurement of neutral trace gases of interest. Indirect measurements utilising the detection of atmospheric ions became scarcer. Since then, to our knowledge, only Möhler et al. (1993) have presented measurements of ambient ions in the UTLS (although these were combined with chemical ionisation measurements), while Eichkorn et al. (2002) observed the existence of large positive ion clusters with masses of up to 2500 Da in the upper troposphere, providing evidence for the ion-induced nucleation of aerosol particles. In addition, Arnold et al. (1998) measured the gaseous ion composition in the exhaust plume of a jet aircraft in flight and derived the number concentration of gaseous sulfuric acid.

The introduction of high-resolution time-of-flight mass spectrometers (HR-TOF-MSs) allowed for a better signal identification of mass spectra, which was also applied to the field of ambient ion measurements. Junninen et al. (2010) presented the first HR-TOF-MS to measure the composition of atmospheric ions. Consequently, this group was also able to identify an enormous number of ambient ions via ground-based measurements in a boreal forest in Hyytiälä, Finland, including organic ion clusters (Ehn et al., 2010). Frege et al. (2017) characterised ambient ions in the lower part of the free troposphere with measurements at the Jungfraujoch research station in Switzerland at 3454 m a.s.l. The dominant negative ions identified were assigned to sulfuric, nitric, malonic, and methanesulfonic acid. Positive ions were assigned to amines, ammonia, and organic clusters. More recently, Beck et al. (2022a) conducted airborne measurements of ambient ions above the boreal forest at an altitude range of 0 to 3200 m around the Station for Measuring Ecosystem Atmospheric Relations (SMEAR) II in Hyytiälä. They identified ions belonging to nitric, iodic, methanesulfonic, sulfuric, and carboxylic acid, as well as highly oxygenated organic molecules (HOMs). Furthermore, they reported diurnal variations of the ions depending on the changing atmospheric layers at different periods of the day. Beck et al. (2022b) also derived concentrations of gaseous sulfuric acid from the measurements of ambient ions. They were able to validate their calculations with chemical ionisation mass spectrometric measurements for daytime in the boreal forest.

In this work, we present the first aircraft-borne measurements of ambient ions with an HR-TOF-MS in the UTLS during the CAFE-EU/BLUESKY campaign in May and June 2020, allowing for an unambiguous identification of the observed ions. We present the observed mass spectrum of negative ambient ions and show the altitude dependence of the most important ions. From the ion signals of nitrate and hydrogen sulfate core ions, we derive an estimate for the gaseous sulfuric acid concentration. For the measurement of positive ambient ions, we provide a proof of principle and a first identification of observed signals.

2 Methods

2.1 Instruments

We used an HR-TOF-MS (Tofwerk AG, Thun, Switzerland) in combination with a new in-house developed and manufactured chemical ionisation (CI) source, named the Switchable CORona Powered ION source (SCORPION); this will be described in more detail in an upcoming publication. The main purpose of this setup was to enable nitrate reagent ion-based CI-TOF-MS measurements on board the High Altitude and LOng range research aircraft (HALO). However, by setting all voltages (including the corona voltage) in the SCORPION source to zero, i.e. to the same potential as the entrance pinhole of the TOF-MS, the measurement of ambient ions was enabled. This measurement mode is called the atmospheric pressure interface (APi) mode. We used an inlet system that is almost completely manufactured from metal in order to avoid the build-up of electrostatic charge spots, which would then deflect the incoming ambient ions to the walls. The only non-metal piece in the inlet system was a 2 mm thick polyether ether ketone (PEEK) spacer that electrically isolates the inner parts of the ion source from the inlet tube. Between the inlet line and the mass spectrometer, two pressure stages regulated by mass flow controllers and critical orifices allowed for a constant pressure of 200 hPa in the ion source (in the APi mode, the ion source can be considered a pressure-controlled pre-chamber in front of the MS). Our inlet system was designed to minimise wall losses; this is beneficial for both chemical ionisation and the ambient ion mode. Nevertheless, certain losses of ions to the inlet walls or in the pressure stages are unavoidable. It can be assumed, however, that the different ions are affected similarly. We used the LiF-OH inlet system that was specifically developed for HALO (this is usually used for OH measurements with the laser-induced fluorescence technique – LiF; Broch, 2011), as well as a 25 mm outer diameter, 1.7 m long stainless-steel inlet tube with high flow (10 to 30 slpm, depending on the flight altitude) to connect the inlet with our instrument. The TOF-MS records data at a 1 Hz acquisition fre-

quency in an m/z range from 4 to 1121, with a mass resolution of $\Delta m/m = 2500$ to 3000 and a mass accuracy of 5 ppm for NO_3^-. From studies on the mass-dependent transmission of the same mass spectrometer (Heinritzi et al., 2016) using a different corona-induced nitrate CI source (Kürten et al., 2011), we estimate a maximum scaling factor of 2 for the transmission difference between NO_3^- and HSO_4^-, which is within our overall experimental uncertainty.

The chemical composition of submicron aerosol particles was measured using a compact time-of-flight aerosol mass spectrometer (C-TOF-AMS) (Drewnick et al., 2005; Schulz et al., 2018). The C-TOF-AMS uses a constant pressure inlet (Molleker et al., 2020) followed by an aerodynamic lens to sample particles in a size range between about 40 and 800 nm from ambient air and then focuses the particle beam onto a tungsten vaporiser operated at 600 °C. The non-refractory components of the particles are vaporised and the gas molecules are ionised by electron impact. The ions are then extracted into the time-of-flight mass spectrometer and detected by a multichannel plate detector. During CAFE-EU/BLUESKY, the C-TOF-AMS was operated at a time resolution of 30 s. The detection limits lie in the range between 20 and 110 ng m^{-3}, depending on the species measured (Schulz et al., 2018).

Particle size distributions for particles larger than 250 nm in diameter were measured using an optical particle spectrometer (Grimm 1.129 Sky-OPC). The nominal size range of this instrument ranges from 250 nm to 32 µm, divided into 31 size channels. Here, the upper size limit was determined by the aerosol inlet of HALO, whose upper size cut lies around 5 µm. The time resolution was 6 s.

The relative humidity was measured by the Sophisticated Hygrometer for Atmospheric ResearCh (SHARC), which employs a tuneable diode laser (TDL) system. Within clouds, the measurement of the relative humidity can be influenced by the evaporation of cloud particles, and thus measured relative humidities exceeding 100 % are possible. Basic meteorological and flight parameters, such as temperature, aircraft position, and altitude, were measured by the BAsic HAlo Measurement And Sensor system (BAHAMAS). More information on the instrumentation of the aircraft during the CAFE-EU/BLUESKY campaign is given in the overview publication by Voigt et al. (2022).

2.2 Measurement flights

The aforementioned instruments, amongst others, were installed on board the HALO research aircraft for the CAFE-EU/BLUESKY campaign. During the campaign, one test flight and eight scientific flights were performed between 21 May and 9 June 2020, i.e. during the COVID-19 lockdowns in most European countries. All flights commenced and terminated at Oberpfaffenhofen airport (Bavaria, Germany). The area covered included Germany, the Netherlands, Switzerland and Italy (flight nos. 01 to 03), the North Atlantic Flight Corridor including Ireland and the United Kingdom (04 and 05), and France, Italy, and Spain bordering the Mediterranean Sea (06 to 08). Details of the campaign are given in the overview publication by Voigt et al. (2022).

During the eight flights, the SCORPION-TOF-MS was operated in the chemical ionisation mode for the majority of the time. During flight nos. 04 to 08, measurements in the APi mode were performed for at least two periods for each flight (called segments). In the negative APi mode, we took data for a total period of 363 min (6 h), covering an altitude range of 4.7 to 13.5 km, a latitude range of 43.0 to 52.9° N, and a longitude range of −13.3 to 10.8° E. In the positive mode, we performed one measurement for 86 min, covering an altitude range of 0.6 to 12.7 km, a latitude range of 47.1 to 48.5° N, and a longitude range of 8.0 to 12.4° E. The details for all APi measurements are summarised in Table 1. For a better overview, the flight tracks of all APi measurements are shown in Fig. 1.

2.3 Data analysis

The recorded mass spectrometric data were post-processed using the IGOR-based *Tofware* software provided by Aerodyne Research Inc. Corrupted data caused by interference of the data acquisition unit with mobile and Wi-Fi radiation were removed. This interference occurred mainly while HALO was on the apron and only affected < 0.2 % of the data obtained during each flight (except flight 01: 1 % of the data). The uncorrupted data were then averaged to 30 s. For typical ground speeds of 160 to 240 m s^{-1}, this relates to a covered ground distance of 5 to 7 km for one averaged data point. The subsequent post-processing included a detailed mass calibration, baseline subtraction, peak identification, and peak integration. The integrated peak values were normalised by the total ion count, yielding the normalised count rates, nCR.

In the laboratory, background measurements of pure synthetic air were conducted. Reproducible peaks occurred at certain mass-to-charge ratios m/z in a range up to 80, with 16, 26, and 19 being the most dominant ones in the negative mode. These background peaks were likely caused by internal chemical processes in the mass spectrometer as their respective appearances were dependent on the sample gas such as synthetic air, nitrogen, or argon. These peaks could also be found in the experimental spectra of the in-flight measurements. As their relative abundance was roughly constant, they were subtracted from the recorded mass spectra of the measurement flights. The only notable overlap with observed ambient ions in the negative mode occurred at nominal mass 62; the ambient ion signals were much stronger than the laboratory background signals at nominal mass 62. The laboratory background signal was 5 % of the total recorded signal at $m/z = 62$ in the highest altitude bin (13.3 km), whilst it constituted 15 % of the total recorded signal in the lowest altitude bin (4.7–5.3 km). These values are within the general mea-

Table 1. Details for all flights in which measurements in the APi mode were conducted.

Flight no. and segment	Mode	Date	Time [UTC]	Duration [min]	Latitude [° N]	Longitude [° E]	Altitude [km]
04.1	negative	30 May 2020	08:08–09:37	89	50.3…52.2	−13.3…9.8	11.1…11.9
04.2	negative	30 May 2020	13:52–15:03	71	50.5…52.2	−9.7…4.6	10.9…11.0
05.1	negative	2 June 2020	09:04–09:55	51	50.3…52.2	−13.3…−3.5	12.2…12.3
05.2	negative	2 June 2020	13:23–14:00	37	51.6…52.9	−8.2…−0.5	13.4…13.5
05.3	negative	2 June 2020	14:43–15:11	28	48.6…49.9	7.8…10.8	4.7…9.7
06.1	negative	4 June 2020	08:25–08:41	16	46.6…47.5	6.5…8.8	11.3
06.2	negative	4 June 2020	10:59–11:06	7	43.0…43.4	9.6…10.1	5.3
07.1	negative	6 June 2020	08:16–08:32	16	47.1…47.7	7.2…9.3	10.2
07.2	negative	6 June 2020	09:38–09:53	15	43.7…44.9	−0.4…1.2	10.2…10.3
08.1	negative	9 June 2020	08:21–08:54	33	45.4…47.4	4.0…8.4	9.2
all negative	negative			363	43.0…52.9	−13.3…10.8	4.7…13.5
08.2	positive	9 June 2020	14:31–15:57	86	47.1…48.5	8.0…12.4	0.6…12.7

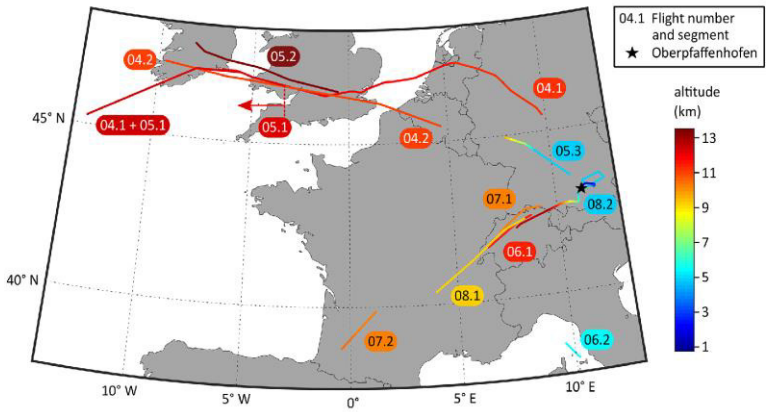

Figure 1. Map showing the flight tracks during the taking of measurements in the APi mode. The colour code indicates the flight altitude. The labels indicate the flight number and segment. The star represents Oberpfaffenhofen airport. National border data were obtained from Greene et al. (2019).

surement uncertainty. Attempting to subtract a background-related portion from the signal recorded during the flights may be detrimental to the results, and therefore this process was omitted.

2.4 Quantification of gaseous sulfuric acid

To quantify the number concentration of gaseous sulfuric acid, we used the steady-state method developed by Arnold and Fabian (1980), which is described in more detail by Arnold and Qiu (1984). This is based on the assumption that hydrogen sulfate ions are virtually only produced by charge transfer from nitrate to sulfuric acid, as given in Reaction (R1).

$$H_2SO_4 + NO_3^- \rightarrow HSO_4^- + HNO_3 \quad \text{(R1)}$$

Nitrate and hydrogen sulfate ions cluster with HNO_3 and H_2SO_4 ligands, yielding $(HNO_3)_m NO_3^-$, called nitrate core ions, and $(H_2SO_4)_k(HNO_3)_m HSO_4^-$, called hydrogen sulfate core ions, respectively (see also Sect. 1). Assuming that other source reactions for HSO_4^- core ions and the aerosol sink are negligible and that the ions recombine subsequently after the reaction, Arnold and Qiu (1984) presented Eq. (1a) to calculate the number concentration of sulfuric acid from the ratio of the product ions (i.e. the HSO_4^- core ions) and the precursor ions (i.e. the NO_3^- core ions) for steady-state conditions:

$$[H_2SO_4] = \frac{1}{k \cdot t_{\mathrm{rec}}} \cdot \frac{\mathrm{CR}\left(HSO_4^-\right)}{\mathrm{CR}\left(NO_3^-\right)}, \quad \text{(1a)}$$

where $\mathrm{CR}(HSO_4^-)$ and $\mathrm{CR}(NO_3^-)$ represent the instrument's count rates of HSO_4^- core ions (i.e. in our case HSO_4^-,

$(HNO_3)HSO_4^-$, and $(H_2SO_4)HSO_4^-$) and NO_3^- core ions (i.e. in our case NO_3^-, $(HNO_3)NO_3^-$, and $(HNO_3)_2NO_3^-$), respectively, in counts per second (cps); k, the reaction rate constant, is 2×10^{-9} cm^3 s^{-1} (Viggiano et al., 1997); and t_{rec} is the ion–ion recombination lifetime in seconds. Equation (1a) represents the special case when $CR(HSO_4^-) \ll CR(NO_3^-)$. This is not always the case; thus, the more accurate logarithmic term according to Eq. (1b) is used (Heinritzi et al., 2016):

$$[H_2SO_4] = \frac{1}{k \cdot t_{rec}} \cdot \ln\left(1 + \frac{CR\left(HSO_4^-\right)}{CR\left(NO_3^-\right)}\right). \quad (1b)$$

The ion–ion recombination lifetime can be calculated with Eq. (2):

$$t_{rec} = \frac{n_+}{q}, \quad (2)$$

where n_+ is the number concentration of positive ions and q is the ion pair production rate. To calculate n_+, Eq. (3) can be used (Franchin et al., 2015):

$$\frac{dn_\pm}{dt} = q - \alpha n_+ n_- - k_{CS} n_\pm, \quad (3)$$

where α is the ion–ion recombination coefficient, and k_{CS} is the condensation sink coefficient. Assuming $n_+ \approx n_-$ and that the term for the condensation sink is negligible due to little aerosol surface in the UTLS for ions to condense onto, Eq. (3) can be simplified to Eq. (4):

$$\frac{dn_\pm}{dt} = q - \alpha n_+^2. \quad (4)$$

For steady-state conditions, Eq. (5) is attained (Thomson and Rutherford, 1896):

$$n_+ = \sqrt{\frac{q}{\alpha}}. \quad (5)$$

α is given as 1.6×10^{-6} cm^3 s^{-1} for conditions at sea level in today's literature (Franchin et al., 2015). This value is taken from Israël (1957, 1971). However, α is temperature- and pressure-dependent and must be adjusted when used for altitudes above 10 km. In a separate work, we discussed different parameterisations and models of the ion–ion recombination rate and concluded that the parameterisation of Israël (1957) is favourable for the troposphere and lower stratosphere (Zauner-Wieczorek et al., 2022); this is characterised by Eq. (6):

$$\alpha = 1.95 \times 10^{-6} \cdot \left(\frac{273}{T}\right)^{1.5} \cdot \varepsilon, \quad (6)$$

where α is in cubic centimetres per second (cm^3 s^{-1}), T is the temperature in Kelvin, and ε is the probability for a successful recombination, given by Eq. (7):

$$\varepsilon = 1 - \frac{4}{x^4} \cdot \left[1 - e^{-x} \cdot (x+1)\right]^2, \quad (7)$$

with

$$x = 0.810 \cdot \left(\frac{273.15}{T}\right)^2 \cdot \left(\frac{p}{1013.25}\right) \cdot \frac{\lambda_{air}}{\lambda_{ion}}, \quad (8)$$

where p is the pressure (hPa), λ_{air} is the mean free path of the surrounding air, λ_{ion} is the mean free path of the ion, and the ratio $\lambda_{air} \cdot \lambda_{ion}^{-1} = 5$.

Notably, this parameterisation yields an almost constant value of approximately 1.7 to 1.8×10^{-6} cm^3 s^{-1} for α from the ground level up to 11 km when the values for the US Standard Atmosphere (National Oceanic and Atmospheric Administration et al., 1976) are used; this is close to the above-mentioned value of 1.6×10^{-6} cm^3 s^{-1}. Above 11 km, the value decreases rapidly, with $\alpha = 1.2 \times 10^{-6}$ cm^3 s^{-1} at 15 km altitude.

The ion production rate q is dependent on the altitude, geomagnetic latitude, and solar activity (Bazilevskaya et al., 2008). While a typical value for q at sea level is 2 ion pairs cm^{-3} s^{-1} (Hensen and van der Hage, 1994), the ion production rate increases with increasing altitude until it reaches a maximum value of 37 ion pairs cm^{-3} s^{-1} at 11 to 14 km for polar latitudes (Bazilevskaya et al., 2008). Moreover, as the ionisation by GCRs is stronger at the poles than at lower latitudes, the geomagnetic latitude must be taken into account. This can also be resembled by the geomagnetic cut-off rigidity, R_C, representing the shielding effect of the Earth's magnetic field (Smart and Shea, 2005). For the latitude range we covered during the measurement flights (43 to 53° N), a geomagnetic cut-off rigidity (R_C) of 2 to 6 GV must be applied (Smart and Shea, 2009); therefore, we estimated a value for q of 90 % of the maximum polar value of q (Bazilevskaya et al., 2008) for this data set. Furthermore, solar activity influences the ion production in the atmosphere. Strong solar activities lead to deflection of GCRs and consequently a weaker ionisation; this is especially the case at an altitude of 11 km where the modulation of q is highly dependent on the 11-year solar cycle, leading to a 20 % to 25 % difference in q between solar activity maxima and minima (Bazilevskaya et al., 2008). In May and June 2020, the solar activity was at a minimum (Royal Observatory of Belgium, 2020); thus, maximum values for q had to be considered. Based on the conditions during our sampling (elaborated above) and the dependencies of q summarised by Bazilevskaya et al. (2008), we estimated an ion pair production rate of 30 ion pairs cm^{-3} s^{-1} for our data.

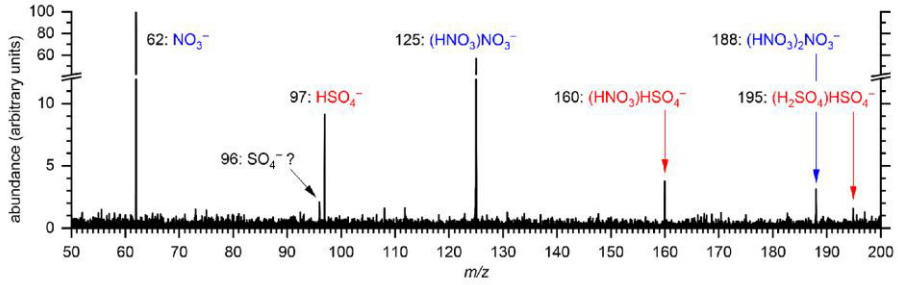

Figure 2. Mass spectrum of ambient negative ions averaged for all measurements in the negative APi mode (i.e. averaged over 6 h). Ions with a nitrate core ion are labelled in blue; those with a hydrogen sulfate core ion are labelled in red.

3 Results and discussion

3.1 Negative ions

3.1.1 Mass spectrum

Figure 2 shows the average mass spectrum for all measurements in the negative APi mode. The most dominant peak was at $m/z = 62$ and was assigned to nitrate, NO_3^- (monomer), followed by the dimer cluster of nitric acid with nitrate, $(HNO_3)NO_3^-$ ($m/z = 125$). In addition, the trimer cluster $(HNO_3)_2NO_3^-$ (188) could be observed. As expected in the UTLS, hydrogen sulfate, HSO_4^- (97), was detected as were its clusters with nitric acid (160, $(HNO_3)HSO_4^-$) and sulfuric acid (195, $(H_2SO_4)HSO_4^-$). Evidence for further clusters with NO_3^- or HSO_4^- core ions could not be retrieved from the mass spectrum, as either their concentrations are too low to exceed the background noise or they experienced fragmentation in the APi section of the instrument and were thus detected as one or more of the above-mentioned ions. The peak at nominal mass 96 could not be assigned to SO_4^- for certain due to the measured exact m/z value being 95.973 compared to the mass of 95.952 of SO_4^-. Water clusters such as $(H_2O)NO_3^-$ (80) could not be observed. The detected peak at nominal mass 80 was also present in the background laboratory measurements and did not exceed the level of the background measurements during the in-flight measurements. The observed ions and their exact masses are listed in Table 2.

The (almost) exclusive detection of the NO_3^- or HSO_4^- core ions in the ambient ion mass spectrum is typical for the UTLS region and is in accordance with previous measurements (Heitmann and Arnold, 1983). The most notable discrepancy from Heitmann and Arnold's results is the relative abundance of the signals. They found $(HNO_3)_2NO_3^-$ to be the most abundant species, followed by $(HNO_3)NO_3^-$ and $(HNO_3)_2HSO_4^-$, with only a slight amount of NO_3^-. In our findings, the smaller ions were more abundant than the bigger clusters. Unfortunately, the resolution was comparatively low in the earlier studies so that the peak identified as the trimer (labelled with the m/z value 188 ± 2) is wide enough to easily include other species with m/z ratios of approximately 170 to 205. Possible explanations for this discrepancy are different mass-dependent transmission efficiencies between Heitmann and Arnold's instrument and ours or the potential fragmentation of larger clusters in our instrument. After the CAFE-EU/BLUESKY campaign, we found that the internal voltage settings of the MS can be further improved in order to detect the ion clusters with larger m/z values more efficiently.

Table 2. Observed signals in the negative mass spectra with their exact mass-to-charge ratio, m/z, and the assigned ions.

m/z	Ion	Remarks
61.988	NO_3^-	
95.973	SO_4^- (?)	exact mass of SO_4^-: 95.952 Da
96.960	HSO_4^-	
124.984	$(HNO_3)NO_3^-$	
159.956	$(HNO_3)HSO_4^-$	
187.980	$(HNO_3)_2NO_3^-$	
194.927	$(H_2SO_4)HSO_4^-$	

3.1.2 Altitude dependence of the ions and quantification of sulfuric acid

Figure 3 shows the altitude dependence of the most abundant ions and gaseous sulfuric acid. Furthermore, the range of the tropopause (10 to 11 km) is indicated by grey shading. In Fig. 3a and b, the normalised count rates of NO_3^- and $(HNO_3)NO_3^-$, respectively, are shown as a function of the altitude in a box plot. The vertical distributions of the count rates of NO_3^- and $(HNO_3)NO_3^-$ show an increasing trend with increasing altitude. The normalised count rates of both ions are elevated above 11.5 km, i.e. elevated in the lower stratosphere compared to the free troposphere. While the values might not differ significantly from one altitude bin to another, the difference between, for instance, the 13.4 km and the 11.0–11.3 km bins is substantial. The average nor-

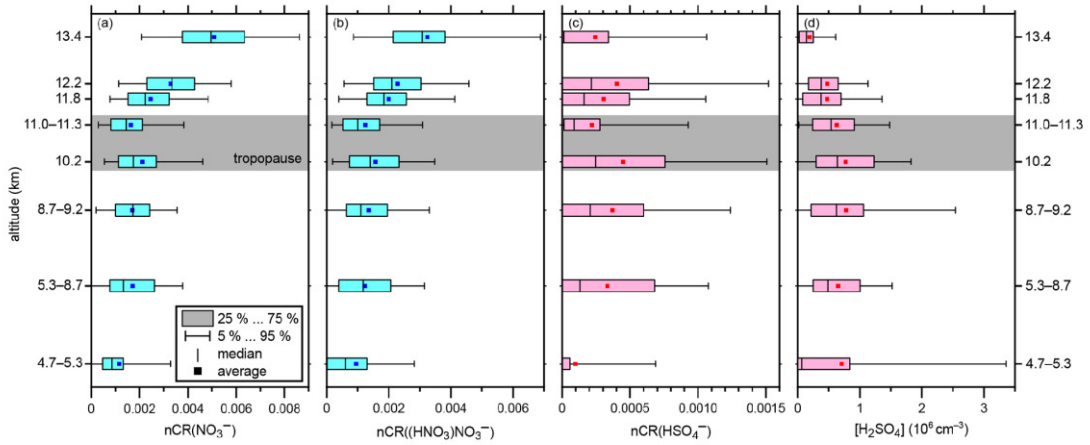

Figure 3. Altitude-resolved box plots of the normalised count rates (nCR) of **(a)** NO_3^-, **(b)** $(HNO_3)NO_3^-$, and **(c)** HSO_4^- (all dimensionless). **(d)** The number concentration of gaseous H_2SO_4 (in cm^{-3}). Please note the different x-axis ranges. The boxes indicate the interquartile range. The outer bars indicate the range of all data points except for the lowermost 5 % and uppermost 5 %. The vertical bars inside the boxes indicate the respective medians, and the squares indicate the respective averages. The grey shading indicates the range of the tropopause.

malised count rates (squares in Fig. 3) for the 13.4 km bin are 5.1×10^{-3} for NO_3^- and 3.2×10^{-3} for $(HNO_3)NO_3^-$. For the 11.0–11.3 km bin, the average count rates are about a factor of 3 lower (1.6×10^{-3} for NO_3^- and 1.2×10^{-3} for $(HNO_3)NO_3^-$). This finding is in accordance with the direct measurements of the corresponding neutral molecule, HNO_3, which has been found to be elevated in the stratosphere (Schneider et al., 1998; Schumann et al., 2000; Jurkat et al., 2016). For HSO_4^-, a clear altitude dependence cannot be retrieved from our data, as Fig. 3c shows. The differences between two altitude bins can be as high as a factor of 2 (e.g. 2.2×10^{-4} at 11.0–11.3 km compared to 4.5×10^{-4} at 10.2 km). The value of 0.97×10^{-4} at 4.7–5.3 km is comparatively small, although the number of data points below 8.3 km is low, and thus the informative value should not be overestimated.

For every 30 s averaged data tuple of the respective sums of the count rates of the NO_3^- core ions and the HSO_4^- core ions, the number concentration of sulfuric acid was calculated according to Eq. (1b). From Eqs. (5) and (2), we derived the number concentration of positive ions n_+ and the ion–ion recombination lifetime t_{rec} for every data tuple. The average $t_{rec} = 136$ s (129 to 151 s) and the average $n_+ = 4090\,cm^{-3}$ (3880 to 4540 cm^{-3}). We checked the term for the condensation sink for each flight (see Eq. 3), derived from the Sky-OPC data, and found that it was 2 orders of magnitude below the recombination term for each flight and that it was thus negligible, except for flight segment 06.2; this is addressed in more detail in the next subsection.

The results for the gaseous sulfuric acid number concentration, $[H_2SO_4]$, are shown as a box plot graph as a function of altitude in Fig. 3d. The smallest average value of $1.9 \times 10^5\,cm^{-3}$ H_2SO_4 was observed at the maximum altitude of 13.4 km. The averages increased with decreasing altitude up to $7.8 \times 10^5\,cm^{-3}$ H_2SO_4 in the 8.7–9.2 km bin; below this altitude, the average concentrations became slightly lower again.

If only the altitudes above 8.7 km, where the data coverage was better, are taken into account, the trend in average concentrations is in accordance with previous findings. Measurements conducted by Heitmann and Arnold (1983) in the altitude range of between 8 and 20 km above western Germany showed that the total number concentration of acidic sulfur gases, of which sulfuric acid is expected to be the most dominant, has a decreasing trend with increasing altitude, with the highest value of $10^7\,cm^{-3}$ being at the minimum altitude of 8 km compared to $10^6\,cm^{-3}$ at 12 km. It should be noted that the SO_2 emissions were significantly higher in Europe in the 1980s compared to today. SO_2 is the most important precursor to H_2SO_4 (Stockwell and Calvert, 1983; Seinfeld and Pandis, 2006). As a rough estimate, one can assume an SO_2 emission reduction of 90 % to 95 % from the mid-1980s to 2020 (Smith et al., 2011; European Environmental Agency, 2021). As SO_2 is the main source for sulfuric acid in the upper troposphere (Seinfeld and Pandis, 2006), the relatively high concentrations of sulfuric acid in the study by Heitmann and Arnold (1983) can be explained by this assumption. Möhler and Arnold (1992) reported H_2SO_4 mixing ratios for the altitude range of 6 to 12 km in northern Scandinavia during February 1987; the mixing ratio of sulfuric acid was slightly elevated in the tropopause region (2 to 6×10^{-14} around 9.5 to 10 km); otherwise, it remained at a rather con-

stant level (1×10^{-14}). When converted to number concentrations, the data reproduce the pattern observed by Heitmann and Arnold (1983), i.e. decreasing H_2SO_4 number concentrations with increasing altitude. The resulting number concentrations are between 6×10^5 cm^{-3} at 12 km and 1×10^4 cm^{-3} at 6 km and are thus much less than those reported by Heitmann and Arnold (1983); this is because there are no local pollution sources in the Arctic, even though the sampled air masses have travelled there from lower latitudes, which are more prone to pollution (Möhler and Arnold, 1992). In both studies, gaseous sulfuric acid concentrations were inferred from the ambient ion measurements of NO_3^- and HSO_4^- using the same approach that we used. In addition, the most recent model for tropospheric ion composition by Beig and Brasseur (2000), based on the observations from the 1980s and 1990s, predicts a strong increase in HSO_4^- core ions and H_2SO_4 below 15 km, with a maximum at around 8 km. Furthermore, Mauldin et al. (2003) reported uniformly low sulfuric acid concentrations in the free troposphere of typically 1 to 8×10^5 cm^{-3} between 5 and 7.5 km altitude and usually 0.5 to 2×10^6 cm^{-3} between 3 and 5 km. Note that the only two reference studies for detecting sulfuric acid in the UTLS by use of ambient ion measurements were conducted under dissimilar conditions compared to our study: Möhler and Arnold (1992) studied air masses in the Arctic winter with very low concentrations of H_2SO_4, whilst the results of Heitmann and Arnold (1983) were influenced by massively larger SO_2 emissions compared to today. Unfortunately, there are no other direct measurements of neutral sulfuric acid molecules in the UTLS reported in the literature. Thus, direct measurements of gaseous sulfuric acid in the UTLS by state-of-the-art chemical ionisation mass spectrometric techniques are needed for further comparison and validation of the ambient ion-inferred results.

3.1.3 In-cloud measurement

In this section, we report an interesting finding that may be attributed to an artefact. A unique observation within the CAFE-EU/BLUESKY data set was captured during APi measurement 06.2 on 4 June 2020 at 11:02 UTC, when the aircraft flew through a cloud at a flight altitude of 5.3 km. During this period, an incident of 30 s in duration consisting of high ambient ion count rates, high aerosol particle concentrations, and high humidity occurred. In Fig. 4, the relevant parameters for this incident are depicted. While the total ion count rate increased from approximately 51 to 61 ions s^{-1}, the total nitrate count rate (i.e. the sum of NO_3^-, $(HNO_3)NO_3^-$, and $(HNO_3)_2NO_3^-$) increased from 0.2–0.4 to 5.3 ions s^{-1}, being responsible for half of the total ion count increase (see Fig. 4a). Between 11:01:57 and 11:02:20 UTC, the relative humidity over water (RH) showed three peaks of 132 %–136 % compared to 114 % before and after this event (see Fig. 4b). Please note that the measurements of the relative humidity are influenced by the evaporation of

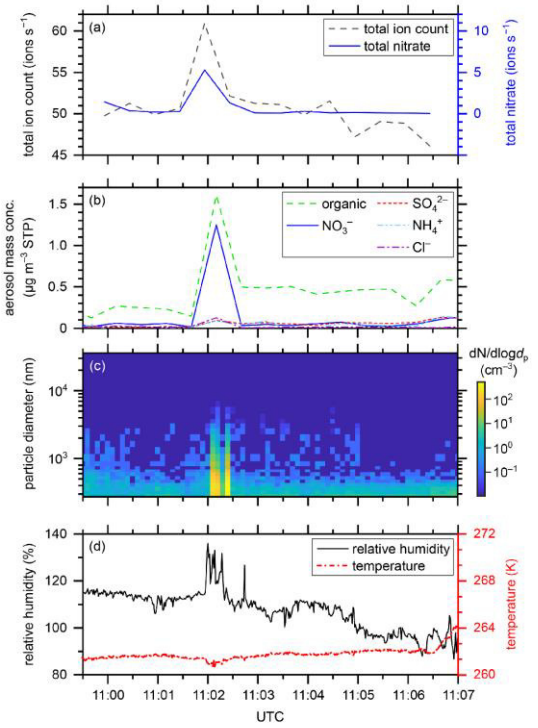

Figure 4. Gas-phase and particle-phase parameters during the APi measurement on flight segment 06.2 on 4 June 2020 above the Mediterranean Sea at a flight altitude of 5.3 km. **(a)** Total ion count rate (dashed black curve) and total nitrate count rate (solid blue curve) (ions s^{-1}) provided by the APi-TOF-MS, **(b)** aerosol mass concentration (µg per standard m^3), as indicated by the chemical composition, provided by the C-TOF-AMS, **(c)** aerosol particle size distribution (nm) and number concentration (cm^{-3}) provided by the Sky-OPC, and **(d)** relative humidity over liquid water (%) (solid black curve) provided by the SHARC as well as temperature (K) (dashed–dotted red curve) provided by the BAHAMAS.

cloud droplets during in-cloud measurements. Thus, the absolute numbers of RH are strongly overestimated here. Nevertheless, one can observe the increased peaks in RH during the event relative to the measured RH values before and after the event. The temperature, however, was constant at 261 K, only decreasing by less than 1 K during the humidity peak events. At this temperature, mixed-phase clouds consist mainly of liquid cloud droplets because the most common ice-nucleating particles, consisting of mineral dust, become active at lower temperatures (Hoose et al., 2010; Hoose and Möhler, 2012; Kanji et al., 2017). The aerosol mass concentration (Fig. 4c) peaked at 11:02:30 (at a time resolution of 30 s) with a total of 3.2 µg cm^{-3} (at standard temperature and pressure, STP). As in the case of the gas-phase ions, nitrate played an important role in this event, representing approxi-

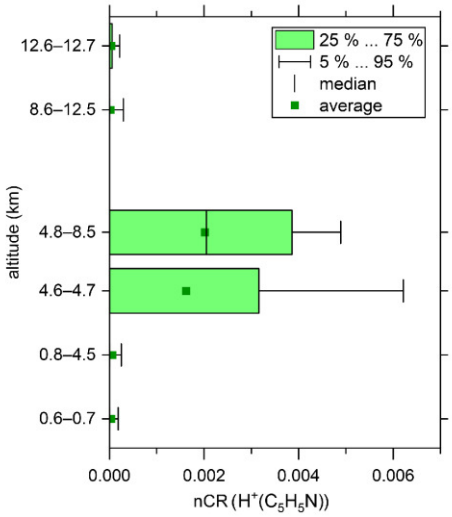

Figure 5. Altitude-resolved box plot of the normalised count rates (nCR) of $H^+(C_5H_5N)$. The boxes indicate the interquartile range. The outer bars indicate the range of all data points except for the lowermost 5 % and uppermost 5 %. The vertical bars inside the boxes indicate the respective medians, and the squares indicate the respective averages.

mately 40 % of the particle mass. Figure 4d reveals the particle size distribution and number concentration. Shortly after 11:02:00, two bands of increased particle number concentrations can be observed that correlate well with the peaks of the humidity data. The concentrations of all particle sizes up to 5 µm diameter increased by a factor of up to 100 compared to before and after the event. Most of the aerosol particles were smaller than 1 µm during the event.

Because the aircraft passed through a mainly liquid mixed-phase cloud during this event, it is likely that the shattering of liquid cloud droplets on the surface of the aircraft or the sampling system caused or at least contributed to the observed increase in aerosol mass concentration. We speculate that this observation can be explained by the balloelectric effect (Christiansen, 1913), which describes the generation of electric charge by the shattering of water droplets. In the process of water shattering on the aircraft or inlet surface, the concentration of ions increased; the subsequent reaction time in the inlet system was, however, too short for nitrate to react with other species in order to transfer its charge. It is known that nitric acid and organics are favourably taken up by liquid cloud droplets (e.g. Schneider et al., 2017), which can explain the dominance of nitrate and organics in the measured data. However, the effect of shattering cloud droplets on the ambient ion concentration is not straightforward such that the confident interpretation of these results requires further in-cloud measurements in the APi mode in the future.

3.2 Positive ions

We recorded the mass spectra of positive ambient ions for a total of 86 min during the end of the last measurement flight at an altitude range of 0.6 to 12.7 km. This data coverage does not allow for a detailed analysis of positive ambient ions as performed for the negative ions. However, we can provide the proof of principle for positive ambient ion analysis with our SCORPION-HR-TOF-MS device. We unambiguously detected protonated pyridine (80, $H^+(C_5H_5N)$), which was especially abundant between 4.6 and 8.5 km (see Fig. 5). Below 4.6 km and above 8.5 km altitude, almost no protonated pyridine was detected. This species was found to be the most abundant positive ion between 3 and 6 km in a previous study (Schulte and Arnold, 1990). There were also signals that strongly hinted to protonated acetonitrile (42, $H^+(C_2H_3N)$) and protonated acetone (59, $H^+(C_3H_6N)$); however, further studies with longer measurement durations must be performed to reliably distinguish those signals from the background and to detect and identify further positive ambient ions.

4 Conclusion

We have presented the first measurement of ambient ions in the free troposphere and lower stratosphere with an HR-APi-TOF-MS above Europe at an altitude range of 4.7 to 13.4 km. We identified the major ambient negative ions NO_3^- and HSO_4^- and their respective clusters with HNO_3 and H_2SO_4, confirming previously reported research. The nitrate core ions are dominant over the hydrogen sulfate ion family. For $(HNO_3)_{0,1}NO_3^-$ and HSO_4^-, the detailed altitude-resolved abundances are presented; the nitrate core ions are elevated in the stratosphere, whereas hydrogen sulfate shows no significant altitude trend. From the ratio of hydrogen sulfate to nitrate core ions, we inferred the number concentration of gaseous sulfuric acid. The resulting average values were determined to be 1.9 to $7.8 \times 10^5\,cm^{-3}$ for the altitude range of 4.7 to 13.4 km, with an overall observed decreasing trend towards higher altitudes. During the transit through a mixed-phase cloud, we observed an event of concurrent elevated aerosol particle concentrations and ambient ion counts that may be explained by the shattering of cloud water droplets on the surface of the airplane or inlet system. Nitrate played the dominant role in the chemical composition of both the measured ions and the particles. Furthermore, we provided a proof of principle for the measurement of positive ions and were able to unambiguously identify protonated pyridine ($H^+(C_5H_5N)$), which is especially abundant between 4.6 and 8.5 km altitude. For future research, more data need to be acquired in order to complete the altitude profiles of ambient ions, especially cations. In addition, up-to-date chemical ionisation mass spectrometric measurements of gaseous sulfuric acid are needed for the UTLS in order to compare and validate the data presented herein.

Code availability. The data shown in the figures were calculated according to the equations provided in the current paper. No numeric model calculations were performed, and therefore no software code was uploaded to a public data repository.

Data availability. Data are available on the HALO database upon request: https://halo-db.pa.op.dlr.de/mission/120 (last access: 8 September 2022) (https://doi.org/10.17616/R39Q0T; re3data.org, 2022).

Author contributions. MZW, MH, and JC designed the study. MZW, MH, MG, TK, KK, and JS prepared and conducted the experiments. MZW analysed the data. MZW, MH, AK, and JC discussed the results. MZW wrote the paper with contributions from MH and JS. All co-authors provided input for revision before submission.

Competing interests. The contact author has declared that none of the authors has any competing interests.

Disclaimer. Publisher's note: Copernicus Publications remains neutral with regard to jurisdictional claims in published maps and institutional affiliations.

Special issue statement. This article is part of the special issue "BLUESKY atmospheric composition measurements by aircraft during the COVID-19 lockdown in spring 2020". It is not associated with a conference.

Acknowledgements. We thank the Max Planck Institute for Chemistry and its staff for organising and conducting the CAFE-EU/BLUESKY campaign and the German Aerospace Center (DLR) and its staff for providing the infrastructure, especially during the Corona lockdown. We thank Frank Malkemper, Laurin Merkel, and Robert Sitals for their contributions to the campaign preparation and instrument development. We thank the two anonymous referees for their valuable feedback.

Financial support. This research has been supported by the Deutsche Forschungsgemeinschaft (grant no. TRR 301 "TP-Change" – project ID 428312742, research project A03), the Messer Foundation (Bad Soden am Taunus, Germany), and the Heinrich Böll Stiftung.

This open-access publication was funded
by the Goethe University Frankfurt.

Review statement. This paper was edited by Andreas Petzold and reviewed by two anonymous referees.

References

Arijs, E.: Stratospheric ion chemistry: Present understanding and outstanding problems, Planet. Space Sci., 40, 255–270, https://doi.org/10.1016/0032-0633(92)90064-U, 1992.

Arijs, E., Ingels, J., and Nevejans, D.: Mass spectrometric measurement of the positive ion composition in the stratosphere, Nature, 271, 642–644, https://doi.org/10.1038/271642a0, 1978.

Arnold, F. and Fabian, R.: First measurements of gas phase sulphuric acid in the stratosphere, Nature, 283, 55–57, https://doi.org/10.1038/283055a0, 1980.

Arnold, F. and Henschen, G.: First mass analysis of stratospheric negative ions, Nature, 275, 521–522, https://doi.org/10.1038/275521a0, 1978.

Arnold, F. and Knop, G.: Stratospheric trace gas detection using a new balloon-borne acims method, Int. J. Mass Spectrom. Ion Process., 81, 33–44, https://doi.org/10.1016/0168-1176(87)80004-6, 1987.

Arnold, F. and Qiu, S.: Upper stratosphere negative ion composition measurements and inferred trace gas abundances, Planet. Space Sci., 32, 169–177, https://doi.org/10.1016/0032-0633(84)90151-X, 1984.

Arnold, F., Krankowsky, D., Wieder, H., and Zähringer, J.: Negative ions in the lower ionosphere: A mass spectrometric measurement, J. Atmos. Terr. Phys., 33, 1169–1175, https://doi.org/10.1016/0021-9169(71)90104-8, 1971.

Arnold, F., Krankowsky, D., and Marien, K. H.: First mass spectrometric measurements of positive ions in the stratosphere, Nature, 267, 30–32, https://doi.org/10.1038/267030a0, 1977.

Arnold, F., Böhringer, H., and Henschen, G.: Composition measurements of stratospheric positive ions, Geophys. Res. Lett., 5, 653–656, https://doi.org/10.1029/GL005i008p00653, 1978.

Arnold, F., Heitmann, H., and Oberfrank, K.: First composition measurements of positive ions in the upper troposphere, Planet. Space Sci., 32, 1567–1576, https://doi.org/10.1016/0032-0633(84)90026-6, 1984.

Arnold, F., Wohlfrom, H., Klemm, M. W., Schneider, J., Gollinger, K., Schumann U., and Busen, R.: First gaseous ion composition measurements in the exhaust plume of a jet aircraft in flight: Implications for gaseous sulfuric acid, aerosols, and chemiions, Geophys. Res. Lett., 25, 2137–2140, https://doi.org/10.1029/98GL01579, 1998.

Aufmhoff, H., Hanke, M., Uecker, J., Schlager, H., and Arnold, F.: An ion trap CIMS instrument for combined measurements of atmospheric OH and H2SO4: First test measurements above and inside the planetary boundary layer, Int. J. Mass Spectrom., 308, 26–34, https://doi.org/10.1016/j.ijms.2011.07.016, 2011.

Bazilevskaya, G. A., Usoskin, I. G., Flückiger, E. O., Harrison, R. G., Desorgher, L., Bütikofer, R., Krainev, M. B., Makhmutov, V. S., Stozhkov, Y. I., Svirzhevskaya, A. K., Svirzhevsky, N. S., and Kovaltsov, G. A.: Cosmic Ray Induced Ion Production in the Atmosphere, Space Sci. Rev., 137, 149–173, https://doi.org/10.1007/s11214-008-9339-y, 2008.

Beck, L. J., Schobesberger, S., Junninen, H., Lampilahti, J., Manninen, A., Dada, L., Leino, K., He, X.-C., Pullinen, I., Quéléver, L. L. J., Franck, A., Poutanen, P., Wimmer, D., Korhonen, F., Sipilä, M., Ehn, M., Worsnop, D. R., Kerminen, V.-M., Petäjä, T., Kulmala, M., and Duplissy, J.: Diurnal evolution of negative atmospheric ions above the boreal forest: from ground level

to the free troposphere, Atmos. Chem. Phys., 22, 8547–8577, https://doi.org/10.5194/acp-22-8547-2022, 2022a.

Beck, L. J., Schobesberger, S., Sipilä, M., Kerminen, V.-M., and Kulmala, M.: Estimation of sulfuric acid concentration using ambient ion composition and concentration data obtained with atmospheric pressure interface time-of-flight ion mass spectrometer, Atmos. Meas. Tech., 15, 1957–1965, https://doi.org/10.5194/amt-15-1957-2022, 2022b.

Beig, G. and Brasseur, G. P.: Model of tropospheric ion composition: A first attempt, J. Geophys. Res., 105, 22671–22684, https://doi.org/10.1029/2000JD900119, 2000.

Bianchi, F., Tröstl, J., Junninen, H., Frege, C., Henne, S., Hoyle, C. R., Molteni, U., Herrmann, E., Adamov, A., Bukowiecki, N., Chen, X., Duplissy, J., Gysel, M., Hutterli, M., Kangasluoma, J., Kontkanen, J., Kürten, A., Manninen, H. E., Münch, S., Peräkylä, O., Petäjä, T., Rondo, L., Williamson, C., Weingartner, E., Curtius, J., Worsnop, D. R., Kulmala, M., Dommen, J., and Baltensperger, U.: New particle formation in the free troposphere: A question of chemistry and timing, Science, 352, 1109–1112, https://doi.org/10.1126/science.aad5456, 2016.

Broch, S.: Ein neues LIF-Instrument für flugzeug-und bodengebundene Messungen von OH-und HO2-Radikalen in der Troposphäre, Schriften des Forschungszentrums Jülich: Energie & Umwelt/Energy & Environment, 122, Zentralbibliothek Verlag, Jülich, 2011.

Christiansen, C.: Elektrizitätserregung beim Zerspritzen von Flüssigkeiten (Balloelektrizität), Annalen der Physik, 345, 107–137, https://doi.org/10.1002/andp.19133450105, 1913.

Dörich, R., Eger, P., Lelieveld, J., and Crowley, J. N.: Iodide CIMS and m/z 62: the detection of HNO_3 as NO_3^- in the presence of PAN, peroxyacetic acid and ozone, Atmos. Meas. Tech., 14, 5319–5332, https://doi.org/10.5194/amt-14-5319-2021, 2021.

Drewnick, F., Hings, S. S., DeCarlo, P., Jayne, J. T., Gonin, M., Fuhrer, K., Weimer, S., Jimenez, J. L., Demerjian, K. L., Borrmann, S., and Worsnop, D. R.: A New Time-of-Flight Aerosol Mass Spectrometer (TOF-AMS) – Instrument Description and First Field Deployment, Aerosol Sci. Technol., 39, 637–658, https://doi.org/10.1080/02786820500182040, 2005.

Ehn, M., Junninen, H., Petäjä, T., Kurtén, T., Kerminen, V.-M., Schobesberger, S., Manninen, H. E., Ortega, I. K., Vehkamäki, H., Kulmala, M., and Worsnop, D. R.: Composition and temporal behavior of ambient ions in the boreal forest, Atmos. Chem. Phys., 10, 8513–8530, https://doi.org/10.5194/acp-10-8513-2010, 2010.

Eichkorn, S., Wilhelm, S., Aufmhoff, H., Wohlfrom, K. H., and Arnold, F.: Cosmic ray-induced aerosol-formation: First observational evidence from aircraft-based ion mass spectrometer measurements in the upper troposphere, Geophys. Res. Lett., 29, 43-1–43-4, https://doi.org/10.1029/2002GL015044, 2002.

Eisele, F. L.: Identification of tropospheric ions, J. Geophys. Res., 91, 7897–7906, https://doi.org/10.1029/JD091iD07p07897, 1986.

Eisele, F. L.: First tandem mass spectrometric measurement of tropospheric ions, J. Geophys. Res., 93, 716–724, https://doi.org/10.1029/JD093iD01p00716, 1988.

Eisele, F. L.: Natural and anthropogenic negative ions in the troposphere, J. Geophys. Res., 94, 2183–2196, https://doi.org/10.1029/JD094iD02p02183, 1989a.

Eisele, F. L.: Natural and transmission line produced positive ions, J. Geophys. Res., 94, 6309–6318, https://doi.org/10.1029/JD094iD05p06309, 1989b.

European Environmental Agency: Air pollutant emissions, European Environmental Agency, https://www.eea.europa.eu/data-and-maps/dashboards/air-pollutant-emissions-data-viewer-3, last access: 8 February 2021.

Franchin, A., Ehrhart, S., Leppä, J., Nieminen, T., Gagné, S., Schobesberger, S., Wimmer, D., Duplissy, J., Riccobono, F., Dunne, E. M., Rondo, L., Downard, A., Bianchi, F., Kupc, A., Tsagkogeorgas, G., Lehtipalo, K., Manninen, H. E., Almeida, J., Amorim, A., Wagner, P. E., Hansel, A., Kirkby, J., Kürten, A., Donahue, N. M., Makhmutov, V., Mathot, S., Metzger, A., Petäjä, T., Schnitzhofer, R., Sipilä, M., Stozhkov, Y., Tomé, A., Kerminen, V.-M., Carslaw, K., Curtius, J., Baltensperger, U., and Kulmala, M.: Experimental investigation of ion–ion recombination under atmospheric conditions, Atmos. Chem. Phys., 15, 7203–7216, https://doi.org/10.5194/acp-15-7203-2015, 2015.

Frege, C., Bianchi, F., Molteni, U., Tröstl, J., Junninen, H., Henne, S., Sipilä, M., Herrmann, E., Rossi, M. J., Kulmala, M., Hoyle, C. R., Baltensperger, U., and Dommen, J.: Chemical characterization of atmospheric ions at the high altitude research station Jungfraujoch (Switzerland), Atmos. Chem. Phys., 17, 2613–2629, https://doi.org/10.5194/acp-17-2613-2017, 2017.

Greene, C. A., Thirumalai, K., Kearney, K. A., Delgado, J. M., Schwanghart, W., Wolfenbarger, N. S., Thyng, K. M., Gwyther, D. E., Gardner, A. S., and Blankenship, D. D.: The Climate Data Toolbox for MATLAB, Geochem. Geophys. Geosyst., 20, 3774–3781, https://doi.org/10.1029/2019GC008392, 2019.

He, X.-C., Tham, Y. J., Dada, L., Wang, M., Finkenzeller, H., Stolzenburg, D., Iyer, S., Simon, M., Kürten, A., Shen, J., Rörup, B., Rissanen, M., Schobesberger, S., Baalbaki, R., Wang, D. S., Koenig, T. K., Jokinen, T., Sarnela, N., Beck, L. J., Almeida, J., Amanatidis, S., Amorim, A., Ataei, F., Baccarini, A., Bertozzi, B., Bianchi, F., Brilke, S., Caudillo, L., Granzin, M., Hansel, A., Heinritzi, M., Hofbauer, V., Junninen, H., Kangasluoma, J., Kemppainen, D., Kim, C., Kong, W., Krechmer, J. E., Kvashin, A., Laitinen, T., Lamkaddam, H., Lee, C. P., Lehtipalo, K., Leiminger, M., Li, Z., Makhmutov, V., Manninen, H. E., Marie, G., Marten, R., Mathot, S., Mauldin, R. L., Mentler, B., Möhler, O., Müller, T., Nie, W., Onnela, A., Petäjä, T., Pfeifer, J., Philippov, M., Ranjithkumar, A., Saiz-Lopez, A., Salma, I., Scholz, W., Schuchmann, S., Schulze, B., Steiner, G., Stozhkov, Y., Tauber, C., Tomé, A., Thakur, R. C., Väisänen, O., Vazquez-Pufleau, M., Wagner, A. C., Wang, Y., Weber, S. K., Winkler, P. M., Wu, Y., Xiao, M., Yan, C., Ye, Q., Ylisirniö, A., Zauner-Wieczorek, M., Zha, Q., Zhou, P., Flagan, R. C., Curtius, J., Baltensperger, U., Kulmala, M., Kerminen, V.-M., Kurtén, T., Donahue, N. M., Volkamer, R., Kirkby, J., Worsnop, D. R., and Sipilä, M.: Role of iodine oxoacids in atmospheric aerosol nucleation, Science, 371, 589–595, https://doi.org/10.1126/science.abe0298, 2021.

Heinritzi, M., Simon, M., Steiner, G., Wagner, A. C., Kürten, A., Hansel, A., and Curtius, J.: Characterization of the mass-dependent transmission efficiency of a CIMS, Atmos. Meas. Tech., 9, 1449–1460, https://doi.org/10.5194/amt-9-1449-2016, 2016.

Heitmann, H. and Arnold, F.: Composition measurements of tropospheric ions, Nature, 306, 747–751, https://doi.org/10.1038/306747a0, 1983.

Hensen, A. and van der Hage, J. C. H.: Parameterization of cosmic radiation at sea level, J. Geophys. Res., 99, 10693–10695, https://doi.org/10.1029/93JD01226, 1994.

Hirsikko, A., Nieminen, T., Gagné, S., Lehtipalo, K., Manninen, H. E., Ehn, M., Hõrrak, U., Kerminen, V.-M., Laakso, L., McMurry, P. H., Mirme, A., Mirme, S., Petäjä, T., Tammet, H., Vakkari, V., Vana, M., and Kulmala, M.: Atmospheric ions and nucleation: a review of observations, Atmos. Chem. Phys., 11, 767–798, https://doi.org/10.5194/acp-11-767-2011, 2011.

Hoell, J. M., Davis, D. D., Liu, S. C., Newell, R. E., Akimoto, H., McNeal, R. J., and Bendura, R. J.: The Pacific Exploratory Mission-West Phase B: February-March, 1994, J. Geophys. Res., 102, 28223–28239, https://doi.org/10.1029/97JD02581, 1997.

Hoell, J. M., Davis, D. D., Jacob, D. J., Rodgers, M. O., Newell, R. E., Fuelberg, H. E., McNeal, R. J., Raper, J. L., and Bendura, R. J.: Pacific Exploratory Mission in the tropical Pacific: PEM-Tropics A, August–September 1996, J. Geophys. Res., 104, 5567–5583, https://doi.org/10.1029/1998JD100074, 1999.

Hoose, C. and Möhler, O.: Heterogeneous ice nucleation on atmospheric aerosols: a review of results from laboratory experiments, Atmos. Chem. Phys., 12, 9817–9854, https://doi.org/10.5194/acp-12-9817-2012, 2012.

Hoose, C., Kristjánsson, J. E., and Burrows, S. M.: How important is biological ice nucleation in clouds on a global scale?, Environ. Res. Lett., 5, 24009, https://doi.org/10.1088/1748-9326/5/2/024009, 2010.

Israël, H.: Atmosphärische Elektrizität: Teil 1. Grundlagen, Leitfähigkeit, Ionen, Akademische Verlagsgesellschaft Geest & Portig K.G., Leipzig, 1957.

Israël, H.: Atmospheric Electricity: Volume I. Fundamentals, Conductivity, Ions, 2nd edn., Israel Program for Scientific Translations Ltd, Jerusalem, 1971.

Johnson, C. Y., Meadow, E. B., and Holmes, J. C.: Ion Composition of the Arctic Ionosphere, J. Geophys. Res., 63, 433, https://doi.org/10.1029/JZ063i002p00443, 1958.

Junninen, H., Ehn, M., Petäjä, T., Luosujärvi, L., Kotiaho, T., Kostiainen, R., Rohner, U., Gonin, M., Fuhrer, K., Kulmala, M., and Worsnop, D. R.: A high-resolution mass spectrometer to measure atmospheric ion composition, Atmos. Meas. Tech., 3, 1039–1053, https://doi.org/10.5194/amt-3-1039-2010, 2010.

Jurkat, T., Kaufmann, S., Voigt, C., Schäuble, D., Jeßberger, P., and Ziereis, H.: The airborne mass spectrometer AIMS – Part 2: Measurements of trace gases with stratospheric or tropospheric origin in the UTLS, Atmos. Meas. Tech., 9, 1907–1923, https://doi.org/10.5194/amt-9-1907-2016, 2016.

Kanji, Z. A., Ladino, L. A., Wex, H., Boose, Y., Burkert-Kohn, M., Cziczo, D. J., and Krämer, M.: Overview of Ice Nucleating Particles, Meteorological Monographs, 58, 1.1–1.33, https://doi.org/10.1175/AMSMONOGRAPHS-D-16-0006.1, 2017.

Kürten, A., Rondo, L., Ehrhart, S., and Curtius, J.: Performance of a corona ion source for measurement of sulfuric acid by chemical ionization mass spectrometry, Atmos. Meas. Tech., 4, 437–443, https://doi.org/10.5194/amt-4-437-2011, 2011.

Lee, B. H., Lopez-Hilfiker, F. D., Veres, P. R., McDuffie, E. E., Fibiger, D. L., Sparks, T. L., Ebben, C. J., Green, J. R., Schroder, J. C., Campuzano-Jost, P., Iyer, S., D'Ambro, E. L., Schobesberger, S., Brown, S. S., Wooldridge, P. J., Cohen, R. C., Fiddler, M. N., Bililign, S., Jimenez, J. L., Kurtén, T., Weinheimer, A. J., Jaegle, L., and Thornton, J. A.: Flight Deployment of a High-Resolution Time-of-Flight Chemical Ionization Mass Spectrometer: Observations of Reactive Halogen and Nitrogen Oxide Species, J. Geophys. Res.-Atmos., 105, 3527, https://doi.org/10.1029/2017JD028082, 2018.

Mauldin, R. L., Cantrell, C. A., Zondlo, M. A., Kosciuch, E., Ridley, B. A., Weber, R., and Eisele, F. E.: Measurements of OH, H_2SO_4, and MSA during Tropospheric Ozone Production About the Spring Equinox (TOPSE), J. Geophys. Res., 108, 1329, https://doi.org/10.1029/2002JD002295, 2003.

Möhler, O. and Arnold, F.: Gaseous sulfuric acid and sulfur dioxide measurements in the Arctic troposphere and lower stratosphere: Implications for hydroxyl radical abundances, Geophys. Res. Lett., 19, 1763–1766, https://doi.org/10.1029/92GL01807, 1992.

Möhler, O., Reiner, T., and Arnold, F.: A novel aircraft-based tandem mass spectrometer for atmospheric ion and trace gas measurements, Rev. Sci. Instr., 64, 1199–1207, https://doi.org/10.1063/1.1144455, 1993.

Molleker, S., Helleis, F., Klimach, T., Appel, O., Clemen, H.-C., Dragoneas, A., Gurk, C., Hünig, A., Köllner, F., Rubach, F., Schulz, C., Schneider, J., and Borrmann, S.: Application of an O-ring pinch device as a constant-pressure inlet (CPI) for airborne sampling, Atmos. Meas. Tech., 13, 3651–3660, https://doi.org/10.5194/amt-13-3651-2020, 2020.

Narcisi, R. S. and Bailey, A. D.: Mass spectrometric measurements of positive ions at altitudes from 64 to 112 kilometers, J. Geophys. Res., 70, 3687–3700, https://doi.org/10.1029/JZ070i015p03687, 1965.

Narcisi, R. S., Bailey, A. D., Della Lucca, L., Sherman, C., and Thomas, D. M.: Mass spectrometric measurements of negative ions in the D- and lower E-regions, J. Atmos. Terr. Phys., 33, 1147–1159, https://doi.org/10.1016/0021-9169(71)90102-4, 1971.

National Oceanic and Atmospheric Administration, National Aeronautics and Space Administration, and United States Air Force: U.S. Standard Atmosphere, 1976, U.S. Government Printing Office, Washington, D.C., https://ntrs.nasa.gov/api/citations/19770009539/downloads/19770009539.pdf (last access: 8 September 2022), 1976.

Perkins, M. D. and Eisele, F. L.: First mass spectrometric measurements of atmospheric ions at ground level, J. Geophys. Res., 89, 9649–9657, https://doi.org/10.1029/JD089iD06p09649, 1984.

re3data.org: HALO database, editing status 17 November 2021, re3data.org – Registry of Research Data Repositories [data set], https://doi.org/10.17616/R39Q0T, 2022.

Royal Obervatory of Belgium: Sunspot Index and Longterm Solar Observations (SILSO): Daily and monthly sunspot number (last 13 years), http://sidc.be/silso/dayssnplot, last access: 4 November 2020.

Schneider, J., Arnold, F., Bürger, V., Droste-Franke, B., Grimm, F., Kirchner, G., Klemm, M., Stilp, T., Wohlfromm, K.-H., Siegmund, P., and van Velthoven, P. F. J.: Nitric acid (HNO3) in the upper troposphere and lower stratosphere at midlatitudes: New results from aircraft-based mass spectro-

metric measurements, J. Geophys. Res., 103, 25337–25343, https://doi.org/10.1029/98JD02240, 1998.

Schneider, J., Mertes, S., van Pinxteren, D., Herrmann, H., and Borrmann, S.: Uptake of nitric acid, ammonia, and organics in orographic clouds: mass spectrometric analyses of droplet residual and interstitial aerosol particles, Atmos. Chem. Phys., 17, 1571–1593, https://doi.org/10.5194/acp-17-1571-2017, 2017.

Schulte, P. and Arnold, F.: Pyridinium ions and pyridine in the free troposphere, Geophys. Res. Lett., 17, 1077–1080, https://doi.org/10.1029/GL017i008p01077, 1990.

Schulz, C., Schneider, J., Amorim Holanda, B., Appel, O., Costa, A., de Sá, S. S., Dreiling, V., Fütterer, D., Jurkat-Witschas, T., Klimach, T., Knote, C., Krämer, M., Martin, S. T., Mertes, S., Pöhlker, M. L., Sauer, D., Voigt, C., Walser, A., Weinzierl, B., Ziereis, H., Zöger, M., Andreae, M. O., Artaxo, P., Machado, L. A. T., Pöschl, U., Wendisch, M., and Borrmann, S.: Aircraft-based observations of isoprene-epoxydiol-derived secondary organic aerosol (IEPOX-SOA) in the tropical upper troposphere over the Amazon region, Atmos. Chem. Phys., 18, 14979–15001, https://doi.org/10.5194/acp-18-14979-2018, 2018.

Schumann, U., Schlager, H., Arnold, F., Ovarlez, J., Kelder, H., Hov, Ø., Hayman, G., Isaksen, I. S. A., Staehelin, J., and Whitefield, P. D.: Pollution from aircraft emissions in the North Atlantic flight corridor: Overview on the POLINAT projects, J. Geophys. Res., 105, 3605–3631, https://doi.org/10.1029/1999JD900941, 2000.

Seinfeld, J. H. and Pandis, S. N.: Atmospheric Chemistry and Physics: From Air Pollution to Climate Change, 2nd edn., John Wiley & Sons, Hoboken, New Jersey, 1248 pp., ISBN 9780471720188, 2006.

Shuman, N. S., Hunton, D. E., and Viggiano, A. A.: Ambient and modified atmospheric ion chemistry: from top to bottom, Chem. Rev., 115, 4542–4570, https://doi.org/10.1021/cr5003479, 2015.

Smart, D. F. and Shea, M. A.: A review of geomagnetic cutoff rigidities for earth-orbiting spacecraft, Adv. Space Res., 36, 2012–2020, https://doi.org/10.1016/j.asr.2004.09.015, 2005.

Smart, D. F. and Shea, M. A.: Fifty years of progress in geomagnetic cutoff rigidity determinations, Adv. Space Res., 44, 1107–1123, https://doi.org/10.1016/j.asr.2009.07.005, 2009.

Smith, S. J., van Aardenne, J., Klimont, Z., Andres, R. J., Volke, A., and Delgado Arias, S.: Anthropogenic sulfur dioxide emissions: 1850–2005, Atmos. Chem. Phys., 11, 1101–1116, https://doi.org/10.5194/acp-11-1101-2011, 2011.

Stockwell, W. R. and Calvert, J. G.: The mechanism of the HO-SO_2 reaction, Atmos. Environ., 17, 2231–2235, https://doi.org/10.1016/0004-6981(83)90220-2, 1983.

Thomson, J. J. and Rutherford, E.: XL. On the passage of electricity through gases exposed to Röntgen rays, The London, Edinburgh, and Dublin Philosophical Magazine and Journal of Science, 42, 392–407, https://doi.org/10.1080/14786449608620932, 1896.

Viggiano, A. A. and Arnold, F.: Ion Chemistry and Composition of the Atmosphere, in: Handbook of Atmospheric Dynamics. Volume 1. Atmospheric Electricity, edited by: Volland, H., CRC Press, Boca Raton, London, Tokyo, 1–25, ISBN 0849386470, 1995.

Viggiano, A. A., Seeley, J. V., Mundis, P. L., Williamson, J. S., and Morris, R. A.: Rate Constants for the Reactions of XO_3-$(H_2O)n$ (X = C, HC, and N) and NO_3-$(HNO_3)n$ with H_2SO_4: Implications for Atmospheric Detection of H_2SO_4, J. Phys. Chem. A, 101, 8275–8278, https://doi.org/10.1021/jp971768h, 1997.

Voigt, C., Lelieveld, J., Schlager, H., Schneider, J., Curtius, J., Meerkötter, R., Sauer, D., Buglario, L., Bohn, B., Crowley, J. N., Erbetseder, T., Groß, S., Hahn, V., Li, Q., Mertens, M., Pöhlker, M., Pozzer, A., Schumann, U., Tomsche, L., Williams, J., Zahn, A., Andreae, M. O., Borrmann, S., Bräuer, T., Dörich, R., Dörnbrack, A., Edtbauer, A., Ernle, L., Fischer, H., Giez, A., Granzin, M., Grewe, V., Harder, H., Heinritzi, M., Holanda, B., Jöckel, P., Kaiser, K., Krüger, O., Lucke, J., Marsing, A., Martin, A., Matthes, S., Pöhlker, C., Pöschl, U., Reifenberg, S., Ringsdorf, A., Scheibe, M., Tadic, I., Zauner-Wieczorek, M., Henke, R., and Rapp, M.: Cleaner Skies during the COVID-19 Lockdown, B. Am. Meteorol. Soc., 103, E1798–E1827, https://doi.org/10.1175/BAMS-D-21-0012.1, 2022.

Weber, R. J., McMurry, P. H., Mauldin, R. L., Tanner, D. J., Eisele, F. L., Clarke, A. D., and Kapustin, V. N.: New Particle Formation in the Remote Troposphere: A Comparison of Observations at Various Sites, Geophys. Res. Lett., 26, 307–310, https://doi.org/10.1029/1998GL900308, 1999.

Weber, R. J., Chen, G., Davis, D. D., Mauldin, R. L., Tanner, D. J., Eisele, F. L., Clarke, A. D., Thornton, D. C., and Bandy, A. R.: Measurements of enhanced H2SO4 and 3-4 nm particles near a frontal cloud during the First Aerosol Characterization Experiment ACE 1, J. Geophys. Res., 106, 24107–24117, https://doi.org/10.1029/2000JD000109, 2001.

Weber, R. J., Lee, S., Chen, G., Wang, B., Kapustin, V., Moore, K., Clarke, A. D., Mauldin, R. L., Kosciuch, E., Cantrell, C., Eisele, F., Thornton, D. C., Bandy, A. R., Sachse, G. W., and Fuelberg, H. E.: New particle formation in anthropogenic plumes advecting from Asia observed during TRACE-P, J. Geophys. Res., 108, 7433, https://doi.org/10.1029/2002JD003112, 2003.

Zauner-Wieczorek, M., Curtius, J., and Kürten, A.: The ion-ion recombination coefficient α: Comparison of temperature- and pressure-dependent parameterisations for the troposphere and lower stratosphere, Atmos. Chem. Phys. Discuss. [preprint], https://doi.org/10.5194/acp-2021-795, in review, 2021.

5 Conclusion and outlook

In this dissertation, a newly developed nitrate-CI source coupled to an APi-TOF-MS for airborne measurements was described, the measurements of atmospheric ions and trace gases such as sulfuric acid, nitrogen oxides, carbon monoxide, and sulfur dioxide on board the research aircraft HALO and Falcon in the troposphere and lower stratosphere were presented, and theories of the ion–ion recombination and its coefficient were reviewed.

The CI source SCORPION was developed to enable high resolution in-situ measurements of low volatile compounds in the troposphere and lower stratosphere. It produces nitrate reagent ions from nitric acid by corona discharge. Furthermore, it features an automated pressure regulation that ensures a constant pressure of 200 hPa inside the IMR, a high laminar inlet flow to minimise wall losses, and a counter-flow setup in the corona discharge ionisation region to exclude reactive products of the discharge process from entering the IMR. In the CI mode, the SCORPION-TOF-MS can detect species such as sulfuric acid, HOMs, C_2 amines, and MSA. When switching off the corona voltage, it can also measure ambient ions in the APi mode. Thus, the SCORPION-TOF-MS was certified for installation on board the HALO.

The first HALO campaign employing the SCORPION-TOF-MS, CAFE-EU/BLUESKY, was conducted successfully during the first COVID lockdown in Europe in May and June 2020 and is described in Voigt et al. (2022). In total, there were eight scientific flights with HALO and twelve scientific flights with the Falcon with complementary instrumentation covering trace gases, aerosol particles, and meteorological parameters over Western Europe, sampling continental, rural, and marine air masses as well as deep convective cloud outflows. A nudged version of the EMAC model was used to simulate emissions for flight planning. Due to the lockdown, significant reductions in the emission of NO_x and CO could be observed over industrial areas, in the Po Valley, and above Frankfurt am Main. Similarly, the number concentrations and the mass of aerosol particles were reduced in continental profiles, especially below 5 km altitude. Moreover, the contrail cover was reduced due to the reduced air travel.

The stratospheric sulfur compounds were found to be perturbed due to the outbreak of the Raikoke volcano in 2019. Further results from this campaign have already been published and are awaiting publication. Future campaigns will focus on biogenic and marine regimes in Brazil and the Western Pacific, respectively.

During the eight scientific flights, the SCORPION-TOF-MS successfully measured atmospheric ions, sulfuric acid, MSA, and C_2 amines, amongst others. These measurements are the first ever reported CI-APi-TOF-MS and APi-TOF-MS measurements in the UTLS region. In Zauner-Wieczorek et al. (2022a), the measurements of atmospheric ions in the APi mode were described in more detail. In the negative APi mode, the ions and ion clusters $(HNO_3)_{0–2}NO_3^-$, HSO_4^-, $(H_2SO_4)HSO_4^-$, $(HNO_3)HSO_4^-$, and presumably SO_4^- were detected. The ion counts of NO_3^- and $(HNO_3)NO_3^-$ showed an increasing trend with increasing altitudes, while there was no significant trend for HSO_4^-. From the ratio of the nitrate and hydrogen sulfate core ions, the number concentration of gaseous sulfuric acid could be inferred. The resulting average concentrations were in the range of 1.9 to $7.8 \cdot 10^5$ cm^{-3} in the altitude range of 4.7–13.4 km. Maximum values were observed in the altitude bin of 8.7–9.2 km, while the concentrations were lower above the tropopause which is in agreement with the literature. Furthermore, an event of increased ion counts, particle concentration, and relative humidity lasting for 30 seconds was observed at a 5.3 km flight altitude while passing through a cloud. This event could have been caused by the shattering of liquid cloud water droplets on the surface of the aircraft or inlet. In the positive APi mode, protonated pyridine was detected and a maximum ion count was observed between 4.6 and 8.5 km altitude. More research is necessary to resolve the temporal or spatial variations and to identify more ions, especially in the positive APi mode.

In order to calculate the number concentration of sulfuric acid from hydrogen sulfate and nitrate core ions as mentioned above, the ion–ion recombination must be known. Since it is pressure and temperature dependent, it has different values at different altitudes. Theories and parameterisations of the ion–ion recombination coefficient α were reviewed in Zauner-Wieczorek et al. (2022b) in order to find a favourable formula to calculate α for different flight altitudes. Thomson and Rutherford introduced a thermodynamic theory of the recombination (Thomson and Rutherford, 1896; Thomson, 1924) and, subsequently, several scientists developed parameterisations according to this theory; these parameterisations were dependent on the temperature, the pressure, the mass of the ions, and the mean free path of the ions and air. In contrast to this, Langevin (1903) developed an electrodynamic theory that was later found

to be valid in the super-atmospheric pressure regime, while Thomson's theory is applicable at 1000 hPa or below. After α was determined from parameters measured in the field by Gringel et al. (1978), Rosen and Hofmann (1981), and Morita (1983), more parameterisations were developed, partly as altitude-dependent formulas. α was also simulated by the Monte Carlo method as well as hybrid continuum-molecular dynamics simulations by Bates (1982) and Tamadate et al. (2020), respectively. Moreover, in the review, ion–aerosol attachment theories were applied to the ion–ion recombination and were considered in an intercomparison which also included laboratory data from Franchin et al. (2015) and model data from Bates (1982), as well as the above-mentioned field data. This intercomparison showed that there is no single theory that can describe the ion–ion recombination throughout the whole troposphere and stratosphere. For altitudes below 22 km, the parameterisation by Israël (1957) was found to be favourable, while above 25 km, the parameterisation by Arijs et al. (1983), and above 30 km, Hoppel and Frick's (1986) theory yielded the best agreement. In addition, the ion–ion trapping distance and the collision probability in the limiting sphere – two parameters that are important in different theories – were determined using the aforementioned field data as input. The need for further research was identified. Measurements of α in the troposphere are necessary to close the existing gap. In addition, measurements in different regions during different seasons are necessary to uncover possible spatial or seasonal variations. Furthermore, the magnitudes of the temperature and pressure dependence of α need to be determined by model simulations since the different theories contradict each other in this regard.

The results of the CI measurements during CAFE-EU/BLUESKY with regard to sulfuric acid, MSA, and C_2 amines will be published elsewhere. The comparison of sulfuric acid measurements in the CI and the APi mode is pending. In the future, simultaneous airborne measurements of these nucleation precursors as well as HOMs and, ideally, NH_3 along with measurements of the size distribution and chemical composition of aerosol particles are necessary in order to study the NPF in the upper troposphere. Due to its relevance in the global atmospheric circulation, the tropical upper troposphere is of special interest in this regard. Therefore, measurement campaigns above the Amazon rainforest in Brazil (CAFE-Brazil) and above the (sub-)tropical Pacific Ocean (CAFE-Pacific) will be conducted in the next months and can be complemented by model simulations. One aim of the CAFE-Brazil campaign is to verify (or falsify) the hypothesis of pure biogenic nucleation in the upper troposphere above the Amazon rainforest; especially the contribution or absence of sulfuric acid in the upper

tropospheric NPF needs to be investigated (Andreae et al., 2018). These data are important for a better understanding of the chemical systems nucleating in the upper troposphere.

In this dissertation, advances in the research of atmospheric ions, nucleation precursors, and air pollutants were presented – pieces in the vast puzzle of atmospheric sciences. The need for future research is unchanged in order to unravel remaining questions and to solve the problems of today and tomorrow.

6 References

Almeida, J., Schobesberger, S., Kürten, A., Ortega, I. K., Kupiainen-Määttä, O., Praplan, A. P., Adamov, A., Amorim, A., Bianchi, F., Breitenlechner, M., David, A., Dommen, J., Donahue, N. M., Downard, A., Dunne, E., Duplissy, J., Ehrhart, S., Flagan, R. C., Franchin, A., Guida, R., Hakala, J., Hansel, A., Heinritzi, M., Henschel, H., Jokinen, T., Junninen, H., Kajos, M., Kangasluoma, J., Keskinen, H., Kupc, A., Kurtén, T., Kvashin, A. N., Laaksonen, A., Lehtipalo, K., Leiminger, M., Leppä, J., Loukonen, V., Makhmutov, V., Mathot, S., McGrath, M. J., Nieminen, T., Olenius, T., Onnela, A., Petäjä, T., Riccobono, F., Riipinen, I., Rissanen, M., Rondo, L., Ruuskanen, T., Santos, F. D., Sarnela, N., Schallhart, S., Schnitzhofer, R., Seinfeld, J. H., Simon, M., Sipilä, M., Stozhkov, Y., Stratmann, F., Tomé, A., Tröstl, J., Tsagkogeorgas, G., Vaattovaara, P., Viisanen, Y., Virtanen, A., Vrtala, A., Wagner, P. E., Weingartner, E., Wex, H., Williamson, C., Wimmer, D., Ye, P., Yli-Juuti, T., Carslaw, K. S., Kulmala, M., Curtius, J., Baltensperger, U., Worsnop, D. R., Vehkamäki, H., and Kirkby, J.: Molecular understanding of sulphuric acid-amine particle nucleation in the atmosphere, Nature, 502, 359–363, https://doi.org/10.1038/nature12663, 2013.

Andreae, M. O., Afchine, A., Albrecht, R., Holanda, B. A., Artaxo, P., Barbosa, H. M. J., Borrmann, S., Cecchini, M. A., Costa, A., Dollner, M., Fütterer, D., Järvinen, E., Jurkat, T., Klimach, T., Konemann, T., Knote, C., Krämer, M., Krisna, T., Machado, L. A. T., Mertes, S., Minikin, A., Pöhlker, C., Pöhlker, M. L., Pöschl, U., Rosenfeld, D., Sauer, D., Schlager, H., Schnaiter, M., Schneider, J., Schulz, C., Spanu, A., Sperling, V. B., Voigt, C., Walser, A., Wang, J., Weinzierl, B., Wendisch, M., and Ziereis, H.: Aerosol characteristics and particle production in the upper troposphere over the Amazon Basin, Atmospheric Chemistry and Physics, 18, 921–961, https://doi.org/10.5194/acp-18-921-2018, 2018.

Arijs, E., Nevejans, D., Ingels, J., and Frederick, P.: Positive ion composition measurements between 33 and 20 km altitude, Annales Geophysicae, 1, 161–166, 1983.

Arnold, F. and Hauck, G.: Lower stratosphere trace gas detection using aircraft-borne active chemical ionization mass spectrometry, Nature, 315, 307–309, https://doi.org/10.1038/315307a0, 1985.

Arnold, F. and Qiu, S.: Upper stratosphere negative ion composition measurements and inferred trace gas abundances, Planetary and Space Science, 32, 169–177, https://doi.org/10.1016/0032-0633(84)90151-X, 1984.

Arnold, F.: Atmospheric Ions and Aerosol Formation, Space Science Reviews, 137, 225–239, https://doi.org/10.1007/s11214-008-9390-8, 2008.

Basu, S., Buchau, J., Rich, F. J., Weber, E. J., Field, E. C., Heckscher, J. L., Kossey, P. A., Lewis, E. A., Dandekar, B. S., McNamara, L. F., Cliver, E. W., Millman, G. H., Aarons, J., Klobuchar, J. A., and Mendillo, M. F.: Chapter 10. Ionospheric radio wave propagation, in: Handbook of geophysics and the space environment, edited by: Jursa, A. S., 1985.

Bates, D. R.: Ion-ion recombination in an ambient gas, Advances in Atomic and Molecular Physics, 20, 1–39, https://doi.org/10.1016/S0065-2199(08)60264-X, 1985.

Bates, D. R.: Recombination of small ions in the troposphere and lower stratosphere, Planetary and Space Science, 30, 1275–1282, https://doi.org/10.1016/0032-0633(82)90101-5, 1982.

Bazilevskaya, G. A., Usoskin, I. G., Flückiger, E. O., Harrison, R. G., Desorgher, L., Bütikofer, R., Krainev, M. B., Makhmutov, V. S., Stozhkov, Y. I., Svirzhevskaya, A. K., Svirzhevsky, N. S., and Kovaltsov, G. A.: Cosmic Ray Induced Ion Production in the Atmosphere, Space Science Reviews, 137, 149–173, https://doi.org/10.1007/s11214-008-9339-y, 2008.

Behera, S. N., Sharma, M., Aneja, V. P., and Balasubramanian, R.: Ammonia in the atmosphere: a review on emission sources, atmospheric chemistry and deposition on terrestrial bodies, Environmental Science and Pollution Research International, 20, 8092–8131, https://doi.org/10.1007/s11356-013-2051-9, 2013.

Bellouin, N., Quaas, J., Gryspeerdt, E., Kinne, S., Stier, P., Watson-Parris, D., Boucher, O., Carslaw, K. S., Christensen, M., Daniau, A.-L., Dufresne, J.-L., Feingold, G., Fiedler, S., Forster, P., Gettelman, A., Haywood, J. M., Lohmann, U., Malavelle, F., Mauritsen, T., McCoy, D. T., Myhre, G., Mülmenstädt, J., Neubauer, D., Possner, A., Rugenstein, M., Sato, Y., Schulz, M., Schwartz, S. E., Sourdeval, O., Storelvmo, T., Toll, V., Winker, D., and Stevens, B.: Bounding Global Aerosol Radiative Forcing of Climate Change, Reviews of Geophysics, 58, e2019RG000660, https://doi.org/10.1029/2019RG000660, 2020.

Berndt, T., Richters, S., Jokinen, T., Hyttinen, N., Kurtén, T., Otkjær, R. V., Kjaergaard, H. G., Stratmann, F., Herrmann, H., Sipilä, M., Kulmala, M., and Ehn, M.: Hydroxyl radical-induced formation of highly oxidized organic compounds, Nature Communications, 7, 13677, https://doi.org/10.1038/ncomms13677, 2016a.

Berndt, T., Herrmann, H., Sipilä, M., and Kulmala, M.: Highly Oxidized Second-Generation Products from the Gas-Phase Reaction of OH Radicals with Isoprene, The Journal of Physical Chemistry A, 120, 10150–10159, https://doi.org/10.1021/acs.jpca.6b10987, 2016b.

Berresheim, H., Elste, T., Plass-Dülmer, C., Eisele, F. L., and Tanner, D. J.: Chemical ionization mass spectrometer for long-term measurements of atmospheric OH and H2SO4, International Journal of Mass Spectrometry, 202, 91–109, https://doi.org/10.1016/S1387-3806(00)00233-5, 2000.

Bliefert, C.: Umweltchemie, 3rd ed., Wiley-VCH, Weinheim, 2002.

Brasseur, G. and Chatel, A.: Modelling of stratospheric ions: a first attempt, Annales Geophysicae, 1, 173–185, available at: https://orfeo.kbr.be/bitstream/handle/internal/6155/Brasseur%281983f%29.pdf?sequence=1&isAllowed=y, 1983.

Broch, S.: Ein neues LIF-Instrument für flugzeug-und bodengebundene Messungen von OH- und HO2-Radikalen in der Troposphäre, Schriften des Forschungszentrums Jülich: Energie & Umwelt / Energy & Environment, 122, Zentralbibliothek Verlag, Jülich, available at: https://d-nb.info/1020476451/34 (last access: 15 Nov 2022), 2011.

Brophy, P. and Farmer, D. K.: Clustering, methodology, and mechanistic insights into acetate chemical ionization using high-resolution time-of-flight mass spectrometry, Atmospheric Measurement Techniques, 9, 3969–3986, https://doi.org/10.5194/amt-9-3969-2016, 2016.

Chen, H., Ezell, M. J., Arquero, K. D., Varner, M. E., Dawson, M. L., Gerber, R. B., and Finlayson-Pitts, B. J.: New particle formation and growth from methanesulfonic acid, trimethylamine and water, Physical Chemistry Chemical Physics, 17, 13699–13709, https://doi.org/10.1039/c5cp00838g, 2015.

Chen, Y., Ebenstein, A., Greenstone, M., and Li, H.: Evidence on the impact of sustained exposure to air pollution on life expectancy from China's Huai River policy, Proceedings of the National Academy of Sciences of the United States of America, 110, 12936–12941, https://doi.org/10.1073/pnas.1300018110, 2013.

Chhabra, P. S., Lambe, A. T., Canagaratna, M. R., Stark, H., Jayne, J. T., Onasch, T. B., Davidovits, P., Kimmel, J. R., and Worsnop, D. R.: Application of high-resolution time-of-flight chemical ionization mass spectrometry measurements to estimate volatility distributions of α-pinene and naphthalene oxidation products, Atmospheric Measurement Techniques, 8, 1–18, https://doi.org/10.5194/amt-8-1-2015, 2015.

Christiansen, C.: Elektrizitätserregung beim Zerspritzen von Flüssigkeiten (Balloelektrizität), Annalen der Physik, 345, 107–137, https://doi.org/10.1002/andp.19133450105, 1913.

Clarke, A. D., Kapustin, V. N., Eisele, F. L., Weber, R. J., and McMurry, P. H.: Particle production near marine clouds: Sulfuric acid and predictions from classical binary nucleation, Geophysical Research Letters, 26, 2425–2428, https://doi.org/10.1029/1999GL900438, 1999.

Crounse, J. D., Nielsen, L. B., Jørgensen, S., Kjaergaard, H. G., and Wennberg, P. O.: Autoxidation of Organic Compounds in the Atmosphere, The Journal of Physical Chemistry Letters, 4, 3513–3520, https://doi.org/10.1021/jz4019207, 2013.

Crounse, J. D., McKinney, K. A., Kwan, A. J., and Wennberg, P. O.: Measurement of gas-phase hydroperoxides by chemical ionization mass spectrometry, Analytical Chemistry, 78, 6726–6732, https://doi.org/10.1021/ac0604235, 2006.

Crutzen, P. J.: The influence of nitrogen oxides on the atmospheric ozone content, Quarterly Journal of the Royl Meteorological Society, 96, 320–325, 1970.

Crutzen, P. J.: The possible importance of CSO for the sulfate layer of the stratosphere, Geophysical Research Letters, 3, 73–76, https://doi.org/10.1029/GL003i002p00073, 1976.

Curtius, J., Lovejoy, E. R., and Froyd, K. D.: Atmospheric Ion-induced Aerosol Nucleation, Space Science Reviews, 125, 159–167, https://doi.org/10.1007/s11214-006-9054-5, 2007.

Donahue, N. M., Kroll, J. H., Pandis, S. N., and Robinson, A. L.: A two-dimensional volatility basis set – Part 2: Diagnostics of organic-aerosol evolution, Atmospheric Chemistry and Physics, 12, 615–634, https://doi.org/10.5194/acp-12-615-2012, 2012.

Donahue, N. M., Epstein, S. A., Pandis, S. N., and Robinson, A. L.: A two-dimensional volatility basis set: 1. organic-aerosol mixing thermodynamics, Atmospheric Chemistry and Physics, 11, 3303–3318, https://doi.org/10.5194/acp-11-3303-2011, 2011.

Dörich, R., Eger, P., Lelieveld, J., and Crowley, J. N.: Iodide CIMS and m/z = 62: the detection of HNO3 as NO3− in the presence of PAN, peroxyacetic acid and ozone, Atmospheric Measurement Techniques, 14, 5319–5332, https://doi.org/10.5194/amt-14-5319-2021, 2021.

Ehn, M., Kleist, E., Junninen, H., Petäjä, T., Lönn, G., Schobesberger, S., Dal Maso, M., Trimborn, A., Kulmala, M., Worsnop, D. R., Wahner, A., Wildt, J., and Mentel, T. F.: Gas phase formation of extremely oxidized pinene reaction products in chamber and ambient air, Atmospheric Chemistry and Physics, 12, 5113–5127, https://doi.org/10.5194/acp-12-5113-2012, 2012.

Ehn, M., Thornton, J. A., Kleist, E., Sipilä, M., Junninen, H., Pullinen, I., Springer, M., Rubach, F., Tillmann, R., Lee, B., Lopez-Hilfiker, F., Andres, S., Acir, I.-H., Rissanen, M., Jokinen, T., Schobesberger, S., Kangasluoma, J., Kontkanen, J., Nieminen, T., Kurtén, T., Nielsen, L. B., Jørgensen, S., Kjaergaard, H. G., Canagaratna, M., Maso, M. D., Berndt, T., Petäjä, T., Wahner, A., Kerminen, V.-M., Kulmala, M., Worsnop, D. R., Wildt, J., and Mentel, T. F.: A large source of low-volatility secondary organic aerosol, Nature, 506, 476–479, https://doi.org/10.1038/nature13032, 2014.

Eisele, F. L. and Tanner, D. J.: Measurement of the gas phase concentration of H2SO4 and methane sulfonic acid and estimates of H2SO4 production and loss in the atmosphere, Journal of Geophysical Research, 98, 9001–9010, 1993.

Fiedler, V., Dal Maso, M., Boy, M., Aufmhoff, H., Hoffmann, J., Schuck, T., Birmili, W., Hanke, M., Uecker, J., Arnold, F., and Kulmala, M.: The contribution of sulphuric acid to atmospheric particle formation and growth: a comparison between boundary layers in Northern and Central Europe, Atmospheric Chemistry and Physics, 5, 1773–1785, https://doi.org/10.5194/acp-5-1773-2005, 2005.

Filippov, A. V.: Charging of Aerosol in the Transition Regime, Journal of Aerosol Science, 24, 423–436, https://doi.org/10.1016/0021-8502(93)90029-9, 1993.

Foote, E.: Circumstances affecting the Heat of the Sun's Rays, American Journal of Science and Arts, 22, 382–383, available at: https://upload.wikimedia.org/wikipedia/commons/5/57/Eunice_Foote_-_%22Circumstances_Affecting_the_Heat_of_the_Sun%27s_Rays%22_%281856%29.png, 1856.

Franchin, A., Ehrhart, S., Leppä, J., Nieminen, T., Gagné, S., Schobesberger, S., Wimmer, D., Duplissy, J., Riccobono, F., Dunne, E. M., Rondo, L., Downard, A., Bianchi, F., Kupc, A., Tsagkogeorgas, G., Lehtipalo, K., Manninen, H. E., Almeida, J., Amorim, A., Wagner, P. E., Hansel, A., Kirkby, J., Kürten, A., Donahue, N. M., Makhmutov, V., Mathot, S.,

Metzger, A., Petäjä, T., Schnitzhofer, R., Sipilä, M., Stozhkov, Y., Tomé, A., Kerminen, V.-M., Carslaw, K., Curtius, J., Baltensperger, U., and Kulmala, M.: Experimental investigation of ion–ion recombination under atmospheric conditions, Atmospheric Chemistry and Physics, 15, 7203–7216, https://doi.org/10.5194/acp-15-7203-2015, 2015.

Fuchs, N. A.: On the stationary charge distribution on aerosol particles in a bipolar ionic atmosphere, Geofisica pura e applicata, 56, 185–193, https://doi.org/10.1007/BF01993343, 1963.

Ge, X., Wexler, A. S., and Clegg, S. L.: Atmospheric amines – Part I. A review, Atmospheric Environment, 45, 524–546, https://doi.org/10.1016/j.atmosenv.2010.10.012, 2011.

Greene, C. A., Thirumalai, K., Kearney, K. A., Delgado, J. M., Schwanghart, W., Wolfenbarger, N. S., Thyng, K. M., Gwyther, D. E., Gardner, A. S., and Blankenship, D. D.: The Climate Data Toolbox for MATLAB, Geochemistry, Geophysics, Geosystems, 20, 3774–3781, https://doi.org/10.1029/2019GC008392, 2019.

Gringel, W., Käselau, K. H., and Mühleisen, R.: Recombination rates of small ions and their attachment to aerosol particles, Pure and Applied Geophysics, 116, 1101–1113, https://doi.org/10.1007/BF00874674, 1978.

Guevara, M.: D8: Scientific content explaining the main outcomes of the project and data analysis, Copernicus Atmosphere Monitoring Service, ECMWF Copernicus Report, 24 pp., 2020.

Haagen-Smit, A. J.: Chemistry and Physiology of Los Angeles Smog, Industrial and Engineering Chemistry, 44, 1342–1346, https://doi.org/10.1021/ie50510a045, 1952.

Harrison, R. G.: Fair weather atmospheric electricity, Journal of Physics: Conference Series, 301, 12001, https://doi.org/10.1088/1742-6596/301/1/012001, 2011.

Hatakeyama, S., Okuda, M., and Akimoto, H.: Formation of sulfur dioxide and methanesulfonic acid in the photooxidation of dimethyl sulfide in the air, Geophysical Research Letters, 9, 583–586, https://doi.org/10.1029/GL009i005p00583, 1982.

He, X.-C., Tham, Y. J., Dada, L., Wang, M., Finkenzeller, H., Stolzenburg, D., Iyer, S., Simon, M., Kürten, A., Shen, J., Rörup, B., Rissanen, M., Schobesberger, S., Baalbaki, R., Wang, D. S., Koenig, T. K., Jokinen, T., Sarnela, N., Beck, L., Almeida, J., Amanatidis, S., Amorim, A., Ataei, F., Baccarini, A., Bertozzi, B., Bianchi, F., Brilke, S., Caudillo, L., Chen, D., Chiu, R., Chu, B., Dias, A., Ding, A., Dommen, J., Duplissy, J., El Haddad, I., Gonzalez-Carracedo, L., Granzin, M., Hansel, A., Heinritzi, M., Hofbauer, V., Junninen, H., Kangasluoma, J., Kemppainen, D., Kim, C., Kong, W., Krechmer, J. E., Kvashin, A., Laitinen, T., Lamkaddam, H., Lee, C. P., Lehtipalo, K., Leiminger, M., Li, Z., Makhmutov, V., Manninen, H. E., Marie, G., Marten, R., Mathot, S., Mauldin, R. L., Mentler, B., Möhler, O., Müller, T., Nie, W., Onnela, A., Petäjä, T., Pfeifer, J., Philippov, M., Ranjithkumar, A., Saiz-Lopez, A., Salma, I., Scholz, W., Schuchmann, S., Schulze, B., Steiner, G., Stozhkov, Y., Tauber, C., Tomé, A., Thakur, R. C., Väisänen, O., Vazquez-Pufleau, M., Wagner, A. C., Wang, Y., Weber, S. K., Winkler, P. M., Wu, Y., Xiao, M., Yan, C., Ye, Q., Ylisirniö, A., Zauner-Wieczorek, M., Zha, Q., Zhou, P., Flagan, R. C., Curtius, J., Baltensperger, U., Kulmala, M., Kerminen, V.-M., Kurtén, T., Donahue, N. M., Volkamer, R., Kirkby, J.,

Worsnop, D. R., and Sipilä, M.: Role of iodine oxoacids in atmospheric aerosol nucleation, Science, 371, 589–595, https://doi.org/10.1126/science.abe0298, 2021.

Heitmann, H. and Arnold, F.: Composition measurements of tropospheric ions, Nature, 306, 747–751, https://doi.org/10.1038/306747a0, 1983.

Hickman, A. P.: Approximate scaling formula for ion–ion mutual neutralization rates, The Journal of Chemical Physics, 70, 4872–4878, https://doi.org/10.1063/1.437364, 1979.

Hirsikko, A., Nieminen, T., Gagné, S., Lehtipalo, K., Manninen, H. E., Ehn, M., Hõrrak, U., Kerminen, V.-M., Laakso, L., McMurry, P. H., Mirme, A., Mirme, S., Petäjä, T., Tammet, H., Vakkari, V., Vana, M., and Kulmala, M.: Atmospheric ions and nucleation: a review of observations, Atmospheric Chemistry and Physics, 11, 767–798, https://doi.org/10.5194/acp-11-767-2011, 2011.

Hoppel, W. A.: Nucleation in the MSA-Water Vapor System, Atmospheric Environment, 21, 2703–2709, https://doi.org/10.1016/0004-6981(87)90202-2, 1987.

Hoppel, W. A. and Frick, G. M.: Ion—Aerosol Attachment Coefficients and the Steady-State Charge Distribution on Aerosols in a Bipolar Ion Environment, Aerosol Science and Technology, 5, 1–21, https://doi.org/10.1080/02786828608959073, 1986.

Huey, L. G., Villalta, P. W., Dunlea, E. J., Hanson, D. R., and Howard, C. J.: Reactions of CF3O- with Atmopsheric Trace Gases, Journal of Physical Chemistry, 100, 190–194, https://doi.org/10.1021/jp951928u, 1996.

Hyttinen, N., Otkjær, R. V., Iyer, S., Kjaergaard, H. G., Rissanen, M. P., Wennberg, P. O., and Kurtén, T.: Computational Comparison of Different Reagent Ions in the Chemical Ionization of Oxidized Multifunctional Compounds, The Journal of Physical Chemistry A, 122, 269–279, https://doi.org/10.1021/acs.jpca.7b10015, 2018.

Hyttinen, N., Rissanen, M. P., and Kurtén, T.: Computational Comparison of Acetate and Nitrate Chemical Ionization of Highly Oxidized Cyclohexene Ozonolysis Intermediates and Products, The Journal of Physical Chemistry A, 121, 2172–2179, https://doi.org/10.1021/acs.jpca.6b12654, 2017.

IPCC AR6 Working Group I (Ed.): Climate Change 2021: The Physical Science Basis. Contribution of Working Group I to the Sixth Assessment Report of the Intergovernmental Panel on Climate Change, Cambridge University Press, Cambridge, New York, 2021.

Israël, H.: Atmosphärische Elektrizität: Teil 1. Grundlagen, Leitfähigkeit, Ionen, Akademische Verlagsgesellschaft Geest & Portig K.G., Leipzig, 1957.

Jardine, K., Yañez-Serrano, A. M., Williams, J., Kunert, N., Jardine, A., Taylor, T., Abrell, L., Artaxo, P., Guenther, A., Hewitt, C. N., House, E., Florentino, A. P., Manzi, A., Higuchi, N., Kesselmeier, J., Behrendt, T., Veres, P. R., Derstroff, B., Fuentes, J. D., Martin, S. T., and Andreae, M. O.: Dimethyl sulfide in the Amazon rain forest, Global Biogeochemical Cycles, 29, 19–32, https://doi.org/10.1002/2014GB004969, 2015.

Jayne, J. T., Pöschl, U., Chen, Y.-m., Dai, D., Molina, L. T., Worsnop, D. R., Kolb, C. E., and Molina, M. J.: Pressure and Temperature Dependence of the Gas-Phase Reaction of SO3

with H2O and the Heterogeneous Reaction of SO3 with H2O/H2SO4 Surfaces, Journal of Physical Chemistry A, 101, 10000–10011, https://doi.org/10.1021/jp972549z, 1997.

Johnson, C. Y., Meadows, E. B., and Holmes, J. C.: Ion composition of the Arctic ionosphere, Journal of Geophysical Research, 63, 443–444, https://doi.org/10.1029/JZ063i002p00443, 1958.

Johnston, H.: Reduction of Stratospheric Ozone by Nitrogen Oxide Catalysts from Supersonic Transport Exhaust, Science, 173, 517–522, https://doi.org/10.1126/science.173.3996.517, 1971.

Jost, C., Sprung, D., Kenntner, T., and Reiner, T.: Atmospheric pressure chemical ionization mass spectrometry for the detection of tropospheric trace gases: the influence of clustering on sensitivity and precision, International Journal of Mass Spectrometry, 223-224, 771–782, https://doi.org/10.1016/S1387-3806(02)00963-6, 2003.

Junninen, H., Ehn, M., Petäjä, T., Luosujärvi, L., Kotiaho, T., Kostiainen, R., Rohner, U., Gonin, M., Fuhrer, K., Kulmala, M., and Worsnop, D. R.: A high-resolution mass spectrometer to measure atmospheric ion composition, Atmospheric Measurement Techniques, 3, 1039–1053, https://doi.org/10.5194/amt-3-1039-2010, 2010.

Kazil, J. and Lovejoy, E. R.: Tropospheric ionization and aerosol production: A model study, Journal of Geophysical Research, 109, 23709, https://doi.org/10.1029/2004JD004852, 2004.

Kazil, J., Harrison, R. G., and Lovejoy, E. R.: Tropospheric New Particle Formation and the Role of Ions, Space Science Reviews, 137, 241–255, https://doi.org/10.1007/s11214-008-9388-2, 2008.

Kebarle, P. and Verkerk, U. H.: Electrospray: From ions in solution to ions in the gas phase, what we know now, Mass Spectrometry Reviews, 28, 898–917, https://doi.org/10.1002/mas.20247, 2009.

Kirkby, J.: Cosmic Rays and Climate, Surveys in Geophysics, 28, 333–375, https://doi.org/10.1007/s10712-008-9030-6, 2007.

Kirkby, J., Duplissy, J., Sengupta, K., Frege, C., Gordon, H., Williamson, C., Heinritzi, M., Simon, M., Yan, C., Almeida, J., Tröstl, J., Nieminen, T., Ortega, I. K., Wagner, R., Adamov, A., Amorim, A., Bernhammer, A.-K., Bianchi, F., Breitenlechner, M., Brilke, S., Chen, X., Craven, J., Dias, A., Ehrhart, S., Flagan, R. C., Franchin, A., Fuchs, C., Guida, R., Hakala, J., Hoyle, C. R., Jokinen, T., Junninen, H., Kangasluoma, J., Kim, J., Krapf, M., Kürten, A., Laaksonen, A., Lehtipalo, K., Makhmutov, V., Mathot, S., Molteni, U., Onnela, A., Peräkylä, O., Piel, F., Petäjä, T., Praplan, A. P., Pringle, K., Rap, A., Richards, N. A. D., Riipinen, I., Rissanen, M. P., Rondo, L., Sarnela, N., Schobesberger, S., Scott, C. E., Seinfeld, J. H., Sipilä, M., Steiner, G., Stozhkov, Y., Stratmann, F., Tomé, A., Virtanen, A., Vogel, A. L., Wagner, A. C., Wagner, P. E., Weingartner, E., Wimmer, D., Winkler, P. M., Ye, P., Zhang, X., Hansel, A., Dommen, J., Donahue, N. M., Worsnop, D. R., Baltensperger, U., Kulmala, M., Carslaw, K. S., and Curtius, J.: Ion-induced nucleation of pure biogenic particles, Nature, 533, 521–526, https://doi.org/10.1038/nature17953, 2016.

Kirkby, J., Curtius, J., Almeida, J., Dunne, E., Duplissy, J., Ehrhart, S., Franchin, A., Gagné, S., Ickes, L., Kürten, A., Kupc, A., Metzger, A., Riccobono, F., Rondo, L., Schobesberger, S., Tsagkogeorgas, G., Wimmer, D., Amorim, A., Bianchi, F., Breitenlechner, M., David, A., Dommen, J., Downard, A., Ehn, M., Flagan, R. C., Haider, S., Hansel, A., Hauser, D., Jud, W., Junninen, H., Kreissl, F., Kvashin, A., Laaksonen, A., Lehtipalo, K., Lima, J., Lovejoy, E. R., Makhmutov, V., Mathot, S., Mikkilä, J., Minginette, P., Mogo, S., Nieminen, T., Onnela, A., Pereira, P., Petäjä, T., Schnitzhofer, R., Seinfeld, J. H., Sipilä, M., Stozhkov, Y., Stratmann, F., Tomé, A., Vanhanen, J., Viisanen, Y., Vrtala, A., Wagner, P. E., Walther, H., Weingartner, E., Wex, H., Winkler, P. M., Carslaw, K. S., Worsnop, D. R., Baltensperger, U., and Kulmala, M.: Role of sulphuric acid, ammonia and galactic cosmic rays in atmospheric aerosol nucleation, Nature, 476, 429–433, https://doi.org/10.1038/nature10343, 2011.

Kürten, A., Rondo, L., Ehrhart, S., and Curtius, J.: Performance of a corona ion source for measurement of sulfuric acid by chemical ionization mass spectrometry, Atmospheric Measurement Techniques, 4, 437–443, https://doi.org/10.5194/amt-4-437-2011, 2011.

Kürten, A., Li, C., Bianchi, F., Curtius, J., Dias, A., Donahue, N. M., Duplissy, J., Flagan, R. C., Hakala, J., Jokinen, T., Kirkby, J., Kulmala, M., Laaksonen, A., Lehtipalo, K., Makhmutov, V., Onnela, A., Rissanen, M. P., Simon, M., Sipilä, M., Stozhkov, Y., Tröstl, J., Ye, P., and McMurry, P. H.: New particle formation in the sulfuric acid–dimethylamine–water system: reevaluation of CLOUD chamber measurements and comparison to an aerosol nucleation and growth model, Atmospheric Chemistry and Physics, 18, 845–863, https://doi.org/10.5194/acp-18-845-2018, 2018.

Kürten, A., Bergen, A., Heinritzi, M., Leiminger, M., Lorenz, V., Piel, F., Simon, M., Sitals, R., Wagner, A. C., and Curtius, J.: Observation of new particle formation and measurement of sulfuric acid, ammonia, amines and highly oxidized organic molecules at a rural site in central Germany, Atmospheric Chemistry and Physics, 16, 12793–12813, https://doi.org/10.5194/acp-16-12793-2016, 2016.

Langevin, M. P.: Recombinaison et mobilités des ions dans les gaz, Annales de chimie et de physique, 433-530, 1903.

Lee, B. H., Lopez-Hilfiker, F. D., Veres, P. R., McDuffie, E. E., Fibiger, D. L., Sparks, T. L., Ebben, C. J., Green, J. R., Schroder, J. C., Campuzano-Jost, P., Iyer, S., D'Ambro, E. L., Schobesberger, S., Brown, S. S., Wooldridge, P. J., Cohen, R. C., Fiddler, M. N., Bililign, S., Jimenez, J. L., Kurtén, T., Weinheimer, A. J., Jaegle, L., and Thornton, J. A.: Flight Deployment of a High-Resolution Time-of-Flight Chemical Ionization Mass Spectrometer: Observations of Reactive Halogen and Nitrogen Oxide Species, Journal of Geophysical Research: Atmospheres, 105, 3527, https://doi.org/10.1029/2017JD028082, 2018.

Lee, B. H., Lopez-Hilfiker, F. D., Mohr, C., Kurtén, T., Worsnop, D. R., and Thornton, J. A.: An iodide-adduct high-resolution time-of-flight chemical-ionization mass spectrometer: application to atmospheric inorganic and organic compounds, Environmental Science & Technology, 48, 6309–6317, https://doi.org/10.1021/es500362a, 2014.

Lee, C., Martin, R. V., van Donkelaar, A., Lee, H., Dickerson, R. R., Hains, J. C., Krotkov, N., Richter, A., Vinnikov, K., and Schwab, J. J.: SO2 emissions and lifetimes: Estimates from

inverse modeling using in situ and global, space-based (SCIAMACHY and OMI) observations, Journal of Geophysical Research, 116, L24113, https://doi.org/10.1029/2010JD014758, 2011.

Lelieveld, J., Klingmüller, K., Pozzer, A., Pöschl, U., Fnais, M., Daiber, A., and Münzel, T.: Cardiovascular disease burden from ambient air pollution in Europe reassessed using novel hazard ratio functions, European Heart Journal, 40, 1590–1596, https://doi.org/10.1093/eurheartj/ehz135, 2019.

Lenz, E.: Die Wiedervereinigung von Ionen in Luft bei niederen Drucken, Zeitschrift für Physik, 76, 660–678, https://doi.org/10.1007/BF01341939, 1932.

Li, F., Lawrence, D. M., Jiang, Y., Liu, X., and Lin, Z.: Fire aerosols slow down the global water cycle, Journal of Climate, [in press], https://doi.org/10.1175/JCLI-D-21-0817.1, 2022.

Liou, K. N.: Radiation and Cloud Processes in the Atmosphere. Theory, Observation, and Modeling, Oxford University Press, New York, Oxford, 1992.

Lopez-Hilfiker, F. D., Pospisilova, V., Huang, W., Kalberer, M., Mohr, C., Stefenelli, G., Thornton, J. A., Baltensperger, U., Prevot, A. S. H., and Slowik, J. G.: An extractive electrospray ionization time-of-flight mass spectrometer (EESI-TOF) for online measurement of atmospheric aerosol particles, Atmospheric Measurement Techniques, 12, 4867–4886, https://doi.org/10.5194/amt-12-4867-2019, 2019.

Maher, S., Jjunju, F. P. M., and Taylor, S.: Colloquium 100 years of mass spectrometry: Perspectives and future trends, Reviews of Modern Physics, 87, 113–135, https://doi.org/10.1103/RevModPhys.87.113, 2015.

Märk, T. D. and Dunn, G. H. (Eds.): Electron Impact Ionization, Springer, Wien, 1985.

Miller, T. M., Shuman, N. S., and Viggiano, A. A.: Behavior of rate coefficients for ion-ion mutual neutralization, 300-550 K, The Journal of Chemical Physics, 136, 204306, https://doi.org/10.1063/1.4720499, 2012.

Möhler, O. and Arnold, F.: Gaseous sulfuric acid and sulfur dioxide measurements in the Arctic troposphere and lower stratosphere: Implications for hydroxyl radical abundances, Geophysical Research Letters, 19, 1763–1766, https://doi.org/10.1029/92GL01807, 1992.

Morita, Y.: Recent measurements of electrical conductivity and ion pair production rate, and the ion-ion recombination coefficient derived from them in the lower stratosphere, Journal of Geomagnetism and Geoelectricity, 35, 29–38, https://doi.org/10.5636/jgg.35.29, 1983.

Natanson, G. L.: The Theory of Volume Recombination of Ions, Journal of Technical Physics, 4, 1263–1269, 1959.

Paul, W. and Steinwedel, H.: Ein neues Massenspektrometer ohne Magnetfeld, Zeitschrift für Naturforschung A, 8a, https://doi.org/10.1515/zna-1953-0710, 1953.

Rosen, J. M. and Hofmann, D. J.: Balloon-borne measurements of electrical conductivity, mobility, and the recombination coefficient, Journal of Geophysical Research: Oceans, 86, 7406–7410, https://doi.org/10.1029/JC086iC08p07406, 1981.

Salcedo, D., Villalta, P. W., Varutbangkul, V., Wormhoudt, J. C., Miake-Lye, R. C., Worsnop, D. R., Ballenthin, J. O., Thorn, W. F., Viggiano, A. A., Miller, T. M., Flagan, R. C., and Seinfeld, J. H.: Effect of relative humidity on the detection of sulfur dioxide and sulfuric acid using a chemical ionization mass spectrometer, International Journal of Mass Spectrometry, 231, 17–30, https://doi.org/10.1016/j.ijms.2003.09.005, 2004.

Sanchez, J., Tanner, D. J., Chen, D., Huey, L. G., and Ng, N. L.: A new technique for the direct detection of HO₂ radicals using bromide chemical ionization mass spectrometry (Br-CIMS): initial characterization, Atmospheric Measurement Techniques, 9, 3851–3861, https://doi.org/10.5194/amt-9-3851-2016, 2016.

Sayed, S.: Weiterentwicklung und Charakterisierung einer Elektrospray-Ionenquelle zur Messung von Spurengasen bei ultraniedrigen Konzentrationen, Bachelor thesis, Institute for Atmospheric and Environmental Sciences, Goethe University Frankfurt am Main, Frankfurt am Main, 2021.

Schervish, M. and Donahue, N. M.: Peroxy radical chemistry and the volatility basis set, Atmospheric Chemistry and Physics, 20, 1183–1199, https://doi.org/10.5194/acp-20-1183-2020, 2020.

Seeley, J. V., Morris, R. A., and Viggiano, A. A.: Rate constants for the reactions of CO3−(H2O)n=0–5 + SO2: Implications for CIMS detection of SO2, Geophysical Research Letters, 24, 1379–1382, https://doi.org/10.1029/97GL01323, 1997.

Seinfeld, J. H. and Pandis, S. N.: Atmospheric chemistry and physics from air pollution to climate change, 3rd ed., Wiley, Hoboken, New Jersey, 2016.

Shen, J., Scholz, W., He, X.-C., Zhou, P., Marie, G., Wang, M., Marten, R., Surdu, M., Rörup, B., Baalbaki, R., Amorim, A., Ataei, F., Bell, D. M., Bertozzi, B., Brasseur, Z., Caudillo, L., Chen, D., Chu, B., Dada, L., Duplissy, J., Finkenzeller, H., Granzin, M., Guida, R., Heinritzi, M., Hofbauer, V., Iyer, S., Kemppainen, D., Kong, W., Krechmer, J. E., Kürten, A., Lamkaddam, H., Lee, C. P., Lopez, B., Mahfouz, N. G. A., Manninen, H. E., Massabò, D., Mauldin, R. L., Mentler, B., Müller, T., Pfeifer, J., Philippov, M., Piedehierro, A. A., Roldin, P., Schobesberger, S., Simon, M., Stolzenburg, D., Tham, Y. J., Tomé, A., Umo, N. S., Wang, D., Wang, Y., Weber, S. K., Welti, A., Wollesen de Jonge, R., Wu, Y., Zauner-Wieczorek, M., Zust, F., Baltensperger, U., Curtius, J., Flagan, R. C., Hansel, A., Möhler, O., Petäjä, T., Volkamer, R., Kulmala, M., Lehtipalo, K., Rissanen, M., Kirkby, J., El-Haddad, I., Bianchi, F., Sipilä, M., Donahue, N. M., and Worsnop, D. R.: High Gas-Phase Methanesulfonic Acid Production in the OH-Initiated Oxidation of Dimethyl Sulfide at Low Temperatures, Environmental Science & Technology, 56, 13931–13944, https://doi.org/10.1021/acs.est.2c05154, 2022.

Shuman, N. S., Hunton, D. E., and Viggiano, A. A.: Ambient and modified atmospheric ion chemistry: from top to bottom, Chemical Reviews, 115, 4542–4570, https://doi.org/10.1021/cr5003479, 2015.

Shumilov, O. I., Kasatkina, E. A., Henriksen, K., and Vashenyuk, E. V.: Enhancement of stratospheric arerosols after solar proton event, Annales Geophysicae, 14, 1119–1123, https://doi.org/10.1007/s00585-996-1119-y, 1996.

Sillman, S., Logan, J. A., and Wofsy, S. C.: The sensitivity of ozone to nitrogen oxides and hydrocarbons in regional ozone episodes, Journal of Geophysical Research: Atmospheres, 95, 1837–1851, https://doi.org/10.1029/JD095iD02p01837, 1990.

Simon, M., Dada, L., Heinritzi, M., Scholz, W., Stolzenburg, D., Fischer, L., Wagner, A. C., Kürten, A., Rörup, B., He, X.-C., Almeida, J., Baalbaki, R., Baccarini, A., Bauer, P. S., Beck, L., Bergen, A., Bianchi, F., Bräkling, S., Brilke, S., Caudillo, L., Chen, D., Chu, B., Dias, A., Draper, D. C., Duplissy, J., El-Haddad, I., Finkenzeller, H., Frege, C., Gonzalez-Carracedo, L., Gordon, H., Granzin, M., Hakala, J., Hofbauer, V., Hoyle, C. R., Kim, C., Kong, W., Lamkaddam, H., Lee, C. P., Lehtipalo, K., Leiminger, M., Mai, H., Manninen, H. E., Marie, G., Marten, R., Mentler, B., Molteni, U., Nichman, L., Nie, W., Ojdanic, A., Onnela, A., Partoll, E., Petäjä, T., Pfeifer, J., Philippov, M., Quéléver, L. L. J., Ranjithkumar, A., Rissanen, M. P., Schallhart, S., Schobesberger, S., Schuchmann, S., Shen, J., Sipilä, M., Steiner, G., Stozhkov, Y., Tauber, C., Tham, Y. J., Tomé, A. R., Vazquez-Pufleau, M., Vogel, A. L., Wagner, R., Wang, M., Wang, D. S., Wang, Y., Weber, S. K., Wu, Y., Xiao, M., Yan, C., Ye, P., Ye, Q., Zauner-Wieczorek, M., Zhou, X., Baltensperger, U., Dommen, J., Flagan, R. C., Hansel, A., Kulmala, M., Volkamer, R., Winkler, P. M., Worsnop, D. R., Donahue, N. M., Kirkby, J., and Curtius, J.: Molecular understanding of new-particle formation from α-pinene between −50 and +25 °C, Atmospheric Chemistry and Physics, 20, 9183–9207, https://doi.org/10.5194/acp-20-9183-2020, 2020.

Smith, D. and Adams, N. G.: Ionic recombination in the stratosphere, Geophysical Research Letters, 9, 1085–1087, https://doi.org/10.1029/GL009i009p01085, 1982.

Stephens, W. E.: A Pulsed Mass Spectrometer with Time Dispersion, Physical Review, 69, 691, 1946.

Stockwell, W. R. and Calvert, J. G.: The mechanism of the HO-SO2 reaction, Atmospheric Environment, 17, 2231–2235, https://doi.org/10.1016/0004-6981(83)90220-2, 1983.

Tamadate, T., Higashi, H., Seto, T., and Hogan, C. J., J.: Calculation of the ion-ion recombination rate coefficient via a hybrid continuum-molecular dynamics approach, The Journal of Chemical Physics, 152, 94306, https://doi.org/10.1063/1.5144772, 2020.

Thomson, J. J.: XXIX. Recombination of gaseous ions, the chemical combination of gases, and monomolecular reactions, The London, Edinburgh, and Dublin Philosophical Magazine and Journal of Science, 47, 337–378, https://doi.org/10.1080/14786442408634372, 1924.

Thomson, J. J.: Rays of positive electricity and their application to chemical analyses, Longmans, Green and Co., London, New York, Mumbai, and Kolkata, 1913.

Thomson, J. J.: XIX. Further experiments on positive rays, The London, Edinburgh, and Dublin Philosophical Magazine and Journal of Science, 24, 209–253, https://doi.org/10.1080/14786440808637325, 1912.

Thomson, J. J. and Rutherford, E.: XL. On the passage of electricity through gases exposed to Röntgen rays, The London, Edinburgh, and Dublin Philosophical Magazine and Journal of Science, 42, 392–407, https://doi.org/10.1080/14786449608620932, 1896.

Tröstl, J., Chuang, W. K., Gordon, H., Heinritzi, M., Yan, C., Molteni, U., Ahlm, L., Frege, C., Bianchi, F., Wagner, R., Simon, M., Lehtipalo, K., Williamson, C., Craven, J. S., Duplissy, J., Adamov, A., Almeida, J., Bernhammer, A.-K., Breitenlechner, M., Brilke, S., Dias, A., Ehrhart, S., Flagan, R. C., Franchin, A., Fuchs, C., Guida, R., Gysel, M., Hansel, A., Hoyle, C. R., Jokinen, T., Junninen, H., Kangasluoma, J., Keskinen, H., Kim, J., Krapf, M., Kürten, A., Laaksonen, A., Lawler, M., Leiminger, M., Mathot, S., Möhler, O., Nieminen, T., Onnela, A., Petäjä, T., Piel, F. M., Miettinen, P., Rissanen, M. P., Rondo, L., Sarnela, N., Schobesberger, S., Sengupta, K., Sipilä, M., Smith, J. N., Steiner, G., Tomè, A., Virtanen, A., Wagner, A. C., Weingartner, E., Wimmer, D., Winkler, P. M., Ye, P., Carslaw, K. S., Curtius, J., Dommen, J., Kirkby, J., Kulmala, M., Riipinen, I., Worsnop, D. R., Donahue, N. M., and Baltensperger, U.: The role of low-volatility organic compounds in initial particle growth in the atmosphere, Nature, 533, 527–531, https://doi.org/10.1038/nature18271, 2016.

van Rooy, P., Drover, R., Cress, T., Michael, C., Purvis-Roberts, K. L., Silva, P. J., Nee, M. J., and Cocker, D.: Methanesulfonic acid and sulfuric acid Aerosol Formed through oxidation of reduced sulfur compounds in a humid environment, Atmospheric Environment, 261, 118504, https://doi.org/10.1016/j.atmosenv.2021.118504, 2021.

Viggiano, A. A., Seeley, J. V., Mundis, P. L., Williamson, J. S., and Morris, R. A.: Rate Constants for the Reactions of XO3-(H2O)n (X = C, HC, and N) and NO3-(HNO3)n with H2SO4: Implications for Atmospheric Detection of H2SO4, Journal of Physical Chemistry A, 101, 8275–8278, https://doi.org/10.1021/jp971768h, 1997.

Viggiano, A. A. and Arnold, F.: Ion Chemistry and Composition of the Atmosphere, in: Handbook of Atmospheric Electrodynamics. Volume I, edited by: Volland, H., CRC Press, Boca Raton, London, Tokyo, 1–25, 1995.

Voigt, C., Lelieveld, J., Schlager, H., Schneider, J., Curtius, J., Meerkötter, R., Sauer, D., Bugliaro, L., Bohn, B., Crowley, J. N., Erbertseder, T., Groß, S., Hahn, V., Li, Q., Mertens, M., Pöhlker, M. L., Pozzer, A., Schumann, U., Tomsche, L., Williams, J., Zahn, A., Andreae, M., Borrmann, S., Bräuer, T., Dörich, R., Dörnbrack, A., Edtbauer, A., Ernle, L., Fischer, H., Giez, A., Granzin, M., Grewe, V., Harder, H., Heinritzi, M., Holanda, B. A., Jöckel, P., Kaiser, K., Krüger, O. O., Lucke, J., Marsing, A., Martin, A., Matthes, S., Pöhlker, C., Pöschl, U., Reifenberg, S., Ringsdorf, A., Scheibe, M., Tadic, I., Zauner-Wieczorek, M., Henke, R., and Rapp, M.: Cleaner Skies during the COVID-19 Lockdown, Bulletin of the American Meteorological Society, 103, E1796-E1827, https://doi.org/10.1175/BAMS-D-21-0012.1, 2022.

Wang, M., Xiao, M., Bertozzi, B., Marie, G., Rörup, B., Schulze, B., Bardakov, R., He, X.-C., Shen, J., Scholz, W., Marten, R., Dada, L., Baalbaki, R., Lopez, B., Lamkaddam, H., Manninen, H. E., Amorim, A., Ataei, F., Bogert, P., Brasseur, Z., Caudillo, L., Menezes, L.-P. de, Duplissy, J., Ekman, A. M. L., Finkenzeller, H., Carracedo, L. G., Granzin, M., Guida, R., Heinritzi, M., Hofbauer, V., Höhler, K., Korhonen, K., Krechmer, J. E., Kürten, A., Lehtipalo, K., Mahfouz, N. G. A., Makhmutov, V., Massabò, D., Mathot, S., Mauldin, R. L., Mentler, B., Müller, T., Onnela, A., Petäjä, T., Philippov, M., Piedehierro, A. A., Pozzer, A., Ranjithkumar, A., Schervish, M., Schobesberger, S., Simon, M., Stozhkov, Y., Tomé, A., Umo, N. S., Vogel, F., Wagner, R., Wang, D. S., Weber, S. K., Welti, A., Wu,

Y., Zauner-Wieczorek, M., Sipilä, M., Winkler, P. M., Hansel, A., Baltensperger, U., Kulmala, M., Flagan, R. C., Curtius, J., Riipinen, I., Gordon, H., Lelieveld, J., El-Haddad, I., Volkamer, R., Worsnop, D. R., Christoudias, T., Kirkby, J., Möhler, O., and Donahue, N. M.: Synergistic HNO3-H2SO4-NH3 upper tropospheric particle formation, Nature, 605, 483–489, https://doi.org/10.1038/s41586-022-04605-4, 2022.

Wang, M., He, X.-C., Finkenzeller, H., Iyer, S., Chen, D., Shen, J., Simon, M., Hofbauer, V., Kirkby, J., Curtius, J., Maier, N., Kurtén, T., Worsnop, D. R., Kulmala, M., Rissanen, M., Volkamer, R., Tham, Y. J., Donahue, N. M., and Sipilä, M.: Measurement of iodine species and sulfuric acid using bromide chemical ionization mass spectrometers, Atmospheric Measurement Techniques, 14, 4187–4202, https://doi.org/10.5194/amt-14-4187-2021, 2021.

Wang, M., Kong, W., Marten, R., He, X.-C., Chen, D., Pfeifer, J., Heitto, A., Kontkanen, J., Dada, L., Kürten, A., Yli-Juuti, T., Manninen, H. E., Amanatidis, S., Amorim, A., Baalbaki, R., Baccarini, A., Bell, D. M., Bertozzi, B., Bräkling, S., Brilke, S., Murillo, L. C., Chiu, R., Chu, B., Menezes, L.-P. de, Duplissy, J., Finkenzeller, H., Carracedo, L. G., Granzin, M., Guida, R., Hansel, A., Hofbauer, V., Krechmer, J., Lehtipalo, K., Lamkaddam, H., Lampimäki, M., Lee, C. P., Makhmutov, V., Marie, G., Mathot, S., Mauldin, R. L., Mentler, B., Müller, T., Onnela, A., Partoll, E., Petäjä, T., Philippov, M., Pospisilova, V., Ranjithkumar, A., Rissanen, M., Rörup, B., Scholz, W., Shen, J., Simon, M., Sipilä, M., Steiner, G., Stolzenburg, D., Tham, Y. J., Tomé, A., Wagner, A. C., Wang, D. S., Wang, Y., Weber, S. K., Winkler, P. M., Wlasits, P. J., Wu, Y., Xiao, M., Ye, Q., Zauner-Wieczorek, M., Zhou, X., Volkamer, R., Riipinen, I., Dommen, J., Curtius, J., Baltensperger, U., Kulmala, M., Worsnop, D. R., Kirkby, J., Seinfeld, J. H., El-Haddad, I., Flagan, R. C., and Donahue, N. M.: Rapid growth of new atmospheric particles by nitric acid and ammonia condensation, Nature, 581, 184–189, https://doi.org/10.1038/s41586-020-2270-4, 2020.

Weber, R. J., McMurry, P. H., Mauldin, R. L., Tanner, D. J., Eisele, F. L., Clarke, A. D., and Kapustin, V. N.: New Particle Formation in the Remote Troposphere A Comparison of Observations at Various Sites, Geophysical Research Letters, 26, 307–310, https://doi.org/10.1029/1998GL900308, 1999.

Wolff, M. M. and Stephens, W. E.: A Pulsed Mass Spectrometer with Time Dispersion, Review of Scientific Instruments, 24, 616–617, https://doi.org/10.1063/1.1770801, 1953.

World Health Organization: Ambient air pollution: a global assessment of exposure and burden of disease, available at: https://apps.who.int/iris/rest/bitstreams/1061179/retrieve (Last access: 15 Nov 2022), 2016.

Yatavelli, R. L. N., Lopez-Hilfiker, F., Wargo, J. D., Kimmel, J. R., Cubison, M. J., Bertram, T. H., Jimenez, J. L., Gonin, M., Worsnop, D. R., and Thornton, J. A.: A Chemical Ionization High-Resolution Time-of-Flight Mass Spectrometer Coupled to a Micro Orifice Volatilization Impactor (MOVI-HRToF-CIMS) for Analysis of Gas and Particle-Phase Organic Species, Aerosol Science and Technology, 46, 1313–1327, https://doi.org/10.1080/02786826.2012.712236, 2012.

Yu, F. and Turco, R. P.: Ultrafine aerosol formation via ion-mediated nucleation, Geophysical Research Letters, 27, 883–886, https://doi.org/10.1029/1999GL011151, 2000.

Zauner-Wieczorek, M.: Development and characterisation of an electrospray ion source coupled with an Atmospheric Pressure interface-Time Of Flight (APi-TOF) mass spectrometer, Master thesis, Institute for Atmospheric and Enviromental Sciences, Goethe University Frankfurt am Main, Frankfurt am Main, 2018.

Zauner-Wieczorek, M., Heinritzi, M., Granzin, M., Keber, T., Kürten, A., Kaiser, K., Schneider, J., and Curtius, J.: Mass spectrometric measurements of ambient ions and estimation of gaseous sulfuric acid in the free troposphere and lowermost stratosphere during the CAFE-EU/BLUESKY campaign, Atmospheric Chemistry and Physics, 22, 11781–11794, https://doi.org/10.5194/acp-22-11781-2022, 2022a.

Zauner-Wieczorek, M., Curtius, J., and Kürten, A.: The ion–ion recombination coefficient α: comparison of temperature- and pressure-dependent parameterisations for the troposphere and stratosphere, Atmospheric Chemistry and Physics, 22, 12443–12465, https://doi.org/10.5194/acp-22-12443-2022, 2022b.

Zhao, L.: Technische Überarbeitung einer Elektrospray-Ionenquelle zur Messung von Spurengasen mit Relevanz bei der atmosphärischen Nukleation, Master thesis, Institute for Atmospheric and Environmental Sciences, Goethe University Frankfurt am Main, Frankfurt am Main, 2019.

Zhao, Y., Chan, J. K., Lopez-Hilfiker, F. D., McKeown, M. A., D'Ambro, E. L., Slowik, J. G., Riffell, J. A., and Thornton, J. A.: An electrospray chemical ionization source for real-time measurement of atmospheric organic and inorganic vapors, Atmospheric Measurement Techniques, 10, 3609–3625, https://doi.org/10.5194/amt-10-3609-2017, 2017.

List of abbreviations and acronyms

AOT	Aerosol optical thickness
APi	Atmospheric pressure interface
BC	Black carbon
CAFE-EU	Chemistry of the Atmosphere: Field Experiment in Europe
CCN	Cloud condensation nucleus/nuclei
CI	Chemical ionisation
CIMS	Chemical ionisation mass spectrometer
DLR	German Aerospace Center
DMA	Dimethylamine
DMS	Dimethyl sulfide
DT	Drift tube
EESI	Extractive electrospray ionisation
ESCI	Electrospray chemical ionisation
ESI	Electrospray ionisation
GC	Gas chromatography
GCR	Galactic cosmic ray
GHG	Greenhouse gas
GOME-2	Global Ozone Monitoring Experiment 2
HALO	High Altitude Long Range research aircraft
HOM	Highly oxygenated organic molecule
HYSPLIT	Hybrid single particle Lagrangian integrated trajectory model

IIN	Ion-induced nucleation
IMR	Ion–molecule reaction
MetOp-B	Meteorogical operational satellite B
MCP	Microchannel plate detector
MD	Molecular dynamics
MFC	Mass flow controller
MODIS	Moderate resolution imaging spectroradiometer
MOZAIC	Measurement of ozone and water vapor by airbus in-service aircraft
MS	Mass spectrometer
MSA	Methanesulfonic acid
NAT	North Atlantic Tracks
NMVOC	Non-methane volatile organic compound
NO_x	Nitrogen oxides NO and NO_2
NO_y	Reactive nitrogen oxide species
NPF	New particle formation
OBF	Oberpfaffenhofen airport
OVOC	Oxidised volatile organic compound
PAN	Peroxyacetyl nitrate or peroxyacyl nitrate
PM1	Particulate matter with a diameter of ≤ 1 µm
SCORPION	Switchable corona-powered ion (source)
SEP	Solar energetic particle
SZA	Solar zenith angle
TOA	Top of the atmosphere
TOF	Time of flight
TP	Tropopause
UTLS	Upper troposphere and lower stratosphere
VBS	Volatility basis set
VOC	Volatile organic compound

List of figures and tables